(6)

Resistance to Fracture, Fatigue and Stress-Corrosion of Al-Cu-Li-Zr Alloys

A. K. Vasudevan, R. C. Malcolm,
W. G. Fricke, and R. J. Rioja

Aluminum Company of America
Aloca Laboratories
Alcoa Center, PA 15069

Final Report
(Period: 1981 July 01 to 1985 February 28)
Contract N00019-80-C-0569
Department of the Navy
Naval Air Systems Command
Washington, D.C. 20361

Approved for public release.
Distribution unlimited.

1985 June 30

"Original contains color plates: All DTIC reproductions will be in black and white"

RESISTANCE TO FRACTURE, FATIGUE AND STRESS-CORROSION OF AL-CU-LI-ZR ALLOYS

A. K. VASUDEVAN
R. C. MALCOLM
W. G. FRICKE
R. J. RIOJA

ALUMINUM COMPANY OF AMERICA
ALCOA LABORATORIES
ALCOA CENTER, PA 15069

FINAL REPORT
(PERIOD: 1981 JULY 01 TO 1985 FEBRUARY 28)
CONTRACT N00019-80-C-0569
DEPARTMENT OF THE NAVY
NAVAL AIR SYSTEMS COMMAND
WASHINGTON, DC 20361

APPROVED FOR PUBLIC RELEASE
DISTRIBUTION UNLIMITED

1985 JUNE 30

TABLE OF CONTENTS

UNCLASSIFIED

SECURITY CLASSIFICATION OF THIS PAGE (When Data Entered)

REPORT DOCUMENTATION PAGE		READ INSTRUCTIONS BEFORE COMPLETING FORM
1. REPORT NUMBER	2. GOVT ACCESSION NO. AD-A158 407	3. RECIPIENT'S CATALOG NUMBER
4. TITLE (and Subtitle) Resistance to Fracture, Fatigue and Stress Corrosion of Al-Cu-Li-Zr Alloys		5. TYPE OF REPORT & PERIOD COVERED FINAL 1981 July 1 to 1985 Feb. 28
		6. PERFORMING ORG. REPORT NUMBER
7. AUTHOR(s) A. K. Vasudevan, R. C. Malcolm, W. G. Fricke, R. J. Rioja		8. CONTRACT OR GRANT NUMBER(s) N00019-80-C-0569
9. PERFORMING ORGANIZATION NAME AND ADDRESS Aluminum Company of America, Alcoa Technical Center, Alcoa Center, PA 15069		10. PROGRAM ELEMENT, PROJECT, TASK AREA & WORK UNIT NUMBERS
11. CONTROLLING OFFICE NAME AND ADDRESS Department of the NAVY, Naval Air Systems Command, Washington, DC 20361		12. REPORT DATE 1985 Feb. 19
		13. NUMBER OF PAGES
14. MONITORING AGENCY NAME & ADDRESS(if different from Controlling Office)		15. SECURITY CLASS. (of this report) Unclassified
		15a. DECLASSIFICATION/DOWNGRADING SCHEDULE

16. DISTRIBUTION STATEMENT (of this Report)

Approved for public release
Distribution unlimited

17. DISTRIBUTION STATEMENT (of the abstract entered in Block 20, if different from Report)

18. SUPPLEMENTARY NOTES

19. KEY WORDS (Continue on reverse side if necessary and identify by block number)

Al-Cu-Li-Zr	Aging Treatment	Stress Corrosion
7075	Microstructure	Fractography
2020	Microscopy	Fatigue Crack Growth
Hydrogen	Texture	Constant Amplitude
Composition	Fracture	Spectrum Loading

20. ABSTRACT (Continue on reverse side if necessary and identify by block number)

This investigation was undertaken to characterize the role of composition/microstructure on the mechanical behavior of Al-Cu-Li-Zr alloys. This characterization is intended to serve as a baseline data for alloy development work directed at improving the mechanical properties of Al-Li alloys. The report summarizes the results on fracture, fatigue and stress corrosion behavior of Al-Cu-Li-Zr alloys.

DD FORM 1473 1 JAN 73 EDITION OF 1 NOV 65 IS OBSOLETE.

UNCLASSIFIED

SECURITY CLASSIFICATION OF THIS PAGE (When Data Entered)

Axial-stress S-N fatigue behavior of Al-Cu-Li-Zr alloys, in general, improved in both smooth and notch conditions comparable to the conventional 7075-T651 alloy. Within the compositional limits studied, one could not observe any simple relationship of smooth or notch fatigue lives with (Li/Cu) ratio. However, addition of 0.6 Mg to Al-3Cu-2Li alloy lead to significant improvement in smooth fatigue resistance compared to 0.0 Mg alloy. Finer grain size (unrecrystallized) alloy 2020 significantly improved the notch fatigue strength at long lives when compared to the coarse grain (recrystallized) alloy 2020. Interestingly, the fatigue-ratio under smooth S-N conditions of Al-3Li binary and Al-3Cu-2Li-0.6Mg alloys were significantly better than Ti-base (or steels) alloys.

Differences in constant-amplitude FCG resistances among Al-Cu-Li alloys are greatest at near-threshold ΔK_o region. The ΔK_o monotonically increased with (Li/Cu) ratio. However, the change in grain-structure (unrecrystallized vs. recrystallized) of 2020 alloy had only a small effect on ΔK_o.

Under single overload FCG conditions, significant resistance to crack growth rates was observed to increase with (Li/Cu) ratio. Significant retardation in FCG rates due to overloads was also observed in the coarse grain alloy 2020 compared to the unrecrystallized alloy 2020. Both constant amplitude and single overload FCG resistance of Al-Cu-Li alloys, in general, were better than 7075-T651 alloy.

Grain structure differences in alloys of 2020-type showed a small effect on fracture toughness at near peak-age condition. At a given yield strength, as (Li/Cu) ratio increased, fracture toughness decreased markedly. Aging effect in Al-2.9Cu-2.1Li alloy has a strong dependence of toughness on yield strength up to peak-age temper. This was correlated to marked differences in crack morphology among the aging conditions.

In general, all the Al-Cu-Li-Zr alloys showed improved resistance to SCC when compared to 7075-T651 alloy. Both the aging treatment in the Al-2.9Cu-2.1Li alloy and the variation in (Li/Cu) ratio did not significantly affect the magnitude of the apparent plateau velocity. The apparent K_{ISCC} decreased with increase in aging treatment for the alloy Al-2.9Cu-2.1Li or increase in (Li/Cu) ratio.

In most cases, the characterization of the trends in the data is qualitatively described; wherever possible, mechanistic implications are suggested.

FOREWORD

This final technical report covers activities performed during the period 1981 July 1 to 1985 February 28 for the Naval Air Systems Command under Navy Contract N00019-80-C-0569. This report is published for information only and does not necessarily represent the recommendations, conclusions, or approval of the Navy.

The contract is with Alcoa Laboratories, Aluminum Company of America, Alcoa Center, Pennsylvania. Mr. M. D. Valentine/Dr. D. Divecha are the Navy contract monitors. This report has been prepared by A. K. Vasudevan, Alcoa Project Manager, R. C. Malcolm, W. G. Fricke and R. J. Rioja, Alcoa principal engineer/scientists for the program.

ACKNOWLEDGMENTS

The authors would like to thank Professor S. Suresh, Brown University, for the fracture and fatigue modeling work done under NSF Grant DMR-8316893; and to Professor P. R. Howell and Mr. M. Tosten, Pennsylvania State University (Alcoa Grant) for the TEM work on one of the alloys.

Thanks are also due to P. D. Emmert, W. C. Richards, A. M. Lowry, R. A. Petri, E. A. Ludwiczak, J. C. Casato, D. M. Dunmire, M. E. Werner, P. E. Bretz, R. R. Sawtell and J. T. Staley for their help during the course of this work. Thanks to J. E. Jacoby for ingot casting and also to P. R. Ziman, A. J. Becker and J. E. Hall for corrosion work. Thanks to Ms. L. A. Coulter for typing the manuscript.

LIST OF TABLES

LIST OF FIGURES

INTRODUCTION

The addition of lithium (Li) to aluminum (Al) results in a substantial reduction of density and an increase in the elastic modulus when compared to conventional Al alloys. For example, each wt. % of Li up to 4 wt. % added to Al reduces the density by 3% and increases the elastic modulus by 6% for Li. Therefore, the development of Al-Li alloys is highly desirable for structural aerospace applications.

One of the early (1950's) commercially produced aluminum alloys containing Li was 2020 (Al-4.5 Cu-1.1 Li-0.5 Mn-0.2 Cd). However, this alloy in the peak strength temper (T6) exhibited low fracture toughness when compared with the toughness of commercial 7XXX and 2XXX alloys, even though resistance to fatigue and stress corrosion was good. This characteristic, coupled with manufacturing difficulties, led to the eventual termination of commercial production of alloy 2020 in 1969. The current need to develop low density, high modulus Al alloys has renewed commercial and military interest in Al-Li alloys.

In the past several decades, Russian scientists have developed two Al-Li alloys; one Al-Mg-Li (01420) and the second, a modified version of alloy 2020 called VAD-23. Also recently, the British patented another Al-Mg-Li alloy. Even though Al-Mg-Li alloys exhibit moderate levels of strength and ductility with lower density, the current trend in alloy design is aimed towards the development of Al-Li-Cu based alloys. This is basically due to the combination of manufacturing difficulties encountered in the fabrication of Al-Mg-Li alloys and the current demand for strengths higher than those that can be obtained by Al-Mg-Li alloys. It has been observed that the strength levels of Cu-containing Al-Li alloys produced via the I/M approach can reach that of 7075-T651 with both lower density and higher modulus.

A literature survey indicates that there has been considerable effort directed towards the study of P/M Al-Li-X alloys (1,2). In contrast, there is a general lack of information on the mechanical properties of I/M Al-Li-X alloys, in particular on Al-Li-Cu type alloys. The purpose of the present work is to investigate the overall mechanical behavior of several Al-Li-Cu-Zr alloys. The alloy compositions were systematically chosen to vary the Li/Cu ratio from about 2.0 to about 25.0 (in terms of atomic % ratio). The fracture, fatigue, stress corrosion properties were characterized with respect to composition and microstructure. The results of such a study should aid in understanding the effects of compositional variations on the mechanical behavior of Al-Li-Cu alloys and, in particular, provide base-line data on the mechanical properties of I/M Al-Li-Cu based alloys.

MATERIALS AND FABRICATION

Alloy Composition

The four Al-Li-Cu-Zr alloys used for the study are shown on the phase diagram in Figure 1 (3). The choice of these alloys was based on the following objectives:

(a) By varying the Li/Cu ratio systematically, the structure-property relationship with varying volume fraction and size of the shearable Al_3Li (δ') phase and the $Al_xCu_yLi_z$ (T-type) phases can be studied. The relative amounts of T-type phases are thought to be critical because of their effects on planar slip (1,2). It has been suggested that planar slip occurs characteristically in binary Al-Li alloys because of the shearable δ' precipitates, and that the degree of slip planarity increases with Li content.

(b) The effect of Mg additions could be characterized by comparing the behavior of an Al-Li-Cu-Zr alloy containing 1.0 wt. % Mg to the same alloy without Mg.

(c) The overall mechanical behavior of Al-Li-Cu based alloys could be compared to the well known behavior of alloys 7075-T651, 2024-T651 and 2020-T651.

Two ingots of each composition listed in Table 1 were cast using laboratory facilities at the Alcoa Technical Center. The alkali impurity levels were maintained at low levels; (Na+Ca) < 0.0034 wt %. In addition, Fe+Si levels were also kept low, ~0.1 wt %.

Hydrogen Analysis

Hydrogen analyses on the as-cast ingots and hot rolled plates (in T651 temper) for all the alloys are tabulated in Table 2. Also for comparison, hydrogen contents of 2024 and 7075 alloys are listed. It is evident that the Li addition, with the exception of the as-cast ingot of Al-2.9Cu-2.1Li results in a significant increase in hydrogen content compared to conventional alloys, irrespective of the Cu and Mg additions. The hydrogen content in the as-cast ingot of Al-2.9Cu-2.1Li alloy is comparable to that in the 2024 and 7075 alloys. Due to the hydrogen pick-up in these alloys during the fabrication process, porosity was checked on ingots (die-penetrant method) and on the plates (ultrasonic method). Porosity was minimal in all ingots. The level of porosity in the plates was below 1 mm size, which is termed as Class A product by ultrasonic classification.

Hydrogen levels also varied with aging treatment. For example, hydrogen content was measured as a function of aging time at 191°C for the alloy Al-2.9Cu2.1Li. This is shown in Table 3. Hydrogen pickup during aging probably is due to the air-furnace aging treatment. The overall hydrogen levels observed in the present alloys are comparable to that observed by Miller et al (4), ~0.27 wt ppm.

Fabrication

The alloys were scalped, preheated, and hot rolled to two different plate thicknesses: 12.7 mm and 35 mm, respectively. While the 12.7 mm thick plate was used in the fracture and fatigue studies, and the 35 mm plate was used in the stress-corrosion experiments. After hot rolling, the plates were solution heat-treated and cold-water quenched, and then stretched ~2% prior to aging treatments. All the alloys, except alloy Al-4.6Cu-1.1Li-0.17Zr were aged at 191°C for various time intervals. Alloy Al-4.6Cu-1.1Li-0.17Zr was aged at 160°C in order to compare the results with those of 2020 (Al-4.5Cu-1.1Li-0.5Mn-0.2Cd) alloy, since the latter was aged at 160°C. Summarized in Table 4 are the heat treatment/hot rolling schedules for the alloys. For clarity, reference to the alloys in the text will be made in terms of the major alloying elements. As an example, alloy with 548465 will be termed as Al-4.6Cu-1.1Li alloy, and so on. Reference to the conventional alloys will be made in terms of their alloy-temper designations.

MICROSTRUCTURAL CHARACTERIZATION

The microstructural characterization of the alloys under study was conducted in the peak-aged condition (or T651 temper). Basic characterization involved optical metallography, electron microprobe, X-ray analysis and transmission electron microscopy.

Optical Metallography

Optical metallography illustrating the grain boundaries and several microstructural features are shown in Figure 2 (a through d) for the 12.7 mm plates and in Figure 3 (a through d) for the 35 mm plates, respectively. All the structures are observed along the longitudinal (L) direction. These photographs were taken under polarized light after electropolishing the samples. The alloys, in general, exhibited nearly unrecrystallized structures elongated along the L-direction in both thicknesses of plate. Laue transmission methods were used to assess the degree of recrystallization in each sample, as shown in Table 5. Recrystallization was more advanced as the (Li/Cu) ratio in the alloys increased. The addition of Mg seems to promote some recrystallization. The 35 mm plates, which received less reduction during hot rolling, exhibited relatively coarser microstructures when compared to the 12.7 mm plates. The generally unrecrystallized structure was confirmed by the X-ray Laue transmission measurement.

Electron Microprobe Analysis

Electron microprobe analysis was used to identify the chemical nature of coarse constituent phases present in the alloys. The elemental-mapping of the phases for the alloys are shown in Figure 4 through 7 for the 12.7 mm plates. In general, the common constituent phase observed was consistent with Al_7Cu_2Fe phase. In the Al-3.1Cu-2.2Li-1Mg alloy, sample 504440, coarse Al_2CuMg phases were observed, in addition to the Al_7Cu_2Fe phase. This can be due to the presence of Mg in the alloy which seems to have exceeded the maximum solubility limit. There is also a trace of Ni (~0.01%) observed in all the alloys. Similar results were noted in the 35 mm plate.

X-ray Guinier Analysis

After the peak aging treatment, X-ray Guinier-de Wolff analysis indicated qualitatively the types of phases present as shown in Table 6. The amount of δ' phase increased with Li content. Small amounts of θ' (Al_2Cu) were observed in the alloys, except in the Mg-containing alloy, where small amounts of S' (Al_2CuMg) phase were resolved. It appears that the expected differences in the amount of T-type phases, as the Li/Cu ratio was increased, could not be identified by this method. These observations were similar in both plate thicknesses for the peak-aging treatment.

EXPERIMENTAL PROCEDURES

Tensile

Tensile test procedures were done in accordance with ASTM standard methods of Tension Testing Wrought and Cast Aluminum - and Magnesium - Alloy Products, B557-84. For each material condition duplicate tensile tests were conducted at room temperature in an instron machine. All the tests were made using round 6.85 mm diameter specimens taken in the longitudinal (L) and transverse (LT) directions of rolling and from the center (T/2) location in the plates. The tensile properties of the alloys in the L-direction, as a function of aging, are shown in Tables 7 through 10. In addition, tensile properties in the LT-direction are shown in the "Results and Discussion" section.

Modulus and Density

Elastic modulus of the Al-Li-Cu-Zr alloys was determined using the Elastomat 1.024 resonant frequency apparatus. Rectangular cross-section samples approximately 125 mm long and 12 mm wide were machined along L-direction for the test. Specimens rested on suspension wires and were excited into vibration by eddy currents induced by magnetic transducers. When the frequency corresponded to a fundamental mode of vibration of the specimen, the frequency was recorded. The Young's modulus was then calculated from the following equation:

$$E = \frac{4}{p^2} \times L^2 \times f^2 \times \rho \qquad (1)$$

where L = specimen length, f = resonant frequency, ρ = sample density and p = the integer corresponding to the mode of vibration (p = 1 for the fundamental mode).

Density was measured by simple weight loss method in de-ionized water. The tabulated results of both density and modulus are shown in Table 11. Density decreased markedly with increase in Li content from the alloy Al-4.6Cu-1.1Li to alloy Al-1.1Cu-2.9Li, respectively. Modulus increased with the Li content. For comparison, data for conventional alloys are given. For a given alloy composition, both the density and the modulus variations with aging treatment were small.

Axial-Stress Fatigue (S-N)

Smooth and notch (K_t=3) axial-stress fatigue (S-N) test procedures adhered to the ASTM Standard Practice for Conducting Constant Amplitude Axial Fatigue Tests of Metallic Materials, E466-82. The tests were conducted in Krouse fatigue machines at a stress ratio ($R = S_{min}/S_{max}$) equal to 0.1 (cyclic-load frequency of 25 Hz) in an ambient-room temperature-laboratory air environment. All the tests were made using round specimens taken in the longitudinal (L) direction of rolling and from the center (T/2) location in the plates.

Fatigue Crack Growth (FCG)

A. Constant-Load Amplitude FCG Tests

Test procedures adhered to the ASTM Standard Method for Constant-Load-Amplitude Fatigue Crack Growth Rates Above 10^{-8} m/cycle, E647-83, and the proposed ASTM Standard test practice for measurement of very slow growth rates ($da/dN < 10^{-8}$ m/cycle) (5). Tests were made using compact-type (CT) specimens ($B = 6.35$ mm, $W = 63.5$ mm, $H/W = 0.6$) and center-crack-tension (CCT) specimens ($B = 6.35$ mm, $W = 102$ mm) taken in the longitudinal (L-T) orientation from the T/2 location.

Testing was generally performed on MTS servo-controlled hydraulically-actuated closed-loop mechanical test machines (some CCT specimens on Krouse machines) at a stress ratio ($R = K_{min}/K_{max}$) equal to 0.33. Cyclic-loading frequencies used were 20 and 25 Hz (MTS machines) and 13.3 Hz (Krouse machines). The test environment was high humidity (relative humjdity > 90%)-room temperature-laboratory air. The moist air was provided by bubbling air through a series of beakers containing water, and then into an air-tight chamber surrounding the specimen.

Tests using the CT specimens employed K-decreasing (load shedding) and K-increasing procedures with crack extension to obtain near-threshold, intermediate and high crack growth rate data, whereas the tests using the CCT specimens employed only K-increasing procedures and only near-threshold data was determined. With one exception, crack length measurements were made visually using photo-etched grids applied to both sides of each CT and CCT specimen. One of the tests made on the commercially produced 2020-T651 plate sample (CT specimen 523713-B-2-L-T-2) was made at Professional Services Group, Inc. (PSG), Materials Research and Testing Division (formerly Del Research), Hellertown, Pa., and the crack length measurements were made using a compliance procedure (6).

B. Simple Overload FCG Tests

Tests were made using the same CCT specimens as those used to obtain near-threshold constant-load-amplitude (CA) data. Testing was performed on MTS test machines.

FCG behavior for spectrum loading was measured using a periodic single overload sequence which has been employed previously for 7XXX alloys (7). This spectrum consists of 8000 CA load cycles at R = 0.33 followed by one overload cycle (OCR = 1:8000) whose peak is 1.8 times the CA maximum load (OLR = 1.8); this sequence was repeated continuously. The applied CA cyclic-load frequency employed was 20 Hz. The test environment was high humidity (R.H. > 90%)-room temperature-laboratory air.

With one exception, the load range for the CA portion of the simple overload spectrum was the same as that to obtain the near-threshold CA data. The exception was a test of the commercially produced 2020-T651 plate (CCT specimen 523713-B-1-L-T-1), wherein the loading for the CA portion of the spectrum test was increased ~42 percent from that to obtain the near-threshold CA data. Programmed loads were provided by an MTS load profiler interfaced with the electrohydraulic test system.

Crack growth in the overload tests was monitored electronically using crack propagation gages, as described in Ref. 8. In addition, crack length was measured visually using grids applied to one side of each CCT specimen.

SCC Tests of Precracked DCB Specimens

Tests were conducted on 35 mm thick plates of Al-Li-Cu-Zr alloys to provide a measure of their relative resistance to SCC in the critical short-transverse (S-L) direction. Bolt loaded double cantilever beam (DCB) specimens, of the type detailed in Figure 8, were used to determine the SCC propagation rates indicative of the relative resistance to SCC.

The DCB test specimens were mechanically precracked in tension with a few drops of 3.5% NaCl solution being added during the final stages of precracking. The specimens were held for a minimum of 30 days in a laboratory environment. A few drops of 3.5% NaCl solution were added to the crack three times each day. Crack growth was monitored with an ultrasonic detection device developed at the Alcoa Laboratories. Visual measurements of the crack extension were also determined at the surfaces of each specimen for comparison with the interior measurements. It has been previously established that the ultrasonic measurements of the interior fractures were generally correct to within 0.06 inches.

Stress-intensity (K) values were calculated as a function of the specimen crack opening displacement (COD) and crack length using the following equation developed by Hyatt (9):

$$K_I = \frac{VEH[3H(a+0.6H)^2 + H^3]^{1/2}}{4[(a+0.6H)^3 + H^2a]} \qquad (2)$$

where V = COD, E = elastic modulus of the material, H = half-height of the DCB, and a = crack length measured from the load line.

Regression analyses were made of the crack lengths as a function of the exposure time of 30 days to obtain the best fit curves from the raw data. Crack growth rates were then obtained by differentiation of the regression equations, and these rates were used to develop curves showing the SCC growth rate as a function of the calculated (EQ1) instantaneous K factor. Stress corrosion crack propagation rates decreased, as expected, with crack growth in these tests since K decreases with crack advance.

Fracture Toughness

Plane-strain fracture toughness, K_{Ic}, test procedures was adhered to the standard Test Method for Plane-strain Fracture Toughness of Metallic Materials, E339-83. The tests were conducted on 12.7 mm thick compact specimens in the T-L orientation. The very underaged samples do not satisfy the criteria for "valid" linear elastic fracture mechanics characterization with the stress-intensity factor K_I (ASTM E-399) because of low yield stress and high toughness. Furthermore, certain underaged and overaged microstructures (where, according to ASTM E-399 guidelines, linear fracture mechanics characterization is justified) require samples thicker than 12.7 mm in order to experimentally obtain "valid plane-strain" fracture toughness values. For the above cases, elastic-plastic fracture toughness. J_{Ic} can be measured using procedures in ASTM E-813-81 Standard Test Method for J_{Ic}, a measure of fracture toughness and then an equivalent K_{Ic} value can be derived from the following equation:

$$K_{Ic} = \left\{\frac{J_{Ic}\,E}{(1-\nu)}\right\}^{1/2} \qquad (3)$$

where E = Young's modulus and ν = Poisson's ratio.

Crack length was monitored using compliance methods and the variation of COD at the initiation of fracture with yield strength was noted. Such a method was used for the alloy Al-2.1Li-2.9Cu-0.12Zr as a function of aging treatment. For the other alloys, K_Q (if valid becomes K_{Ic}) was measured as a function of composition and aging. All the specimens were fatigue precracked to nearly the same crack length, prior to the fracture toughness tests.

RESULTS AND DISCUSSION

In the following section the results obtained from experiments are discussed in light of the composition and microstructure. The results are listed in the following test sequence: axial stress S-N fatigue, constant-amplitude FCG, single-overload FCG, fracture toughness and stress-corrosion cracking. All the fatigue tests were conducted on specimens oriented longitudinally in T651 temper. The tensile properties of all the alloys are listed in Table 12. On the other hand, fracture toughness tests were done on the T-L oriented specimens and the properties are given in the "fracture toughness" section. Finally, tensile properties for the stress-corrosion tests in the S-L orientation are listed under the appropriate section.

In most cases, the characterization of the trends in the experimental observations will be qualitatively described; wherever possible, mechanistic implications are suggested. This is in view of the fact that the level of understanding of the structure-property relationships are not fully developed in the areas of fatigue, fracture and stress corrosion.

AXIAL STRESS S-N FATIGUE

(Li/Cu) Ratio:

Smooth and notch axial stress fatigue S-N data for three Al-Li-Cu-Zr alloys with varying Li and Cu contents are shown in Figures 9 through 11. The mechanical properties of these alloys are given in Table 12. In general, the notch fatigue data for each alloy showed less scatter compared to the respective smooth fatigue results. It was observed that there was a tendency towards higher fatigue resistance in smooth samples at low stress amplitudes and longer fatigue lives around 10^7 cycles, as the Li content (or (Li/Cu) ratio) was increased. At lower stress amplitudes, higher Li containing alloys (e.g. 548468) exhibited shorter lives. This could be due to the increase in the degree of planar slip with Li content creating a tendency toward early crack nucleation which could degrade the fatigue resistance (10,11). The notch fatigue data, on the other hand, showed subtle improvement in fatigue life at 10^7 cycles. Within the composition limits studied, one could not observe any simple relationship of smooth or notch S-N fatigue lives with (Li/Cu) ratio. This could be partly due to the lack of experimental data points.

Role of Mg

Adding 0.6% Mg to the base alloy of Al-3Cu-2Li, generally, lead to significant improvement in smooth S-N fatigue resistance. On the other hand, there was no improvement in notch fatigue resistance. This can be observed by comparing Figure 12 to Figure 15. The mechanistic behavior of the trend in the results in not clear. The 0.6% Mg alloy is ~35 MPa lower in tensile yield strength (Table 12) compared to the base alloy with similar unrecrystallized grain structure. It should be noted that due to the limited length of the plate, the alloy plate containing 0.6% Mg could not be stretched. As a result, part of the low stress amplitude S-N fatigue resistance in the 0.6 Mg alloy could be due to the stretching effect.

Increasing the Mg level to 1.0% resulted in ~4.0 vol. % of Al_2CuMg constituents. The S-N fatigue behavior of alloy Al-3.1Cu-2.2Li-1Mg is shown in Figure 13. Comparison of the test results for the 0% Mg and 1.0% Mg containing alloys is shown in Figure 14. The data indicate a significant loss in notch fatigue resistance of 1.0% Mg containing alloy over the entire range of stress examined. With such a high vol. % of coarse constituents, crack initiation at the base of the notch could occur at particle sites, in spite of the planar slip deformation. However, small differences in the smooth S-N fatigue behavior could be indicating the importance of the competition of crack initiation processes due to planar slip and high vol. % of the constituents. All three alloys, in both smooth and notch fatigue conditions, are compared in Figure 15 giving a summary of Mg-effect on S-N fatigue behavior.

Several investigations have examined the role of constituent particles in fatigue crack initiation of conventional aluminum alloys. Hunter and Fricke (12) examined crack initiation of conventional aluminum alloys and reported that fatigue cracks were associated with cracked constituent particles in 2024-T3. Grosskreutz and Shaw (13) suggested in the same alloy and temper that debonding between the particle-matrix interface was responsible for the initiation of fatigue cracks. Kung & Fine (14) investigated surface crack initiation in a 2024-T4 alloy. They observed that at high stresses most cracks formed in the slip bands and that at low stresses cracks were predominantly nucleated at the constituent particles. Recently, Sigler et al (15) have extended the work of Kung and Fine to study the effect of constituents on crack initiation in a alloy 2024 in an overaged condition. They observed that at all the stresses examined, the most common initiation sites were constituent particles. Such studies were mostly done on the 2XXX type alloys. In the 7XXX alloys, for example, Ostermann & Reimann (16) observed significant improvement in the fatigue resistance of high purity alloy 7475 compared to that of low purity alloy 7075.

Al-Li-Cu-Zr alloys, with and without constituents, showed very little effect on smooth fatigue behavior compared to conventional aluminum alloys. The present study did not include the effectiveness of various crack initiation sites in the Li-containing aluminum alloys.

Grain-Size Effect in 2020 Alloy

The commercial coarse grain ~380 μm recrystallized alloy 2020 plate sample was given a thermomechanical process (TMP) to obtain an unrecrystallized grain structure. The TMP process was similar to that described by Feng, Lin & Starke (10). The alloy, after TMP, was solutionized, stretched, and aged to a T651 temper. The alloy remained in an unrecrystallized (2-3 μm grains) condition after the heat treatment. Both 2020 alloy samples in T651 temper had nearly the same tensile yield strength, as shown in Table 12.

The data in Figure 16 shows that the unrecrystallized alloy has greater smooth fatigue resistance at high stresses compared to the recrystallized alloy, while for notch fatigue the significant improvement in fatigue resistance of the unrecrystallized alloy is at the lower stresses. The constituent size and Vol. % did not differ significantly between the two materials. The finer grain structure significantly improved the notch fatigue strengths at lives greater than 10^5 cycles.

Starke & Lutjering (11) have observed in high purity 7475 alloy that, at all stress amplitudes, the fine grain size (30 μm) alloy exhibited improved smooth fatigue resistance compared to the coarse grain (220 μm) alloy having the same peak aged tensile yield strength. The present study shows the improvement in smooth fatigue resistance only at high stress amplitudes. Test data in notch fatigue behavior were not available in other aluminum alloys to compare to the present data. Bretz, et al (17) in axial-stress fatigue tests and Starke and co-workers (10,11) in strain control fatigue tests have shown that crack initiation in alloy 2020-T651 occurs at constituent particles (Al_7Cu_2Fe) and that the coarse grain recrystallized structure with planar slip could result in early crack nucleation. Details of the mechanisms of crack nucleation in Al-Li-Cu alloys are not clear at the present time.

Fractography

Fractography using scanning electron microscopy (SEM) could not be performed on fractured smooth axial-stress fatigue specimens since the fractured surfaces were damaged during the last stage of testing. As a result, only the fractured notched fatigue specimens were used to examine fracture surface features. Fractured specimens which had been tested at a 145

MPa maximum stress level were selected for the examination. Photographs of fracture surfaces were taken at low magnifications to identify the fatigue and final fracture regions, and at higher magnifications in the fatigue region to identify the crack initiation region. Fracture surface topographs of all the alloys under study are shown in Figures 17 through 23. A circle shown in each of the low magnification photographs indicates the approximate area of a crack initiation site.

The fracture surfaces shown in Figures 17, 18, and 19 represent alloys with increasing (Li/Cu) ratios. Crystallographic features are observed and occasionally secondary cracks (as indicated by arrows) are found. The fatigue region extends across a large portion of the fracture surface of each specimen. The effect of Mg content can be compared when seen on the surfaces shown in Figures 20 and 21 with that in Figure 18. The fracture surface shown in Figure 20(b) seems to indicate the fracture initiation site, along with the crystallographic features observed on the surfaces shown in both Figures 18 and 21. Addition of 1.0 Mg did not suppress the crystallographic features; however, only a few constituents were observed in the fatigue region. At lower magnifications, there was a clear distinction between the fatigue and tensile overload regions. The tensile fracture region showed significant amount of constituents.

The effect of grain structure in the 2020 alloys are shown in Figures 22 and 23. Fracture initiation appears to have taken place over the circumferential edge of the specimen shown in Figure 22, while the fine grain alloy shown in Figure 23 fracture initiated at one side and extended significantly across the specimen. Crystallographic fractures are also observed in Figures 22 and 23. The SEM work on the coarse grain alloy was done on a specimen tested at maximum stress of 137 MPa compared to 145 MPa for the fine grain alloy. The above SEM fracture surface observation gives only a qualitative description of the fracture process relating to the S-N fatigue behavior.

Comparison of Al-Cu-Li-Zr (S-N) Data With Other Alloys

In general, the Al-Li-Cu alloys showed better smooth and notch axial-stress fatigue resistance when compared to conventional aluminum alloys. A comparison of the notch S-N fatigue data (R=0.1) for the four Al-Li-Cu-Zr alloys in T651 temper, with data (R=0.1) for 7075-T651 alloy is shown in Figure 24. Clearly, all the Al-Li-Cu-Zr alloys exhibit improvements in notch fatigue behavior, except for the 1.0 Mg containing alloy.

Summarized in Figure 25 are variations in the fatigue-ratio (σ_{max} @ 10^7 cycles/σ_{UTS}) for the smooth S-N fatigue conditions as a function of normalized ultimate tensile strength to Young's modulus for all the Al-Li-X alloys in comparison to various aluminum and non-aluminum base alloys. Line-data for Ti, Steel, Cu and Al alloys represent the middle of the scatter-band of the results taken from a paper by Laird (18). For example, the line representing

Al-alloys at about 600 MPa tensile strength (~0.0081 on the UTS/E scale) the variation of fatigue-ratio is from about 0.28 to 0.32. Most of the data for the aluminum alloys listed in Figure 25 are in the neighborhood of the Al-alloy trend. Interestingly, compared to Ti-alloys and Steels, the Al-3Li binary and Al-3Cu-2Li-0.6Mg alloys exhibit comparable or better fatigue resistance.

CONSTANT-LOAD-AMPLITUDE FATIGUE CRACK GROWTH

Effect of (Li/Cu) Ratio

Early studies of the fatigue crack growth (FCG) resistance of peak-aged (T651) aluminum alloy 2020 (Al-4.5Cu-1.1Li-X) were carried out by Sanders and co-workers (19,20). They found that this alloy exhibited superior crack growth properties compared to the widely used aluminum alloy 7075-T651 in the Paris regime of crack propagation. Subsequent work by Vasudevan, et al. (21) revealed that the superior fatigue behavior in alloy 2020 is even more pronounced in the near-threshold regime, where the propagation rates are more than two orders of magnitude lower than conventional aluminum alloys of the 2XXX and 7XXX series. Such initial work (1,2,19,21) has shown that the improved resistance to cyclic crack advance in the Al-Li system can be attributed tohighly inhomogeneous slip behavior (and the resulting non-linear crack profile) induced by the ordered δ' (Al_3Li) precipitates.

The fatigue crack growth rate data for each of the three Al-Cu-Li alloys are shown in Figures 26 through 28, respectively, while crack propagation rates for the three alloys are compared in Figure 29. Also shown in Figure 29 for comparison are curves representing typical FCG rates for two commercial alloys, 2124-T851 and 7075-T651, tested under similar conditions. The variation of threshold stress intensity factor range ΔK_0 is replotted in Figure 30 as a function of Li/Cu ratio expressed in atomic fractions. Threshold stress intensity factor range increases monotonically with increasing values of Li/Cu ratio.

It previously has been suggested that while lithium additions to aluminum alloys enhance fracture surface oxidation in fatigue (21,22,23), the presence of Cu in 7XXX alloys tends to inhibit oxide formation (24). Secondary ion mass spectroscopy (SIMS) analyses of fatigue fracture surfaces, in the present work, showed that thickness of the oxide on the crack faces generated at threshold was 0.04 ($\pm$0.02) μm for all three Al-Li-Cu materials. Although this value is about twice that for (non-lithium-containing) Al-Cu alloys (21,22), the absence of a composition effect in the three materials indicates that oxide-induced crack closure (25,26) processes may not be the primary cause for the apparent differences in their fatigue crack growth response.

Optical micrographs of the fatigue crack profiles obtained on polished and etched specimen surfaces for the three Al-Li-Cu alloys are shown in Figures 31 through 33, respectively, for growth in the near-threshold to intermediate regime. Alloy Al-4.6Cu-1.1Li exhibits very linear crack growth even at high magnifications (Figures 31a and 31b), compared to the crack profiles normally seen for 2X24 type alloys. Alloys Al-2.9Cu-2.1Li and Al-1.1Cu-2.9Li, respectively, show more non-linear crack profiles (Figures 32 and 33). This is especially evident for alloy Al-1.1Cu-2.9Li shown in Figures 33a and 33b, where a deflection in crack path occurs every time the crack-tip encounters a high angle grain boundary, thereby resulting in a highly tortuous crack profile. Such results give further support to previous hypotheses (10,19,24) that increasing the amount of coherent and shearable δ' precipitates in the matrix (as occurs with increased lithium content, from alloy Al-4.6Cu-1.1Li to alloy Al-1.1Cu-2.9Li leads to an enhanced crystallographic crack advance during cyclic fracture, which in turn gives rise to improved resistance to crack growth. Precise analyses of the changes in fatigue behavior due to non-linear crack growth are not currently feasible because of the uncertainties in fracture mechanics characterization of complex deflection geometries. However, some approximate estimates of the effects of crack profile on overall fatigue behavior can be attempted based on some existing models (27,28).

Simple two-dimensional linear elastic models of crack deflection suggest (65, 66) that the apparent driving force ΔK_I for a deflected crack is:

$$\Delta K_I = \left\{ \frac{D \cos^2 (\theta/2) + S}{D+S} \right\}^{-1} \Delta K_{eff} \qquad (4)$$

where Δk_{eff} is the driving force for a straight crack, D/(D+S) and S/(D+S), the fractions of deflected and linear crack advance, and θ the average angle of deflection from the Mode I growth plane. Consider, for purposes of approximate analyses, the two extreme cases of alloys Al-4.6Cu-1.1Li and Al-1.1Cu-2.9Li. If Figure 31 is assumed to represent an ideally straight crack (i.e., for Al-4.6Cu-1.1Li alloy, $\theta \sim 0°$, $D/D+S \sim 0.0$ and Figure 33, a deflected crack (i.e., for alloy Al-1.1Cu-2.9Li, average $\theta \sim 45°$, and $D/D+S \sim 0.75$), then the deflected near-threshold crack growth for alloy Al-1.1Cu-2.9Li would require an apparently larger driving force of $\Delta K_I = 1.12\ \Delta k_{eff}$ (Eq. 4). Furthermore, as crack length is measured only along the Mode I direction, alloy Al-1.1Cu-2.9Li has an apparent 22% slower growth rate, as derived from the expression (27):

$$(da/dN) = [(D \cos \theta + S)/(D+S)]\ (da/dN)_L \tag{5}$$

where $(da/dN)_L$ is the growth rate for the linear crack profile of alloy Al-4.6Cu-1.1Li at identical effective driving force. Such simple calculations reveal that a significant portion of the differences in the measured threshold ΔK_0 values for alloy Al-4.6Cu-1.1Li and Al-1.1Cu-2.9Li can be traced back to their differences in crack profiles. In addition to slower growth rates due to the deflection mechanism (27,28), the non-linear crack path for alloy Al-1.1Cu-2.9Li also enhances roughness-induced crack closure. Correlation of the present experimental results with the linear-elastic models for the combined effects of deflection and closure (27) suggests that about 10% relative mismatch between the two crack faces in alloy Al-1.1Cu-2.9Li is sufficient to cause the observed enhancement in ΔK_0. This is also consistent with the crack closure measurements using compliance techniques, where the deflected crack profile of alloy Al-1.1Cu-2.9Li leads to a larger closure load in the near-threshold regime.

The above description on crack branching and its effect on ΔK pertains to the observations of the cracks made on the surface. While such surface observations have stress state effects, it could be argued that the calculated ΔK values from surface crack branching profiles underestimate the magnitude of ΔK. This is shown in earlier work on 2020-T651 alloy (21), where relatively more crack branching was observed in the half thickness plane of the sample compared to the surface.

In conclusion, the study has shown that increasing the (Li/Cu) ratio in aluminum alloys leads to an improved resistance to cyclic FCG in a room temperature high humidity air environments. Such beneficial fatigue properties appear to arise from the crystallographic crack growth mechanism and crack deflection processes induced by the δ′ precipitates in the alloys of higher lithium content.

Grain Size Effect in 2020 Type Alloys

The constant amplitude fatigue crack growth rate data for the thermomechanically processed 2020 plate sample is shown in Figure 34. The data for this unrecrystallized 2020 plate is compared with data for commercially produced coarse grain 2020 alloy and Al-4.6Cu-1.1Li plate in Figure 35. All the alloys were tested in their T651 condition. The tensile yield strength of all the plates are nearly the same (Table 12). In Figure 35, the results of two coarse grain 2020 alloys were taken from the references (6) and (21). Within the scatter of the data, the FCG does not appear to differ significantly with different grain structures. The present observation differs from the previous investigators who observed significant improvement in FCG rates with coarser grain 2024-T351 (29) and 7091-T7X (30) P/M materials. The present work needs to be extended to different R-ratios along with closure measurements in order to assess the effect of grain structure on fatigue crack growth.

Fractography

It has been observed that the changing relationship between FCG rates and alloy microstructure indicates that fatigue mechanisms and fracture surface topographies can vary with FCG rates (7,30). At low FCG rates, fatigue cracks tend to grow by a crystallographic mechanism. Intermediate FCG extension in aluminum alloys generally takes place through the formation of fatigue striations. It is observed that, at high FCG rates fracture can occur by the initiation and growth of microvoids from large second phase constituent particles.

In the present work, at very low FCG rates, or near-threshold ΔK_0 region, fracture mode appears to be crystallographic. The crystallographic facets on the fracture surface are observed on all the alloy compositions at ΔK_0, Figures 36(a), 37(a), 38, respectively. Even at higher stress intensities,

$\Delta K = 8 MPa\sqrt{m}$, predominantly crystallographic features were observed, Figures 36(b), 37(b), 39. Microvoids were not usually observed at high ΔK levels in any of the alloys, since the Fe and Si levels were low. The occurrence of crystallographic growth features have been attributed to the planar slip deformation of the Al-Li-Cu alloys (1,2,31). At low ΔK levels, FCG rates corresponds to an average increment of crack advance per cycle which is significantly less than the size of the matrix precipitates. The coherent δ' precipitate will be sheared by the dislocation motion as the crack tip deformation occurs, thereby constraining the dislocation movement to a few slip systems in the crack tip plastic zone. This leads to strain localization allowing preferred crack paths along slip systems where damage has occurred. Since these slip systems may not be oriented perpendicular to the axis of applied loading, the fatigue crack tends to branch through the microstructure, thereby reducing the macroscopically determined FCG rate. It can be seen, as the Li content is increased in an Al-Cu-Li alloy, the size and vol. % of shearable δ' precipitate increases which tend to result in slip damage through strain localization leading to crack branching, Figures 31 through 33; hence, improving the FCG resistance of higher Li containing alloys. As the crack tip plasticity and incremental crack advance per cycle increases with ΔK level, improvements in FCG resistance attributed to reduced δ' spacing would be small. As a result, FCG data at intermediate and high ΔK show modest differences, while the significant improvements in FCG resistance occur at ΔK_0 region, Figure 29.

The FCG at the near-threshold ΔK_0 region for the two grain-structure (coarse grain vs. unrecrystallized) alloys of 2020 were small, while at intermediate growth rates, the fine-grain unrecrystallized 2020 alloy showed small increase in FCG rates compared to the coarse-grain alloy. The fracture surface at ΔK_0 for the unrecrystallized 2020 alloy (Figure 40) is smoother when compared to that of the coarse grain 2020 alloy (6,17,21), even though crystallographic features were observed in both the alloys. At a higher stress intensity $\Delta K = 8 MPa\sqrt{m}$, microvoids with constituents were observed with fewer crystallographic facets in the unrecrystallized 2020 alloy, as shown in Figure 40(b); whereas in comparison, the coarse grain 2020 alloy exhibited more crystallographic facets (17,21). The differences in the fracture surface observations due to grain size effect at ΔK_0 regime was subtle. There appears to be no clear explanation for the small differences in the FCG rate behavior due to grain size in 2020 alloy.

SINGLE OVERLOAD SPECTRUM FATIGUE CRACK GROWTH

Grain Size Effect in 2020 Type Alloys

In the previous section, we observed that under CA loading at R=0.33 and ν=25 Hz, the grain size effect on FCG in 2020-type alloys is not significant. However, for the tests using a single OL spectrum the same alloys exhibited marked differences in the FCG rates. Comparisons of the CA FCG rates with OL spectrum data for the 2020-type alloys are shown in Figures 41 through 43. The difference between the FCG rates for CA and OL spectrum tests represent the degree of retardation caused by the periodic single OL cycle. For alloys Al-4.6Cu-1.1Li and TMP 2020 (Figures 41, 43) respectively, both having fine grain unrecrystallized structures, the OL spectrum FCG rates are as much as 5 to 10 times lower than the CA rates at about $\Delta K=8MPa\sqrt{m}$. For the coarse grain commercially produced 2020 alloy (Figure 43), the retardation in FCG rates due to the OL spectrum was as much as 100 times lower than CA rates at the same $\Delta K=8MPa\sqrt{m}$. Comparison of only the OL spectrum FCG data for all three alloys is shown in Figure 44. This comparison clearly demonstrates that the OL spectrum FCG rates for the coarse grain recrystallized 2020 alloy are significantly lower, as much as 10 times, than both the fine grain unrecrystallized alloys at ΔK levels greater than $6MPa\sqrt{m}$, however differences at ΔK levels less than $6MPa\sqrt{m}$ are considerably smaller. While mechanistic reasons for this benavior is not known at present, one may speculate that part of the reason for the reduced FCG rates due to OL in the coarse grain 2020 alloy could be due to crack branching. The degree of crack branching may increase with ΔK.

(Li/Cu) Ratio

As the (Li/Cu) ratio is increased in the Al-Cu-Li-Zr alloys, the degree of FCG retardation due to applying periodic OL increases significantly. This is represented in Figure 45 by the total crack length versus number of elapsed cycles data from single periodic OL FCG tests of all three Al-Cu-Li-Zr alloys. The data are, also, compared to data for conventional alloy 7075-T651 plate. It can be seen from Figure 45 that the crack length decreases significantly with number of cycles, as the Li-content (or Li/Cu ratio) is increased in the alloy. In particular, the alloy Al-1.1Cu-2.9Li showed significant FCG retardation even with ~30% increase in the loads. This was intentionally carried out since there was no observable crack growth for about 100 million cycles at comparable loaas used for the other alloys. Details of the load-history for all the alloys are given in Figure 45. Figure 45 can also be represented in terms of the standard FCG rate dependence on stress intensity, Figure 46. It may be noted that with increased ΔK, over 1 to 2 orders of magnitude lower FCG rates observed in the higher Li-containing alloys when compared to alloy 7075-T651. One can qualitatively invoke the planar-slip arguments, previously discussed, as a possible explanation for the improved FCG resistance in Al-Cu-Li alloys. The mechanistic understanding in Al-Cu-Li alloys is not known since there are competing effects of planar-slip, environment, and microstructure. Figures 47a and 47b show the comparision of CA & OL results for Al-2.9Cu-2.1Li and Al-1.1Cu-2.9Li alloys, respectively.

The mechanism associated with variable amplitude FCG in aluminum alloys is examined by Suresh and Vasudevan (32). It is shown that for high strength aluminum alloys, the post-overload retarded FCG is governed by the mechanism of near-threshold crack propagation. In addition, pronounced crack branching occurs in Li-containing alloys, and in underaged tempered alloy 7075 upon the application of an OL. Detailed description of possible mechanisms are given in the reference (32).

Fractography

The OL FCG fracture surface features of the three 2020-type alloys, with various grain sizes, at a low stress intensity ($\Delta K=4MPa\sqrt{m}$) are shown in Figures 48 through 50. The spacings of the OL arrest lines are uniform and nearly same for the three alloys. Appearance of broken constituent particles on the OL fracture surfaces were observed, even at $\Delta K=4MPa\sqrt{m}$, (Figure 48 and 49) which could be due to OL spikes. In contrast, at the same ΔK levels little or no constituent particle fracture is seen in CA specimens. This observation suggests that constituent particles could play a different role in the fracture process during OL spectrum than during CA loading. However, at higher stress intensities where the coarse grain alloy 2020 plate showed significantly lower FCG rates, the OL arrest lines tend to become non-uniform and propagate in different directions, as shown by arrows in Figure 51 for $\Delta K=8\ Pa\sqrt{m}$. This OL arrest line spacing widens as the grain structure becomes unrecrystallized, as shown in Figures 52 and 53, for alloys TMP-2020 and Al-4.6Cu-1.1Li, respectively. The crystallographic fracture features between the overload arrest lines can be observed in Figure 53(b), suggesting that post OL FCG could be governed by near-threshold crack growth mechanism (32).

The higher Li-containing alloy, Al-2.9Cu-2.1Li exhibits very finely spaced OL arrest lines, even at $\Delta K=8MPa\sqrt{m}$, as shown in Figure 54. The overall OL FCG seems to deviate from the main direction of crack propagation, as shown by arrows, in Figure 54. This observation is similar to the coarse grain alloy 2020, Figure 51. In addition, a secondary crack can be seen in Figure 54.

Such secondary cracks can relieve some of the crack tip strain energy, thereby lowering the effective ΔK and reducing FCG rates (33). Such fracture surface observations qualitatively describe the intrinsic behavior of the FCG resistance of Al-Cu-Li alloys.

FRACTURE TOUGHNESS

Grain Structure Effect in 2020 Alloy

Alloy 2020 in the peak-aged temper exhibits planar-slip deformation (1,10). It has been observed (10) that the alloy 2020 in fine grain form has higher elongations compared to coarse grain. The tensile and toughness (K_Q) properties of the coarse grain recrystallized 2020 and the fine grain (TMP-2020) unrecrystallized alloys, along long-transverse direction are shown in Table 13. The toughness (K_Q) variation with yield strength (YS) for both the alloys is shown in Figure 55. The lines denote the trends in the data. Although the K_Q values above ~25MPa$\sqrt{m}$ are not valid K_{Ic} values the trends in the data indicate small increases in K_Q for the unrecrystallized TMP-2020 alloy at YS < 500MPa than for the coarse grain alloy. At higher yield strength, near the peak-age temper, the differences in K_Q for the two grain structures are negligible. The present data suggests that refining the grain structure alone in 2020-type alloys, at higher strength levels, does not appear to improve the toughness.

(Li/Cu) Ratio

It has been observed that as the Li-content is increased in an Al-Li alloy, the degree of planar-slip deformation increases resulting in intergranular fracture and hence lower toughness properties. The long-transverse tensile and K_Q properties of Al-4.6Cu-1.1Li and Al-1.1Cu-2.9Li alloys are given in Table 14. The plot of K_Q vs. yield strength of the Al-Cu-Li alloys when (Li/Cu) ratio is increased systematically is shown in Figure 56. The data for Al-2.9Cu-2.1Li alloy is shown in Table 15. At a given yield strength, higher the (Li/Cu) ratio lower is the K_Q value. With increase in (Li/Cu) ratio, there appears to be an increase in amount of matrix δ' as well as grain boundary precipitates (δ, T-phase) (?4). As a result, there is a combined effect of planar slip and grain boundary precipitates that leads to intergranular failure. At lower Li levels, Cu in its T-type phase homogenizes in part the planar-slip; while, in 2.9Li-containing alloy, the high density of δ' promotes planar slip which cannot be partitioned to the next grain due to the grain boundary precipitates (δ, T-phase) results in poor toughness (53).

Aging Effect in Al-2.9Cu-2.1Li Alloy

The alloy Al-2Li-3Cu (S-548466) was artificially aged at 191°C for various time intervals to provide a range of microstructural conditions of widely varying strengths, from the very underaged to severely overaged tempers, Table 15.

Figure 57 shows the variation of plane strain fracture toughness, K_{Ic}, with yield stress, σ_y. It is noted that an increase in strength, from the underaged microstructure UA-1 to the peak-aged microstructure PA, leads to a decrease in K_{Ic}. For aging beyond the peak-strength, however, the value of K_{Ic} is almost independent of yield strength. This trend is at variance with the results of prior studies on conventional commercial aluminum alloys, where over-aging was observed to provide an increase in toughness (e.g. references (1) and (4)). In the very over-aged microstructure OA-3, there is a drop in K_{Ic} which is also accompanied by excessive grain boundary fracture. A similar trend is obtained when the fracture toughness is characterized in terms of J_{Ic}, as shown in Figure 58. Listed in Table 20 are the measured values of plane stress fracture toughness K_c, plane strain fracture toughness K_{Ic}, elastic-plastic fracture toughness J_{Ic} as well as K_{Ic} inferred from J_{Ic}. A reasonably good correlation exists between the values of K_{Ic} actually measured and inferred from J_{Ic} under plane-strain conditions in tempers PA, OA-1 and OA-3. Figure 59 shows profiles of cracks on polished and etched surfaces of the fracture toughness specimens, obtained by interrupting the test during quasi-static fracture and monitoring the crack path after unloading. Figures 59a and 59b the crack profiles indicate that in the under-aged tempers, the crack "forks" at the onset of monotonic fracture, with the angle between the arms of the fork vary between 60° and 90°. However, crack paths shown in the micrographs of Figures 60 and 61 demonstrate highly linear crack advance for the peak-aged and over-aged tempers. The profiles of cracks at the center-thickness section are shown in Figure 62 for both the under-aged, and over-aged microstructures. These figures suggest that for all the aging conditions, the fracture paths observed on the specimen surfaces are also representative of the fracture modes at the center thickness section. It is interesting to note that crack propagation along the arms of a fork occurs over distances of up to 1.5 mm. Furthermore, crack profiles shown in Figures 59a, 59b, and 62a and similar ones obtained on other Al-Cu-Li-X alloys examined in this ongoing research program (34) indicate that forking of the crack in the under-aged microstructures occurs along the intense shear bands (at around 30°-45° from the nominal Mode I crack plane) formed within the plastic zone at the tip of the uniaxially loaded crack. In microstructures aged at or beyond the peak strength temper the fracture mode is predominantly intergranular, as inferred from observations of failure due to precipitates along the (low angle) sub-grain boundaries (Figure 61) as well as the prior-cast (high angle) boundaries. In concurrence with this result, no significant deflections in crack path, away from the nominal Mode I growth plane, were observed for the over-aged microstructures.

Literature Survey

The majority of research studies on the role of microstructural factors in the fracture behavior of aluminum alloys have focused on the size, shape and volume fraction of particles (constituents and dispersoids) and their influence on ductile fracture through void initiation and growth (35-40,42). Based on Rice and Johnson's hypothesis (43) that crack extension occurs when the extent of heavily deformed region at the crack tip becomes comparable to the width of the unbroken ligaments separating cracked particles, Hahn and

Rosenfield (35) suggested the following relationship for the fracture toughness of commercial aluminum alloys:

$$K_{Ic} \approx [2\sigma_y E\left(\frac{\pi}{6}\right)^{1/3} D]^{1/2} \bullet f_c^{-1/6} \qquad (6)$$

where σ_y=yield strength, E=elastic modulus, and f_c and D are the volume fraction and diameter, respectively, of the constituent particles. Although there was a good correlation between K_{Ic} and $(f_c)^{-1/6}$, eq. (6) predicts, contrary to experimental observations, an increase in fracture toughness and increasing yield strength, at constant volume fraction and distribution of inclusions. Furthermore, experiments suggest that toughness does not increase with increasing D size of the constituents, while all the other parameters in Eq. (6) are held constant (37). Invoking the criterion that fracture will occur when the maximum strain ahead of the crack tip exceeds a critical value, ε_c^*, Garrett and Knott (38) suggested the following relationship for the effect of microstructure (or aging treatment) on the fracture initiation toughness of aluminum alloys:

$$K_{Ic} \approx \left[\frac{2CE\,\varepsilon_c^*\sigma_y n^2}{(1-\nu^2)}\right]^{1/2} \qquad (7)$$

where C is a constant ($\approx$1/40), n the strain hardening exponent, and all the other letters denote variables defined earlier. Noting that the true strain at fracture in commercial aluminum alloys, having a constant distribution and volume fraction of constituents, is essentially constant, Garrett and Knott

(38) found a direct correlation between K_{Ic} and $n\sqrt{\sigma_y}$ for several of the alloys. This was in accordance with the simple model described by Eq. (6). Chen and Knott (40) obtained a similar relationship between fracture initiation toughness K_i (denoting plane-stress or plane-strain conditions) and the tensile properties n and σ_y in their study of the effects of Zr- and Cr-based dispersoids on the fracture of 7XXX series alloys. In the latter case, however, it was assumed that the critical step for the fracture process is the decohesion of the dispersoids from the matrix. The corresponding fracture criterion that failure is initiated when the tensile stress at the dispersoid/matrix interface exceeds the cohesive strength, σ_c, leads to the following relationship (35):

$$K_i \approx \sqrt{\frac{mb}{10A} \bullet E\sigma_c\sigma_y n^2 \bullet \frac{\lambda}{d}} \qquad (8)$$

where m is a constant ($\approx$1.5-3.0), b the Burgers vector, A a proportionality constant of magnitude $\frac{\mu b}{2}$ (where μ is the shear modulus) and λ and d the average spacing and diameter of the dispersoids, respectively. Since the variation of strain-hardening exponent, n, with aging runs counter to the dependence of the yield strength on heat treatment, the combination of n and σ_y, as described by Eqs. 7 and 8 was considered to provide a better correlation between fracture behavior and tensile properties (38,40).

In the present study, the high-purity Al-Cu-Li-Zr alloy was used so that mechanisms of quasi-static fracture due solely to microstructural variations could be examined by minimizing the process of void nucleation at constituent particles in the under-aged structures. A careful examination of the data in Table 14 and Figure 57 revealed that there does not exist a unique correlation between K_{Ic} and $n\sqrt{\sigma_y}$ (nor was there a correlation between the measured values of COD at initiation, δ_{ic} and n^2). Furthermore, it appears unrealistic to characterize the fracture toughness in terms of nominal Mode I stress intensity based on far-field loads parameters, when considerable local mixed-mode loading occurs due to crack bifurcation in the under-aged microstructures prior to the peak load corresponding to fracture initiation. As standard measurements of valid plane-strain fracture toughness (ref. ASTM E-399) allow certain amounts of stable crack growth, the geometry of the crack tip developed during the onset of quasi-static fracture can strongly influence the apparent values of measured K_{Ic}. The specific role of crack deflection in influencing fracture toughness is analyzed in the following section on Fracture Toughness.

Fracture Toughness Calculations (Al-2.9Cu-2.1Li)

It is well known that under-aged microstructures of precipitation hardened aluminum alloys are characterized by shearable and coherent precipitates, which offer resistance to the motion of dislocations. Previous studies (21,23,44) have shown that this effect is especially pronounced in the under-aged tempers of lithium-containing aluminum alloys, when the ordered δ' precipitates in the matrix enhance the propensity for planar slip and lead to a highly tortuous fracture morphology under cyclic-loading conditions. In the over-aged tempers of the present unrecrystallized alloys, T_1 and θ'

precipitates at subgrain boundaries and, more predominantly, δ' precipitates at high angle boundaries give rise to intercrystalline fracture, as shown in Figure 62, whereas the matrix deformation promotes uniform distribution of slip (34,23). In contrast to these processes, there is experimental evidence indicating that in the peak-aged structures of aluminum alloys, slip is concentrated in widely spaced slip bands, which leads to large slip offsets and strain localization at grain boundaries and hence may reduce the fracture toughness (35).

The crack profiles shown in Figures 59 through 62 indicate that, prior to the onset of stable ductile crack growth in the under-aged alloys containing shearable matrix precipitates, pronounced branching of the crack occurs along the intense shear bands (~30°-45° from the nominal Mode I crack plane) enveloped by the plastic zone. The branches of the bifurcated crack easily penetrate through (both low and high angle) grain boundaries and extend up to 1.5 mm during crack advance. As a non-linear crack-tip geometry is developed prior to the attainment of the peak load or stable crack growth, it becomes necessary to characterize fracture toughness in terms of the actual crack tip driving force, rather than the nominal K_{Ic} value.

A schematic of a two-dimensional elastic crack of length, a, which is forked by an angle 2θ, symmetrical about the Mode I plane, over a distance, b is shown in Figure 64. For this branched crack, the local Mode I and Mode II stress intensity factors, k_1 and k_2, respectively, can be expressed as functions of the nominal stress intensity factor, K_I, as follows:

$$k_1 = a_{11}(\theta)\ K_I \tag{9}$$

$$k_2 = a_{21}(\theta)\ K_I \tag{10}$$

For continued crack growth (co-planar) along the arms of the fork, estimation of the effective driving force using the maximum strain energy release rate, g, criterion yields (44) the following:

$$g = g_I + g_{II} \tag{11}$$

where the subscripts denote the local loading mode. In terms of effective stress intensity factor, K_D, this reduces to the following:

$$K_D = (k_1^2 + k_2^2)^{1/2} \tag{12}$$

The angular functions, $a_{ij}(\theta)$ in Eqs. (9,10) can be obtained from the analyses of Bilby et al. (45) for a semi-infinite elastic crack with a fork of unit length at its tip (b<<a) or from an alternative method suggested by Kitagawa et al. (46) for $\frac{b}{a}\lesssim 0.01$. For example, a forked crack with $2\theta = 90°$ and $\frac{b}{a}\lesssim 0.01$ has local stress intensity values $k_1 \approx 0.6\ K_I$, $k_2 \approx 0.3\ K_I$ and $K_D \approx 0.67\ K_I$ (45,46).

The variation of deflection-modified plane strain fracture toughness, $[K_c]_D$, as a function of yield strength is shown in Figure 64. Here, the scatter bands for the under-aged structures correspond to model calculations for angles of deflection $2\theta \approx 60 - 90°$ and $b \ll a$, based on the actual crack profiles observed on the specimen surface (Figures 59 through 61) and at the center-thickness section (Figure 62). For the peak-aged and over-aged conditions, however, $2\theta \approx 0°$ and hence $[K_c]_D \approx K_{Ic}$ (Figures 57 and 58). A major portion of the differences in K_{Ic} among a variety of microstructures is eliminated as indicated in Figure 64, when the effective local stress intensity accounting for crack branching is plotted against the yield strength. In fact, except for the very under-aged temper UA-1, $[K_c]_D$ is found to be fairly independent on yield strength. In the very low strength microstructure of UA-1, there exists some uncertainty in the definition of a "valid" plane-strain fracture toughness given by the equivalent stress intensity parameter, as linear elasticity is not appropriate in this case. Furthermore, it is not feasible to make a precise calculation of $[K_c]_D$ for this low strength temper because of the current paucity of a reliable fracture mechanics characterization procedure for non-linear cracks with extensive crack-tip plasticity. Indeed, the linear elastic calculations of local effective stress intensity factors for deflected cracks in the under-aged structures are only a crude first order estimation of the actual values, as the size of effective crack tip plastic zone may be comparable to the extent of crack bifurcation length, b. Despite such uncertainties, the clear experimental evidence of crack branching in the under-aged heat treatments (Figures 60 through 63) and the constancy of $[K_c]_D$ over a wide range of strength levels, convincingly, show that microstructurally-influenced crack deflection is an important mechanism responsible for the effects of aging treatment on quasi-static fracture in this aluminum alloy.

It is important to note here that the overall fracture behavior is dictated by the concurrent influence of several competing mechanisms, which involve slip characteristics, grain boundary failures, strength differences between the matrix and PFZ, strain hardening capacity, the size, shape and distribution of constituents, dispersoids and strengthening particles, and crack deflection processes. For the present high purity Al-Cu-Li-Zr alloy containing ordered δ' precipitates in the UA tempers, microstructure - and slip-induced deflection mechanisms seem to dominate over the other phenomena. This study specifically focuses on the role of such deflection in fracture. A careful evaluation of the relative importance of all the phenomena is essential for a complete description of the failure mechanisms. In general, materials which promote heterogeneous deformation, such as the under-aged tempers of precipitation-hardened aluminum, alloys of the aluminum-lithium system containing δ' precipitates that enhance slip planarity and certain titanium alloys (e.g. alloys with acicular α structure), will be expected to have a quasi-static fracture behavior that is strongly dictated by microstructure-induced changes in crack geometry.

Crack Growth Toughness (Al-2.9Cu-2.1Li)

The variation of nominal stress intensity factor, K_I, with the change in (effective) crack length, Δa (measured by compliance techniques) is shown in

Figure 66 for microstructures UA-3 (with the highest strength among the under-aged conditions studied, where the crack tip stress intensity calculations for non-planar geometries are likely to have the least error), PA (peak-aged) and OA-1 (an over-aged condition of comparable strength to under-aged temper UA-3). As crack advance in the under-aged structures occurs over distances of up to 1.5 mm along the arms of the fork, prior to unstable fracture along one of the branches of the fork, it appears reasonable to characterize the K-resistance curves shown in Figure 65 also in terms of a deflection-modified stress intensity factor, K_D. The variation of K_D with Δa for microstructures UA-3, PA and OA-1 is shown in Figure 66. The differences in quasi-static crack propagation characteristics among the three aging conditions are markedly reduced when the local K_D is plotted against the change in Δa.

This study has shown that differences in crack morphology, promoted by variations in intrinsic microstructural features and slip characteristics, account for an appreciable fraction of the effects of aging treatment on the fracture initiation toughness and quasi-static crack growth behavior in the high purity Al-Cu-Li-Zr alloy. In the very highly over-aged tempers, excessive intercrystalline fracture dictates toughness, whereas in the under-aged structures UA-1, with coherent and shearable precipitates, considerable bifurcation of the crack occurs along the bands of intense shear enveloped by the plastic zone, at the onset of fracture. Despite the uncertainties in the linear elastic fracture mechanics characterization of deflected cracks, this work shows that crack bifurcation is a major and viable mechanism for quasi-static fracture in certain microstructures of the aluminum-lithium alloy. Characterization of fracture in terms of a deflection-modified stress intensity factor, which takes into account microstructurally-influenced changes in crack geometry, leads to a constant fracture initiation toughness over a range of yield strength obtained by artificial aging. Specifically, for the Al-2.9Cu-2.1Li-0.12Zr alloy, deflection-modified fracture toughness $[K_c]_D$ is a constant (~30MPa$\sqrt{m}$) for a wide range of tempering times (2.25 through 200) at 191°C, or in terms of yield strength, from about 380-490MPa. The present work represents the first systematic and quantitative account of the effect of microstructurally-influenced crack deflection on fracture toughness in metallic materials and emphasizes the need to consider the role of crack geometry in the characterization of fracture. There is, also, some similar evidence in the literature where references have been made to the possible role of crack path in the fracture toughness of titanium alloys (47,48), and the effects of "shear-type" fracture in steels (49,50). These results for metallic materials are analogous to the well known phenomenon of deflection-induced toughening in ceramics and composites (51,52), where statistical approaches to estimate the improvements in fracture toughness due to crack deflection have been developed for various sizes, shapes and distribution of secondary particles (51). Recent work (27,28,31) on cyclic fracture in steel and aluminum alloys has also shown that microstructurally-influenced deflection can lead to a substantial enhancement in crack growth resistance, and simple linear elastic deflection models are now available for estimating the changes in growth rates for various degrees and extents of tilts and different levels of fatigue crack closure. It should be noted that this investigation has specifically focused on identifying and documenting the role of microstructure-induced crack deflection in fracture toughness. Other concurrent mechanisms of ductile fracture such as the effects of void nucleation and growth involving constituents and dispersoids, strain localization, precipitate free zones and grain boundaries should also be evaluated for the specific aluminum microstructures under study, before a complete understanding of the fracture behavior can be achieved. Detailed discussions on the role of crack geometry on K_{Ic} is given in reference (54).

Fractography

The 2020-type alloys with differing grain structures exhibit mix-mode fracture in the peak-aged temper, as shown in Figures 67 and 68. Ductile dimples and intergranular regions can be seen in both the figures. In addition, grain boundary separations are evident. The dimples contain constituent particles and the intergranular region at higher magnifications, Figures [67(b) and 68(b)], show shallow dimples. These shallow dimples on the intergranular fracture surface is thought to be due to precipitate free zones (10).

With increase in the Li content from about 1.1% Li in the Al-4.6Cu-1.1Li alloy to 2.9% Li in the Al-1.1Cu-2.9Li alloy, the fracture surfaces are predominantly intergranular in the T651 temper as shown in Figures 69, 70, respectively. At higher magnifications, shallow dimples can be clearly seen on the intergranular fracture surfaces of both the alloys, Figures 69(b) and 70(b), respectively.

Upon aging the alloy Al-2.9Cu-2.1Li, the fracture surface topography markedly changes from a total ductile-dimpled surface in a 1.25 hr at 191°C aged sample to a completely intergranular fracture in the severely over-aged (70 hr. at 191°C) sample, Figures 71 through 73. Even underaging at 2.25 hrs. at 191°C intergranular fracture can be seen with shallow dimples as shown in Figure 72. Further, aging to peak-aged and overaged tempers (16 to 70 hrs. at 191°C) there is completely intergranular mode of fracture, as shown in Figure 73.

STRESS CORROSION CRACKING

Aging Effect in Al-2.9Cu-2.1Li-0.12Zr Alloy

The SCC resistance of high strength aluminum alloys, in general, is strongly affected by the aging treatment. The present work is conducted on an Al-Cu-Li alloy to observe whether there are any similarities in the SCC behavior to that of conventional alloys. The experiment on the effect of aging on SCC growth resistance of Al-2.9Cu-2.1Li alloys was conducted in a 3.5% NaCl solution (drop-wise) for 92 days along S-L direction.

The variation of crack growth (in terms of crack length) with exposure time, for various aging treatments, starting from the very underaged (191°C/2 hrs.) to severely overaged (191°C/150 hrs.) conditions is shown in Figure 74. The data indicate that with increasing aging time, the crack growth is markedly reduced, the severely underaged alloy showing the maximum crack growth with exposure time. Figure 75 shows the SCC crack velocity vs. stress intensity data for all the aging conditions. The plateau velocity changes appears to be less significant compared to the changes in the apparent threshold stress intensities (K_{ISCC}). With increasing aging time, the K_{ISCC} is reduced to lower values. The range of plateau velocity of the present alloy seems to be of the same order of magnitude as that observed for alloys 2024-T351 and 7075-T651. The overall trend in the data is summarized in Figure 76. For comparison, Rockwell-R_B scale hardness is plotted, along with the initial pop-in stress intensities (K_{Ii}) and apparent K_{ISCC}. The gradual decrease in the K_{ISCC} with increasing aging time seems to be partly related to the initial K_{Ii} values, since these alloys have low S-L toughness at longer aging treatments.

Christodolou et al (55) studied the SCC susceptibility in binary Al-Li alloys and observed that the degree of susceptibility is dependent on the aging condition, the peak-aged temper being the most susceptible. They have suggested that hydrogen embrittlement may play a role in the SCC mechanism of binary Al-Li alloys (55). Rinker et al (56) studied the SCC performance of alloy 2020 as a function of aging. They observed excellent SCC resistance of alloy 2020 in its peak-aged temper. Poor SCC resistance was observed for the severely underaged temper. It was suggested (56) that SCC mechanism in alloy 2020 is due to the electrochemical potential difference between the grain boundary T_1 precipitate and the matrix, which provides a driving force for the preferential precipitate dissolution. Pizzo and co-workers (57) studied the stress-corrosion behavior of P/M Al-Li alloys containing Cu and Mg. They concluded that the stringer oxide particles play a key role in determining the SCC behavior of the P/M Al-Li-Cu alloys. In the present study, mechanistic interpretation of SCC behavior in high strength Al-Cu-Li-Zr alloys is not clear, since the mechanism could be masked by poor S-L toughness. One may speculate that precipitate dissolution leading to crack blunting could be leading to improved SCC resistance in the higher Li-containing alloys.

Composition Effect

SCC behavior of various Al-Cu-Li-Zr alloys in the T651 temper was monitored for 30 days. Tensile properties of the Al-Cu-Li-Zr alloys in the short-transverse (S-T) direction, are given in Table 17. A comparison of all the experimental SCC crack growth data with that of alloy 7075-T651 is shown in Figure 77. The results indicate clearly that most of the Al-Cu-Li alloys have good SCC resistance, except for the Mg-containing alloy. Addition of 1.0% Mg to Al-3.1Cu-2.2Li alloy decreased the SCC resistance significantly, since these alloys contained high vol. % of S-phase constituents. High Li-containing alloys (with no Mg) showed better resistance to SCC compared to the lower Li-containing (with no Mg) alloys. Upon converting the environmental crack growth plot of Figure 77 to the SCC velocity vs. stress intensity plot, shown in Figure 78, it is observed that the apparent plateau velocity is similar to that of 7075-T651 and does not appear to significantly differ with composition. On the other hand, the apparent K_{ISCC} seems to decrease with increasing Li-content. In general, the K_{ISCC} (and K_Q) decreased with increase in the (Li/Cu) ratio, as shown in Figure 79. This decrease is in K_{ISCC} with increase in (Li/Cu) ratio, could be in part related to the low S-L toughness values of the alloys.

Fractography

To characterize the trend in the SCC data described in the previous sections, SEM fractography on the broken DCB specimens was conducted. Fractographs are shown in Figures 80 through 83. No details of the SCC fractures could be observed for any of the alloys, because the fracture surfaces were covered with thick corrosion products. Attempts to dissolve such corrosion products by conventional means used in alumi..um alloys was unsuccessful. On the contrary, 7075-T651 alloy showed the classic SCC intergranular fracture, as shown in Figure 83.

Crack Profiles

Crack-tip profiles for all the alloys investigated (including 7075) are shown in Figures 84 through 88. In gene.'al, all the crack-paths are along the high angle grain boundaries and occasionally, as in the alloy Al-1.1Cu-2.9Li (Figure 88) some subgrain attack is observed. Optical photomicrographs of the crack-tip profiles of the Al-2.9Cu-2.1Li alloy in the underaged and overaged conditions are shown in Figure 84. The crack path is mainly along the high angle grain boundaries, with some areas of general corrosion.

The above observation indicates that corrosion proceeded primarily along grain boundaries in most of the alloy compositions and tempers. The propensity for intergranular attack is observed to be less in the 2020-type alloys, Figures 87(a) and (b).

SUMMARY

1. AXIAL-STRESS (S-N) FATIGUE

- o Axial-stress S-N fatigue behavior of Al-Cu-Li-Zr alloys is, in general, improved in both the smooth and notch conditions comparable to the conventional 7075-T651 alloy. Within the compositional limits studied, one could not observe any simple relationship of smooth or notch S-N fatigue lives with (Li/Cu) ratio.

- o Addition of 0.6 Mg to Al-3Cu-2Li alloy lead to significant improvement in smooth S-N fatigue resistance compared to 0.0 Mg alloy, which could be partly due to stretching effect. However, addition of 1.0 Mg showed less resistance to notch fatigue when compared to 0.0 Mg alloy. This is due to the formation of high vol. % of S-phase constituents in the 1.0 Mg alloy.

- o Finer grain size (unrecrystallized) alloy 2020 significantly improved the notch fatigue strengths at lives greater than 10^5 cycles when compared to the coarse grain (recrystallized) alloy 2020. The difference could be due to complex crack initiation mechanisms in the two grain structure alloys.

2. FATIGUE CRACK GROWTH (FCG)

- Constant-Load FCG: Differences in the constant-load amplitude FCG resistances among Al-Cu-Li alloys are greatest at the near-threshold (ΔK_0) region, which has the greatest impact on fatigue crack growth life. The ΔK_0 monotonically increased with (Li/Cu) ratio. Such beneficial FCG properties appear to arise from the crystallographic crack growth mechanism and crack deflection processes induced by the ordered δ' precipitates in the alloys of higher Li content.

  The change in grain structure from recrystallized coarse grain to the unrecrystallized grain in the alloy 2020 had only a small effect on the FCG behavior at near-threshold FCG rates. The effect of grain size on ΔK_0 in 2020 is not understood.

- Single Overload Spectrum FCG: Under single overload FCG conditions, significant resistance to crack growth rates was observed with increase in (Li/Cu) ratio. Significant retardation in FCG rates due to OL spectrum loading was also observed in the coarse grain alloy 2020 compared to the TMP 2020 unrecrystallized alloy. In general, the OL FCG resistance in Al-Cu-Li alloys could be attributed to crack branching processes even though detailed mechanisms are not understood in Al-Li alloys due to complex interactions of environment, microstructure, load-ratio and deformation.

3. FRACTURE TOUGHNESS

- Grain structure differences in alloys of 2020-type showed a small effect on toughness at near peak-age condition. At lower yield strength, in the under-aged condition, the unrecrystallized Al-4.6Cu-1.1Li alloy showed higher toughness (K_Q) compared to both fine and coarse grain 2020 alloys. This difference is due to the lack of constituent particles in the high purity Al-4.6Cu-1.1Li alloy.

- At a given yield strength, (Li/Cu) ratio had significant effect on toughness in Al-Cu-Li alloys. This could be due to planar slip deformation in higher Li containing alloys initiating failure at the grain boundaries due to the presence of grain boundary precipitates. Experiments to separate the role of planar slip and grain boundary precipitates are in progress.

- Aging effect in the Al-2.9Cu-2.1Li alloy had strong dependence of toughness on yield strength up to peak-aged condition. In the overaged conditions where both high and low angle grain boundaries are decorated with precipitates, toughness was nearly independent of yield strength. Such variations in toughness was correlated to the marked differences in crack morphology among the aging conditions. The underaged microstructures promote severely branched cracks. In contrast to this,

REFERENCES

1. Al-Li Alloys, Ed. by T. H. Sanders, Jr. and E. A. Starke, Jr., Metallurgical Society of AIME Publication, 1981.

2. Al-Li Alloy II, Ed. by T. H. Sanders, Jr. and E. A. Starke, Jr., Metallurgical Society of AIME Publication, 1984.

3. Phase Diagram of Al-Cu-Li Alloy, H. Stumpf, Unpublished Work, 1969.

4. W. S. Miller, A. J. Cornish, A. E. Titchner and D. A. Bennett, Al-Li Alloys II, Ed. by T. H. Sanders, Jr. and E. A. Starke, Jr., Metallurgical Society of AIME Publication, p. 335, 1984.

5. R. J. Bucci, "Development of a Proposed Standard Practice for Near-Threshold Fatigue Crack Growth Rate Measurement," ASTM STP 738, American Society for Testing and Materials, pp. 5-28, 1981.

6. R. C. Malcolm, A. K. Vasudevan, R. J. Bucci, P. E. Bretz, "Evaluation of the Engineering Properties of a Commercially Produced Aluminum Alloy 2020-T651 Plate," Amendment to Naval Air Systems Command Contract No. N00019-79-C-0258, 1981 December 18.

the overaged tempers, tested at comparable yield strength levels, showed a linear crack profile. Such differences in the local mode of crack advance seem to account for a significant extent of microstructural (or aging) effects on fracture toughness in this alloy.

4. STRESS CORROSION CRACKING (SCC)

In general, all the Al-Cu-Li-Zr alloys showed improved resistance to SCC when compared to the conventional aluminum alloys. Both the aging treatment in the Al-2.9Cu-2.1Li alloy and the compositional differences of the alloys in terms of (Li/Cu) ratio did not significantly affect the magnitude of the apparent plateau velocity. The apparent K_{ISCC}, however, decreased with increase in the aging treatment for the alloy Al-2.9Cu-2.1Li or increase in (Li/Cu) ratio. This observation is partly due to the low toughness of the alloys in the S-L orientation. To date, mechanistic understanding of SCC behavior in the Al-Cu-Li alloys is not clear, even though precipitate dissolution and hydrogen embrittlement mechanisms have been proposed by previous investigators.

7. P. E. Bretz, A. K. Vasudevan, R. J. Bucci, and R. C. Malcolm, "Effect of Microstructure on 7XXX Aluminum Alloy Fatigue Crack Growth Behavior Down to Near-Threshold Rates," Final Report, Naval Air Systems Command Contract No. N00019-79-C-0258, 1983 October 30.

8. T. H. Sanders, Jr., R. R. Sawtell, J. T. Staley, R. J. Bucci, and A. B. Thakker, "Effect of Microstructure on Fatigue Crack Growth of 7XXX Aluminum Alloys Under Constant Amplitude and Spectrum Loading," Final Report, Naval Air Development Center, Contract No. N0019-C-0482, 1978 April 14.

9. M. V. Hyatt, Corrosion-NACE, Vol. 26, #11, p. 487, Nov. 1970.

10. W. X. Feng, F. S. Lin and E. A. Starke, "Proceedings Aluminum-Lithium Alloys II," T. H. Sanders and E. A. Starke, Eds., AIME, 235, 1983.

11. E. A. Starke, Jr., and G. Lutjering, Fatigue and Microstructure, Ed. M. Meshii, ASM Publ., p. 205, 1979.

12. M. S. Hunter and W. G. Fricke, Jr., Proc. ASTM, Vol. 54, p. 717, 1954.

13. J. C. Grosskreutz and G. G. Shaw, 2nd International Conference on Fracture, Ed. P. L. Pratt, Chapman and Hall, London, p. 620, 1969.

14. C. Y. Kung and M. E. Fine, Met. Trans. A, Vol. 10A, p. 603, 1979.

15. D. Sigler, M. C. Montpetit and W. L. Haworth, Met. Trans. A, Vol. 14A, p. 931, 1983.

16. F. G. Osterman and W. H. Reimann, ASTM STP 467, ASTM Publ., p. 169, 1970.

17. P. E. Bretz, L. N. Mueller, and A. K. Vasudevan, Al-Li Alloys II, E. A. Starke, Jr. and T. H. Sanders, Jr., AIME Publ., p. 543, 1984.

18. C. Laird, Alloy and Microstructural Design, Ed. J. Kitien and G. S. Anseu, Academic Press, p. 175, 1976.

19. T. H. Sanders, Jr., Final Report, NAVAIR Contract No. N62269-76-C-0217, 1979.

20. E. J. Coyne, Jr., T. H. Sanders, Jr. and E. A. Starke, Jr., Al-Li Alloys, Ed. T. H. Sanders, Jr. and E. A. Starke, Jr., TMS-AIME Publ., p. 293, 1981.

21. A. K. Vasudevan, P. E. Bretz, A. C. Miller and S. Suresh: Mater. Sci. Eng., Vol. 62, p. 113, 1984.

22. A. K. Vasudevan and S. Suresh: Metall. Trans. A, Vol. 13A, p. 2271, 1982.

23. S. Suresh, A. K. Vasudevan and P. E. Bretz: Metall. Trans. A, Vol. 15A, p. 369, 1984.

24. F. S. Lin and E. A. Starke, Jr.: Mater. Sci. Eng., Vol. 43, p. 65, 1980.

25. S. Suresh, G. F. Samiski and R. O. Ritchie: Metall. Trans. A, Vol. 12A, p. 1435, 1981.

26. S. Suresh, I. G. Palmer and R. E. Lewis: Fat. Eng. Mater. Struct., Vol. 5, p. 133, 1982.

27. S. Suresh: Metall. Trans. A, Vol. 14A, p. 2375, 1983.

28. S. Suresh: Metall. Trans. A, 1984, Vol. 15A, p. 249, 1985; Also, Brown University Report E-153, March, 1984.

29. J. I. Petit and P. E. Bretz, High Strength P/M Aluminum Alloys, Eds. M. J. Koczak and G. J. Hildeman, TMS-AIME, p. 147, 1982.

30. P. E. Bretz, J. I. Petit and A. K. Vasudevan, Fatigue Crack Growth Threshold Concepts, Eds. D. L. Davidson and S. Suresh, TMS-AIME, p. 163, 1984.

31. A. K. Vasudevan and S. Suresh, Met. Trans. A, Vol. 15A, p. 475, 1985.

32. S. Suresh and A. K. Vasudevan, Fatigue Crack Growth Threshold Concepts, Eds. D. L. Davidson and S. Suresh, TMS-AIME, p. 361, 1984.

33. P. E. Bretz, A. K. Vasudevan, R. J. Bucci and R. C. Malcolm, ASTM-STP 833, p. 242, 1984.

34. A. K. Vasudevan, S. Suresh, M. Tosten and P. R. Howell, to be published 1984.

35. G. T. Hahn and A. R. Rosenfield, Met. Trans. A, Vol. 6A, p. 653, 1985.

36. R. H. Van Stone, R. H. Merchant and J. R. Low, ASTM STP 556, p. 93, 1974.

37. R. H. Van Stone and J. A. Psoida, Met. Trans. A, Vol. 6A, p. 668, 1975.

38. G. G. Garrett and J. F. Knott, Met. Trans. A, Vol. 9A, p. 1187, 1978.

39. G. M. Ludtka and D. E. Laughlin, Met. Trans. A, Vol. 13A, p. 411, 1982.

40. C. Q. Chen and J. F. Knott, Met. Sci., Vol. 15, p. 357, 1981.

41. A. K. Vasudevan, A. C. Miller and M. M. Kersker, in Aluminum-Lithium Alloys II, edited by T. H. Sanders, Jr. and E. A. Starke, Jr., The Metallurgical Society of AIME, Warrendale, PA, p. 181, 1984.

42. J. D. Embury, in Alloy Design for Fatigue and Fracture resistance, AGARD Conference Proceedings No. 185, NATO, Nemilly Sur Seine, France, p. 1-1, 1976.

43. J. R. Rice and M. A. Johnson, in Inelastic Behavior of Solids, edited by M. F. Kanninen et al., McGraw-Hill, N.Y., p. 641, 1970.

44. P. C. Paris and G. C. Sih, in ASTM STP 381, American Society for Testing and Materials, Philadelphia, PA, p. 30, 1965.

45. B. A. Bilby, G. E. Cardew and I. C. Howard, in Fracture 1977, edited by D. M. R. Taplin, The University of Waterloo Press, Vol. 3, p. 201, 1977.

46. H. Kitagawa, R. Yuuki and T. Ohira, Eng. Fract. Mech., Vol. 7, p. 515, 1975.

47. A. Zarkades and F. R. Larson, in Titanium Science and Technology, Plenum Press, Vol. 2, p. 1321, 1973.

48. C. A. Stubbington, in Alloy Design for Fatigue and Fracture Resistance, AGARD Conference Proceedings No. 185, NATO, Nemilly Sur Seine, France, p. 3-1, 1976.

49. C. Beachem and G. R. Yoder, Met. Trans. A, Vol. 4, p. 1145, 1973.

50. J. Q. Clayton and J. R. Knott, Metal Sci., Vol. 10, p. 63, 1976.

51. K. T. Faber and A. G. Evans, Acta. Met., Vol. 31, p. 565, 1983.

52. M. Gomina, J. L. Chermant and F. Osterstock, in Creep and Fracture of Engineering Materials and Structures, edited by B. Wilshire and D. R. J. Owen, Pineridge Press, Swansea Part I, p. 541, 1984.

53. A. K. Vasudevan, E. A. Ludwiczak, S. F. Baumann, R. D. Doherty and M. M. Kersker, Matls. Science & Engg., 1985, in press.

54. A. K. Vasudevan and S. Suresh, Materials Sc. & Engg, 1985, Vol. 70, 1985, in press.

55. L. Christodolou, L. Struble and J. R. Pickens, Al-Li Alloys II, Ed. by T. H. Sanders and E. A. Starke, AIME Publ., p. 561, 1984.

56. J. G. Rinker, M. Marek and T. H. Sanders, Al-Li Alloys II, Ed. by T. H. Sanders and E. A. Starke, AIME Publ., p. 597, 1984.

57. P. P. Pizzo, R. P. Galvin and H. G. Nelson, Al-Li Alloys II, Ed. by T. H. Sanders and E. A. Starke, AIME Publ., p. 627, 1984.

TABLE 1

AVERAGE COMPOSITION (WT %) OF AL-CU-LI-ZR ALLOYS

Sample No.	Cu	Li	Mg	Zr	Fe	Si	Ti	Na	Ca	Al	(Li/Cu) Ratio (at %)
548465	4.6	1.1	0.0	0.17	0.06	0.04	0.01	0.0001	0.0009	Balance	2.2
548466	2.9	2.1	0.0	0.12	0.06	0.04	0.01	0.0002	0.0010	Balance	6.5
504440	3.1	2.2	1.0	0.13	0.06	0.05	0.02	0.0004	0.0030	Balance	6.5
548468	1.1	2.9	0.0	0.11	0.06	0.04	0.01	0.0004	0.0014	Balance	25.2

TABLE 2

HYDROGEN CONTENT (WT. PPM) IN T651 AL-CU-LI-ZR ALLOYS

Sample No.	As Cast Ingots	12.7 mm Plate	35 mm Plate
548465	0.26	0.32	0.36
548466	0.24	0.29	0.25
504440	0.25	0.41	0.28
548468	0.63	0.52	0.38
2024-T351	--	--	0.17
7075-T651	--	--	0.11

TABLE 3

VARIATION OF HYDROGEN CONTENT (WT PPM) WITH AGING IN ALLOY AL-2.9CU-2.1LI (S-548466)

AGING TEMP.	AGING TIME (HOURS)	HYDROGEN CONCENTRATION (WT PPM)
191°C	2.25	0.20
191°C	3.5	0.21
191°C	6.5	0.27
191°C	18	0.27
191°C	70	0.27
191°C	200	0.28
191°C	520	0.33

TABLE 4

HEAT-TREATMENT AND HOT-ROLLING SCHEDULES FOR THE AL-CU-LI-ZR ALLOYS

Sample No.	Preheat Treatment	Starting Hot Rolling Temperature	Solution Heat Treatment	Aging Temperature
548465	520°C/8 hrs	520°C	528°C/1 hr+CWQ	160°C/[illegible] hrs
548466	520°C/8 hrs	520°C	552°C/1 hr+CWQ	191°C/t hrs
504440	520°C/48 hrs	520°C	528°C/1 hr+CWQ	191°C/t hrs
548468	520°C/8 hrs	520°C	552°C/1 hr+CWQ	191°C/t hrs

TABLE 5

LAUE TRANSMISSION ANALYSIS OF AL-CU-LI-ZR ALLOYS

Sample No.	Cu	Li	Mg	Zr	Laue Transmission Analysis - Remarks
548465	4.6	1.1	0	.17	Structure appears both coarse and fine-mixed. Several recrystallized fine grains present. (Strain present.)
548466	2.9	2.1	0	.12	Structure predominantly coarse. Several recrystallized grains - both coarse and fine - appear to be present. (Strain present.)
548468	1.1	2.9	0	.11	Fine structure. Appears partially recrystallized. (Strain present.)
504440	3.1	2.2	1.0	.13	Fine structure. Some recrystallization present. Less than in 548468 but considerably more than in 548465 and 548466. (Strain present.)

TABLE 6

X-RAY GUINIER ANALYSIS OF AL-CU-LI-ZR ALLOYS

Sample No.	Cu	Li	Mg	Al_7Cu_2Fe	θ^1 ($CuAl_2$)	s^1 (Al_2CuMg)	δ^1 Al_3Li	T_2 Al_5CuLi_3	$FeAl_3$
548465	4.6	1.1	0	Sml.	Sml.	--	V. Sml.	--	--
548466	2.9	2.1	0	Sml.+	V. Sml.	--	Med +	Trace	--
548468	1.1	2.9	0	--	--	--	Med -	--	V. Sml.
504440	3.1	2.1	1.0	Sml.	V. Sml.	V. Sml.	Med +	V. Sml.	--

TABLE 7

LONGITUDINAL TENSILE PROPERTIES OF ALLOY AL-4.6CU-1.1LI

Aging Time at 160°C (hours)	Yield Stress (MPa)	Tensile Stress (MPa)	% Elongation (in 4D)
2	140	448	14
4	385	511	18
8	413	539	18
16	490	560	14
32	529	582	14
64	531	593	12
100	525	588	12

TABLE 8

LONGITUDINAL TENSILE PROPERTIES OF ALLOY AL-2.9CU-2.1LI

Aging Time at 191°C (hours)	Yield Stress (MPa)	Tensile Stress (MPa)	% Elongation (in 4D)
2	420	476	8
4	469	511	6
8	497	536	8
16	487	543	10
18	490	544	10
32	475	532	10
48	455	530	10
64	406	483	10
128	378	462	10

TABLE 9

LONGITUDINAL TENSILE PROPERTIES OF ALLOY AL-1.1CU-2.9LI

Aging Time at 191°C (hours)	Yield Stress (MPa)	Tensile Stress (MPa)	% Elongation (in 4D)
2	336	441	6
4	364	469	6
8	399	504	6
16	420	518	6
30	434	524	6
32	437	526	6
48	417	508	6
64	409	504	8
100	392	483	6
128	374	462	6

TABLE 10

LONGITUDINAL TENSILE PROPERTIES OF ALLOY AL-3.1CU-2.2LI-1.0MG

Aging Time at 191°C (hours)	Yield Stress (MPa)	Tensile Stress (MPa)	% Elongation (in 4D)
2	434	511	9
4	476	546	8
8	511	563	7
16	527	562	6
32	518	553	5

TABLE 11

DENSITY AND ELASTIC MODULUS OF Al-Cu-Li-Zr ALLOYS

Sample No.	Density (10^3 kg/m^3)	% Lower Density from Alloy 7075	Elastic Modulus (GPa)
548465	2.71	3.6	76
548466	2.61	7.1	79
504440	2.59	7.8	79
548468	2.51	10.7	83
2020-T651	2.71	--	77
2024-T351	2.78	--	72
7075-T651	2.81	--	71

TABLE 12

LONGITUDINAL TENSILE PROPERTIES OF AL-LI-X ALLOYS
IN T651 TEMPER

Sample No.	Cu	Li	Mg	Yield Stress (MPa)	Tensile Stress (MPa)	% Elongation (in 4D)
548465	4.6	1.1	--	531	593	12
548466	2.9	2.1	--	490	544	10
548468	1.1	2.9	--	434	524	6
504793*	2.8	2.0	0.6	465	514	7
504440	3.1	2.2	1.0	527	562	6
504794	--	3.1	--	309	425	5
523713-B	2020 - recrystallized			522	557	4
523713-X	2020 - unrecrystallized			531	566	4

*alloy plate not stretched

TABLE 13

LONG-TRANSVERSE TENSILE/TOUGHNESS PROPERTIES OF 2020 ALLOYS

Sample No.	L-T Yield Stress (MPa)	L-T Tensile Stress (MPa)	% Elongation (in 4D)	T-L K_Q (MPa$\sqrt{m}$)
523713-B	323	431	12	73.2
Recrystallized	384	465	8	53.9
	463	538	5	32.5
	504	550	3	26.0
	533	557	2	20.6
523713-X	337	450	13	69.2
Unrecrystallized	439	510	13	51.4
	509	550	7	26.4
	515	561	8	24.8
	527	570	7	21.8

TABLE 14

LONG-TRANSVERSE TENSILE/TOUGHNESS PROPERTIES OF
AL-4.6CU-1.1LI & AL-1.1CU-2.9LI ALLOYS

Sample No.	L-T Yield Stress (MPa)	L-T Tensile Stress (MPa)	% Elongation (in 4D)	T-L K_Q (MPa$\sqrt{m}$)
548465	388	490	13	78.0
(Al-4.6Cu-1.1Li)	451	530	11	52.5
	495	541	8	28.9
	505	552	5	25.2
	511	559	4	20.5
548468	274	404	9	44.6
(Al-1.1Cu-2.9Li)	316	453	8	40.5
	355	482	8	28.4
	393	495	6	19.0

TABLE 15

LONG-TRANSVERSE TENSILE PROPERTIES OF ALLOY AL-2.9CU-2.1LI

Microstructure	Aging Time (hrs) at 191°C	Yield Stress (MPa)	Tensile Stress (MPa)	% Elongation (in 4D)	Strain Hardening Exponent (n)
UA-1	1.25	328	383	7	0.078
UA-2	2.25	410	461	4	0.046
UA-3	3.50	435	470	4	0.044
PA	18.0	487	507	6	0.039
OA-1	70.0	421	461	2	0.050
OA-2	200.0	394	442	2	0.059
OA-3	520.0	344	381	2	0.080

TABLE 16

SUMMARY OF FRACTURE TOUGHNESS PARAMETERS IN ALLOY AL-2.9CU-2.1LI

Microstructure	Measured J_{Ic} (MPa$\sqrt{m}$)	K_{Ic} derived from J_{Ic} (MPa$\sqrt{m}$)	Measured K_c or (K_{Ic}) (MPa$\sqrt{m}$)
UA-1	0.068	77.0	--
UA-2	0.026	46.6	42.3
UA-3	0.017	39.0	40.6
PA	0.008	26.6	(30.0)
OA-1	0.011	31.1	(30.5)
OA-2	0.007	25.1	31.4
OA-3	0.007	24.8	(24.5)

TABLE 17

SHORT-TRANSVERSE TENSILE PROPERTIES OF AL-CU-LI-ZR ALLOYS

Sample No.	Composition Cu	Li	Mg	YS (ksi)	TS (ksi)	% Elongation (in 4D)
S-548465	4.6	1.1	--	65.[illegible]	67.4	2.0
S-548466	2.9	2.1	--	--	52.2	0.0
S-504440	3.1	2.2	1.0	61.9	68.4	4.0
S-548468	1.1	2.9	--	47.7	50.6	0.0
7075-T651	--	--	--	63.7	70.6	4.0

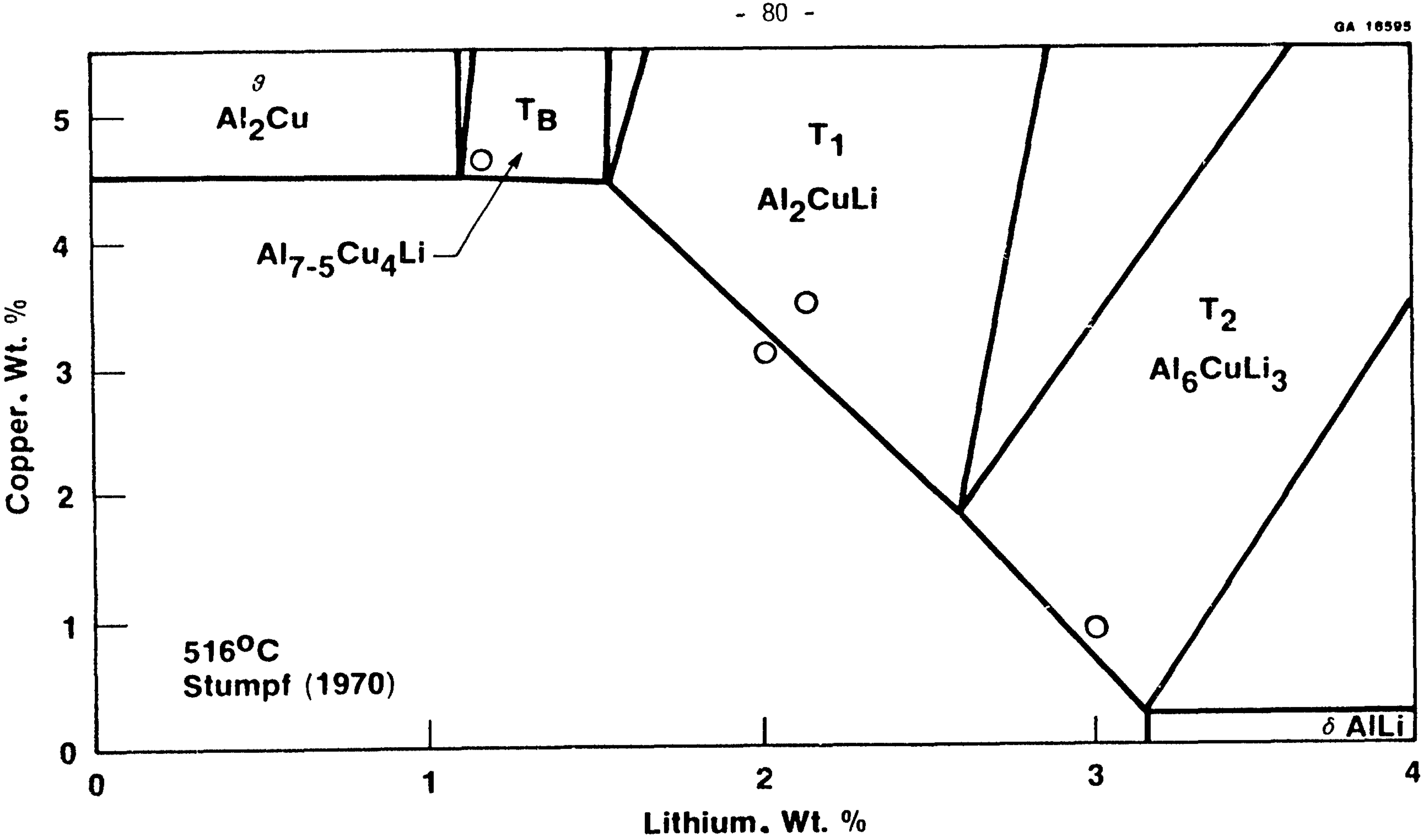

**Phase Diagram at 516°C of Al-Cu-Li System.
Present Alloy Compositions Denoted by Circles.**

Figure 1

GA 16595

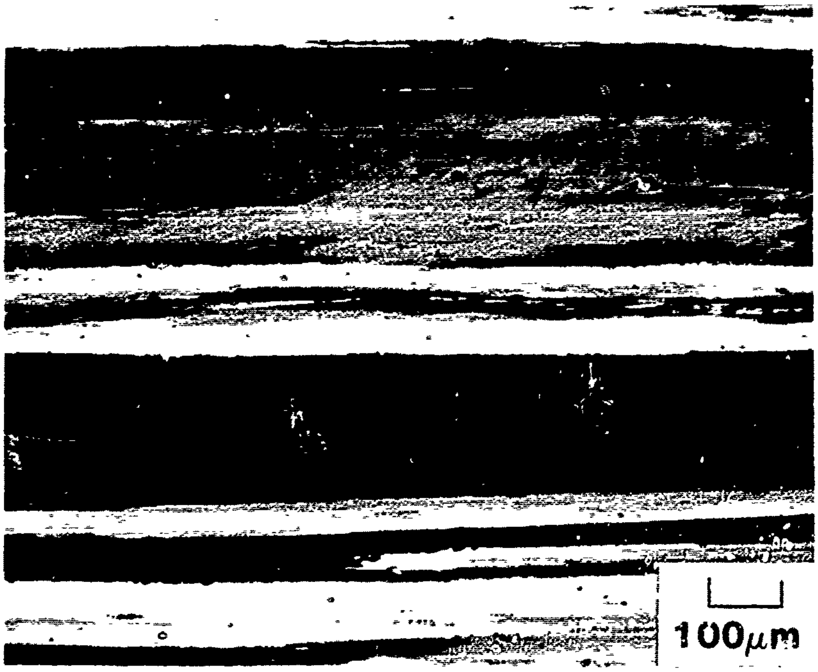

(a) Optical micrograph showing grain structure in the L direction of sample 548465 (Al - 4.6 Cu - 1.1 Li alloy plate, 12.7 mm thick)

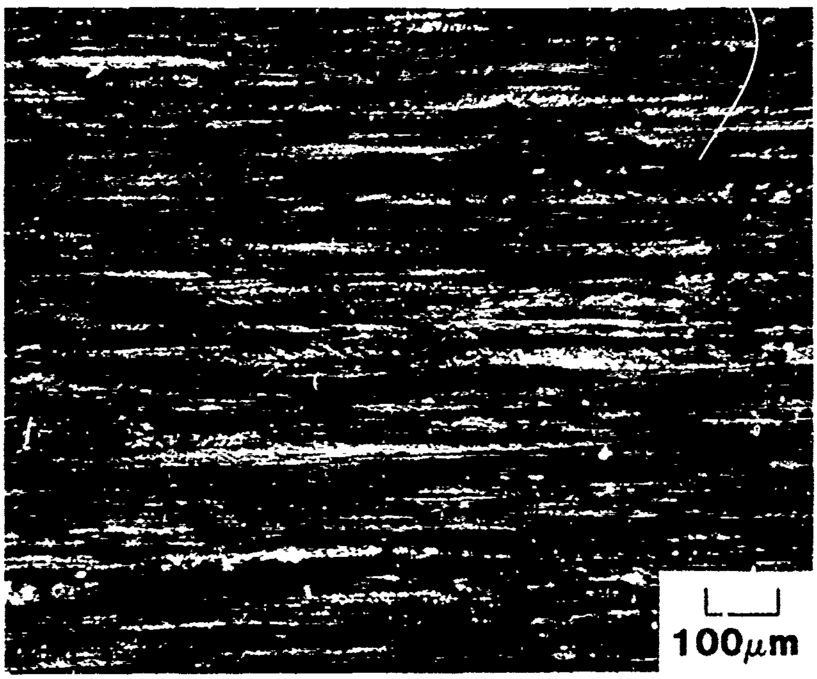

(b) Optical micrograph showing grain structure in the L direction of sample 548468 (Al -1.1 Cu -2.9 Li alloy plate, 12.7 mm thick)

Figure 2 (a, b)

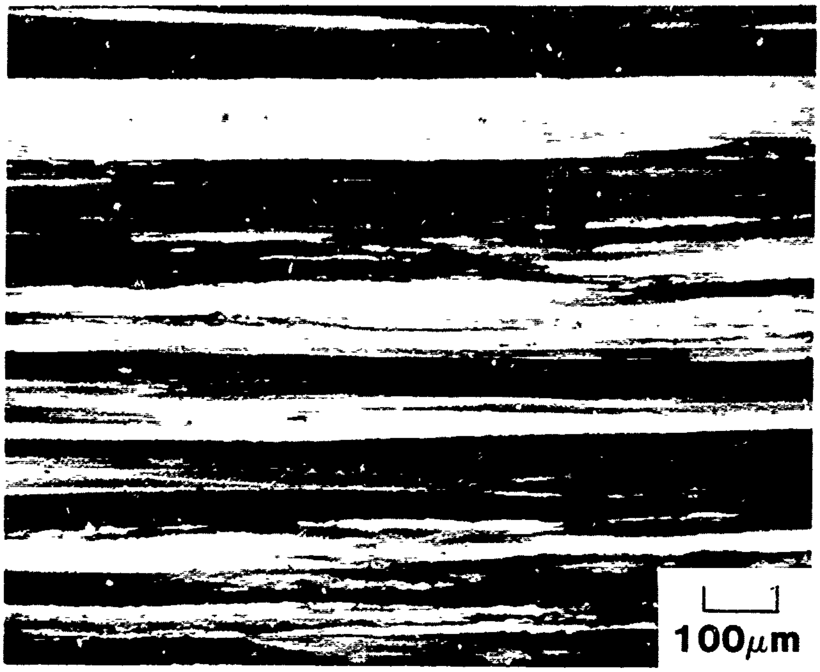

(c) Optical micrograph showing grain structure in the L direction of sample 548466 (Al -2.9 Cu -2.1 Li alloy plate, 12.7 mm thick)

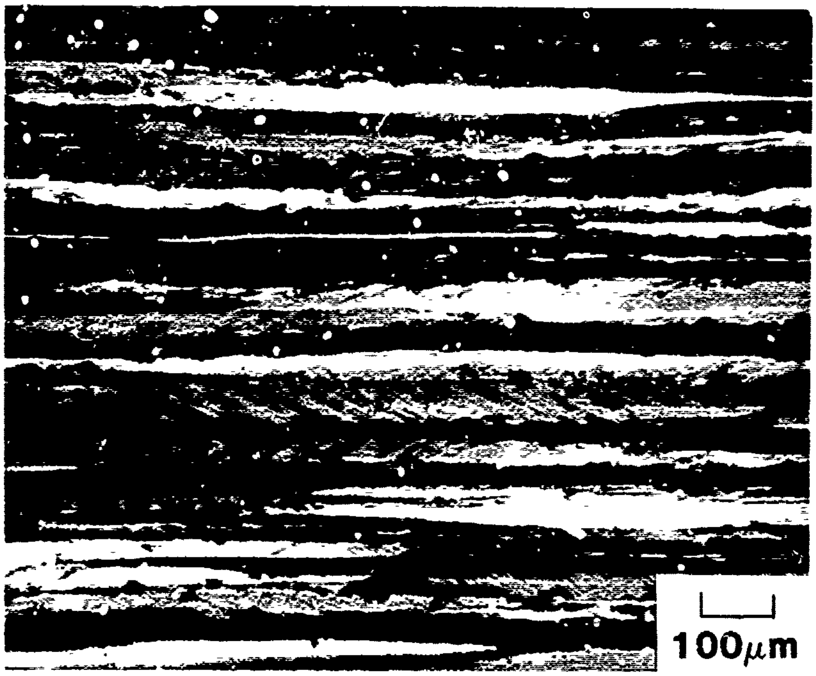

(d) Optical micrograph showing grain structure in the L direction of sample 504440 (Al -3.1 Cu -2.2 Li - 1 Mg alloy plate, 12.7 mm thick)

Figure 2 (c, d)

GA 16595

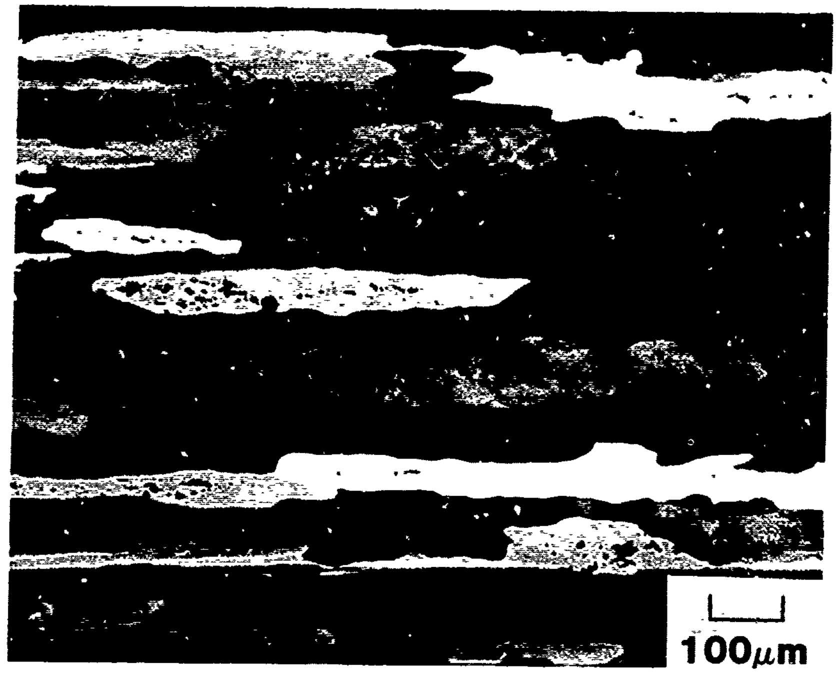

(e) Optical micrograph showing grain structure in the L direction of sample 523713-B (2020-T651 plate, 28 mm thick)

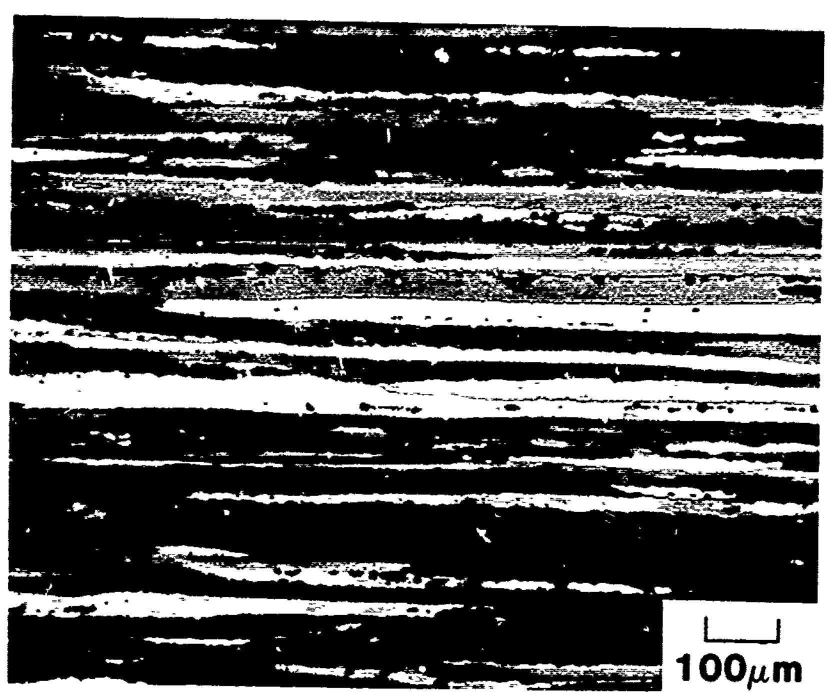

(f) Optical micrograph showing grain structure in the L direction of sample 523713-X (TMP 2020 plate, 12.7 mm thick)

Figure 2 (e, f)

GA 16595

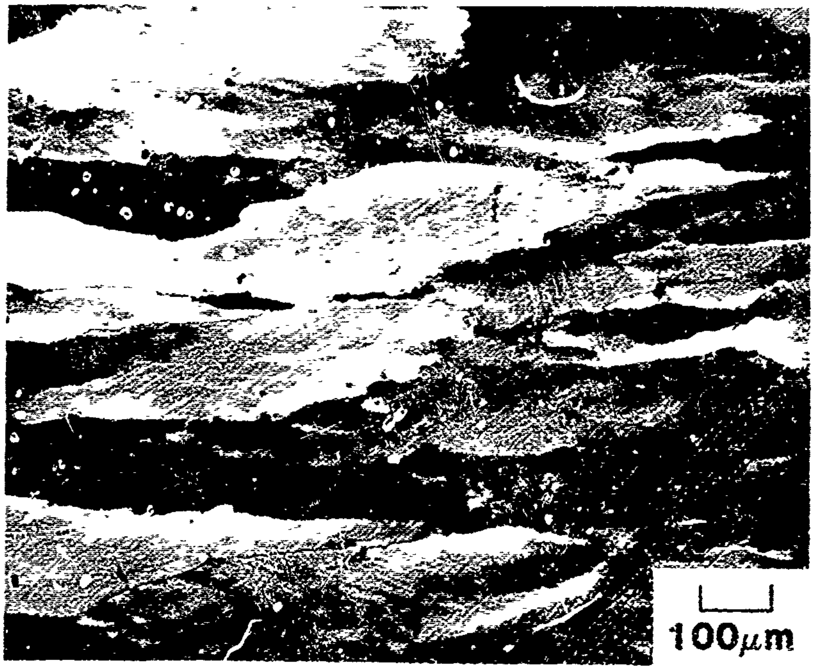

(a) Optical micrograph showing grain structure in the L direction of sample 548465 (Al - 4.6 Cu - 1.1 Li alloy plate, 35 mm thick)

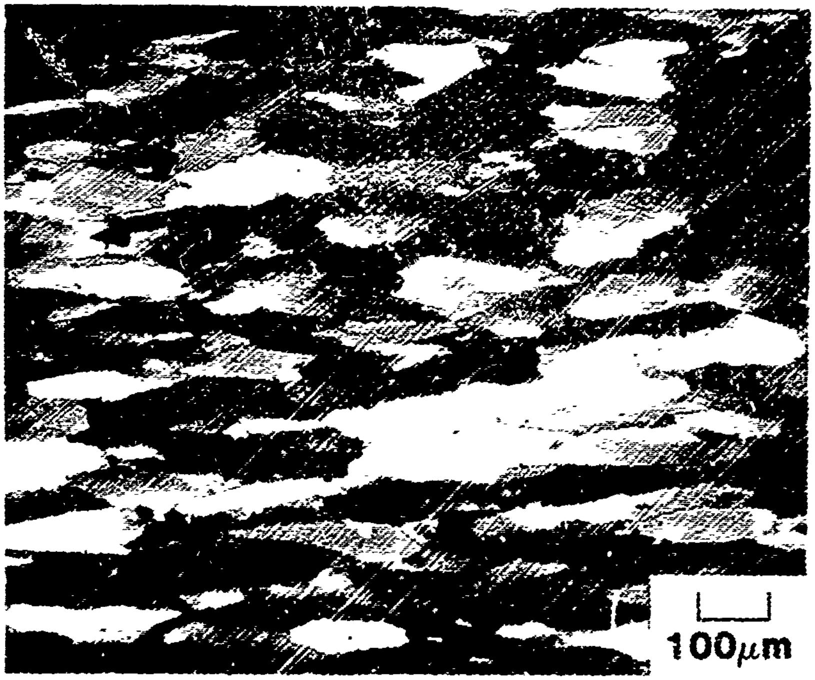

(b) Optical micrograph showing grain structure in the L direction of sample 548468 (Al -1.1 Cu -2.3 Li alloy plate, 35 mm thick)

Figure 3 (a, b)

GA 16595

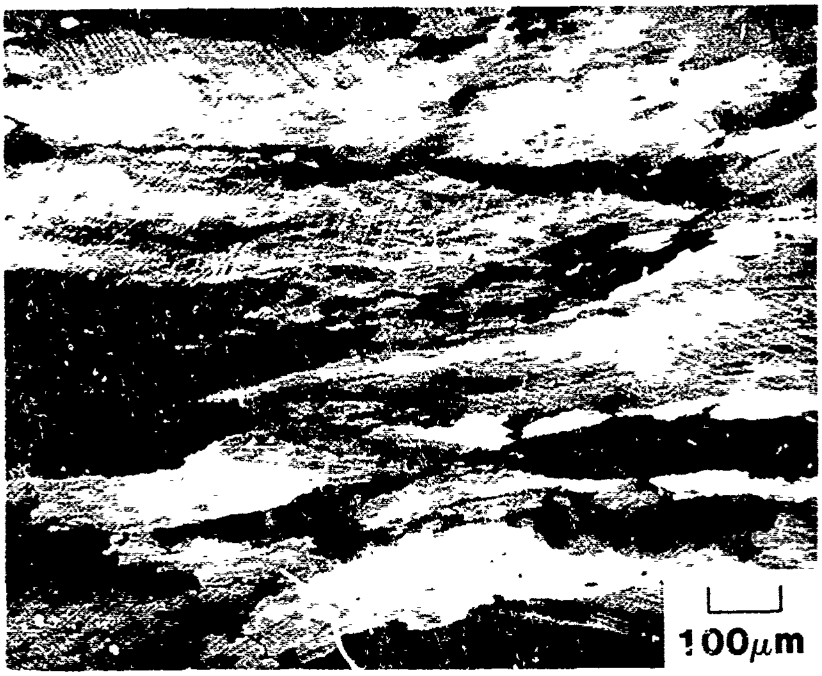

(c) Optical micrograph showing grain structure in the L direction of sample 548466 (Al -2.9 Cu -2.1 Li alloy plate, 35 mm thick)

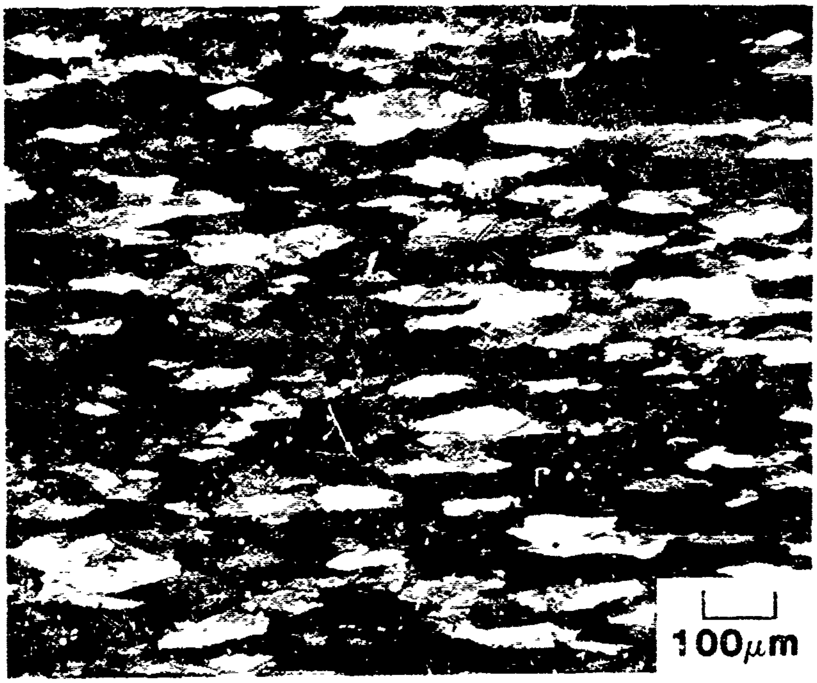

(d) Optical micrograph showing grain structure in the L direction of sample 504440 (Al -3.1 Cu -2.2 Li - 1 Mg alloy plate, 35 mm thick)

Figure 3 (c, d)

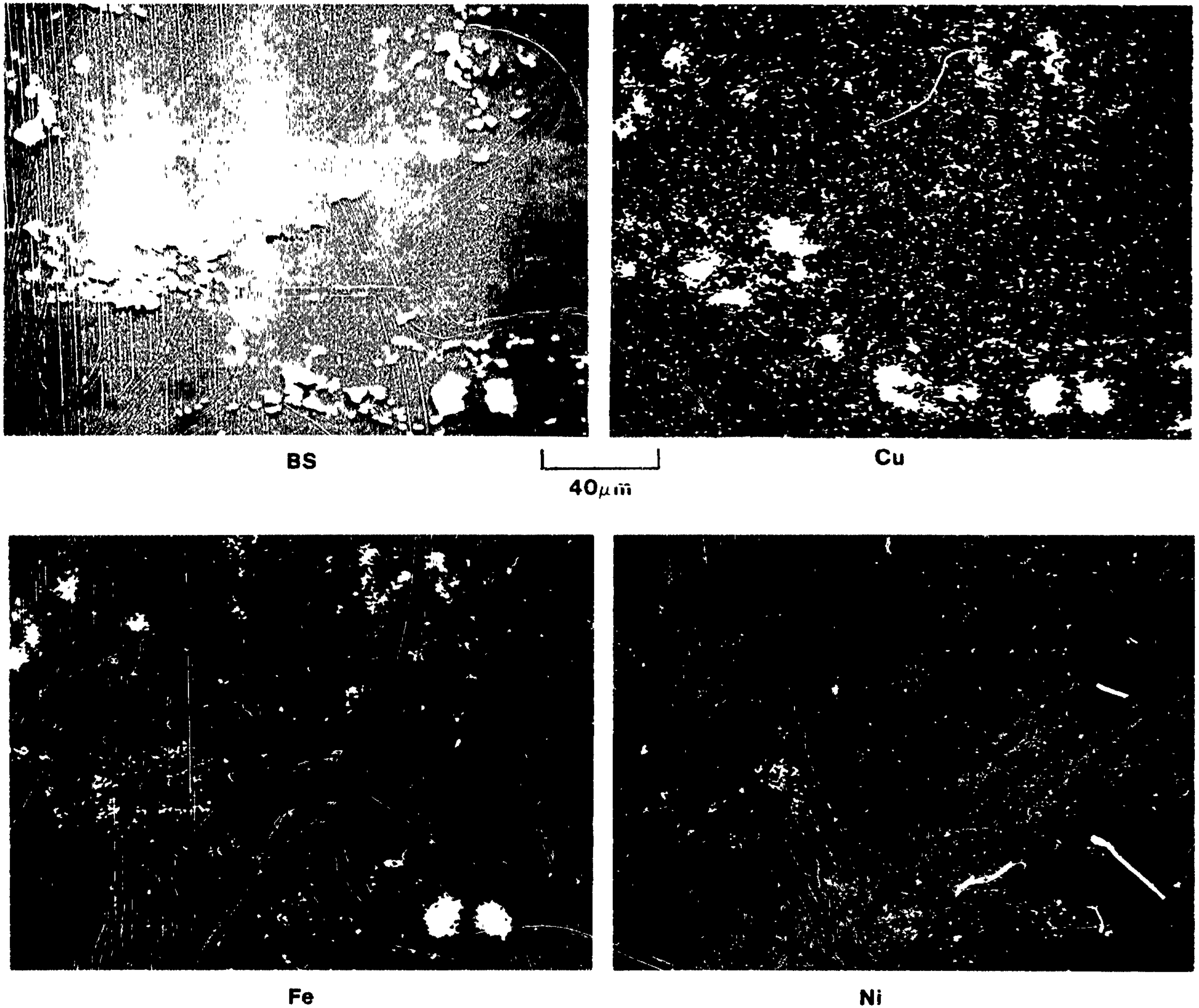

Electron microprobe x-ray maps of constituent particles in sample 548465
(Al - 4.6 Cu - 1.1 Li alloy T651 plate)

Figure 4

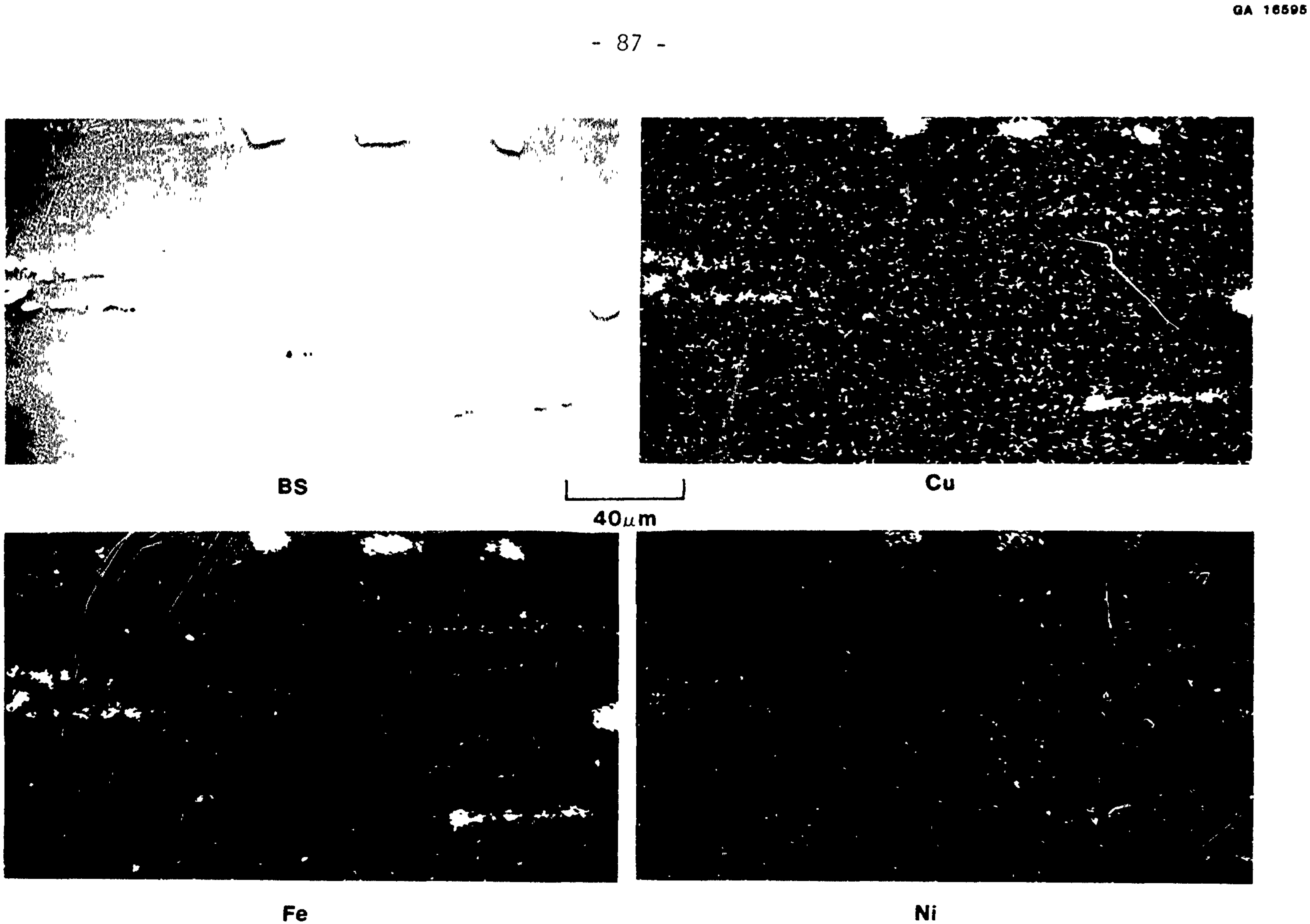

Electron microprobe x-ray maps of constituent particles in sample 548466
(Al -2.9 Cu -2.1 Li alloy T651 plate)

Figure 5

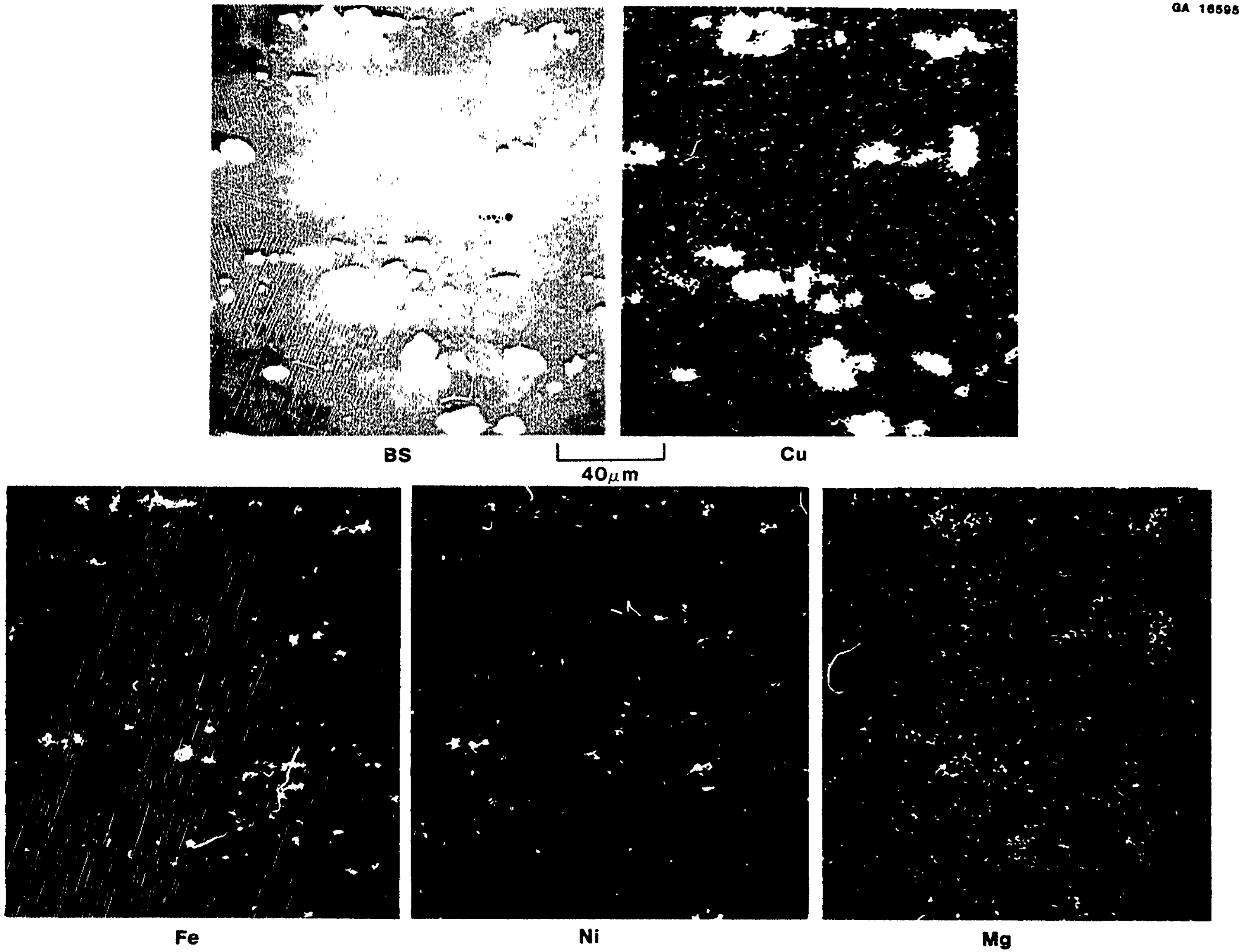

Electron microprobe x-ray maps of constituent particles in sample 504440
(Al-3.1Cu-2.2Li-1 Mg alloy T651 plate)

Figure 6

GA 16595

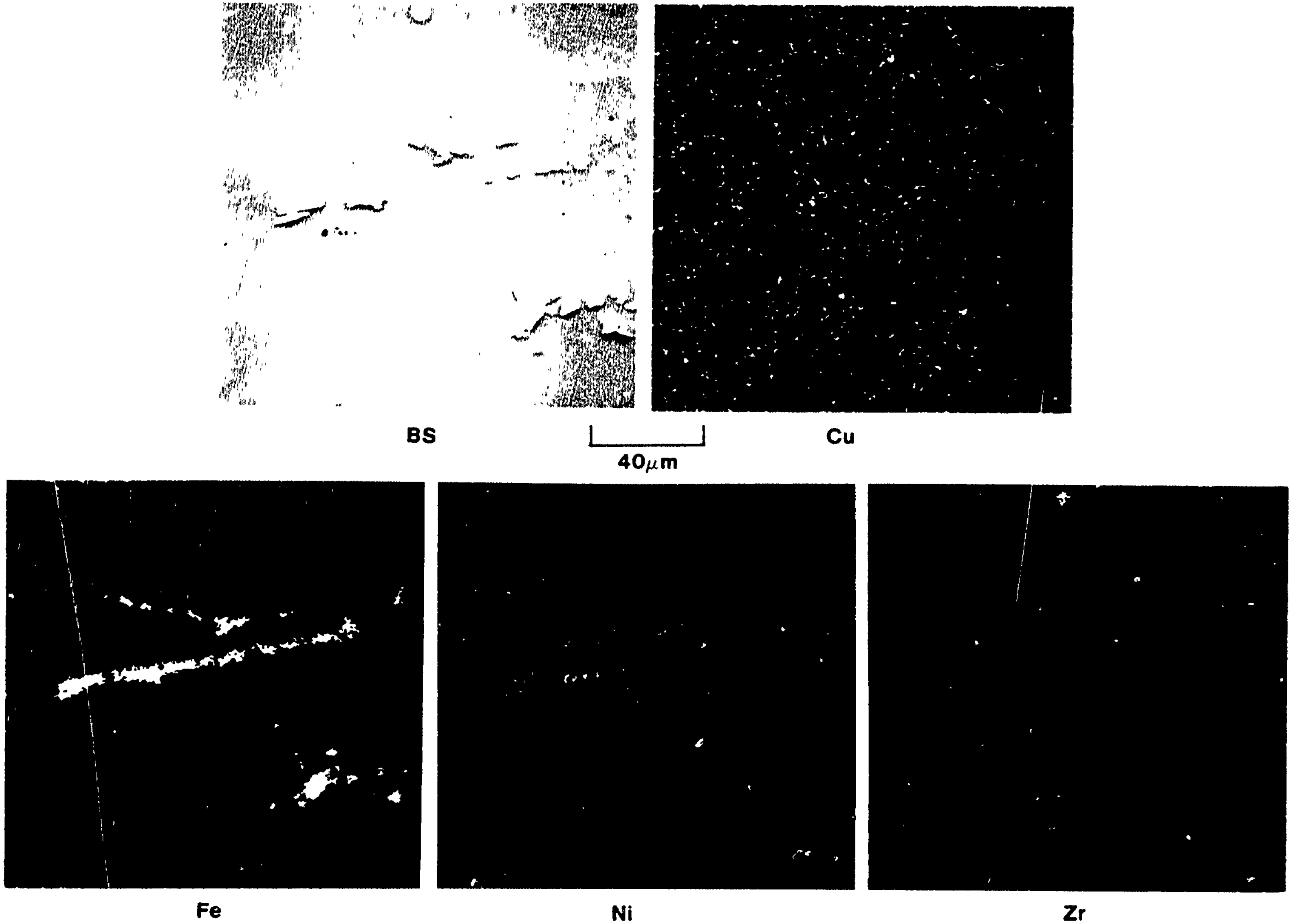

Electron microprobe x-ray maps of constituent particles in sample 548468 (Al -1.1Cu -2.9Li alloy T651 plate)

Figure 7

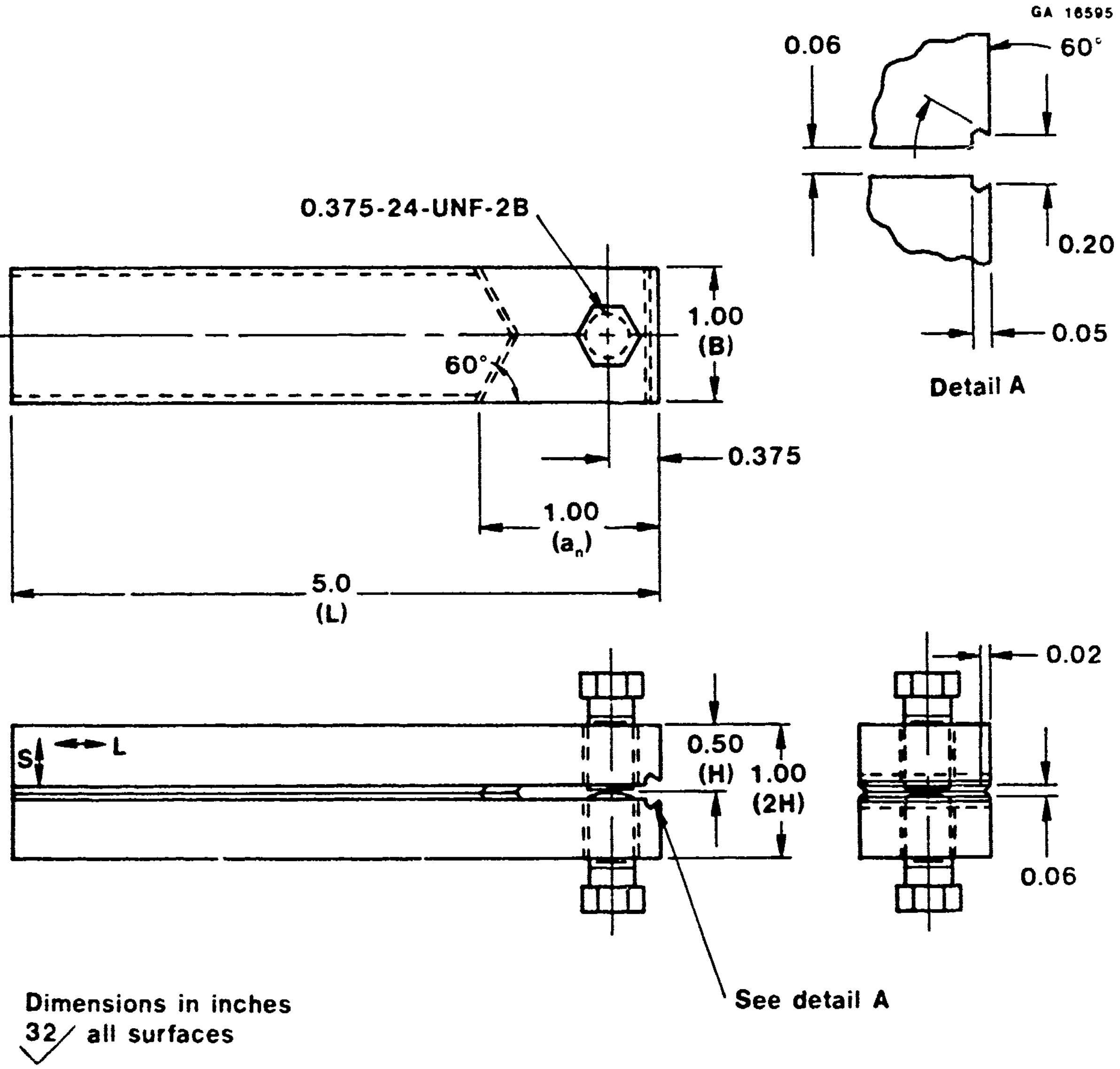

Detailed Machine Drawing for DCB Specimen

Figure 8

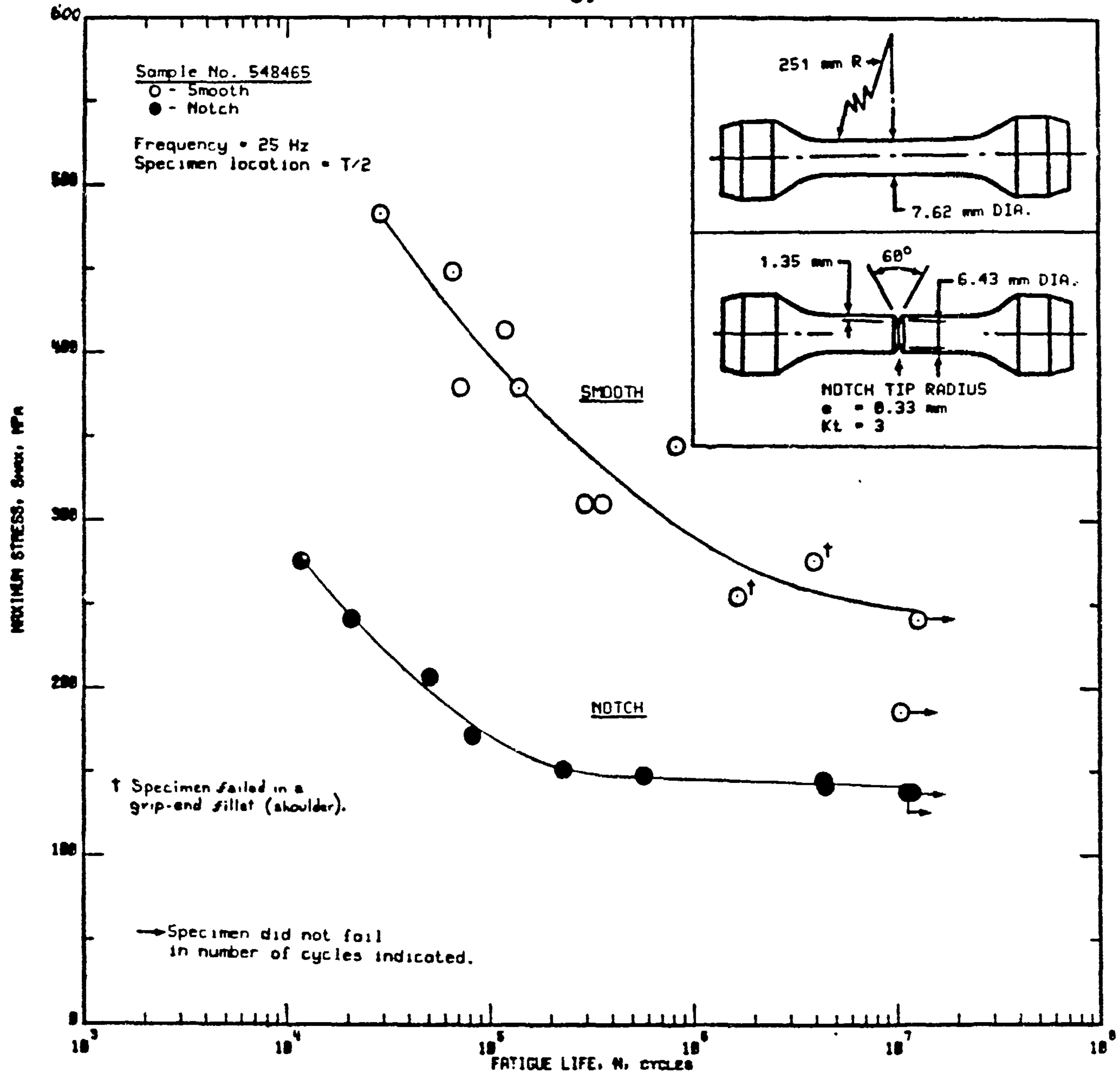

SMOOTH AND NOTCH (K_T=3) AXIAL-STRESS FATIGUE (S-N) DATA FOR LABORATORY FABRICATED ALUMINUM ALLOY (4.6Cu-1.1Li)-T651 PLATE (12.7 MM THICK) R-RATIO = +0.1, AMBIENT AIR, L DIRECTION

Figure 9

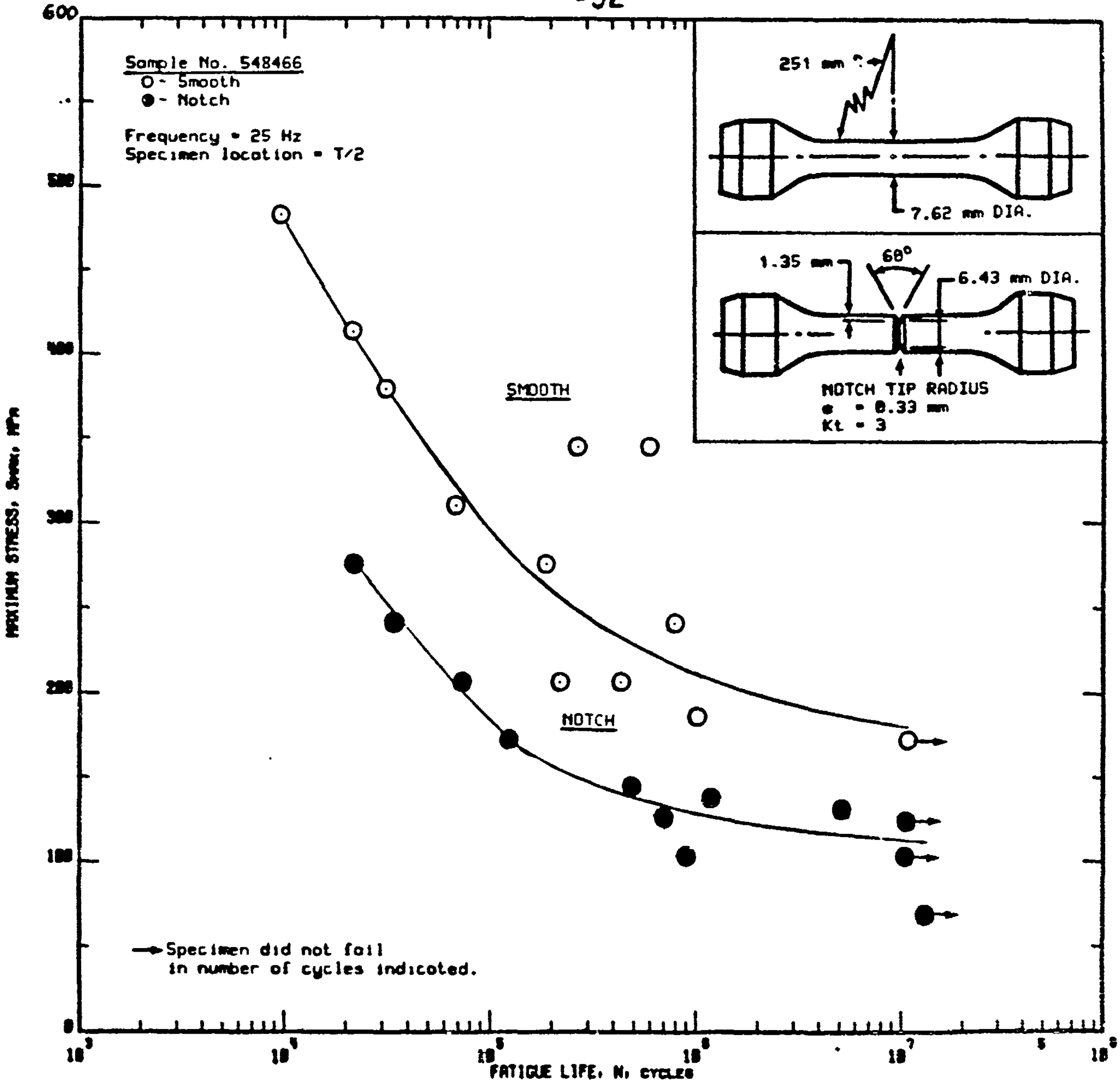

SMOOTH AND NOTCH (KT=3) AXIAL-STRESS FATIGUE (S-N) DATA FOR LABORATORY FABRICATED ALUMINUM ALLOY (2.9Cu-2.1Li)-T651 PLATE (12.7 MM THICK)
R-RATIO = +0.1, AMBIENT AIR, L DIRECTION

Figure 10

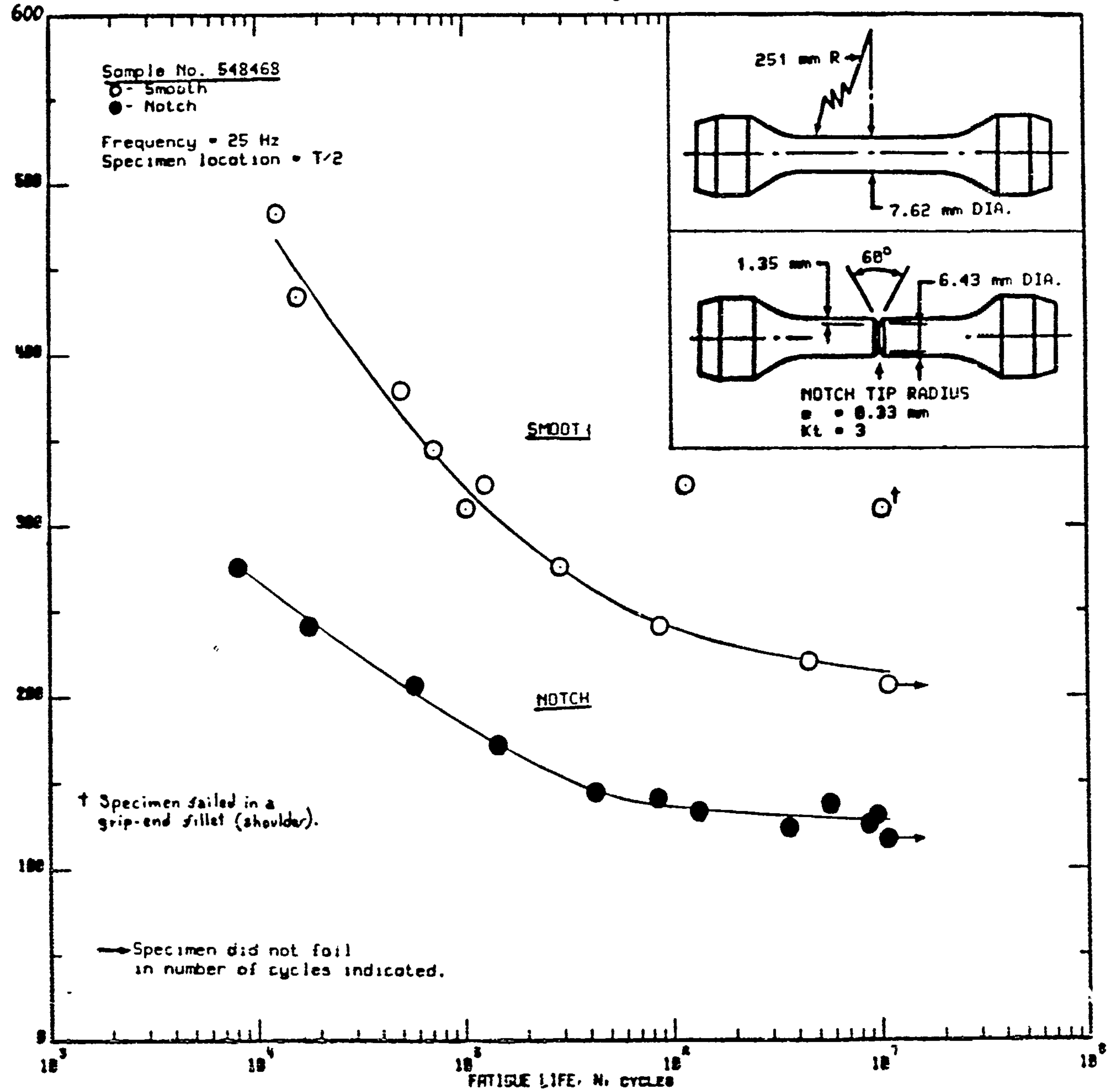

SMOOTH AND NOTCH (K_T=3) AXIAL-STRESS FATIGUE (S-N) DATA FOR LABORATORY FABRICATED ALUMINUM ALLOY (1.1Cu-2.9Li)-T651 PLATE (12.7 MM THICK) R-RATIO = +0.1, AMBIENT AIR, L DIRECTION

Figure 11

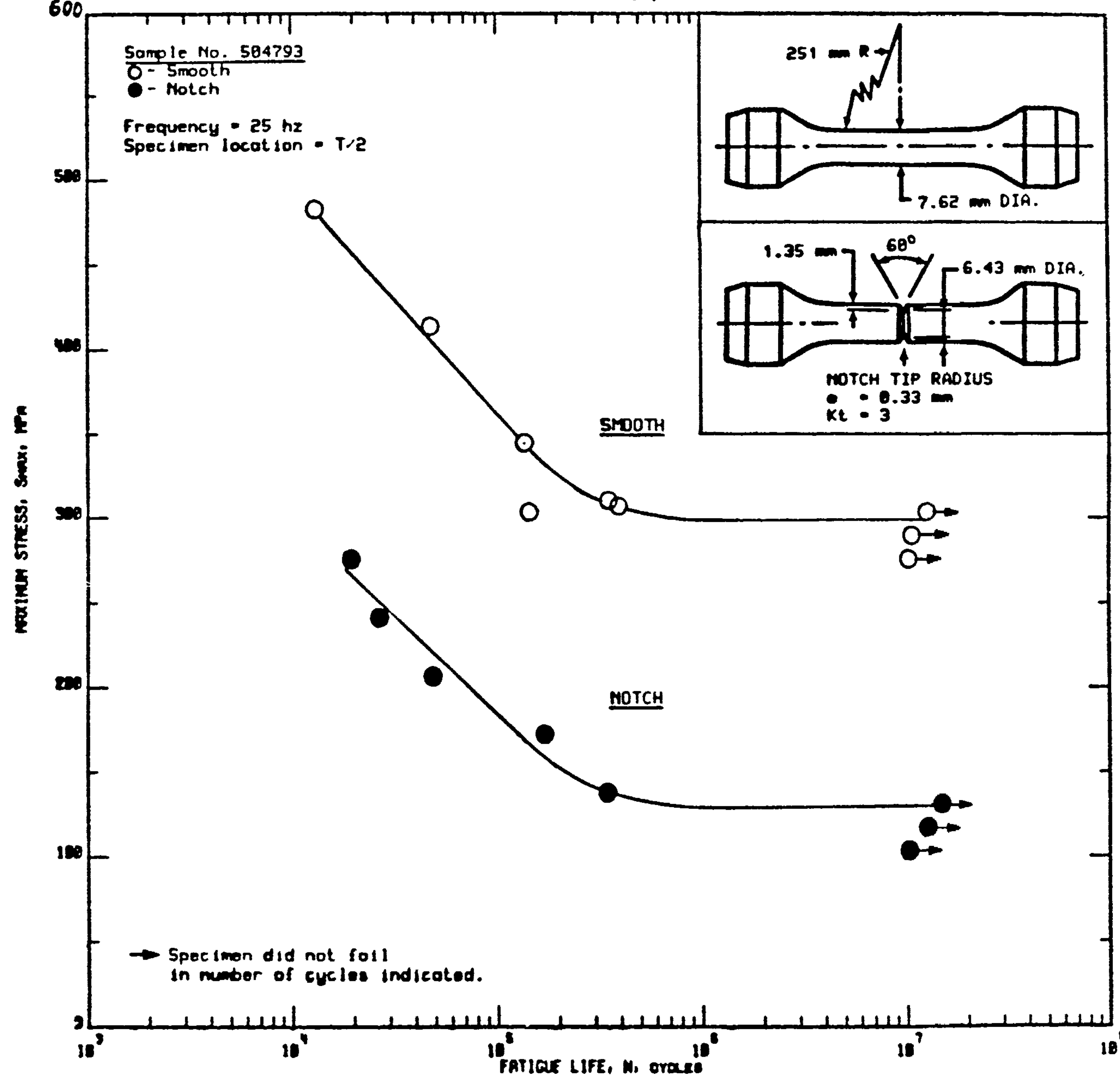

SMOOTH AND NOTCH (K_T=3) AXIAL-STRESS FATIGUE (S-N) DATA FOR LABORATORY FABRICATED ALUMINUM ALLOY (2.0Cu-2.0Li-0.6Mg)-T6 PLATE (12.7 MM THICK)
R-RATIO = +0.1, AMBIENT AIR, L DIRECTION

Figure 12

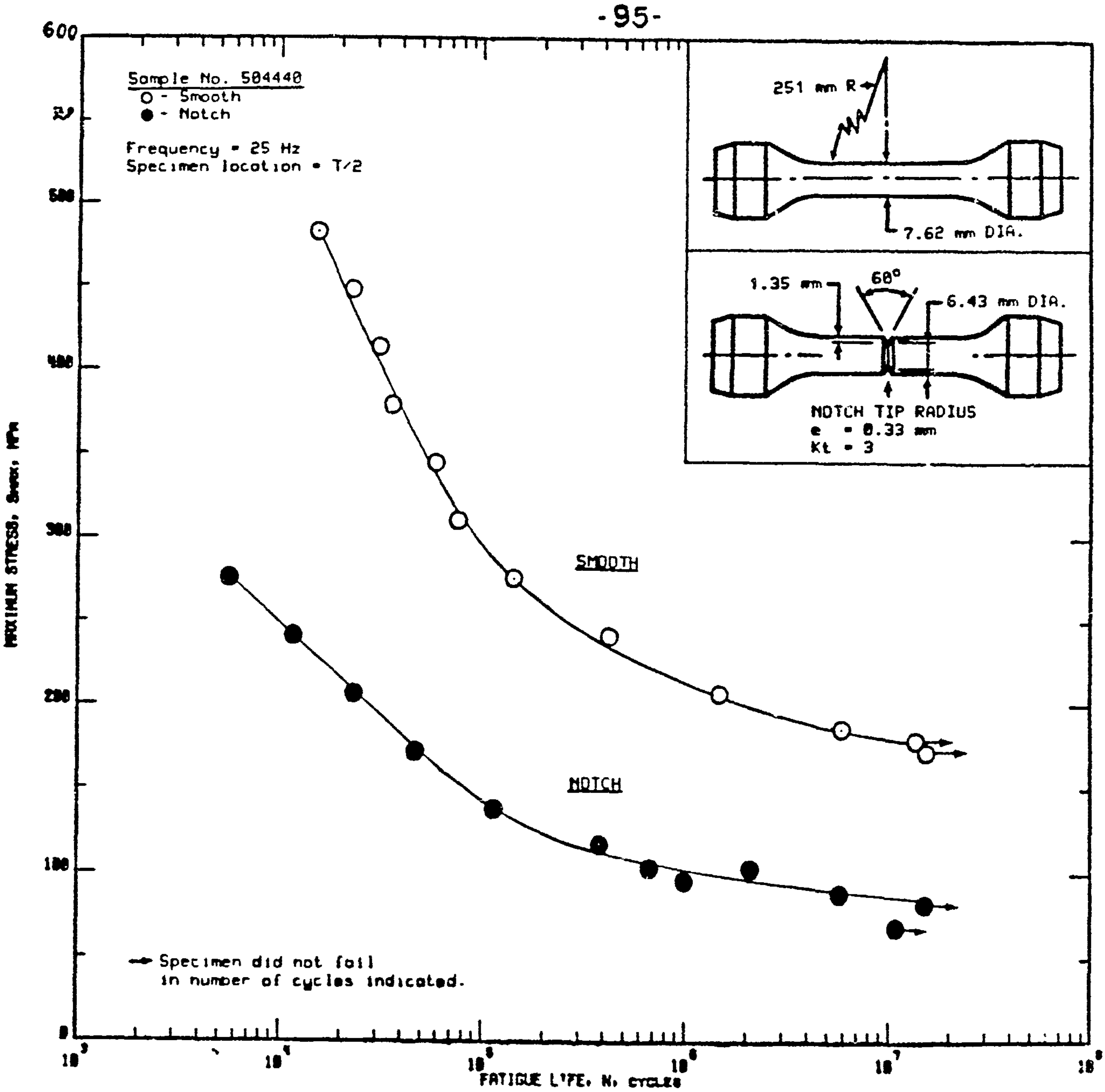

SMOOTH AND NOTCH (Kt=3) AXIAL-STRESS FATIGUE (S-N) DATA FOR
LABORATORY FABRICATED ALUMINUM ALLOY (3.1Cu-2.2Li-1.0Mg)-T651 PLATE (12.7 MM THICK)
R-RATIO = +0.1, AMBIENT AIR, L DIRECTION

Figure 13

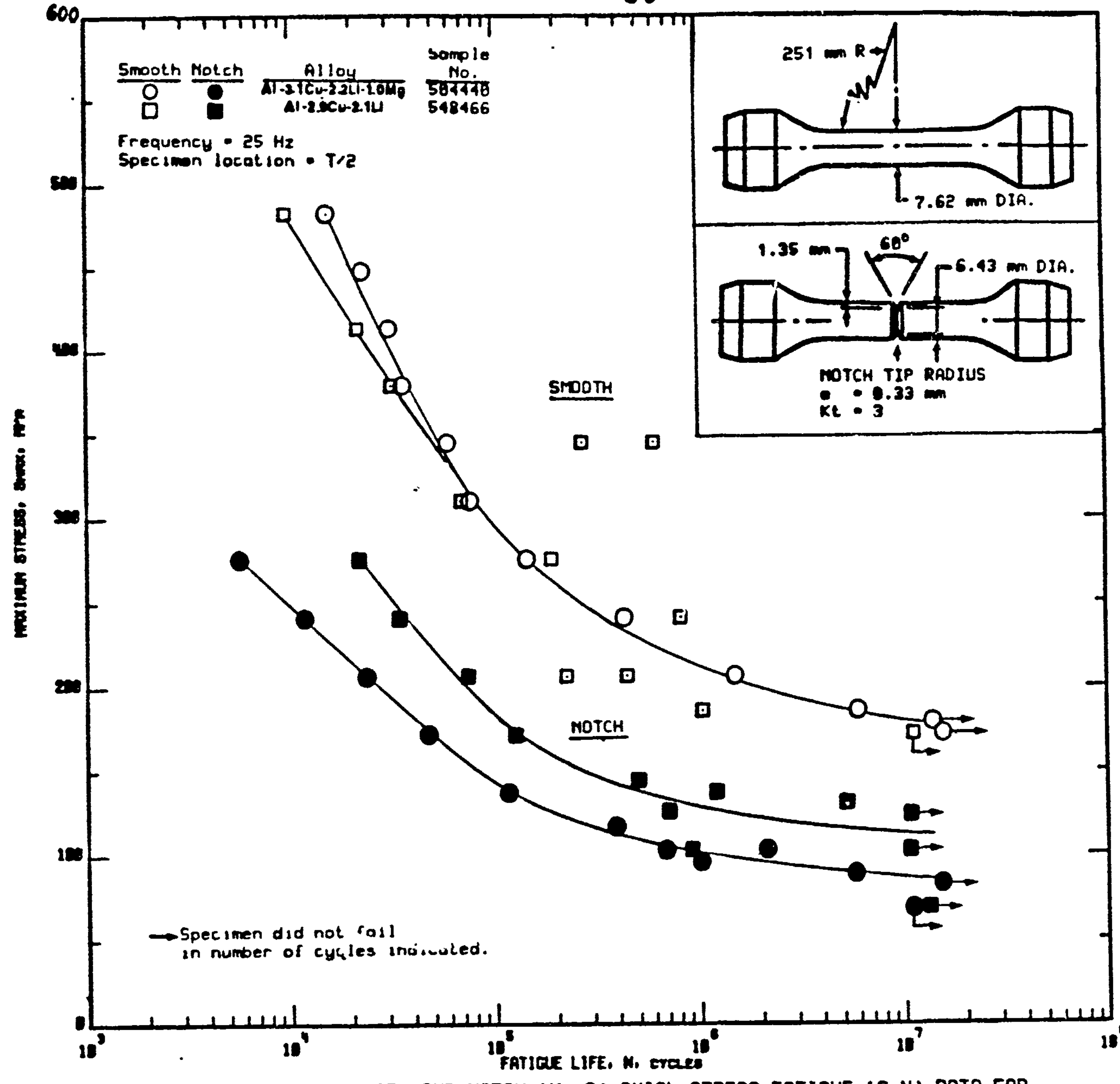

COMPARISON OF SMOOTH AND NOTCH (K_T=3) AXIAL-STRESS FATIGUE (S-N) DATA FOR LABORATORY FABRICATED ALUMINUM ALLOYS (3.1Cu-2.2Li-1.0Mg)-T651 AND (2.9Cu-2.1Li)-T PLATE (12.7MM THICK), R-RATIO = +0.1, AMBIENT AIR, L DIRECTION

Figure 14

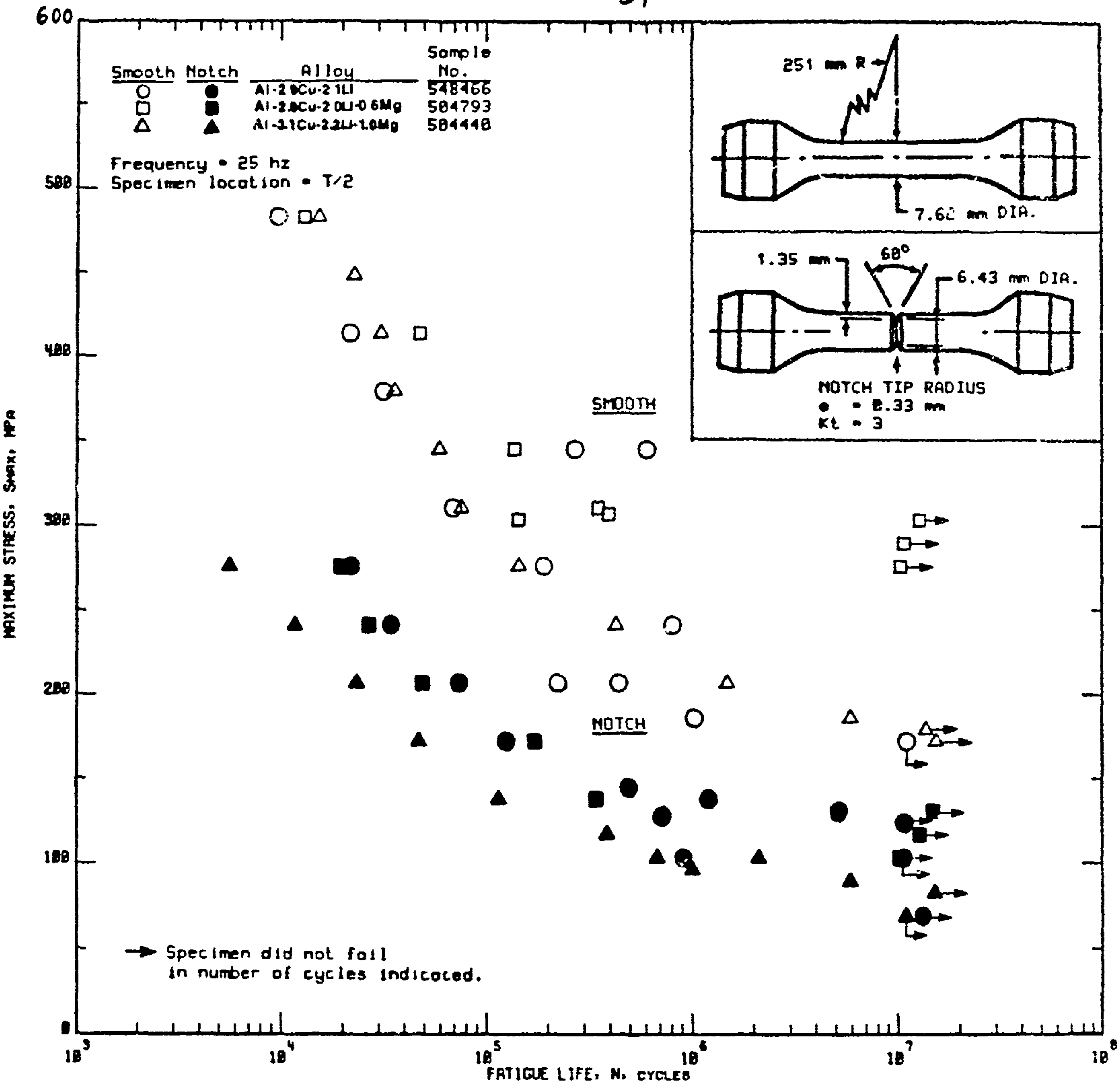

COMPARISON OF SMOOTH AND NOTCH (K_T=3) AXIAL-STRESS FATIGUE (S-N) DATA FOR LABORATORY FABRICATED ALUMINUM ALLOYS (2.9Cu-2.1Li)-T651, (2.8Cu-2.0Li-0.6Mg)-T6, (3.1Cu-2.2Li-1.0Mg)-T651 PLATE (12.7MM THICK), R-RATIO=+0.1, AMBIENT AIR, L DIRECTION

Figure 15

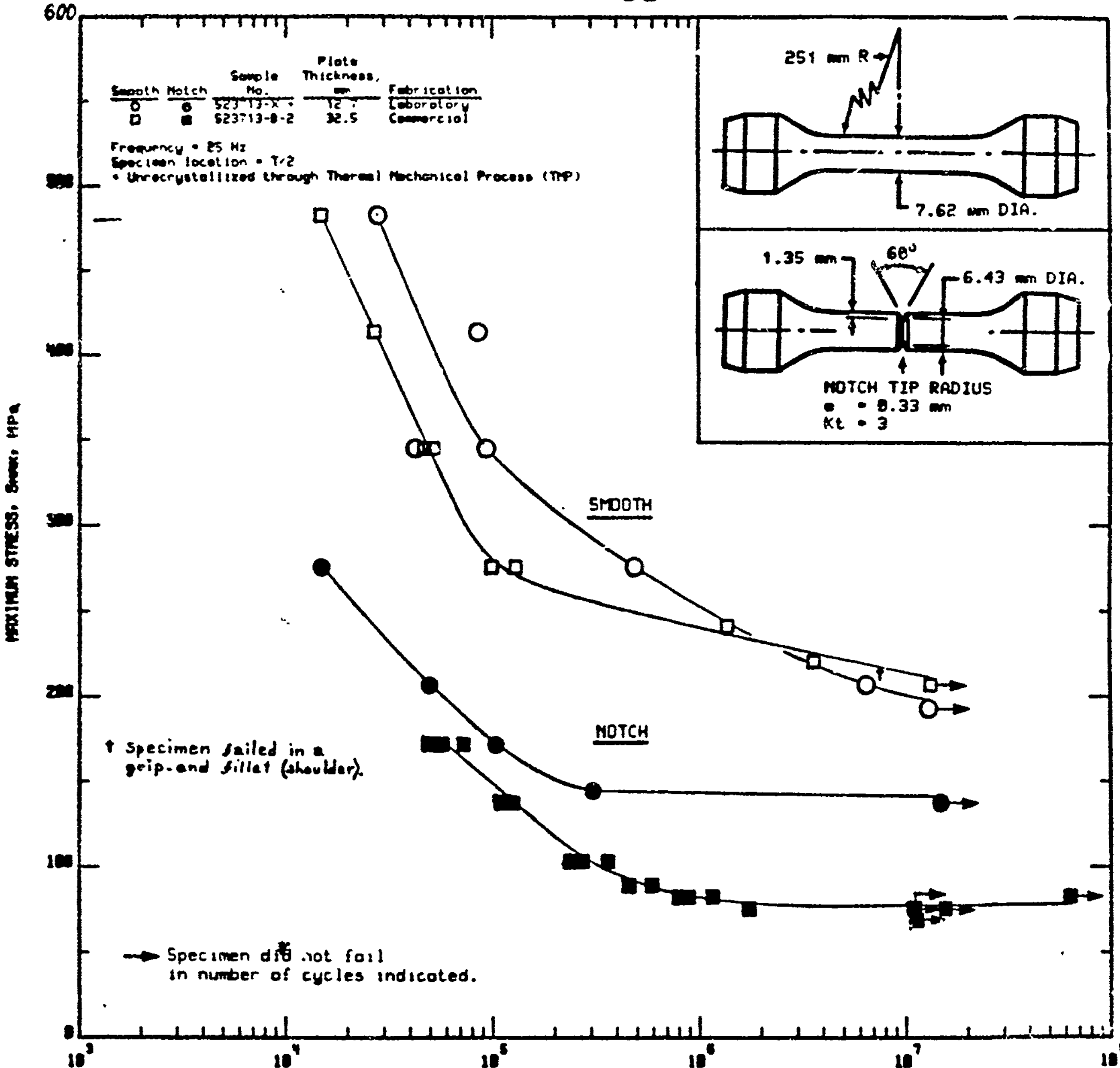

COMPARISON OF SMOOTH AND NOTCH (KT=3) AXIAL-STRESS FATIGUE (S-N) DATA FOR TWO SAMPLES OF ALUMINUM ALLOY 2020-T651 PLATE (ONE LABORATORY FABRICATED AND ONE COMMERCIALLY PRODUCED), R-RATIO = +0.1, AMBIENT AIR, L DIRECTION

Figure 16

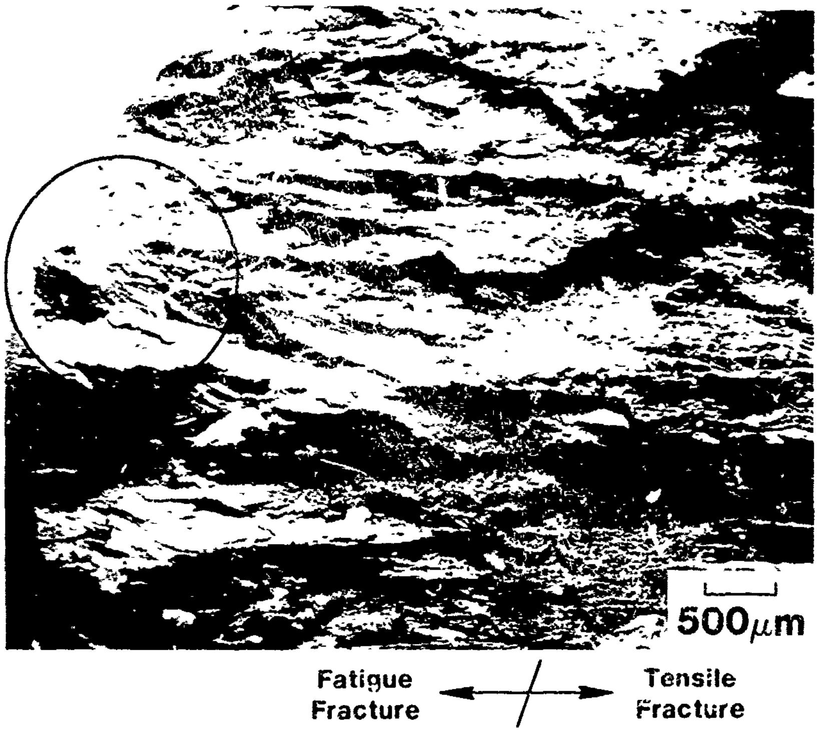

(a) SEM fractograph of a fracture surface (partial) of notched axial-stress fatigue specimen 548465-L-5 (Al - 4.6 Cu - 1.1 Li alloy T651 plate)

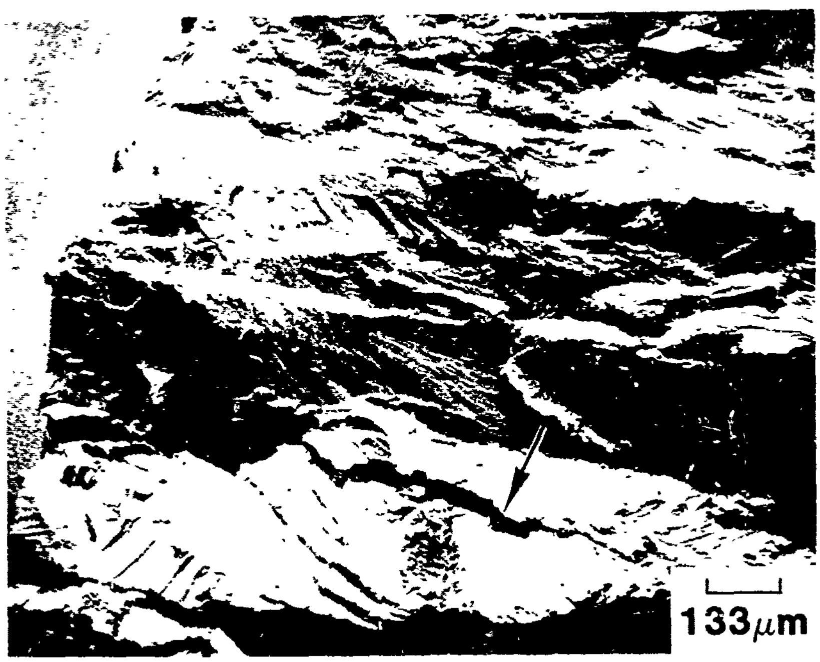

(b) SEM fractograph of fracture surface within circled area shown in (a)

Figure 17

GA 16595

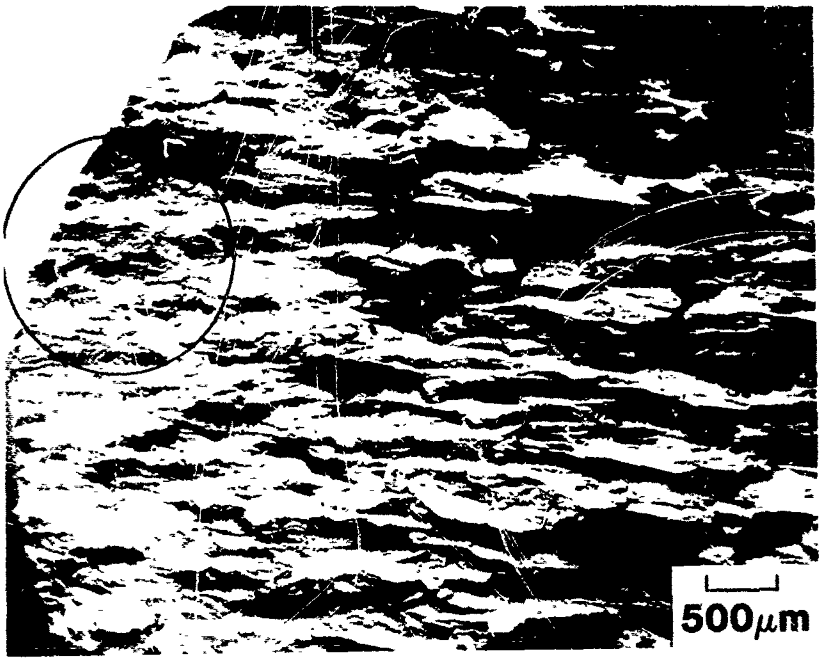

(a) SEM fractograph of a fracture surface (partial) of notched axial-stress fatigue specimen 548466-L-11 (Al -2.9Cu -2.1Li alloy T651 plate)

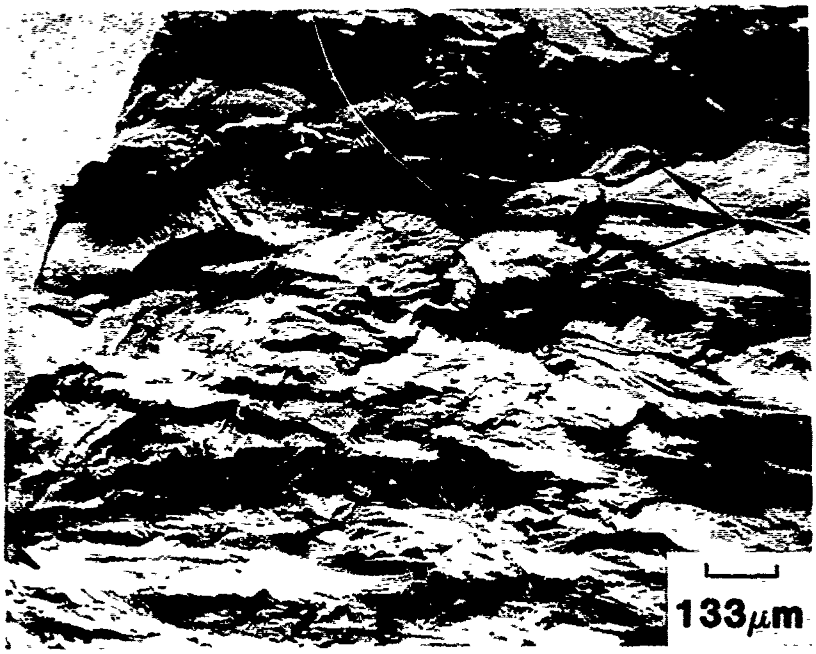

(b) SEM fractograph of fracture surface within circled area shown in (a)

Figure 18

GA 16595

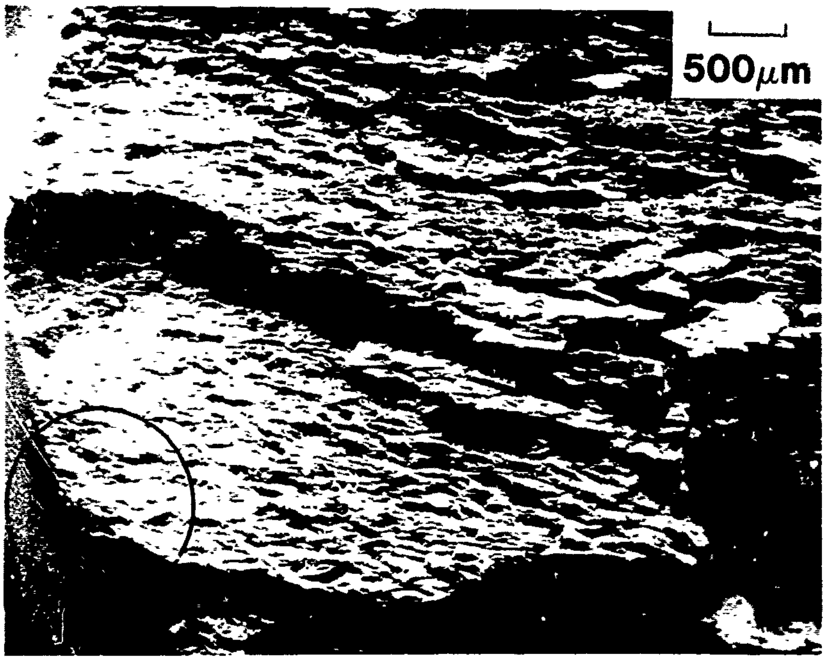

Fatigue Fracture ← → Tensile Fracture

(a) SEM fractograph of a fracture surface (partial) of notched axial-stress fatigue specimen 548468-L-6 (Al -1.1Cu -2.9Li alloy T651 plate)

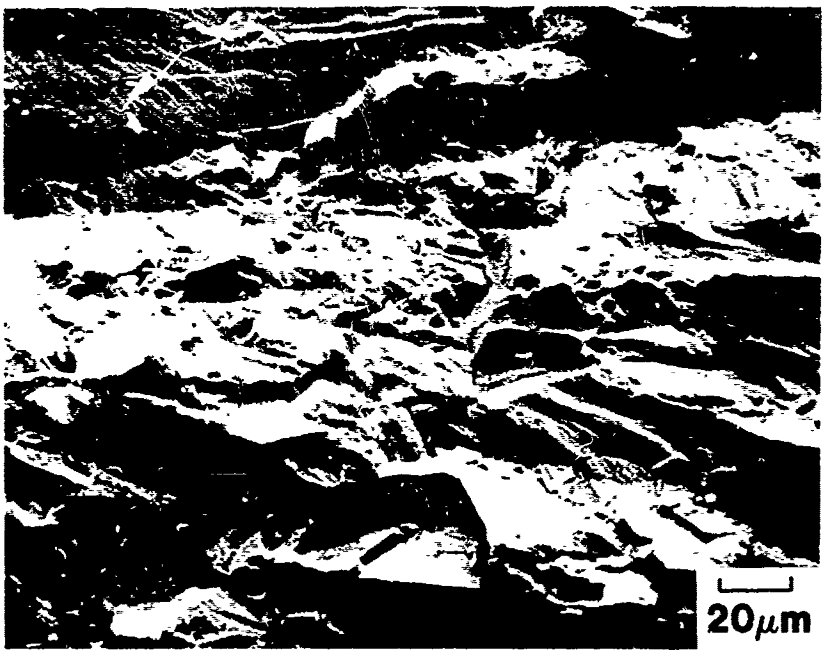

(b) SEM fractograph of fracture surface within circled area shown in (a)

Figure 19

GA 16595

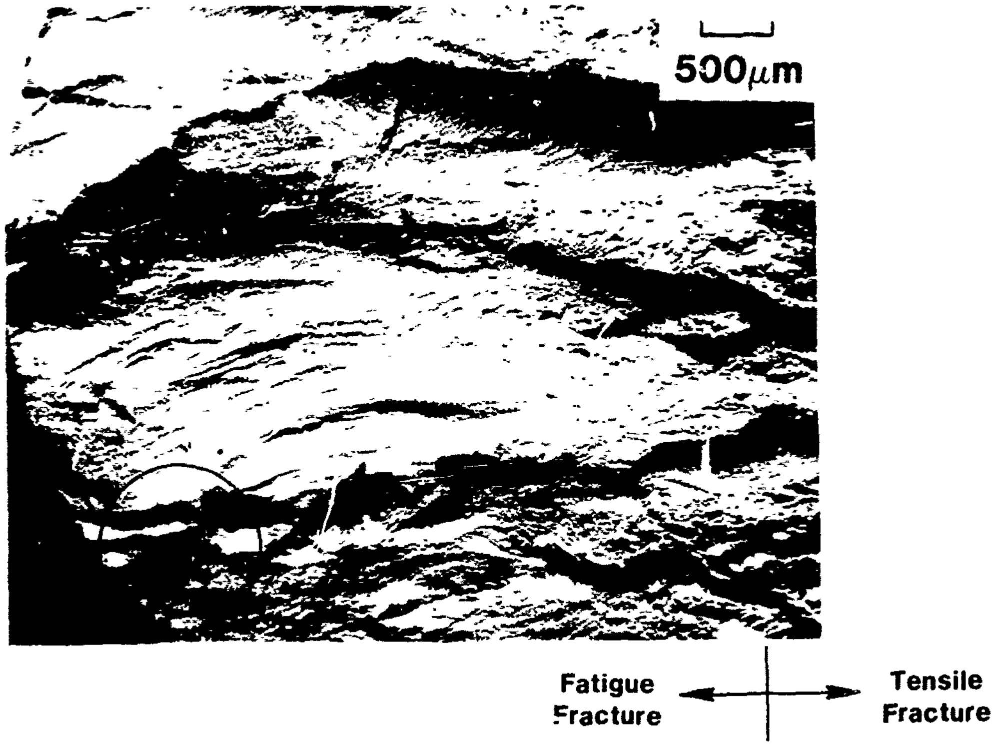

(a) SEM fractograph of a fracture surface (partial) of notched axial-stress fatigue specimen 504793-L-3 (Al -2.8Cu - 2 Li - 0.6 Mg alloy T6 plate)

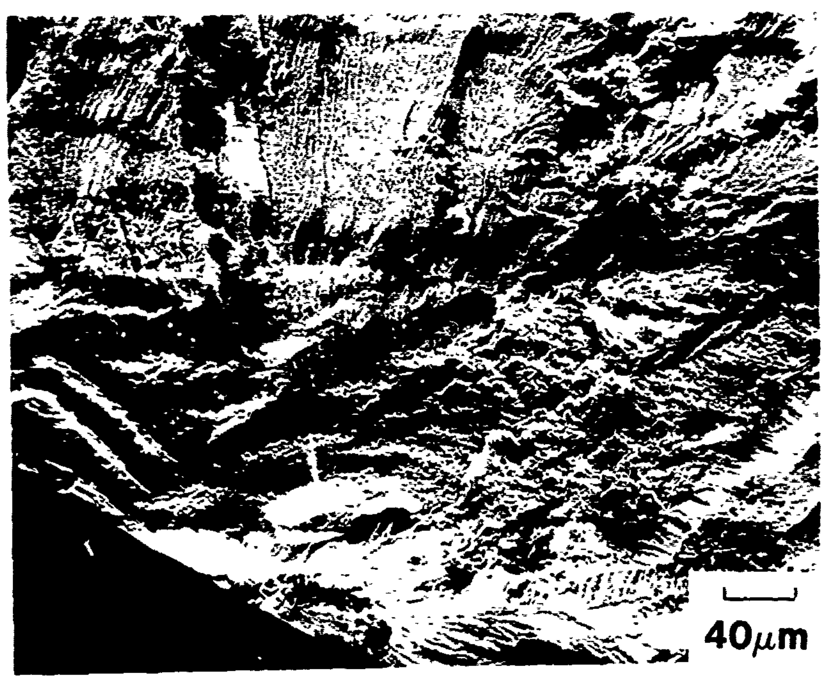

(b) SEM fractograph of fracture surface within circled area shown in (a)

Figure 20

GA 16595

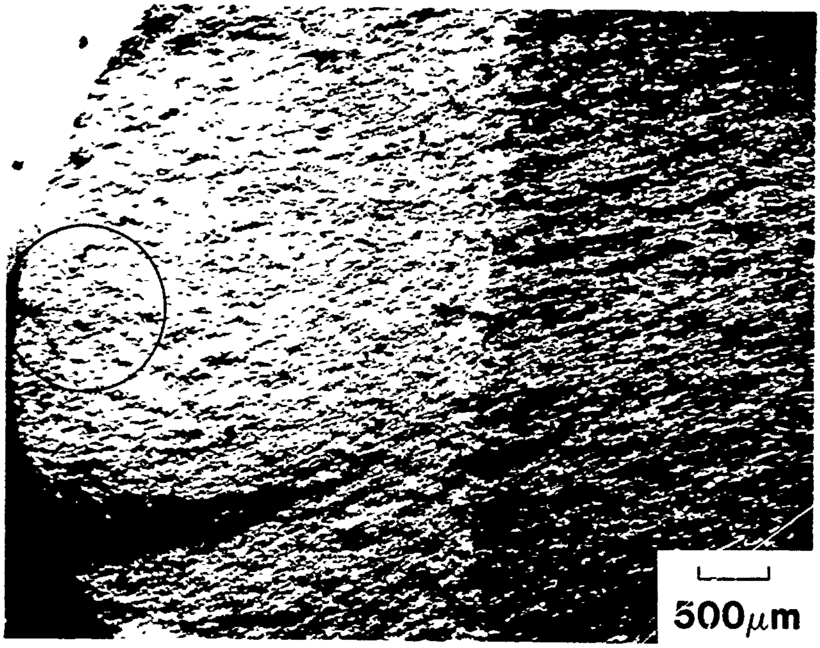

(a) SEM fractograph of a fracture surface (partial) of notched axial-stress fatigue specimen 504440-L-1 (Al -3.1Cu -2.2Li - 1 Mg alloy T651 plate)

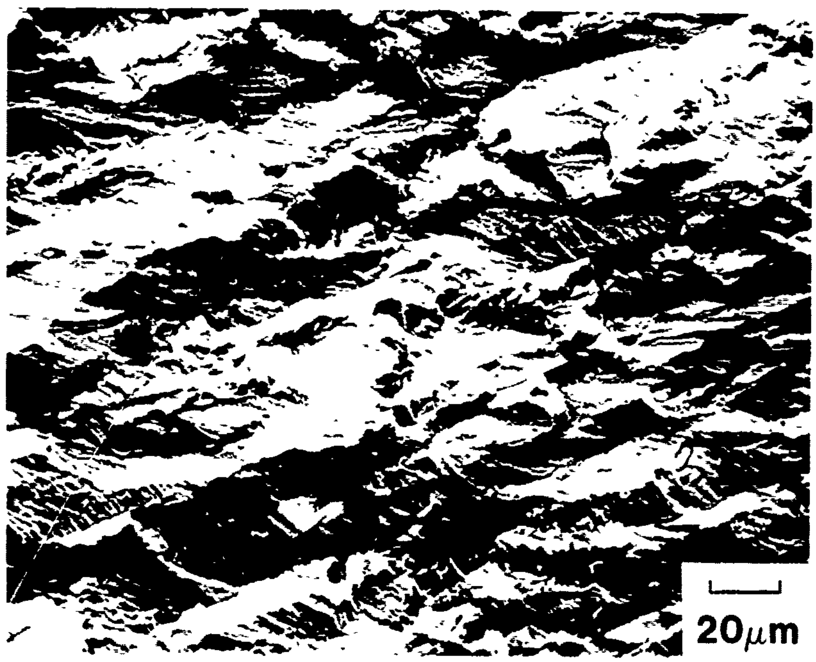

(b) SEM fractograph of fracture surface within circled area shown in (a)

Figure 21

GA 16595

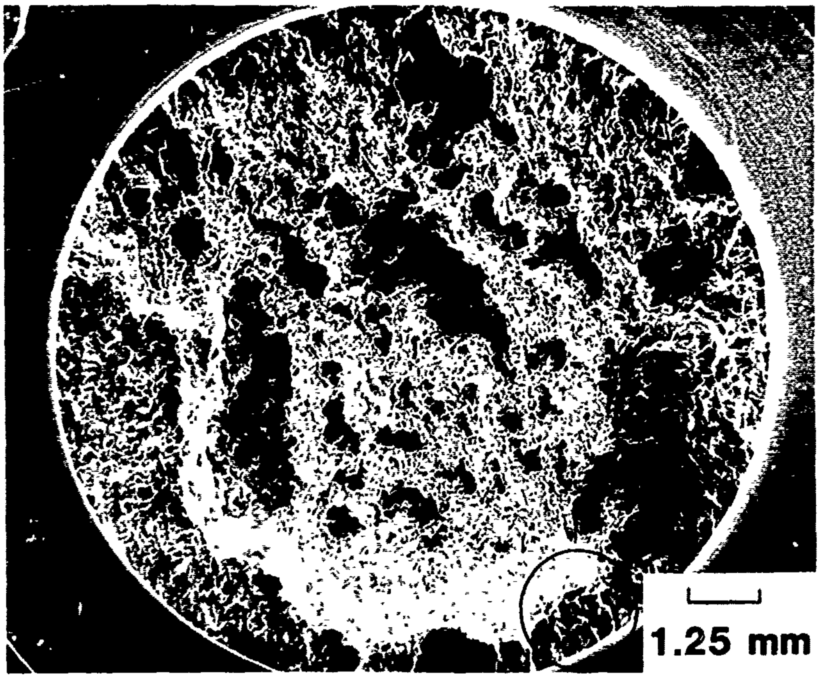

(a) SEM fractograph of a fracture surface of notched axial-stress fatigue specimen 523713-B-2-L-14 (2020-T651 plate)

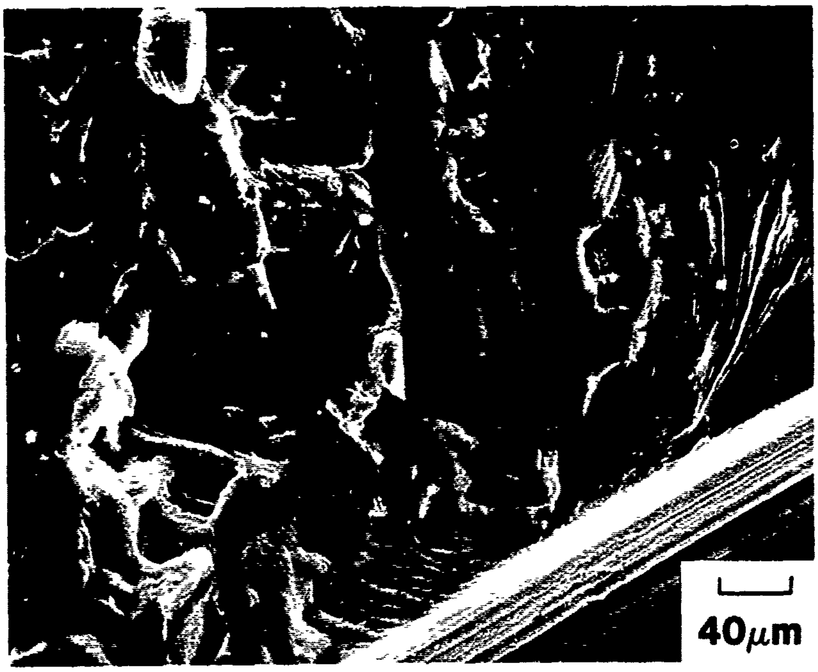

(b) SEM fractograph of fracture surface within circled area shown in (a)

Figure 22

GA 16595

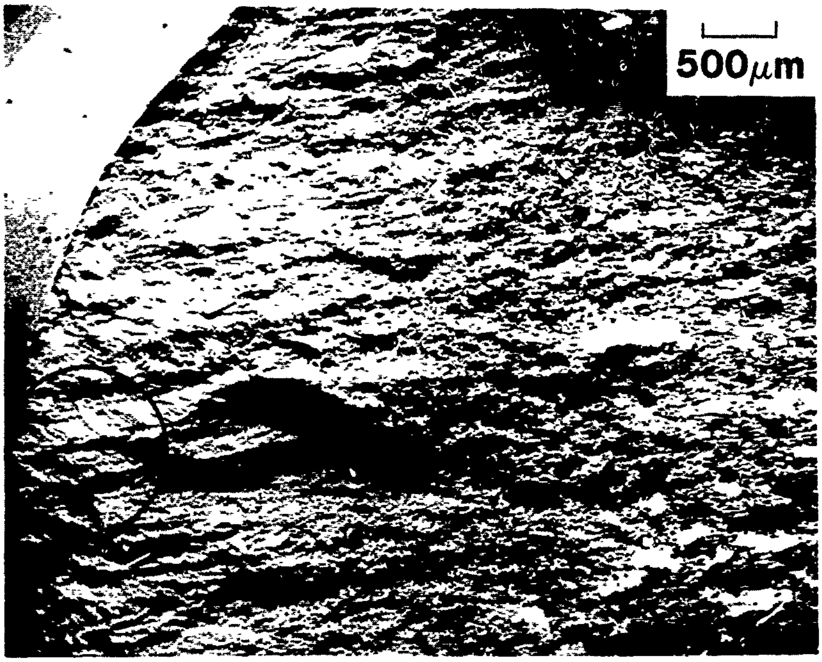

Fatigue Fracture ← → Tensile Fracture

(a) SEM fractograph of a fracture surface (partial) of notched axial-stress fatigue specimen 523713-X-L-9 (TMP 2020-T651 plate)

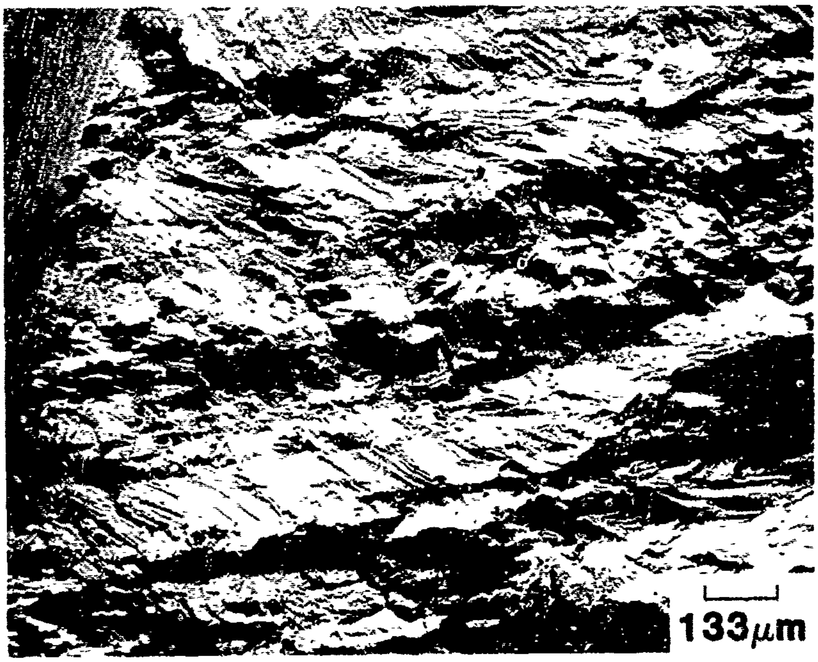

(b) SEM fractograph of fracture surface within circled area shown in (a)

Figure 23

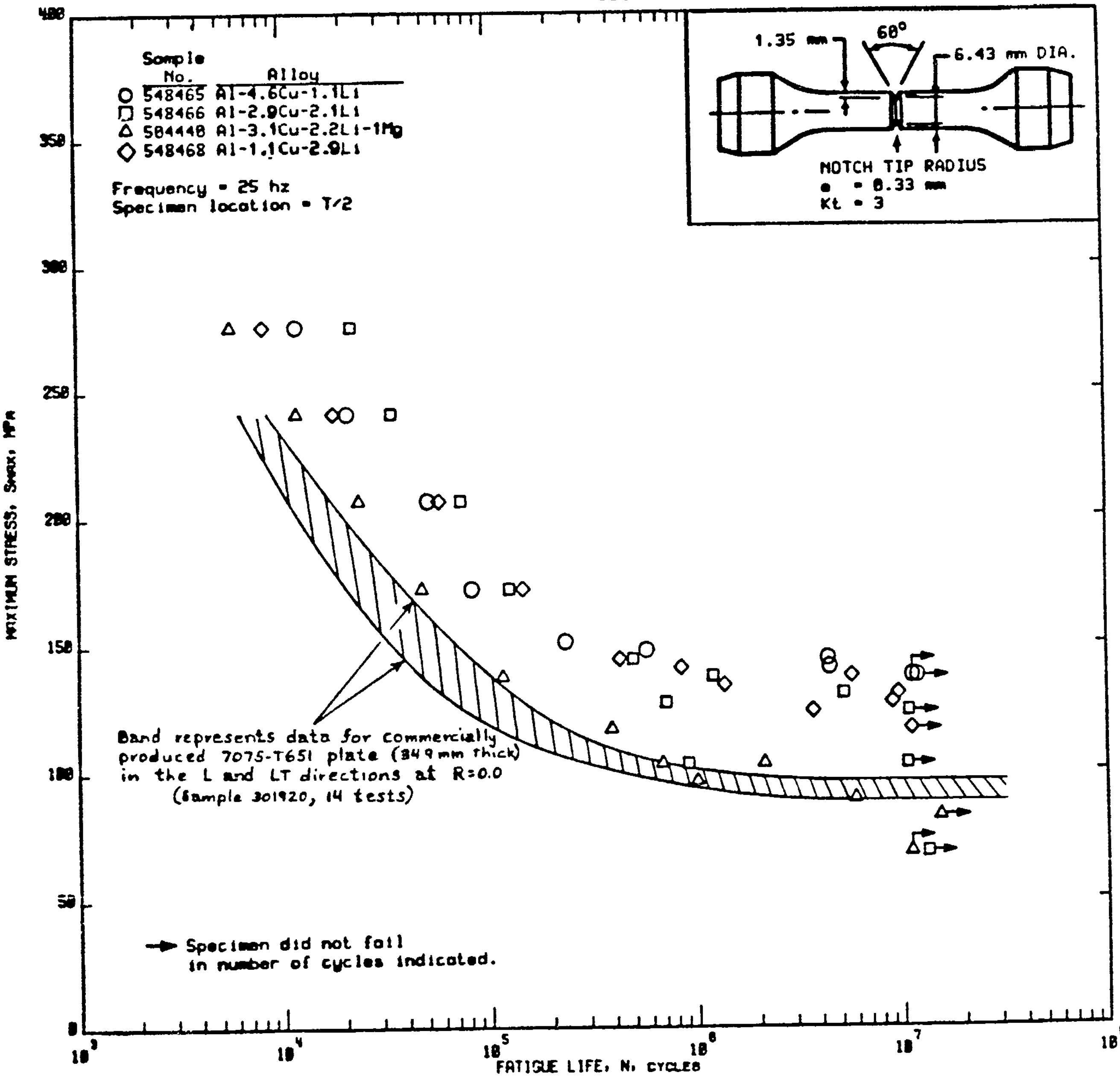

COMPARISON OF NOTCH (K_T=3) AXIAL-STRESS FATIGUE (S-N) DATA FOR LABORATORY FABRICATED ALUMINUM ALLOYS (4.6Cu-1.1Li)-T651, (2.9Cu-2.1Li)-T651, (1.1Cu-2.9Li)-T651, (3.1Cu-2.2Li-1.0Mg)-T651 PLATE (12.7 MM THICK), R-RATIO=+0.1, AMBIENT AIR, L DIR.

Figure 24

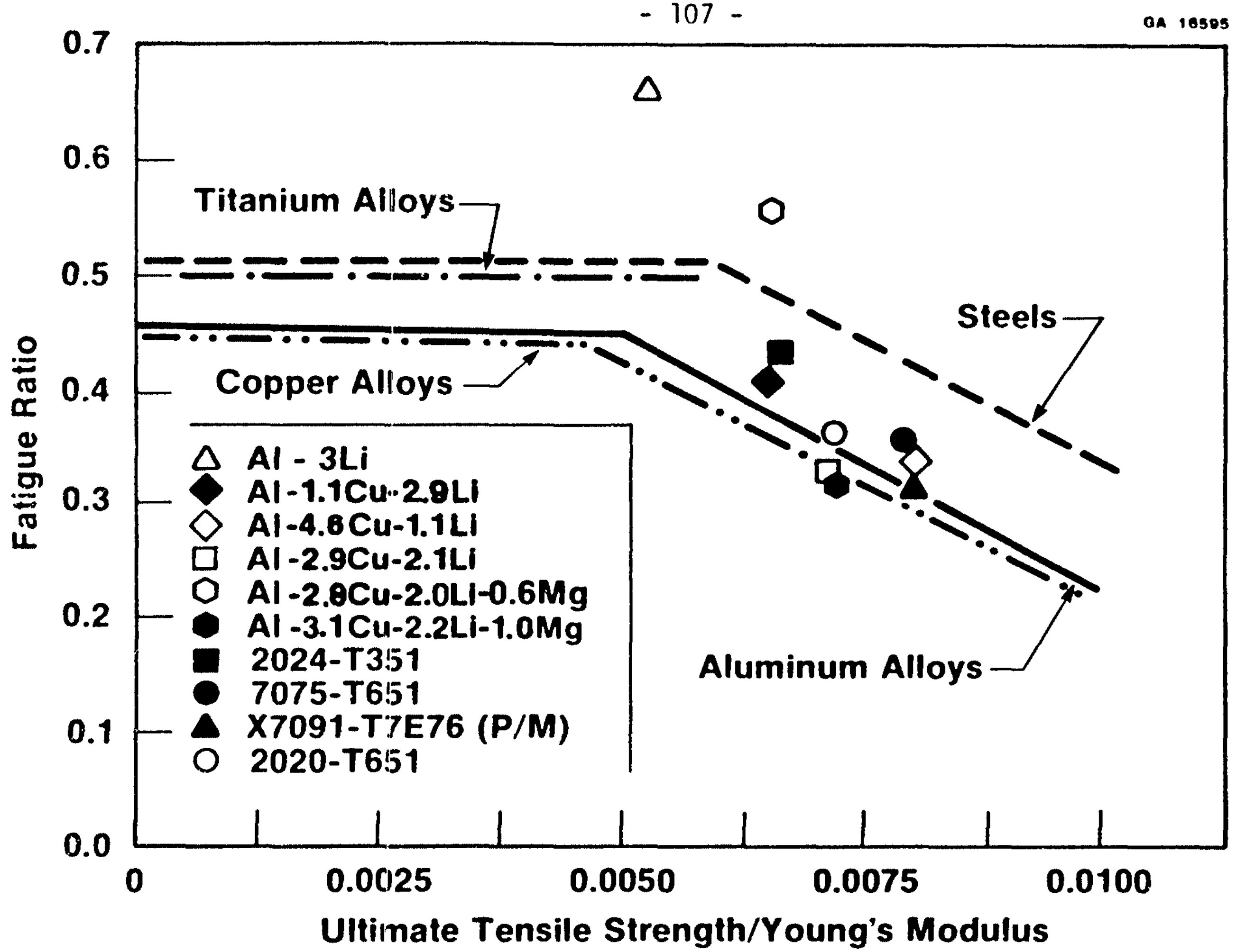

Fatigue Ratio of Al - Li -X Alloys as a Function of Normalized Ultimate Strength with Respect to Young's Modulus, and Comparison of the Present Data with Various Other Alloy Systems.

Figure 25

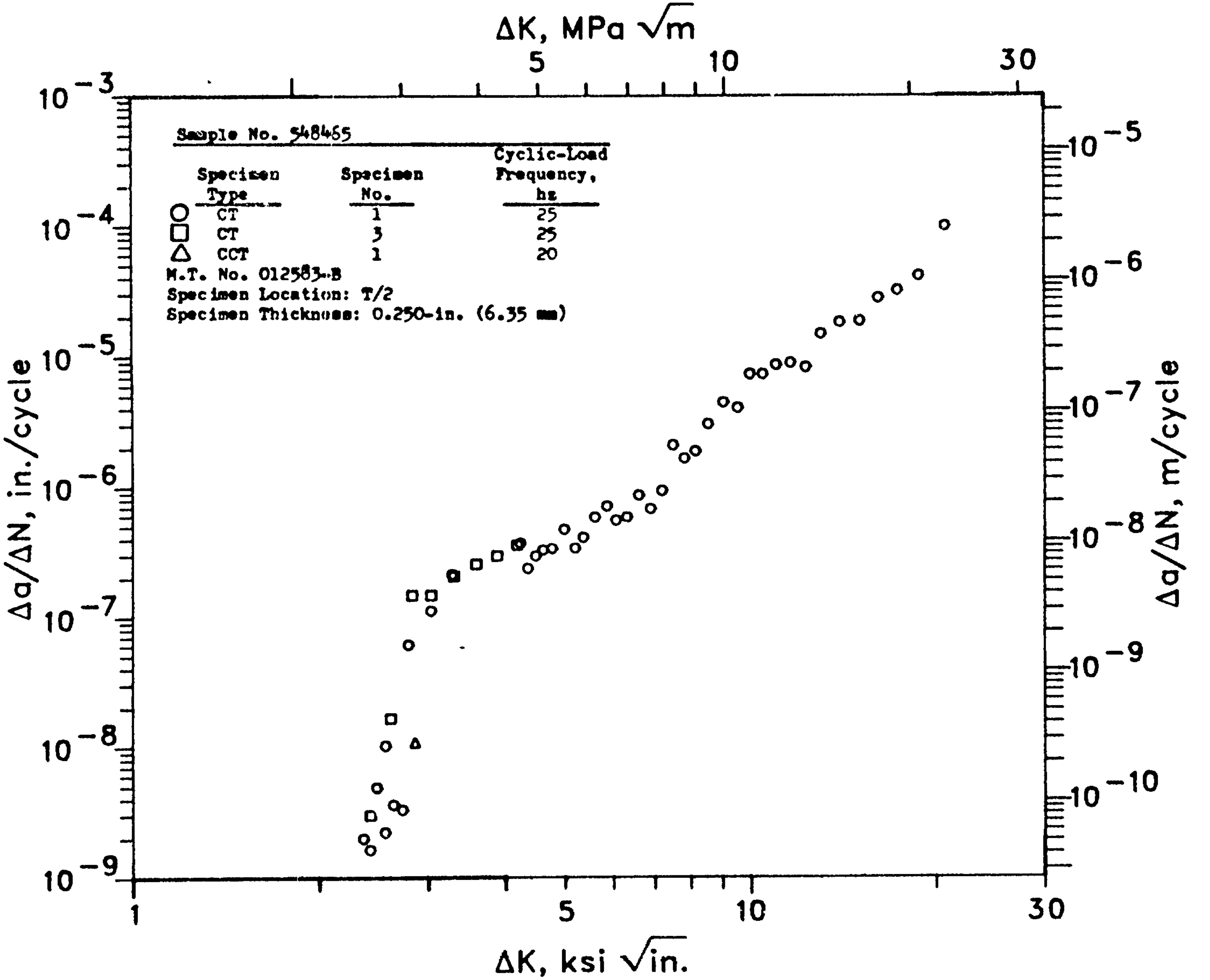

Constant-Load-Amplitude Fatigue Crack Propagation Data for
Laboratory Fabricated Aluminum Alloy (4.6 Cu - 1.1 Li) - T651 Plate, 0.5-in. (12.7mm) thick
L-T orientation, R-Ratio = +0.33, High Humidity (R.H.>90%) Air

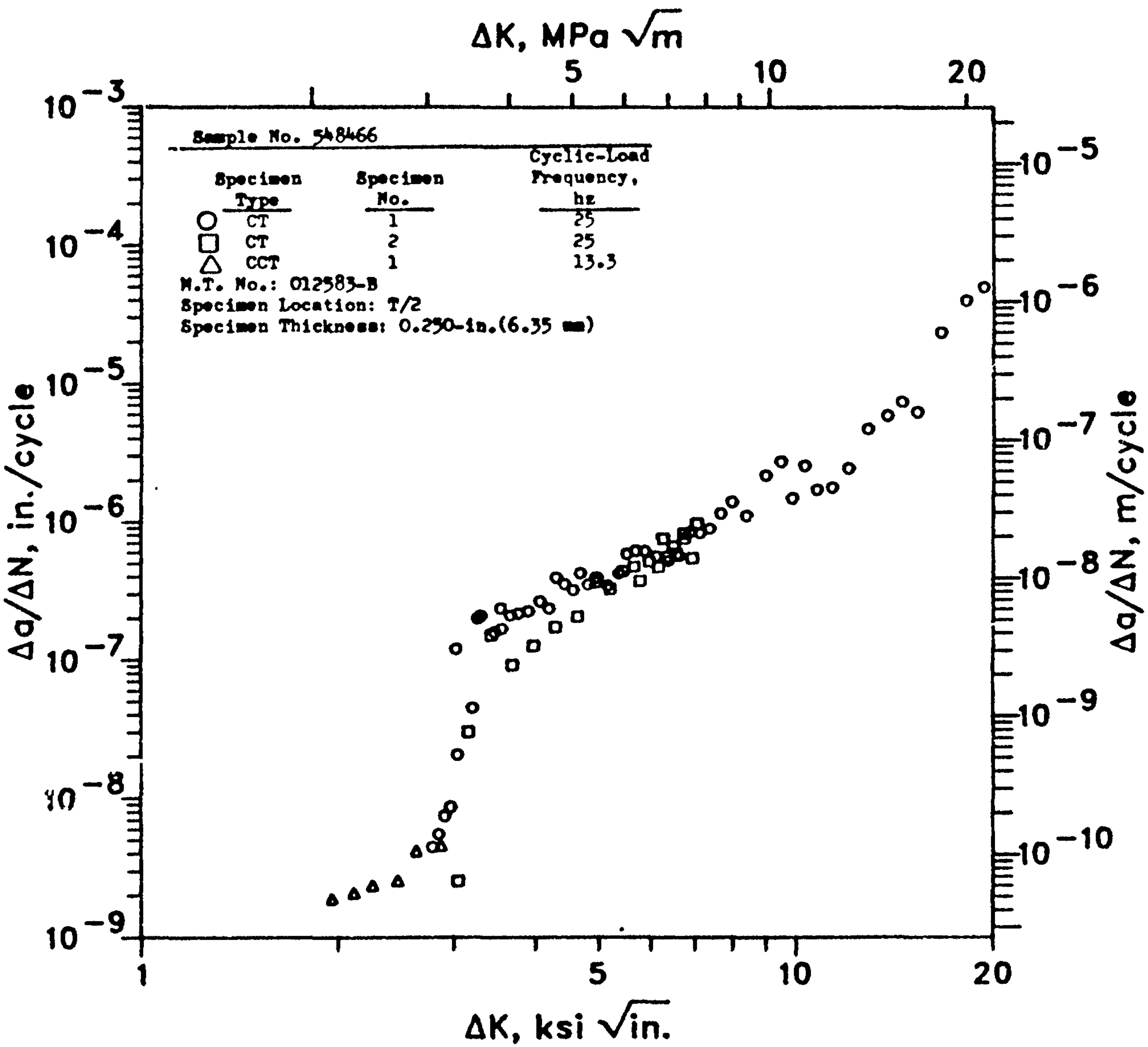

Constant-Load-Amplitude Fatigue Crack Propagation Data for Laboratory Fabricated Aluminum Alloy (2.9 Cu - 2.1 Li) - T651 Plate, 0.5-in. (12.7 mm) thick L-T orientation, R-Ratio = +0.33, High Humidity (R.H.>90%) Air

Figure 27

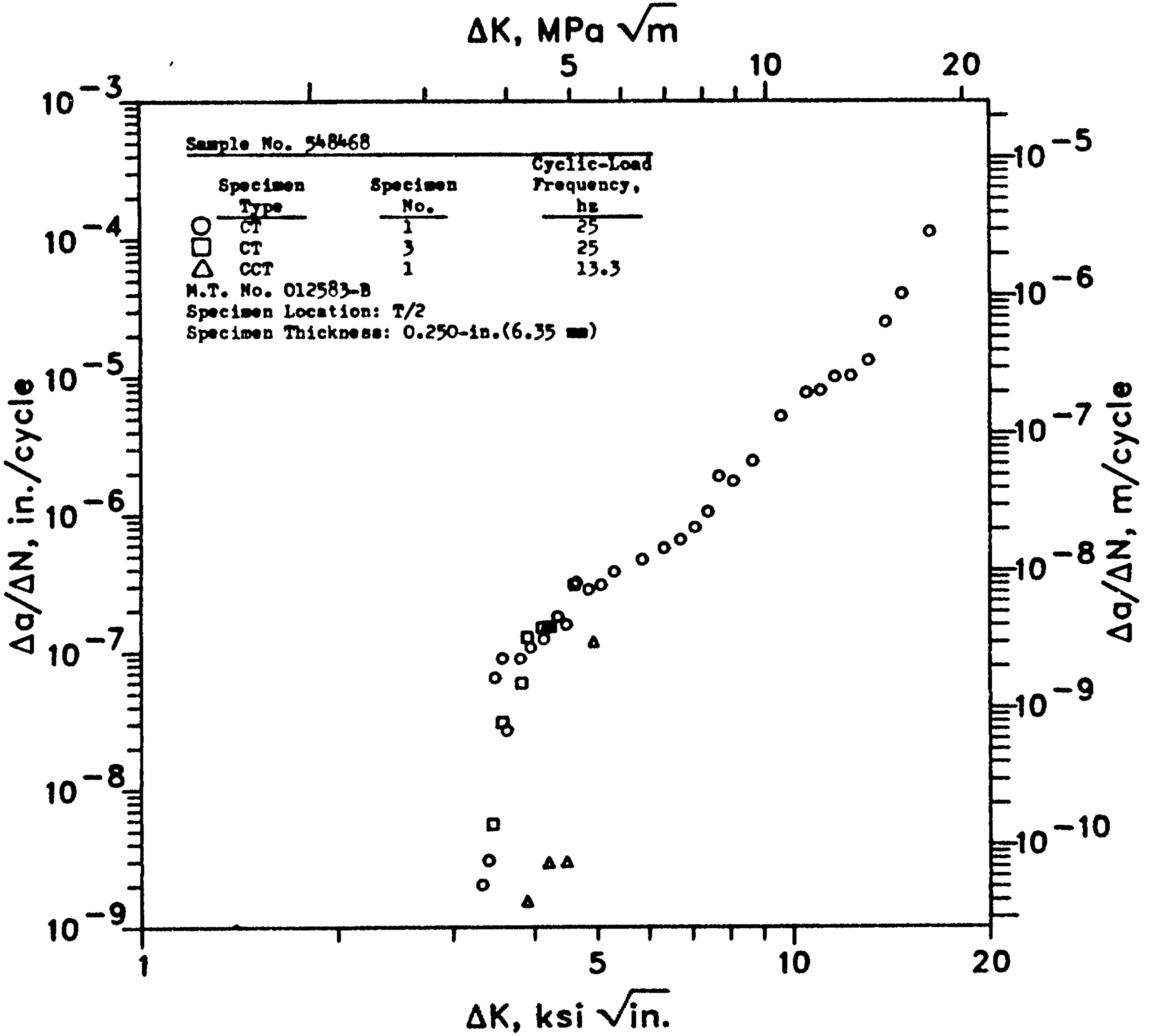

Constant-Load-Amplitude Fatigue Crack Propagation Data for Laboratory Fabricated Aluminum Alloy (1.1Cu-2.9Li)-T651 Plate, 0.5-in. (12.7 mm) thick L-T orientation, R-ratio = +0.33, High Humidity (R.H.>90%) Air

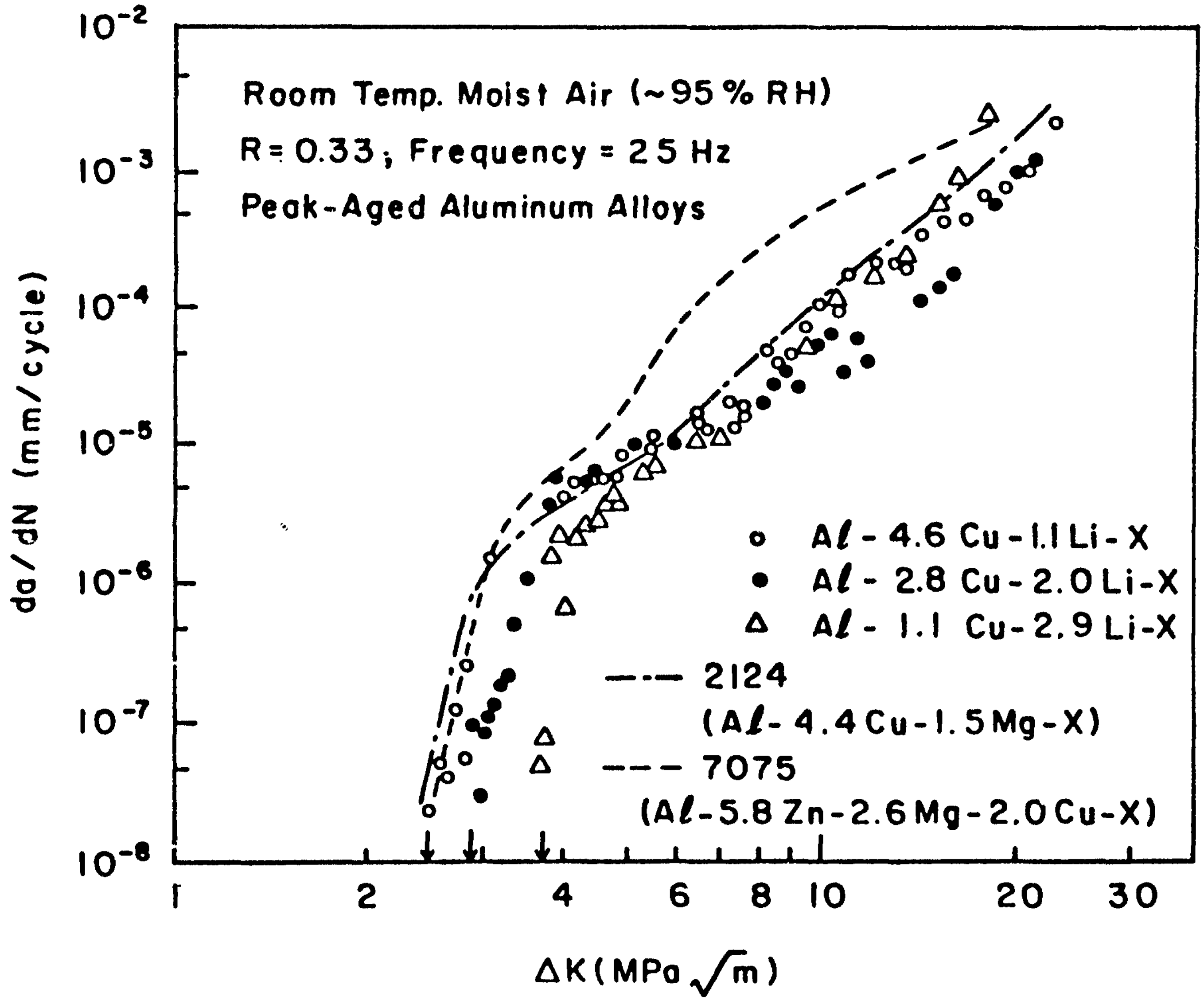

Comparison of the constant-load-amplitude FCG data of the three Al-Cu-Li-Zr alloys investigated. The dashed lines indicate FCG behavior of peak-aged alloys 2124 and 7075.

Figure 29

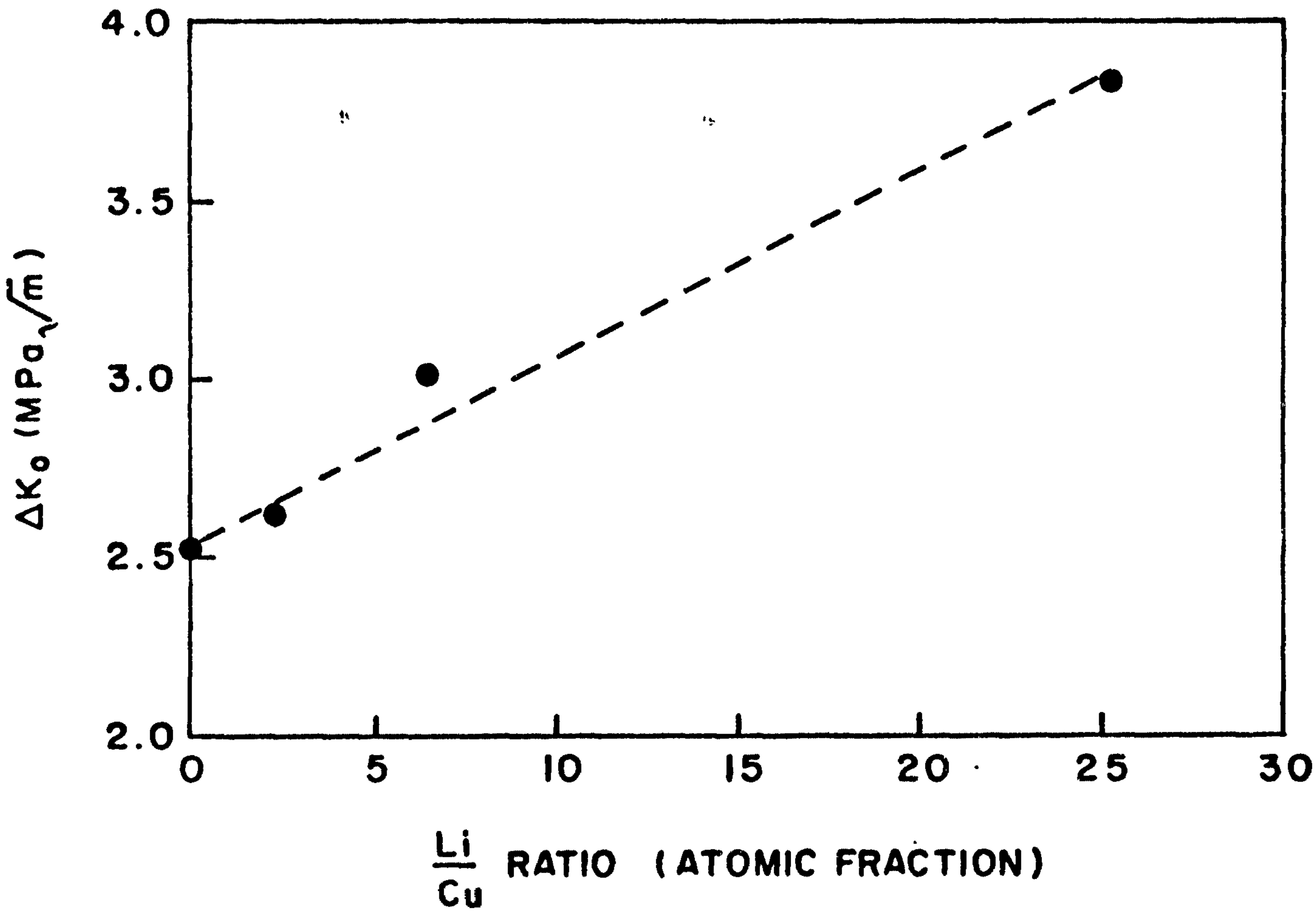

Variation of threshold stress-intensity factor range with (Li/Cu) ratio expressed in terms of atomic fractions.

Figure 30

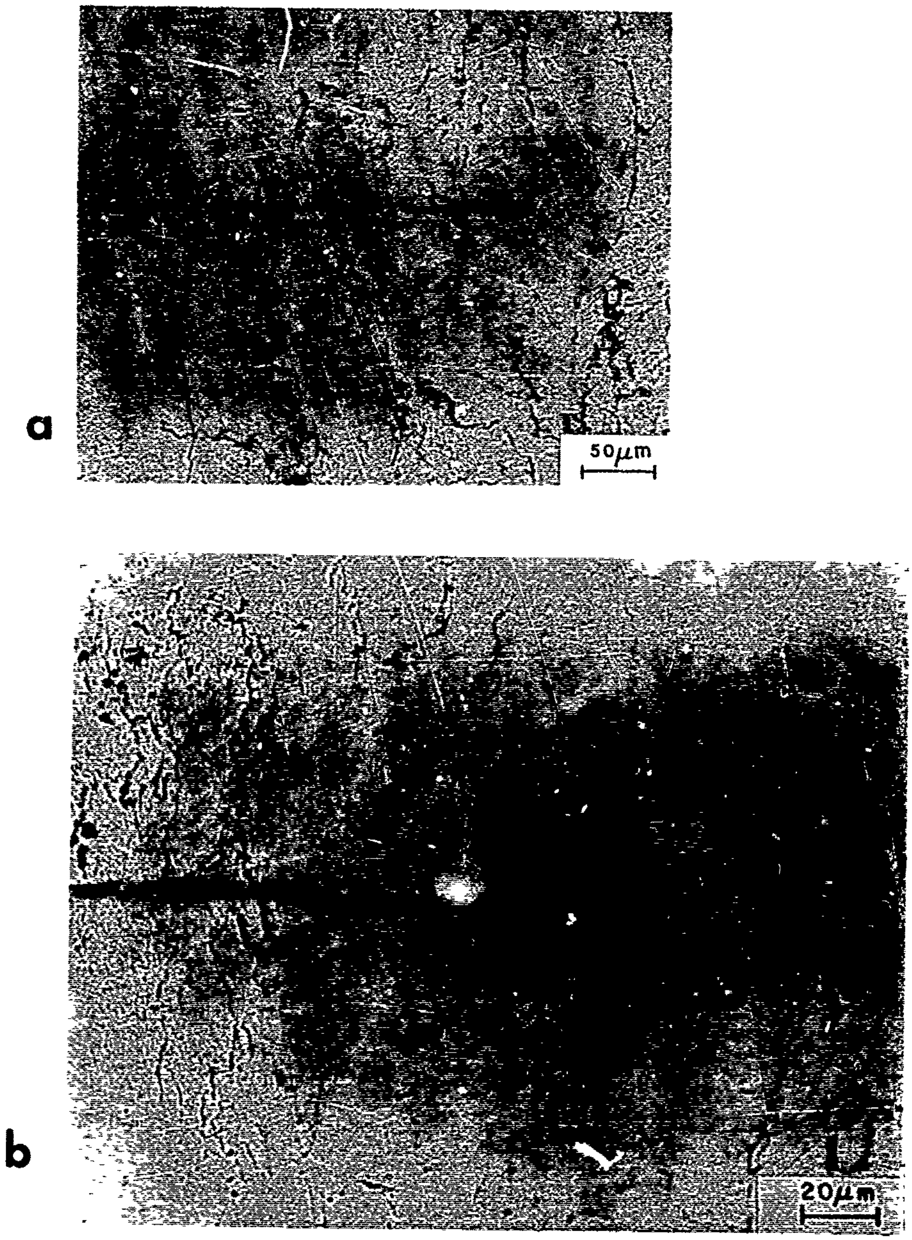

Fatigue crack profile for alloy Al-4.6Cu-1.1Li(range of $\Delta K \sim 2.6$-$6 MPa\sqrt{m}$)

Figure 31

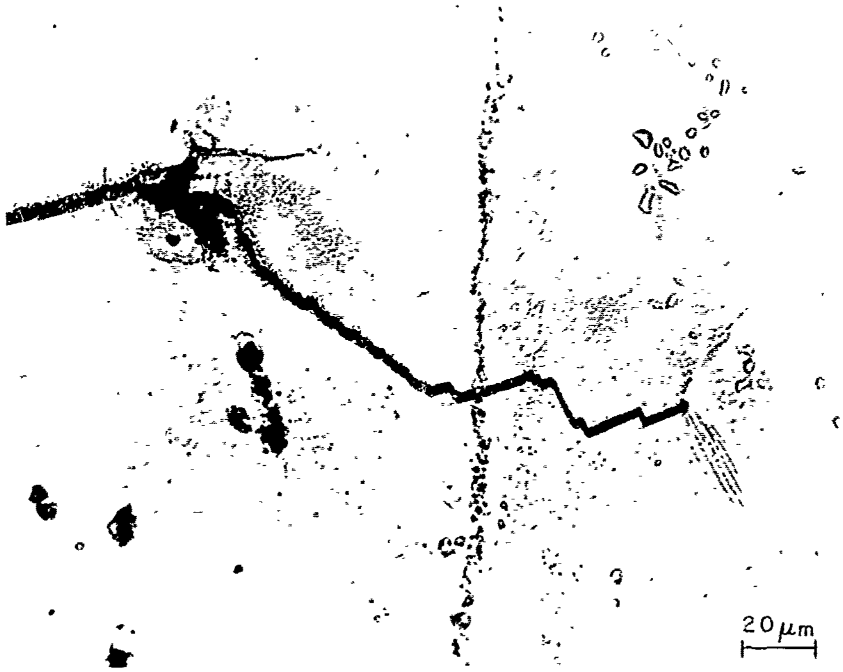

Fatigue crack profile for alloy Al-2.9Cu-2.1Li(range of $\Delta K \sim 3.0\text{-}8MPa\sqrt{m}$).

Figure 32

a

b

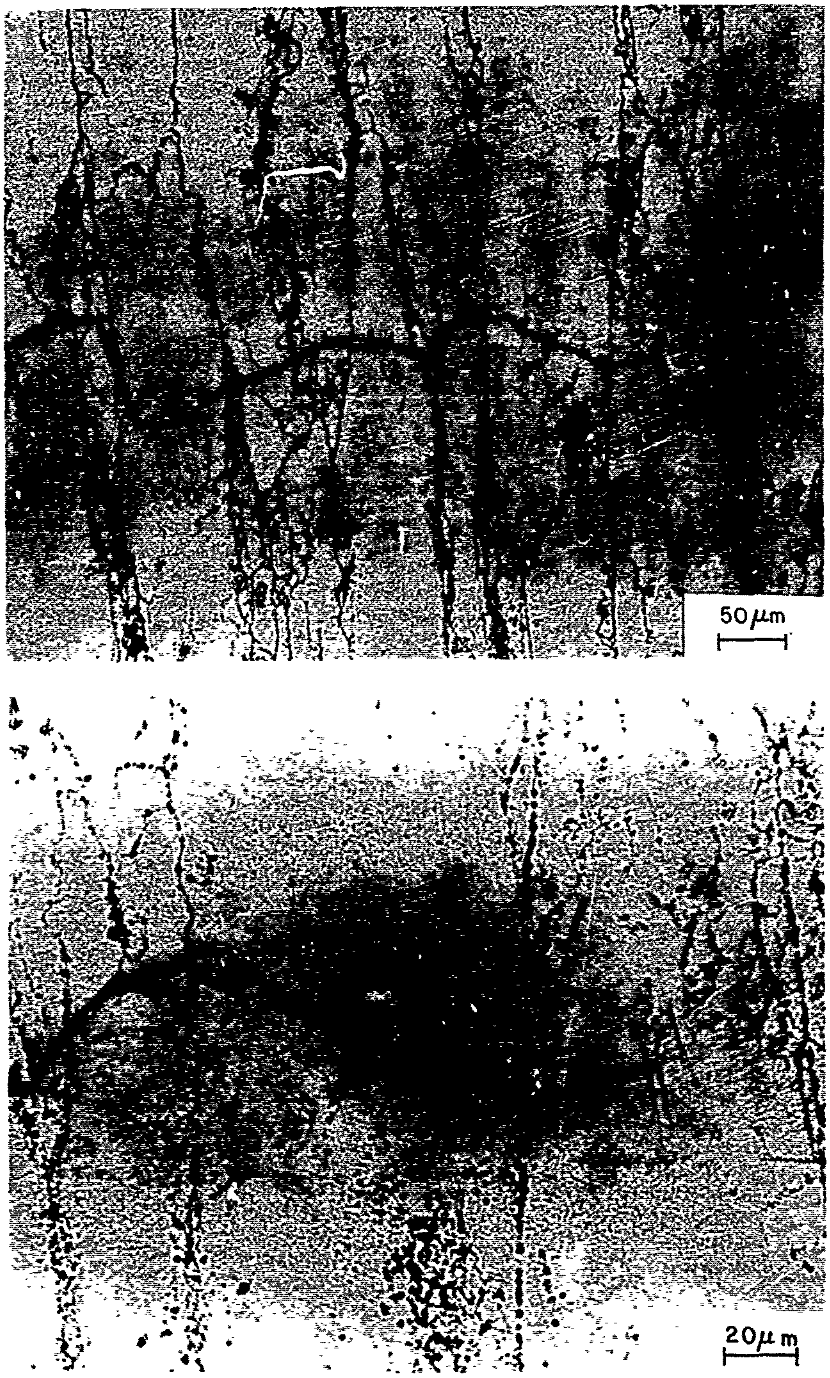

Fatigue crack profile for alloy Al-1.1Cu-2.9Li(range of $\Delta K \sim 5.8$-$8 MPa\sqrt{m}$)

Figure 33

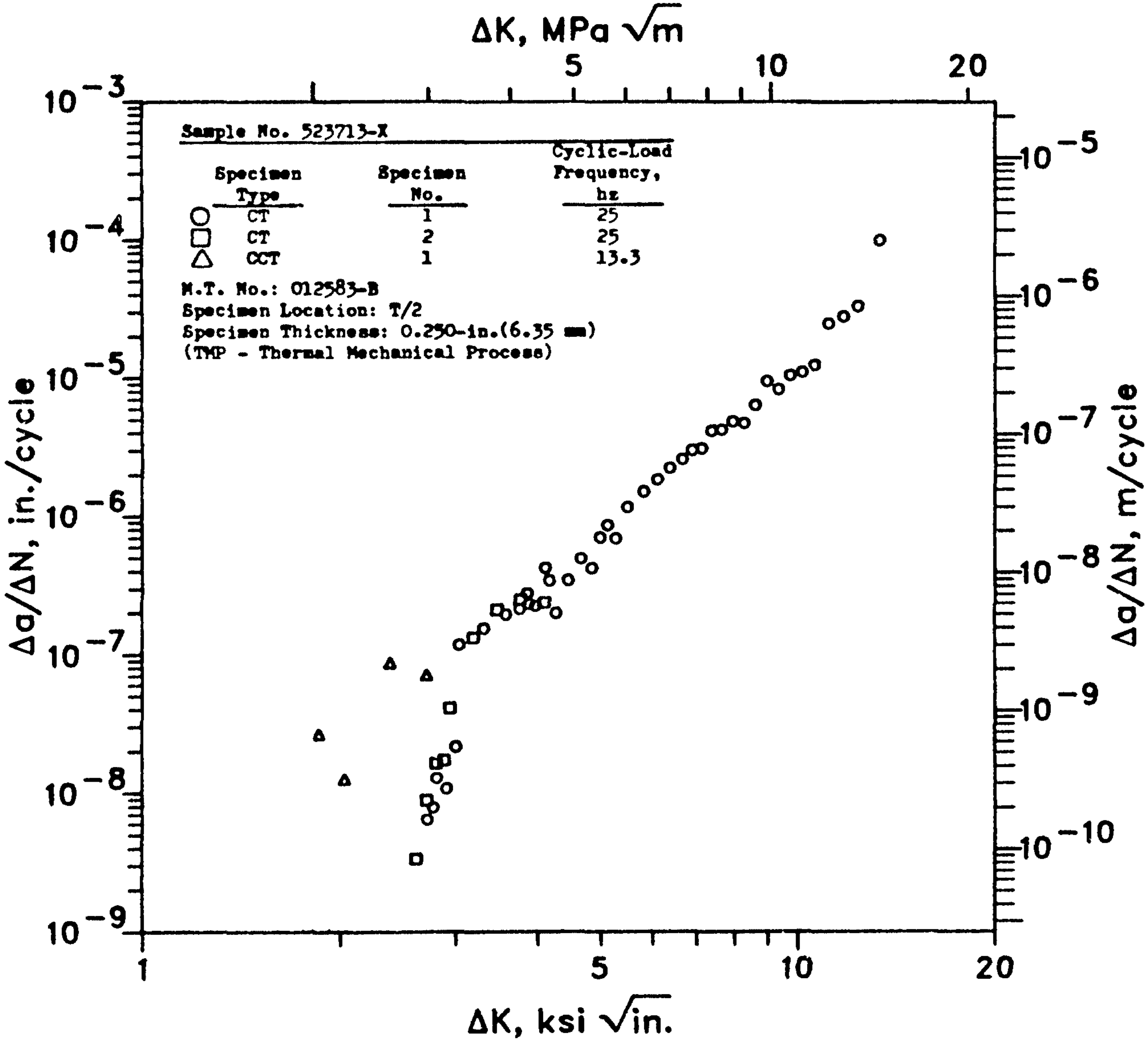

Constant-Load-Amplitude Fatigue Crack Propagation Data for
Laboratory Fabricated Aluminum Alloy 2020-T651 Plate (Unrecrystallized through TMP)
0.5-in. (12.7 mm) thick, L-T orientation, R-Ratio = +0.33, High Humidity (R.H.>90%) Air

Figure 34

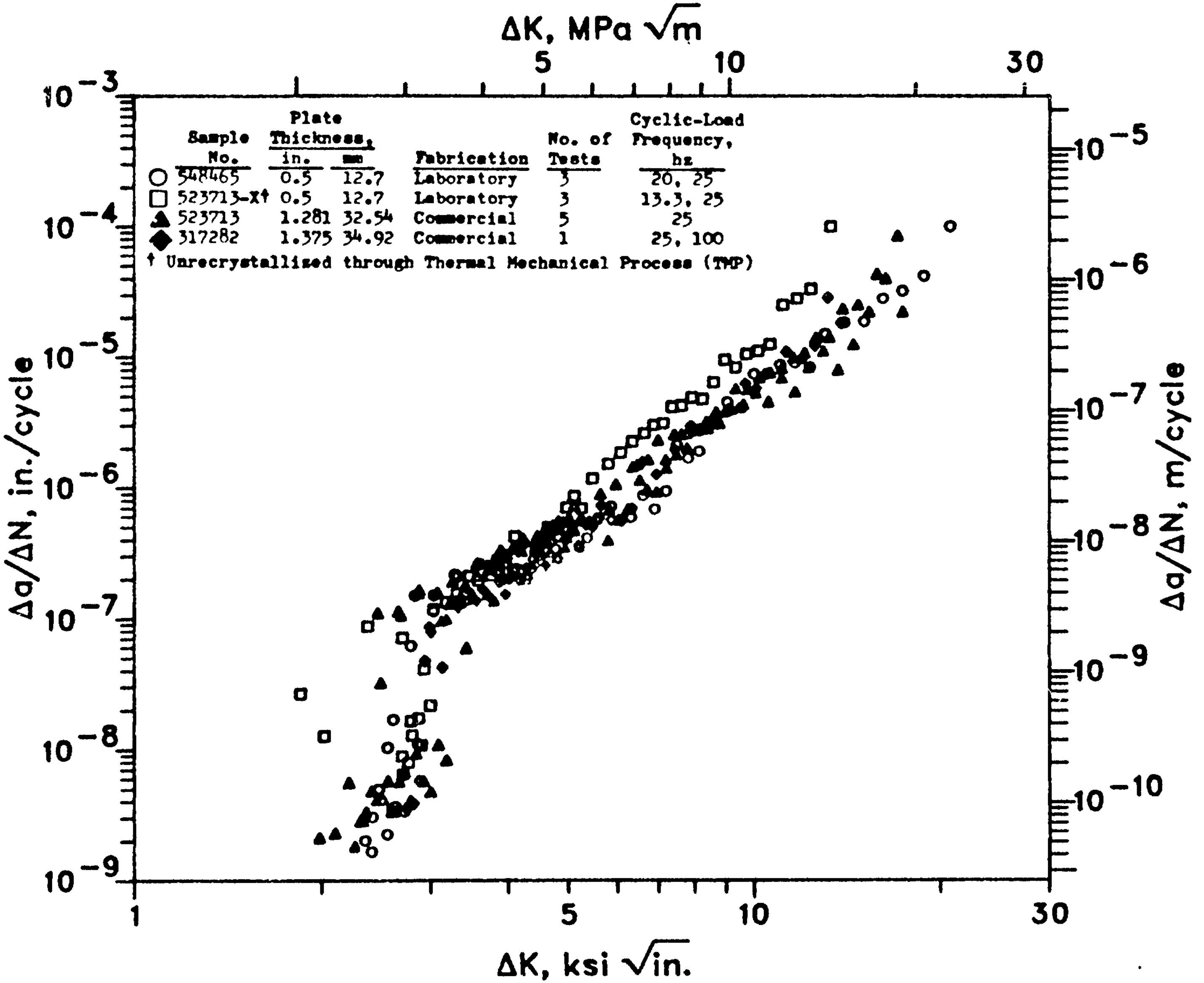

Comparison of Constant–Load–Amplitude Fatigue Crack Growth Data for Four Samples of Aluminum Alloy 2020–T651 Plate (two laboratory fabricated and two commercially produced) L–T orientation, R–Ratio = +0.33, High Humidity (R.H.>90%) Air

Figure 35

GA 16595

(a)

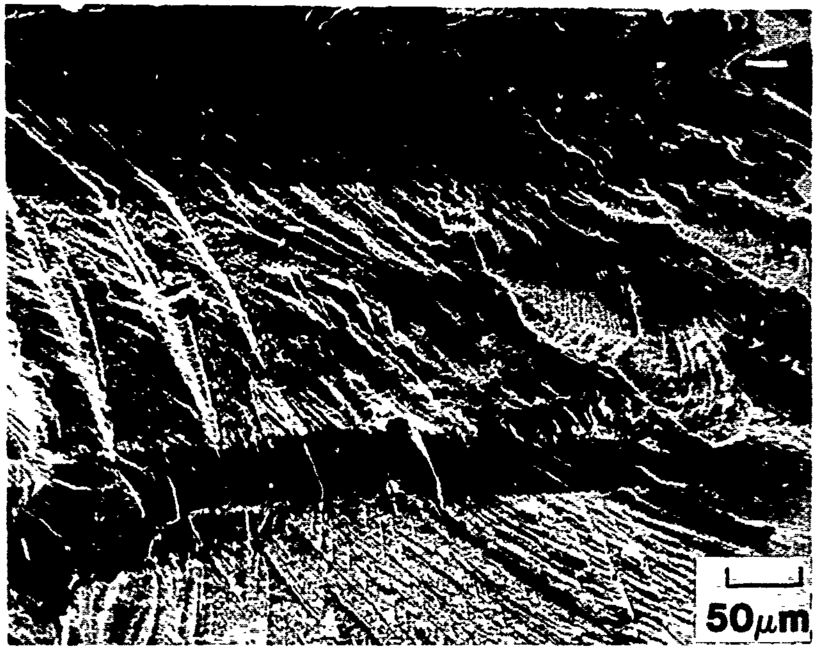

ΔK = 2.5 MPa $\sqrt{m}$

Direction of
crack propagation

(b)

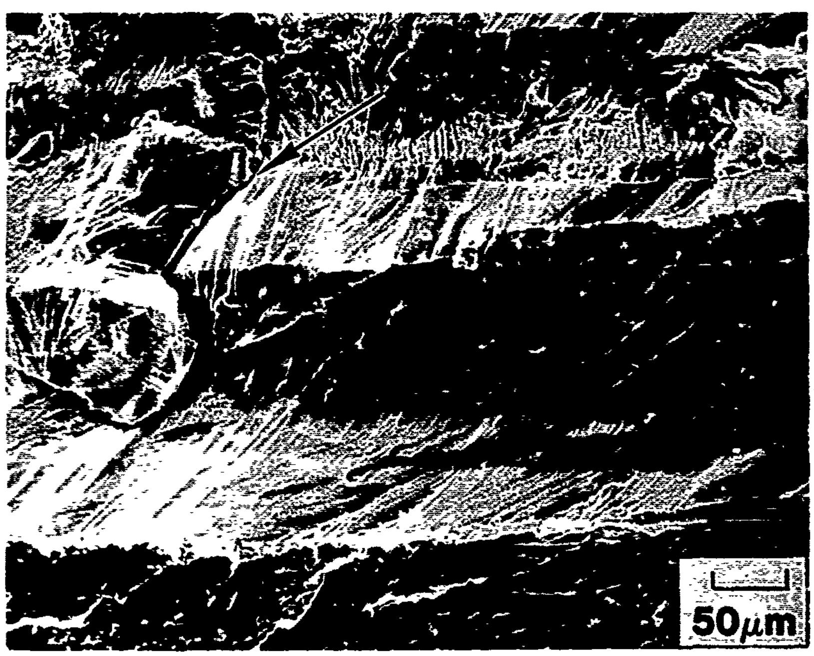

ΔK = 8 MPa $\sqrt{m}$

SEM fractographs of CA fracture surface of CT FCG specimen 548465-L-T-1 (Al - 4.6 Cu - 1.1 Li alloy T651 plate) at ΔK = 2.5 and 8 MPa$\sqrt{m}$

Figure 36

GA 16595

(a)

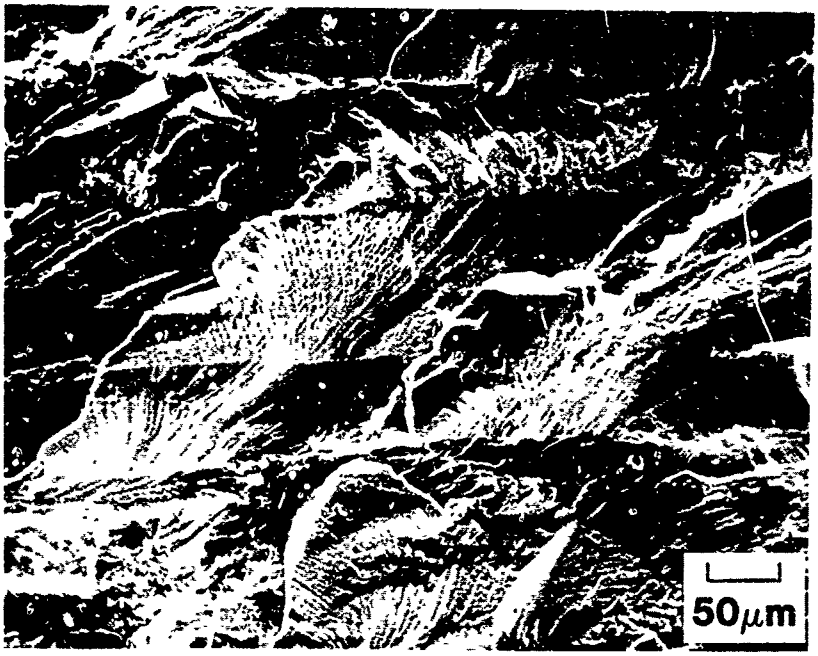

$\Delta K = 3.1$ MPa $\sqrt{m}$

Direction of
crack propagation

(b)

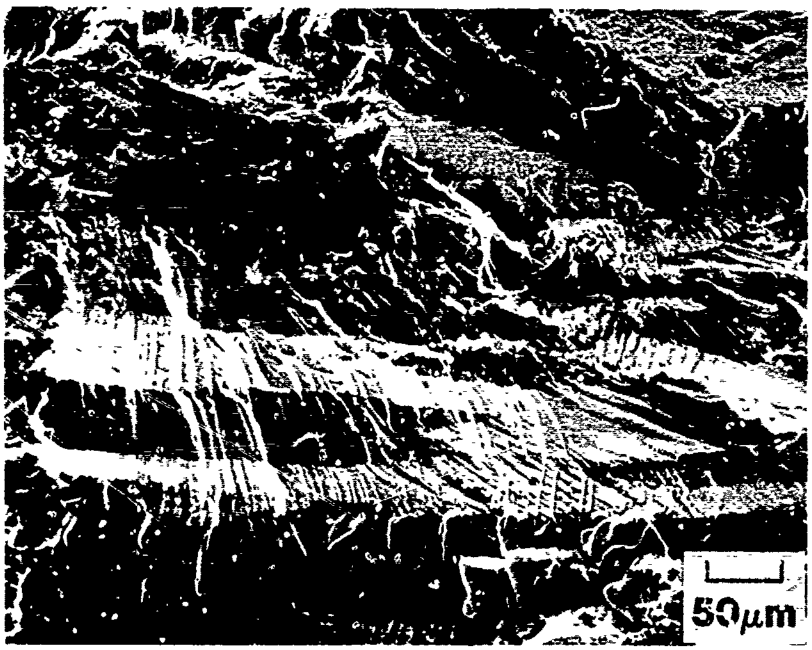

$\Delta K = 8$ MPa $\sqrt{m}$

SEM fractographs of CA fracture surface of CT FCG specimen 548466-L-T-1 (Al -2.9Cu -2.1Li alloy T651 plate) at $\Delta K = 3.1$ and 8 MPa $\sqrt{m}$

Figure 37

GA 10595

(a)

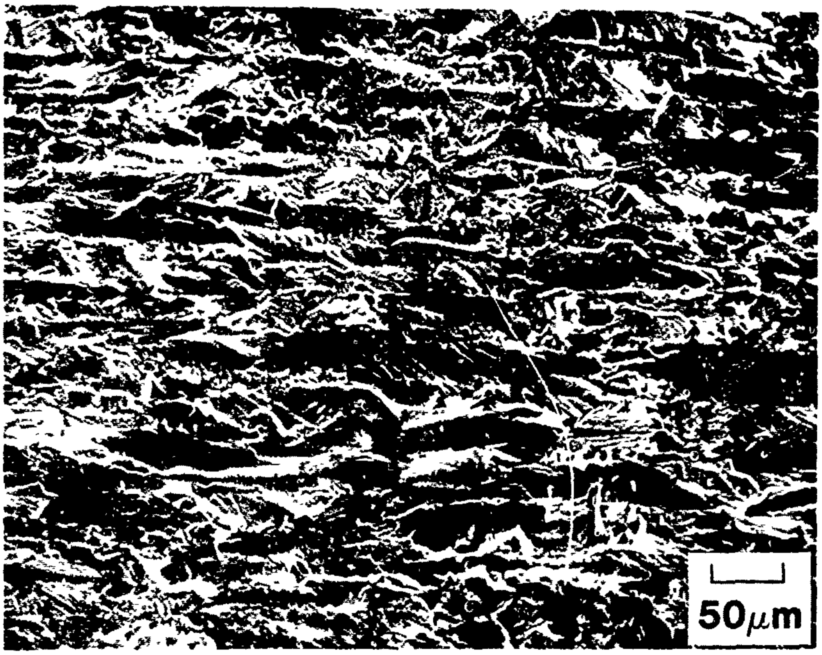

$\Delta K = 3.7$ MPa $\sqrt{m}$

Direction of
crack propagation

(b)

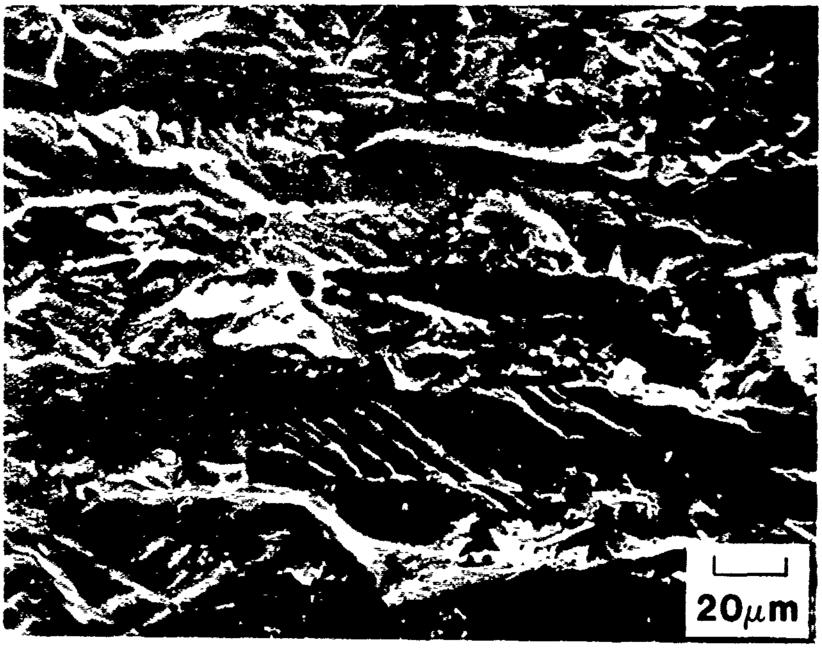

$\Delta K = 3.7$ MPa $\sqrt{m}$

SEM fractographs of CA fracture surface of CT FCG specimen 548468-L-T-1 (Al -1.1Cu -2.9Li alloy T651 plate) at $\Delta K = 3.7$ MPa $\sqrt{m}$

Figure 38

GA 16595

(a)

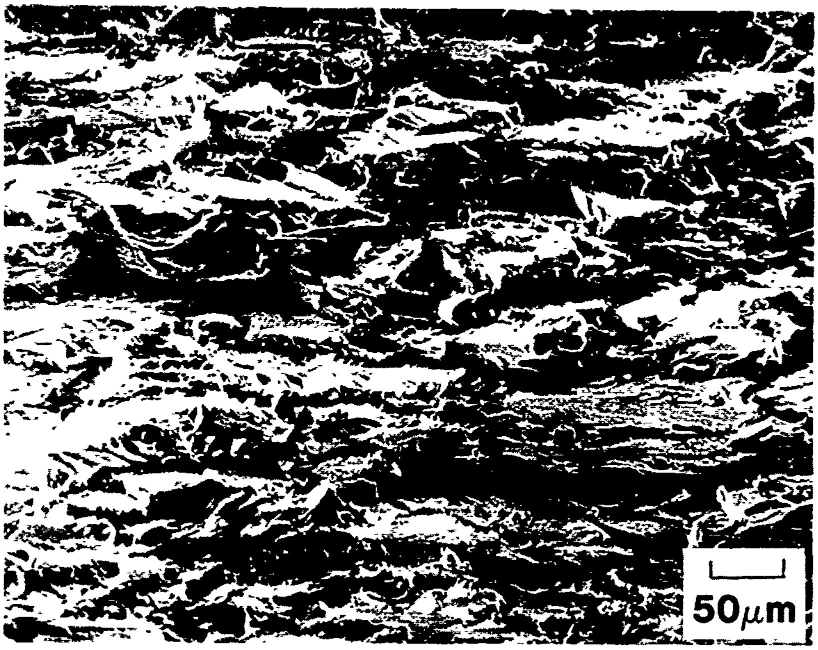

$\Delta K = 8$ MPa $\sqrt{m}$

Direction of
crack propagation
⟶

(b)

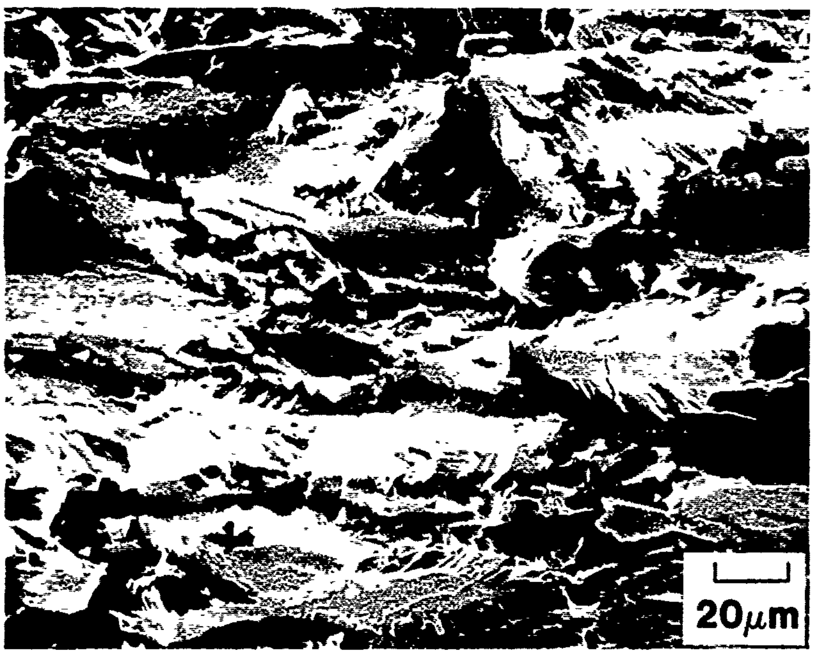

$\Delta K = 8$ MPa $\sqrt{m}$

SEM fractographs of CA fracture surface of CT FCG specimen 548468-L-T-I (Al -1.1Cu -2.9Li alloy T651 plate) at $\Delta K = 8$ MPa $\sqrt{m}$

Figure 39

GA 16595

(a)

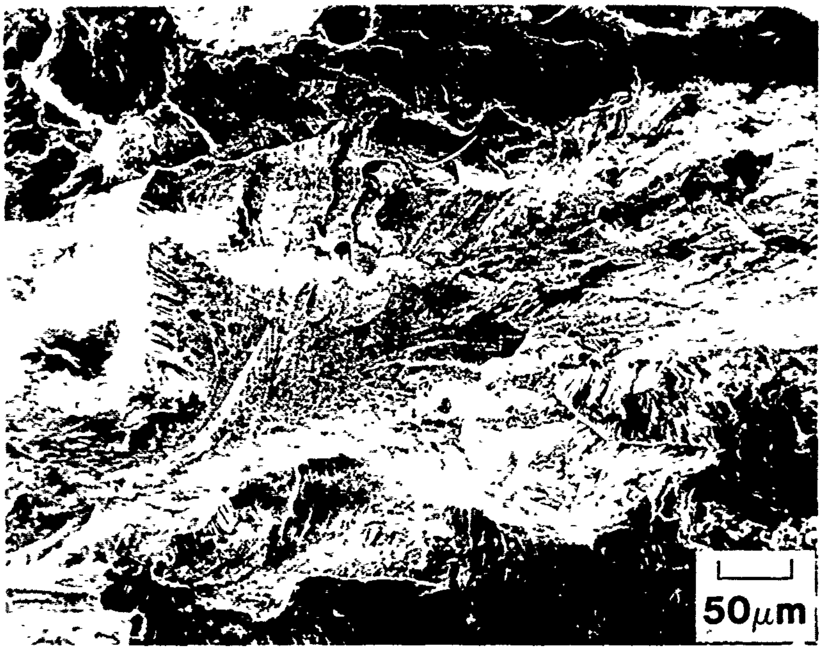

$\Delta K = 3$ MPa $\sqrt{m}$

Direction of
crack propagation

(b)

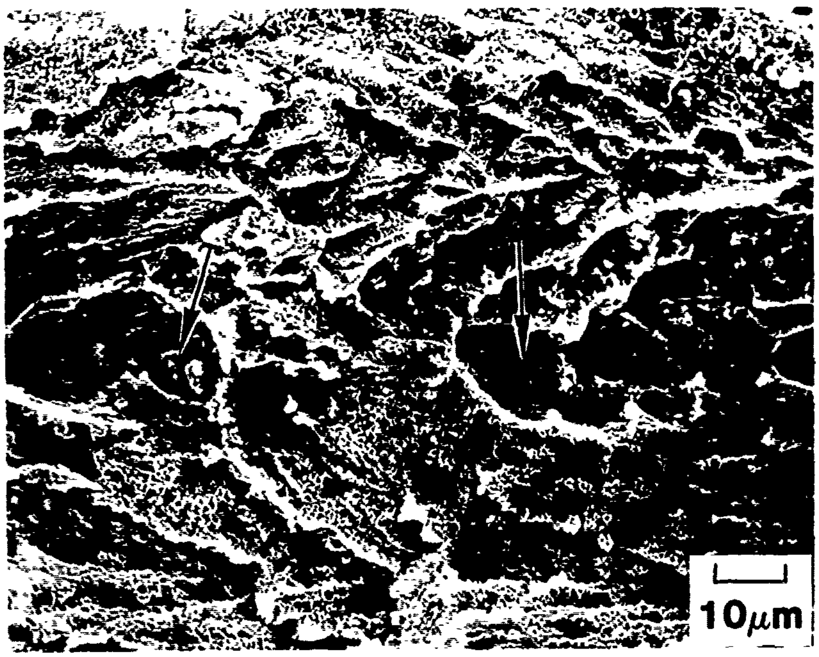

$\Delta K = 8$ MPa $\sqrt{m}$

SEM fractographs of CA fracture surface of CT FCG specimen 523713-X-L-T-1 (TMP 2020-T651 plate) at $\Delta K = 3$ and 8 MPa $\sqrt{m}$

Figure 40

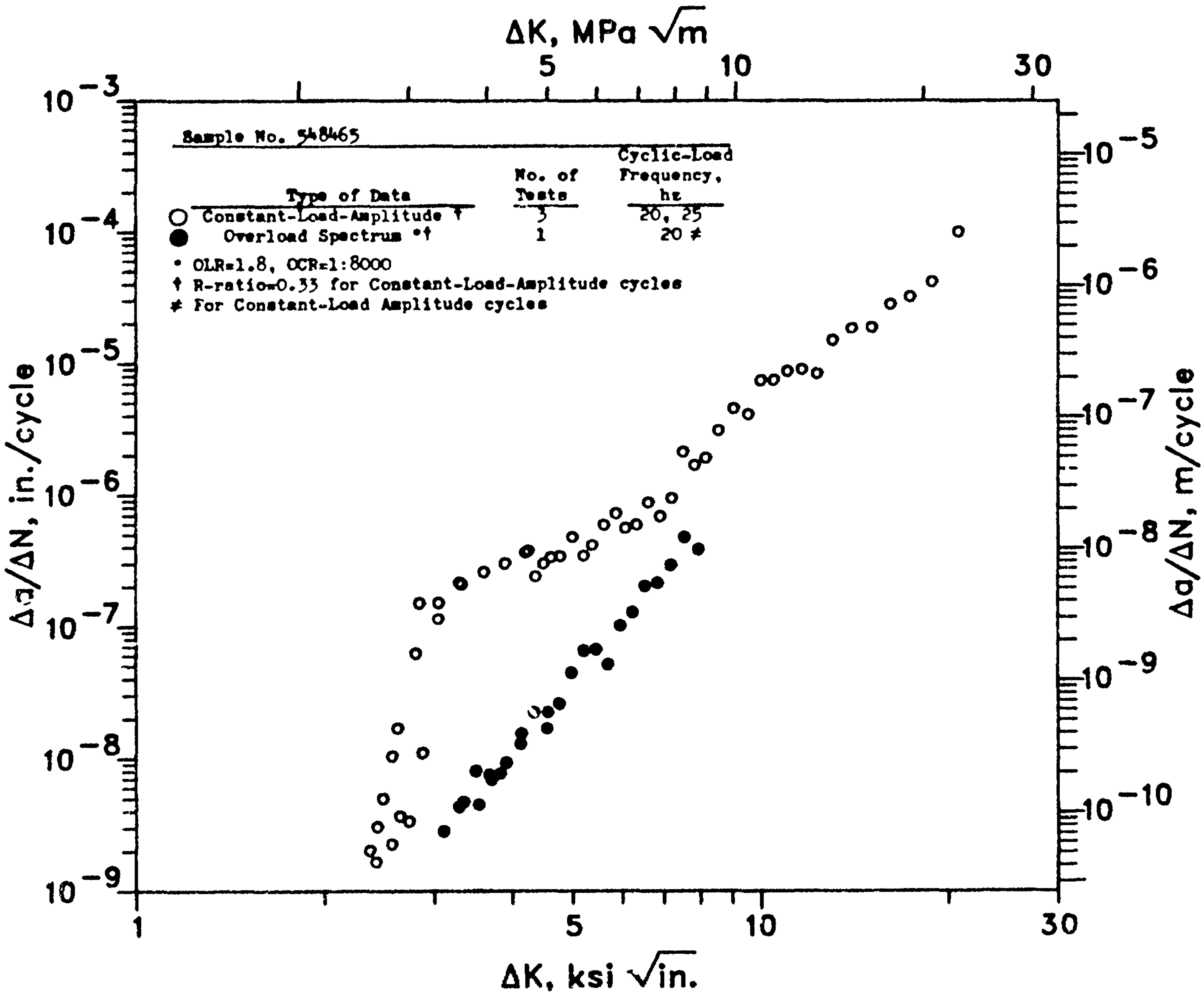

Comparison of Constant–Load–Amplitude and Overload Spectrum Fatigue Crack Growth Data for Laboratory Fabricated Aluminum Alloy (4.6 Cu – 1.1 Li) – T651 Plate, 0.5–in. (12.7 mm) thick L–T orientation, High Humidity (R.H.>90%) Air

Figure 41

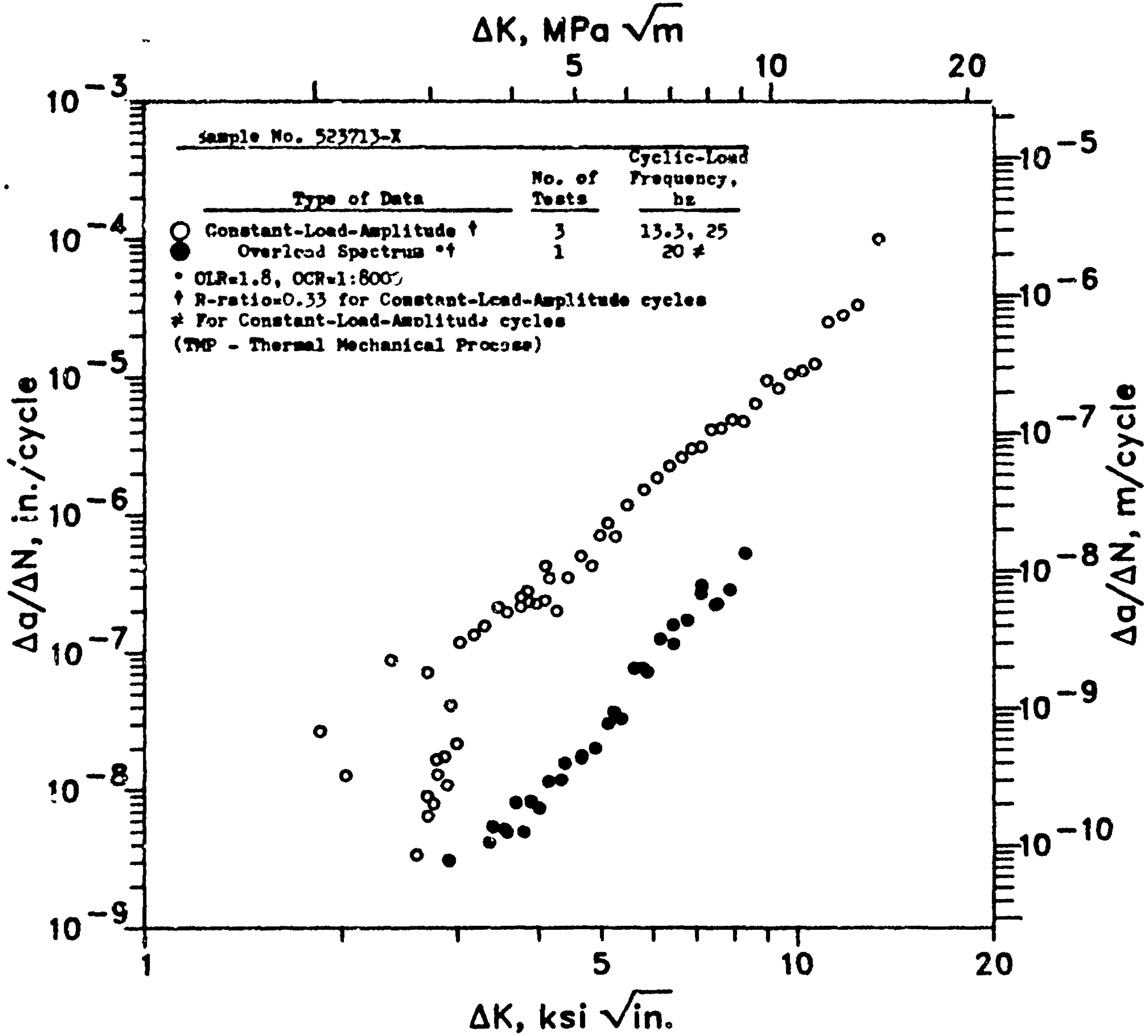

Comparison of Constant–Load–Amplitude and Overload Spectrum Fatigue Crack Growth Data for Laboratory Fabricated Aluminum Alloy 2020–T651 Plate (Unrecrystallized through TMP), 0.5–in. (12.7 mm) thick ... High Humidity (R.H. >90%) Air

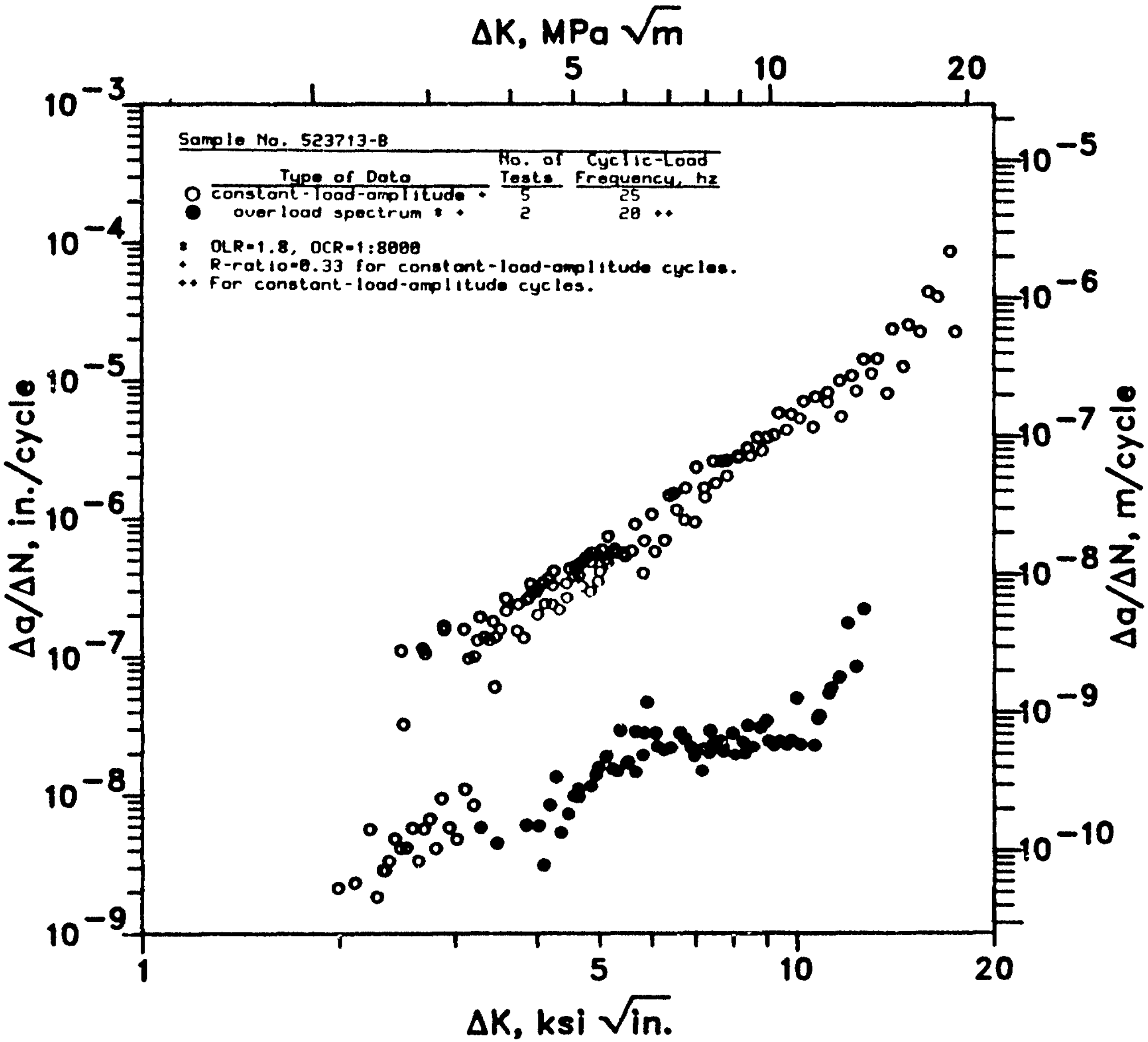

Comparison of Constant–Load–Amplitude and Overload Spectrum Fatigue Crack Growth Data for Commercially Produced Aluminum Alloy 2020–T651 Plate, 1.281–in. (32.54 mm) thick L–T orientation, high humidity (r.h.>90%) air

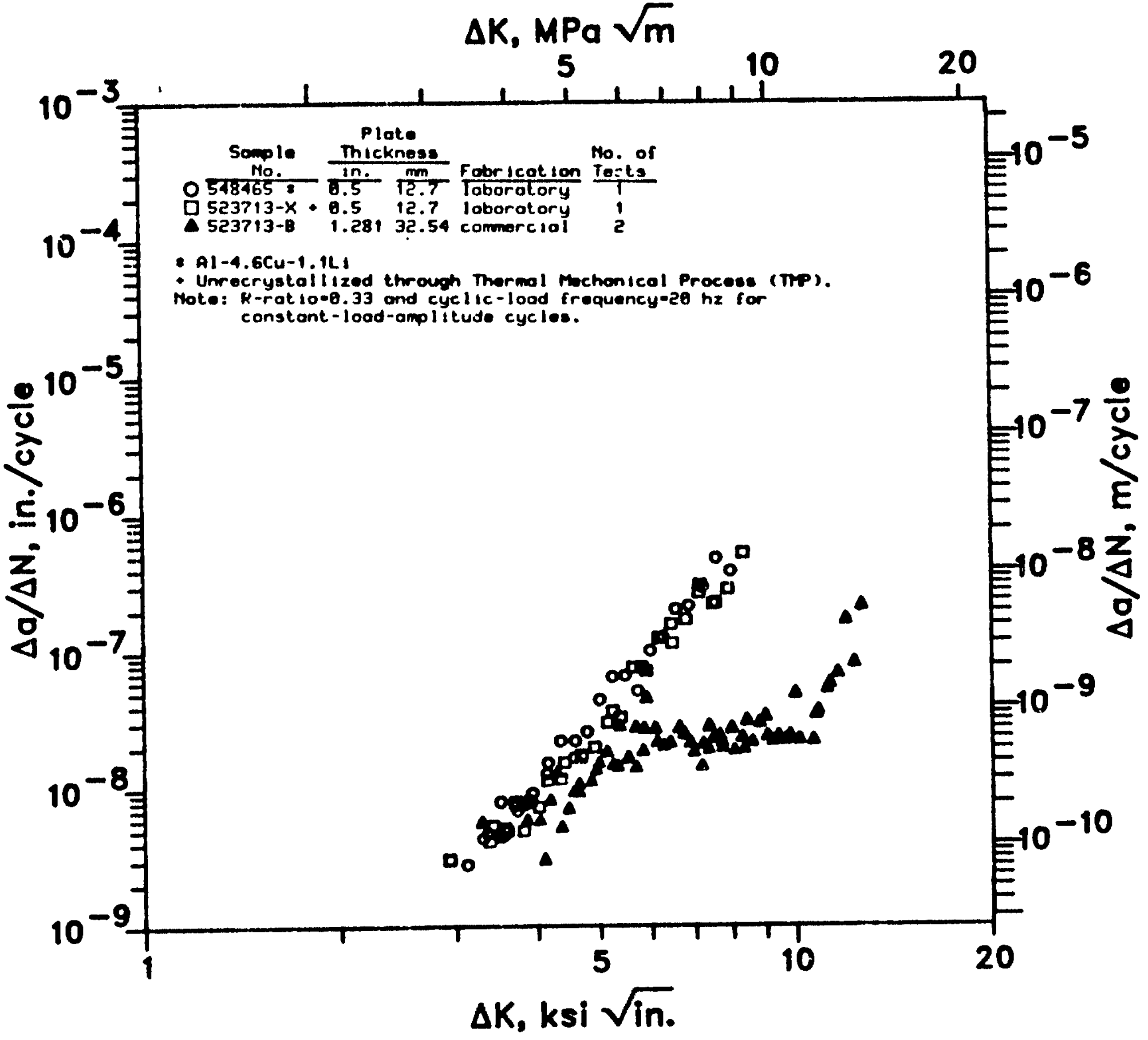

Comparison of Overload Spectrum (OLR=1.8,OCR=1:8000) Fatigue Crack Growth Data for Three Samples of Aluminum Alloy 2020–T651 Plate (two laboratory fabricated and one commercially produced) L–T orientation, high humidity (r.h.>90%) air

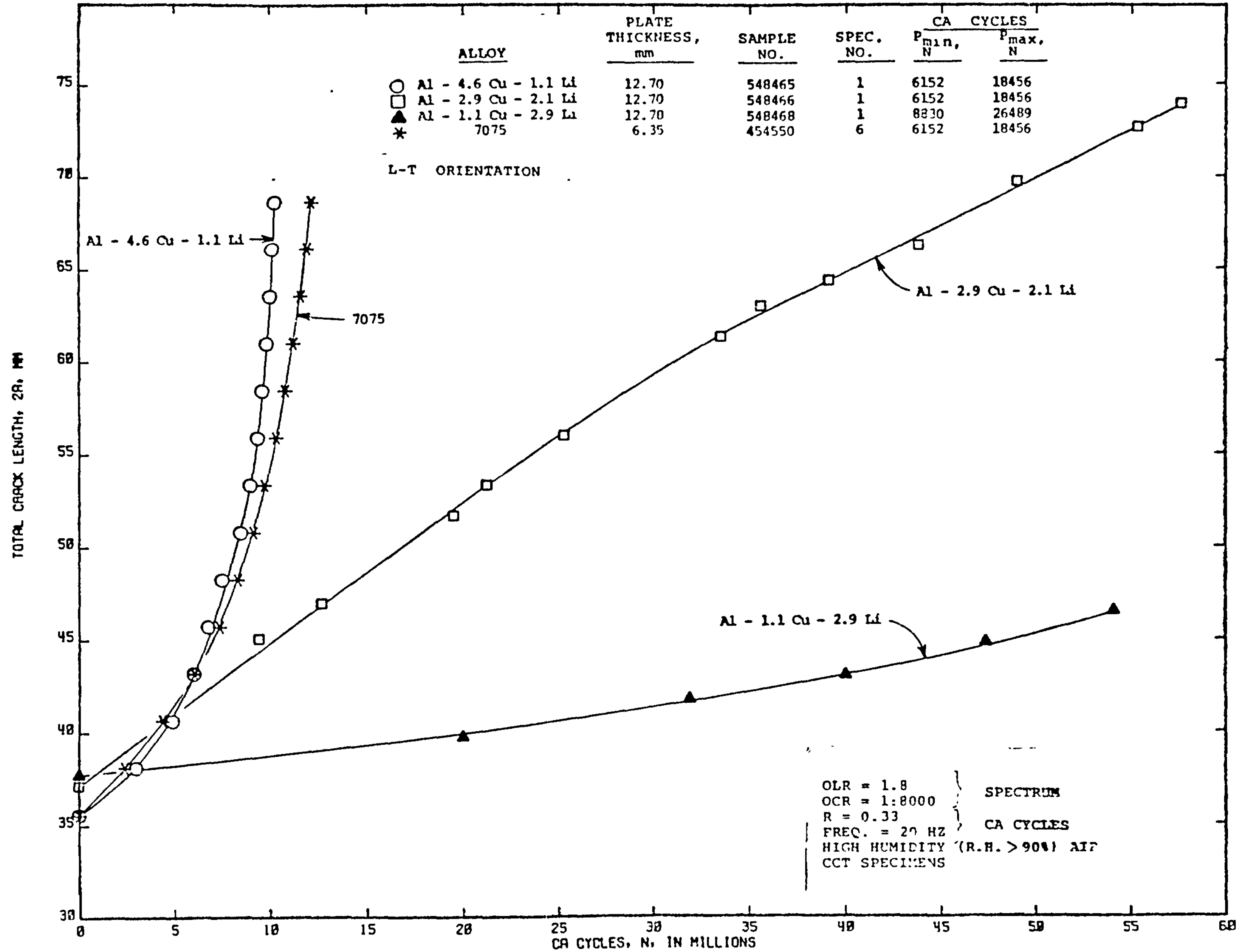

COMPARISON OF TOTAL CRACK LENGTH VERSUS NUMBER OF CA CYCLES DATA OF SINGLE PERIODIC OVERLOAD FCG TESTS OF LABORATORY FABRICATED PLATES OF THREE (AL - CU - LI) - T651 ALLOYS AND 7075-T651

Figure 45

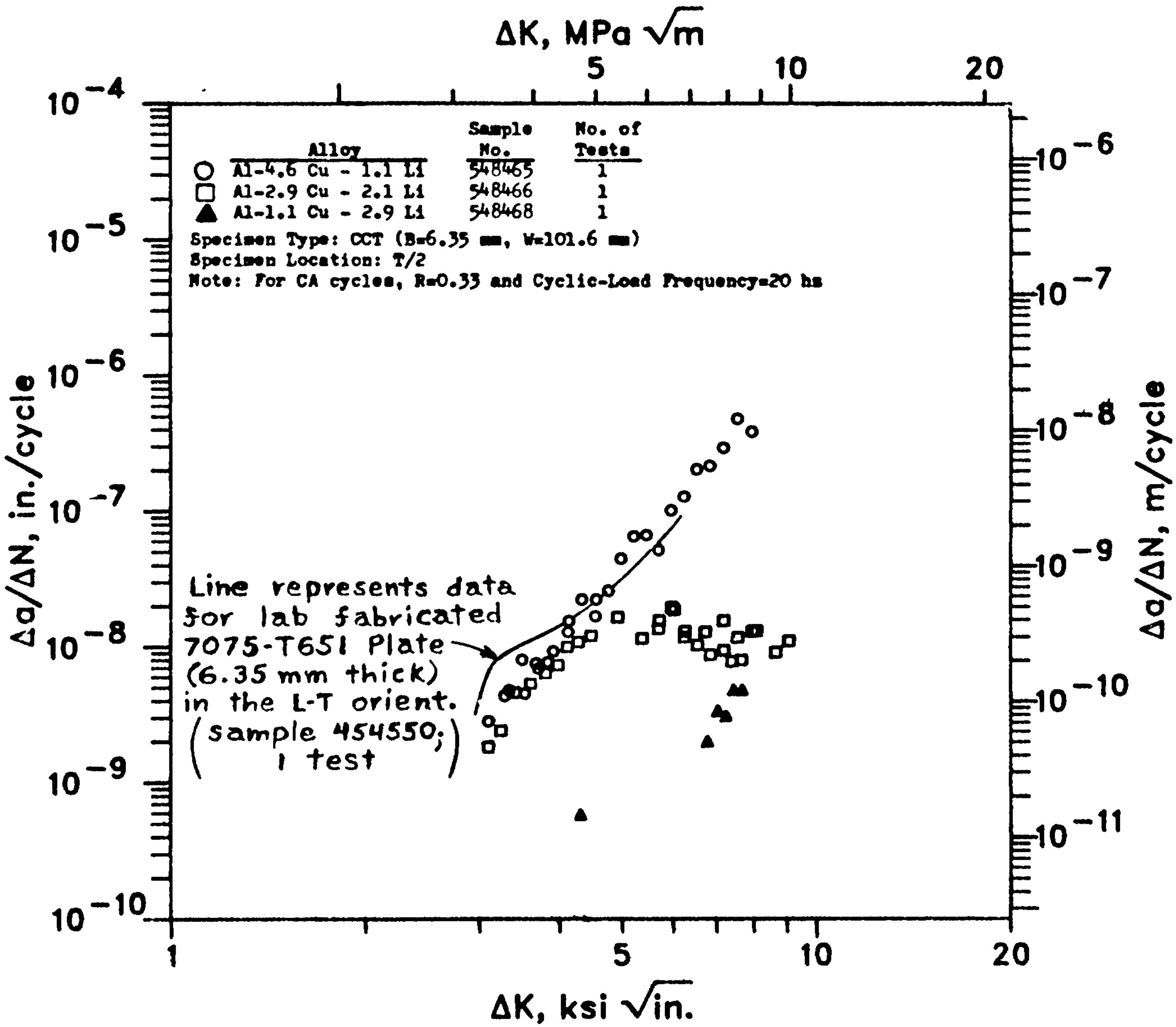

Comparison of Overload Spectrum (OLR = 1.8, OCR = 1:8000) Fatigue Crack Growth Data for Laboratory Fabricated Plates, 0.5-in. (12.7 mm) thick, of Three Al-Li Alloys (T651 Temper) L-T orientation. High Humidity (R.H.>90%) Air

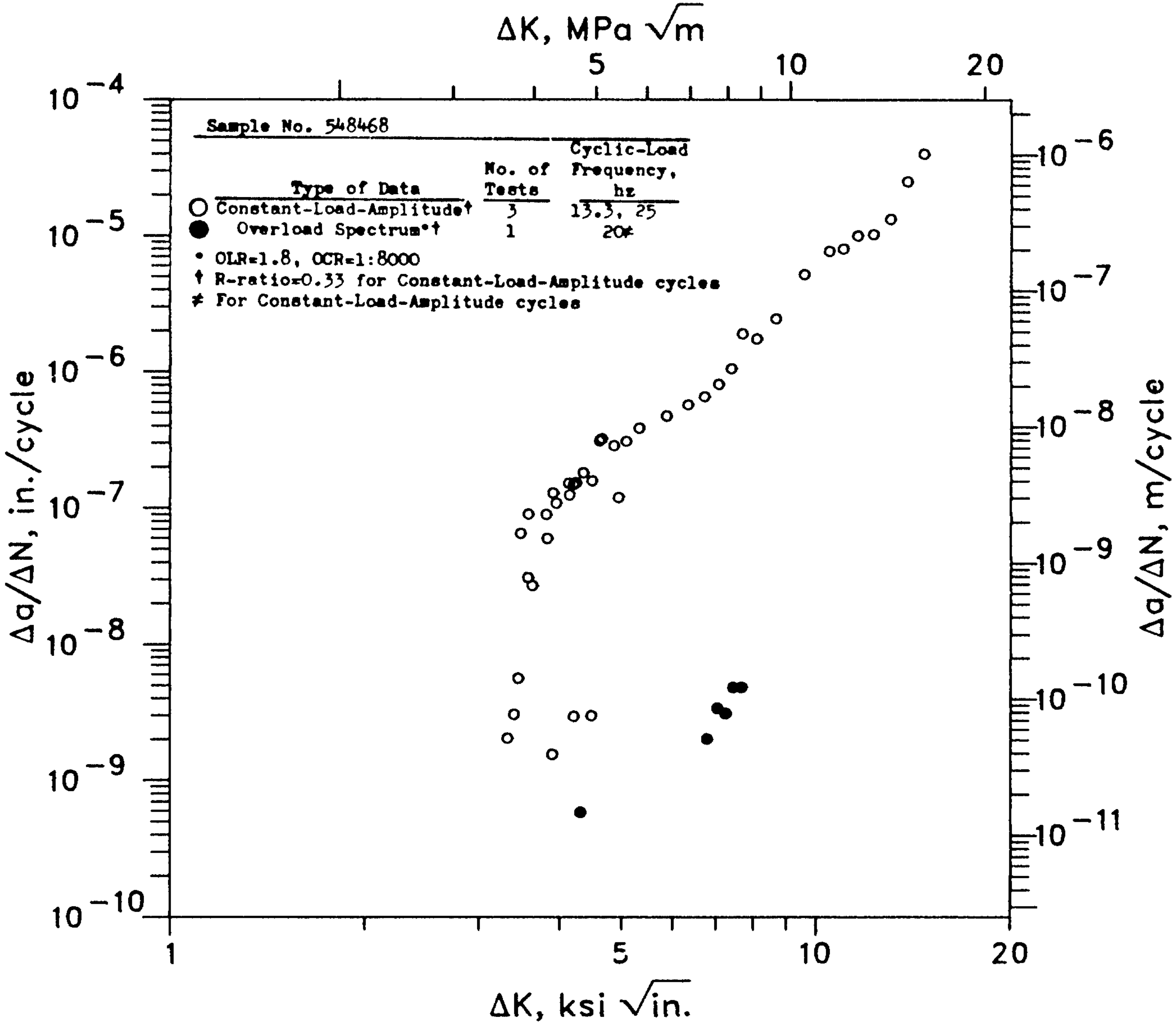

Comparison of Constant-Load-Amplitude and Overload Spectrum Fatigue Crack Growth Data for Laboratory Fabricated Aluminum Alloy (1.1 Cu – 2.9 Li) – T651 Plate, 0.5-in. (12.7mm) thick L-T orientation, High Humidity (R.H.>90%) Air

Figure 47(b)

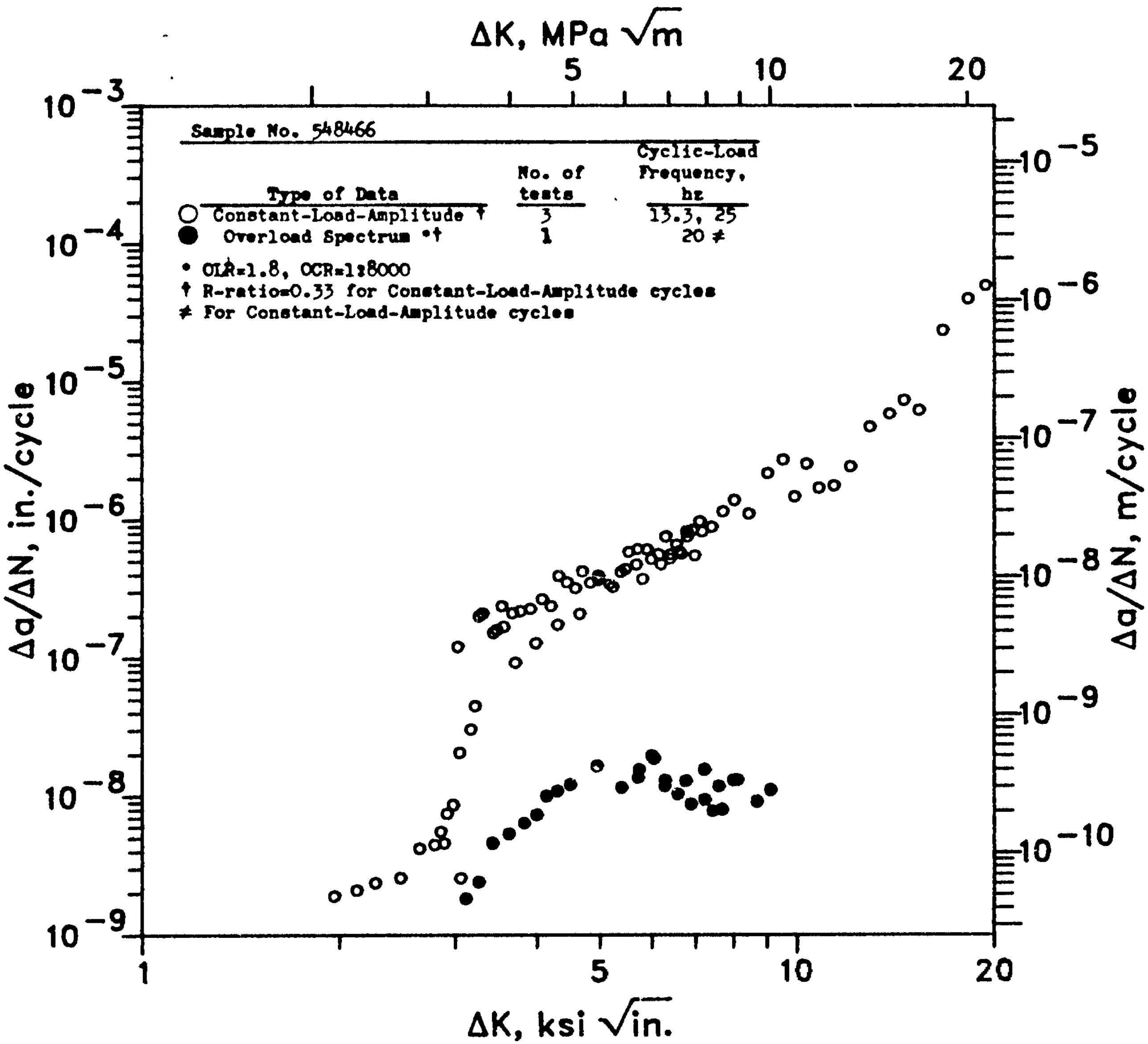

Comparison of Constant–Load–Amplitude and Overload Spectrum Fatigue Crack Growth Data for Laboratory Fabricated Aluminum Alloy (2.9 Cu – 2.1 Li) – T651 Plate, 0.5–in. (12.7 mm) thick L–T orientation, High Humidity (R.H. >90%) Air

Direction of
crack propagation

GA 16595

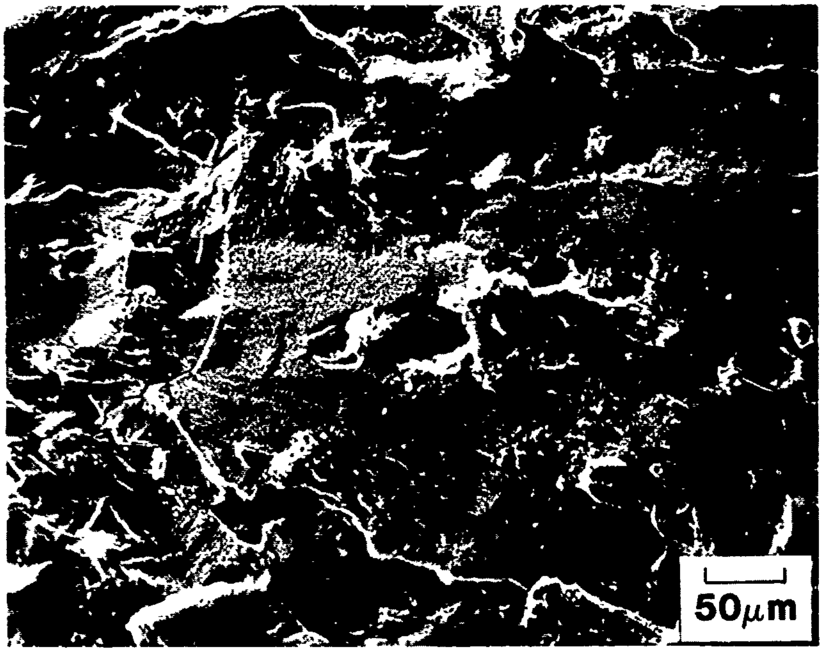

(a) SEM fractograph of OL fracture surface of CCT FCG specimen 523713-B-1-L-T-2 (2020-T651 plate) at $\Delta K = 4$ MPa $\sqrt{m}$

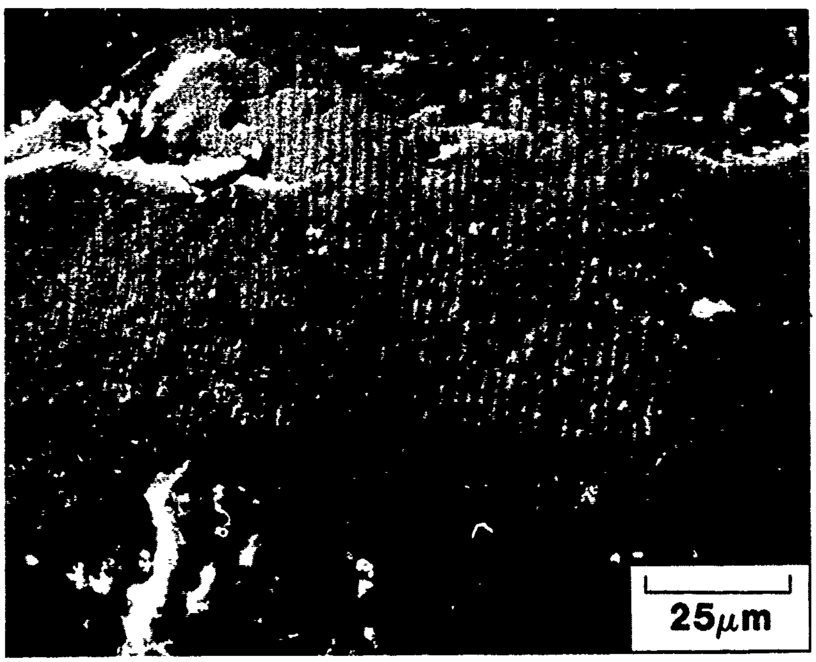

(b) SEM fractograph of fracture surface within circled area shown in (a)

Figure 48

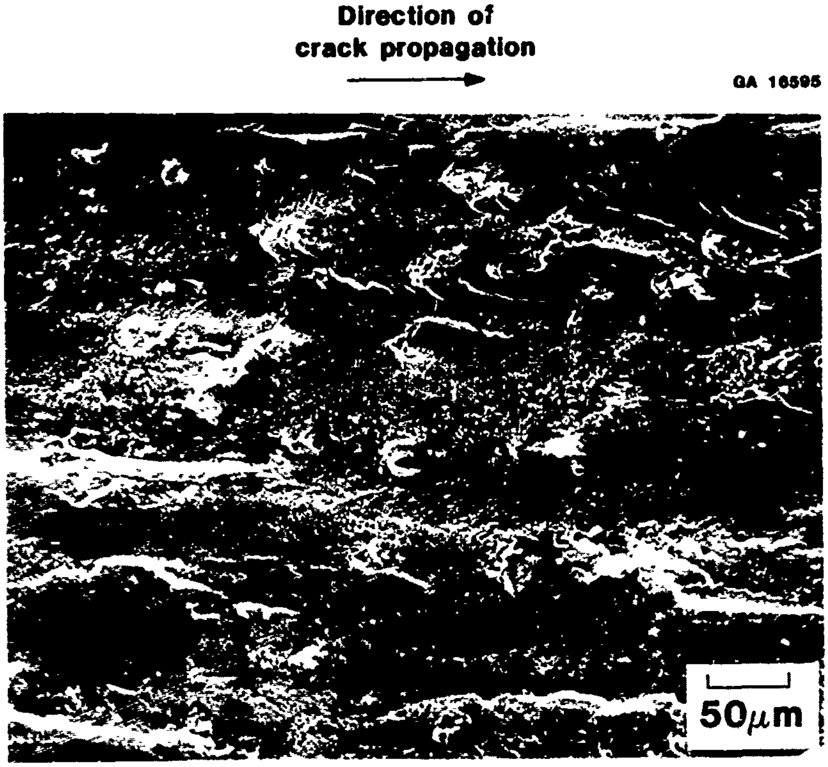

(a) SEM fractograph of OL fracture surface of CCT FCG specimen 523713-X-L-T-1 (TMP 2020-T651 plate) at $\Delta K = 4$ MPa $\sqrt{m}$

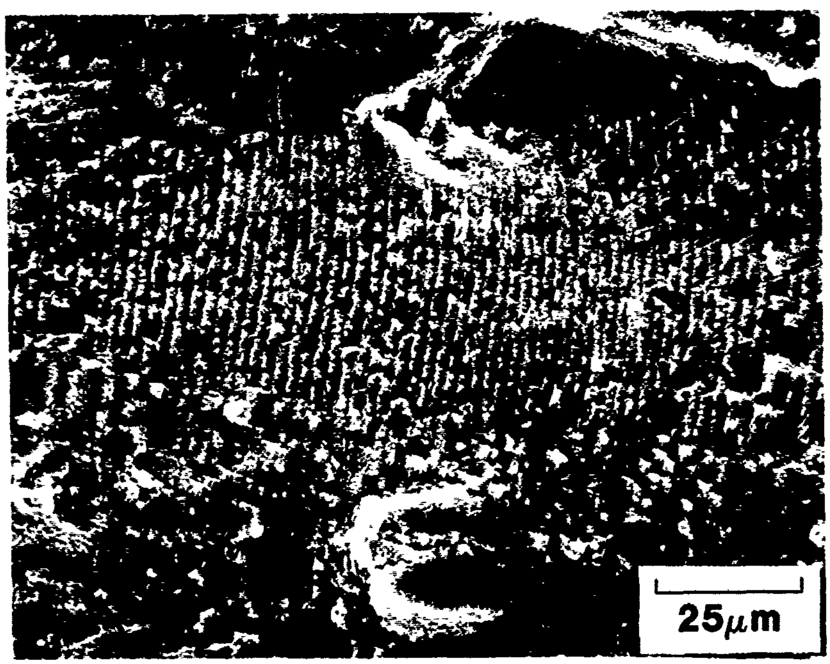

(b) SEM fractograph of fracture surface within circled area shown in (a)

Figure 49

Direction of
crack propagation
→

GA 16595

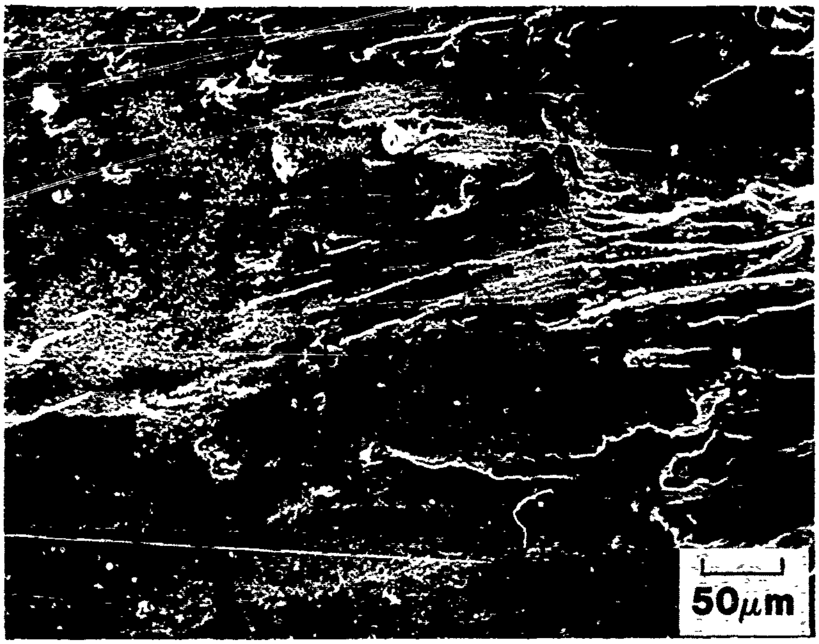

(a) SEM fractograph of OL fracture surface of CCT FCG specimen 548465-L-T-1 (Al - 4.6 Cu - 1.1 Li alloy T651 plate) at $\Delta K = 4$ MPa $\sqrt{m}$

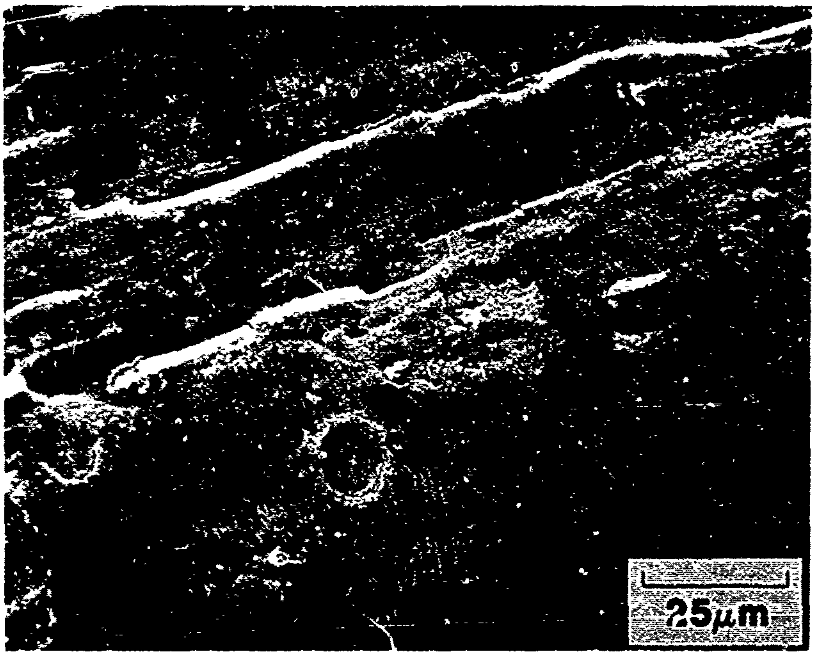

(b) SEM fractograph of fracture surface within circled area shown in (a)

Figure 50

Direction of
crack propagation

GA 16595

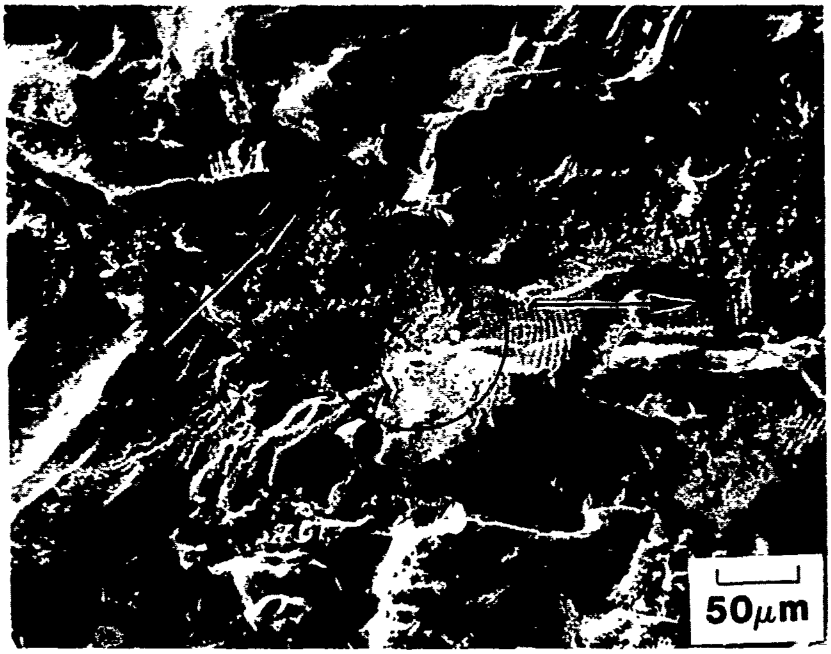

(a) SEM fractograph of OL fracture surface of CCT FCG specimen 523713-B-1-L-T-2 (2020-T651 plate) at $\Delta K = 8$ MPa $\sqrt{m}$

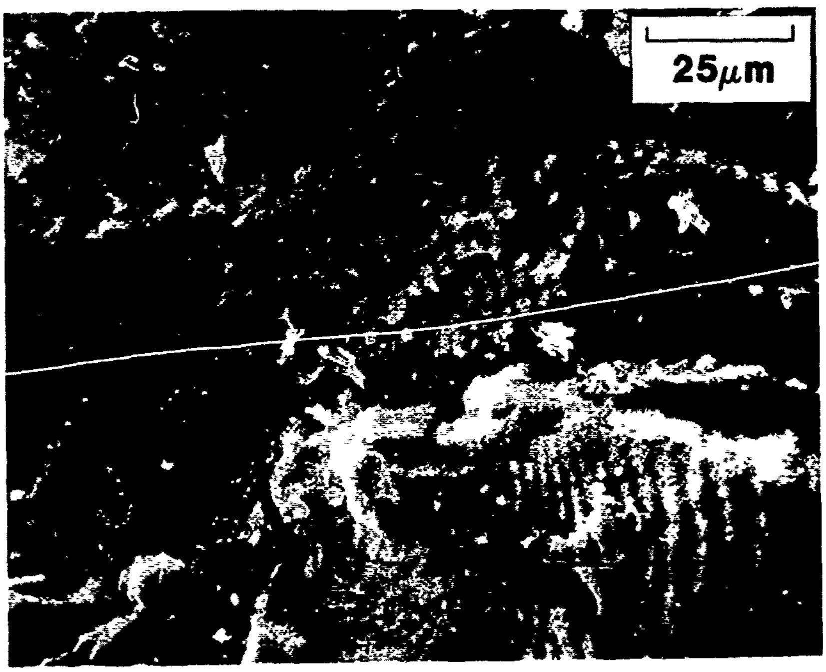

(b) SEM fractograph of fracture surface within circled area shown in (a)

Figure 51

GA 16595

(a)

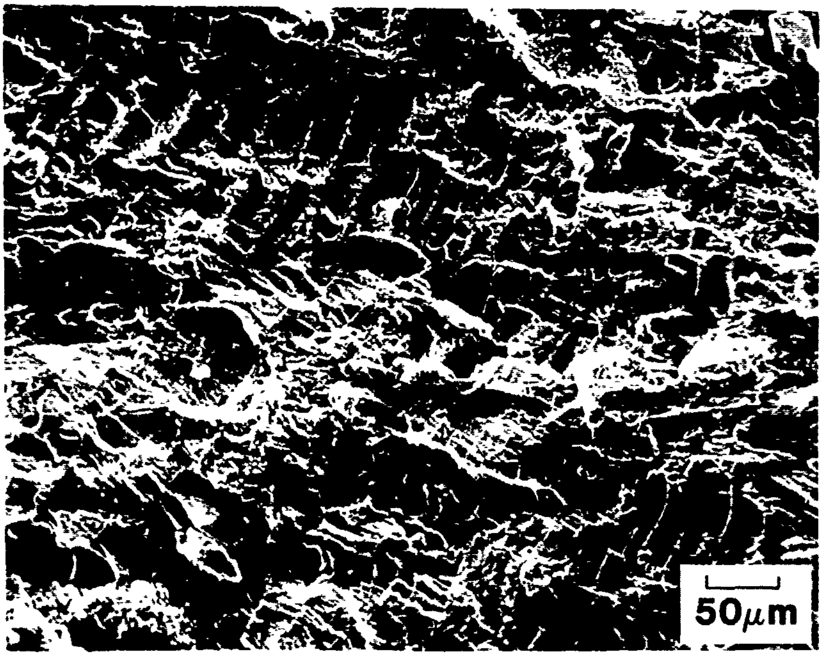

$\Delta K = 6$ MPa $\sqrt{m}$

Direction of
crack propagation

(b)

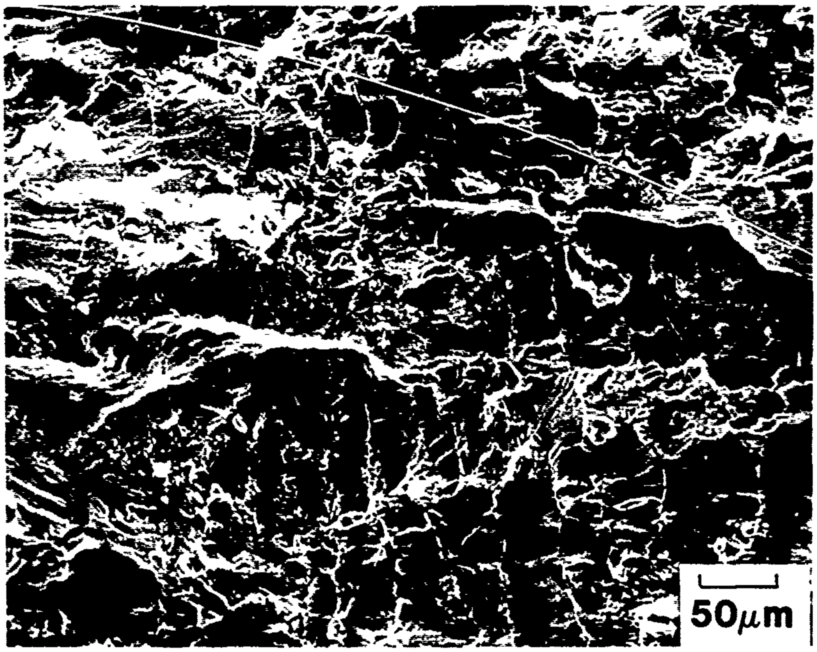

$\Delta K = 8$ MPa $\sqrt{m}$

SEM fractograph of OL fracture surface of CCT FCG specimen 523713-X-L-T-1 (TMP 2020-T651 plate) at $\Delta K = 6$ and 8 MPa $\sqrt{m}$

Figure 52

Direction of
crack propagation

GA 16595

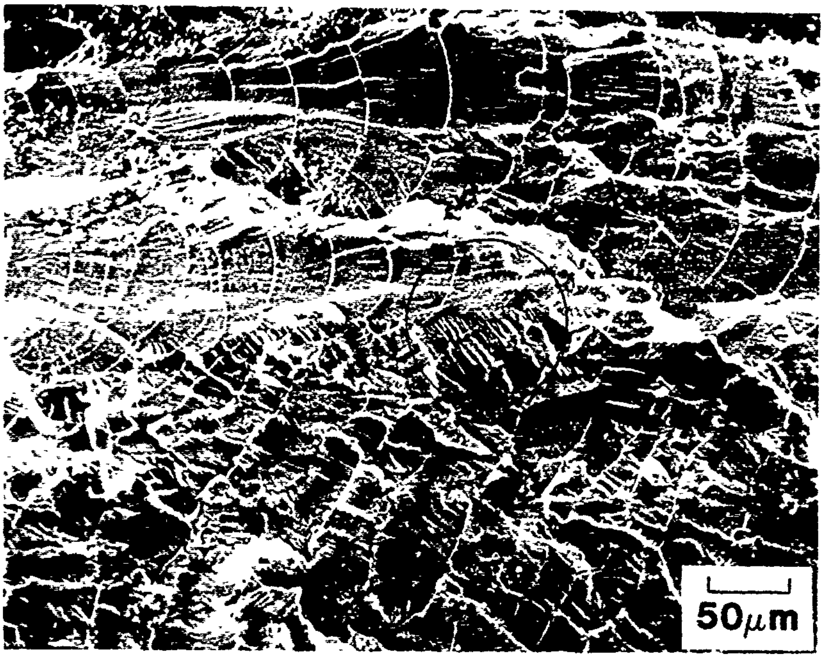

(a) SEM fractograph of OL fracture surface of CCT FCG specimen 548465-L-T-1 (Al - 4.6 Cu - 1.1 Li alloy T651 plate) at $\Delta K = 8$ MPa $\sqrt{m}$

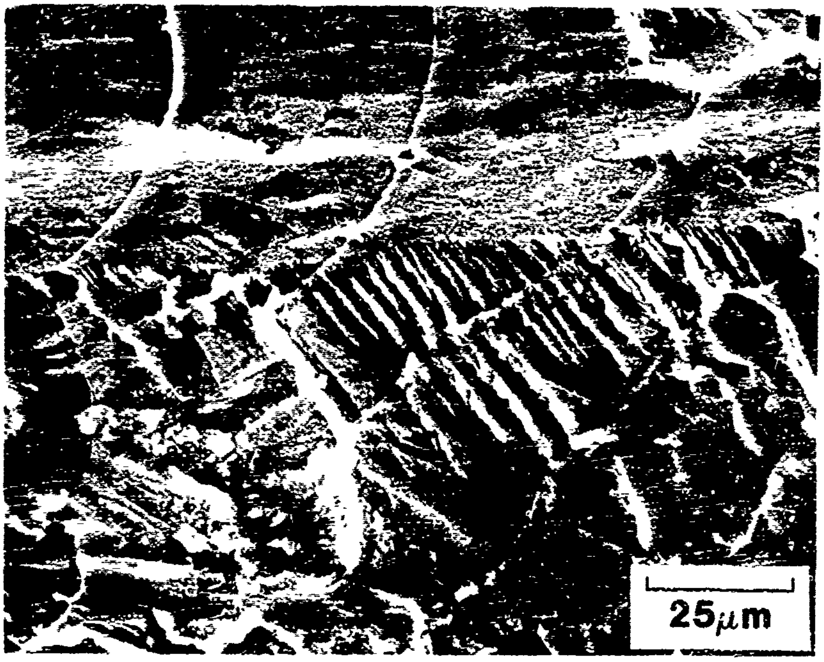

(b) SEM fractograph of fracture surface within circled area shown in (a)

Figure 53

Direction of
crack propagation

GA 16595

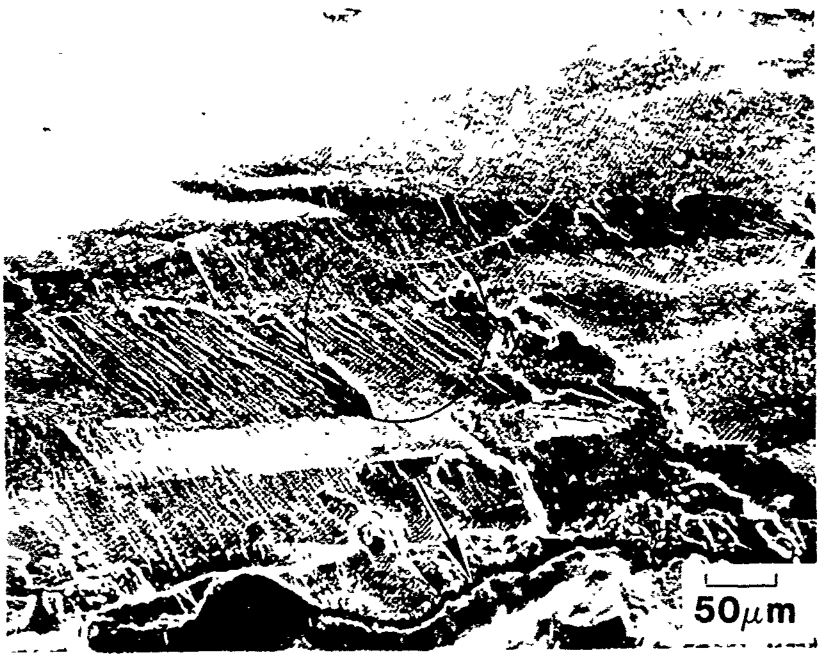

(a) SEM fractograph of OL fracture surface of CCT FCG specimen 548466-L-T-1 (Al - 2.9 Cu - 2.1 Li alloy T651 plate) at $\Delta K = 8$ MPa $\sqrt{m}$

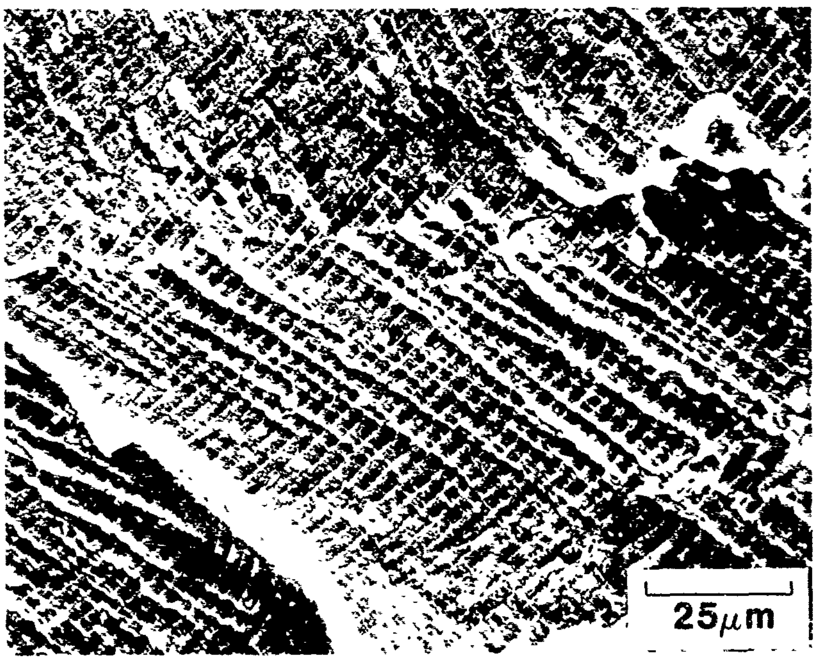

(b) SEM fractograph of fracture surface within circled area shown in (a)

Figure 54

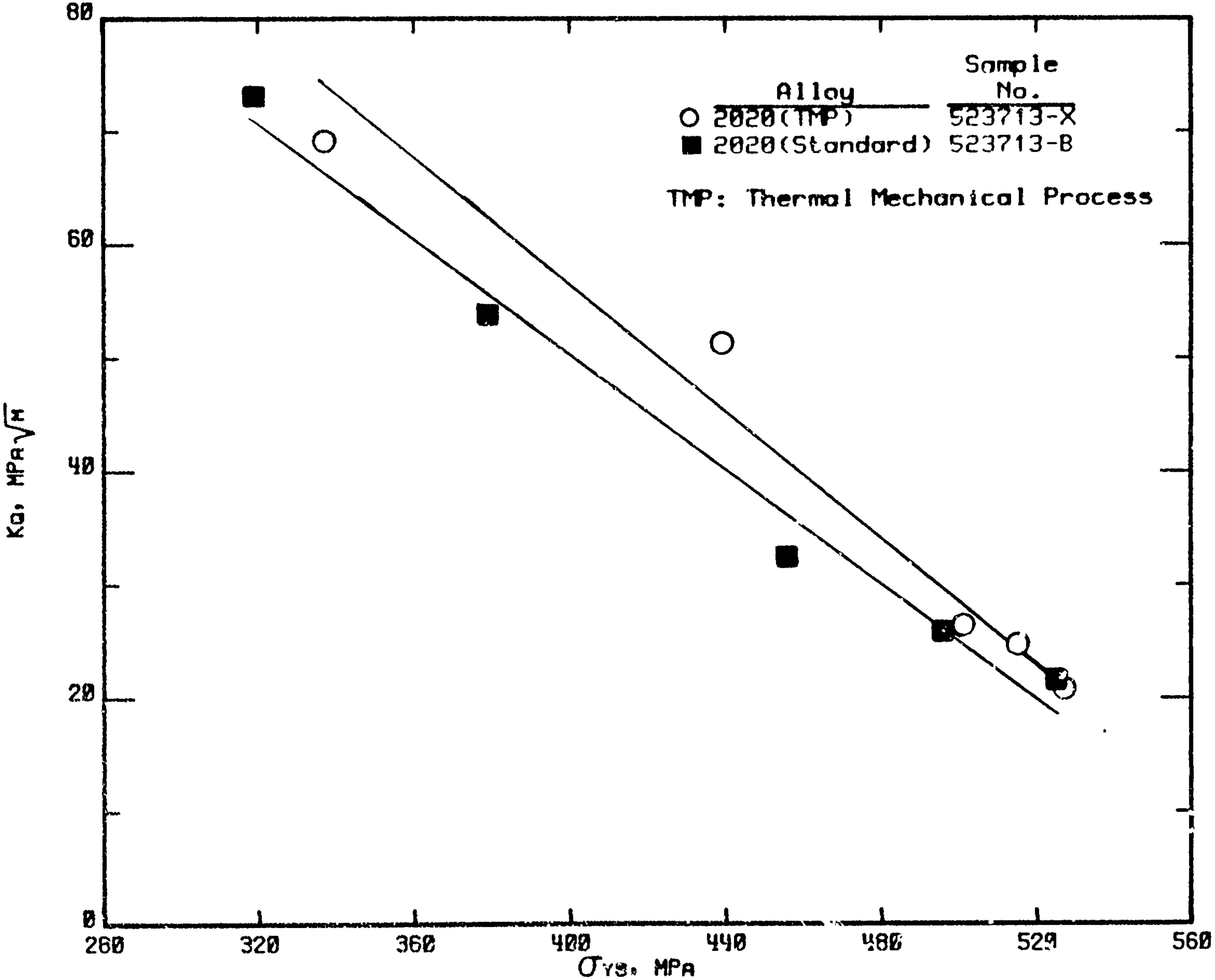

FRACTURE TOUGHNESS (KQ) VERSUS TENSILE YIELD STRENGTH (σ_{YS})
COMPARISON OF TMP 2020 AND STANDARD 2020 ALUMINUM ALLOYS.

Figure 55

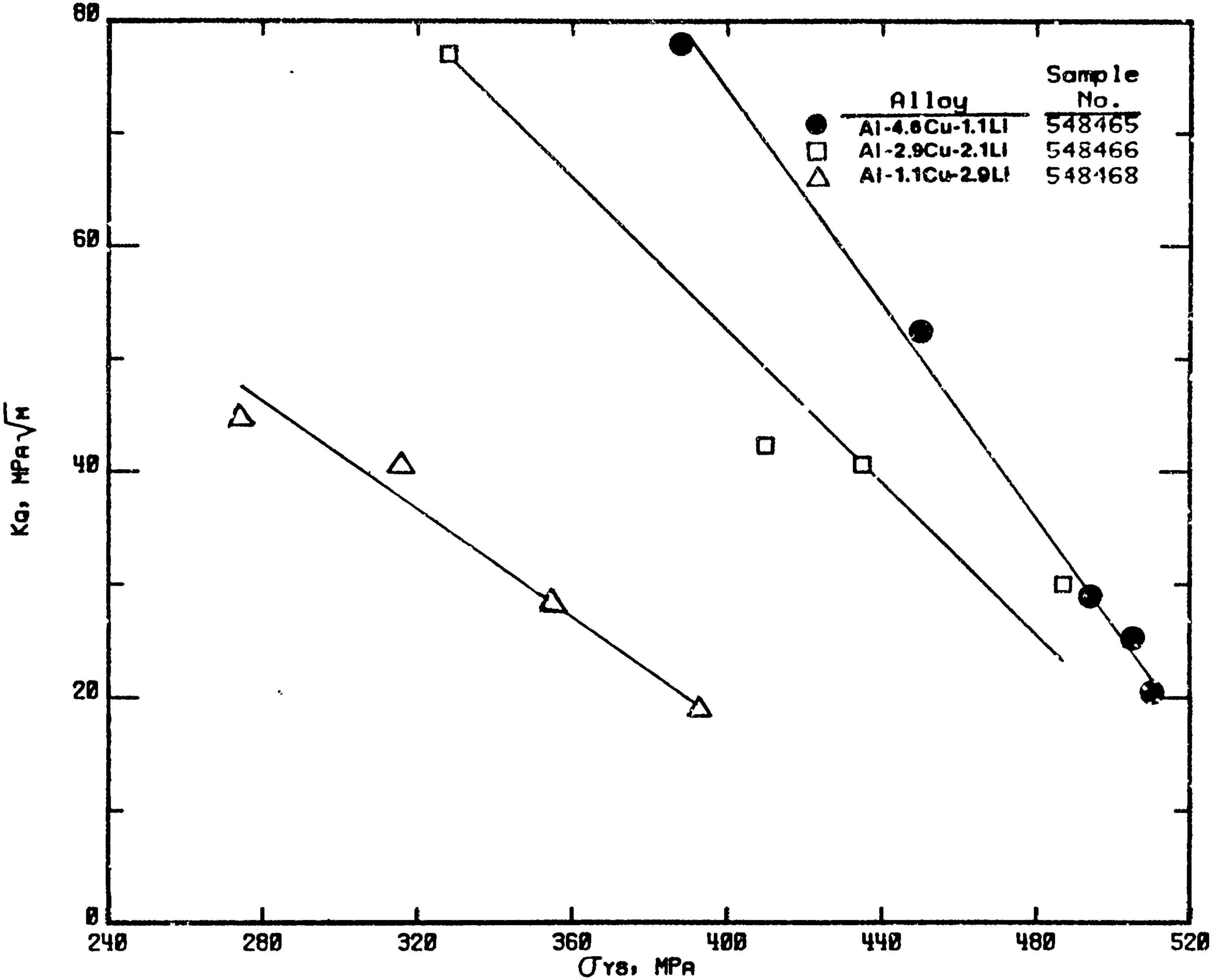

EFFECT OF CU AND LI CONTENT VARIATIONS ON THE FRACTURE TOUGHNESS (K_Q) VERSUS TENSILE YIELD STRENGTH (σ_{YS}) OF THREE AL-LI ALLOY SAMPLES (548465, 548466, 548468)

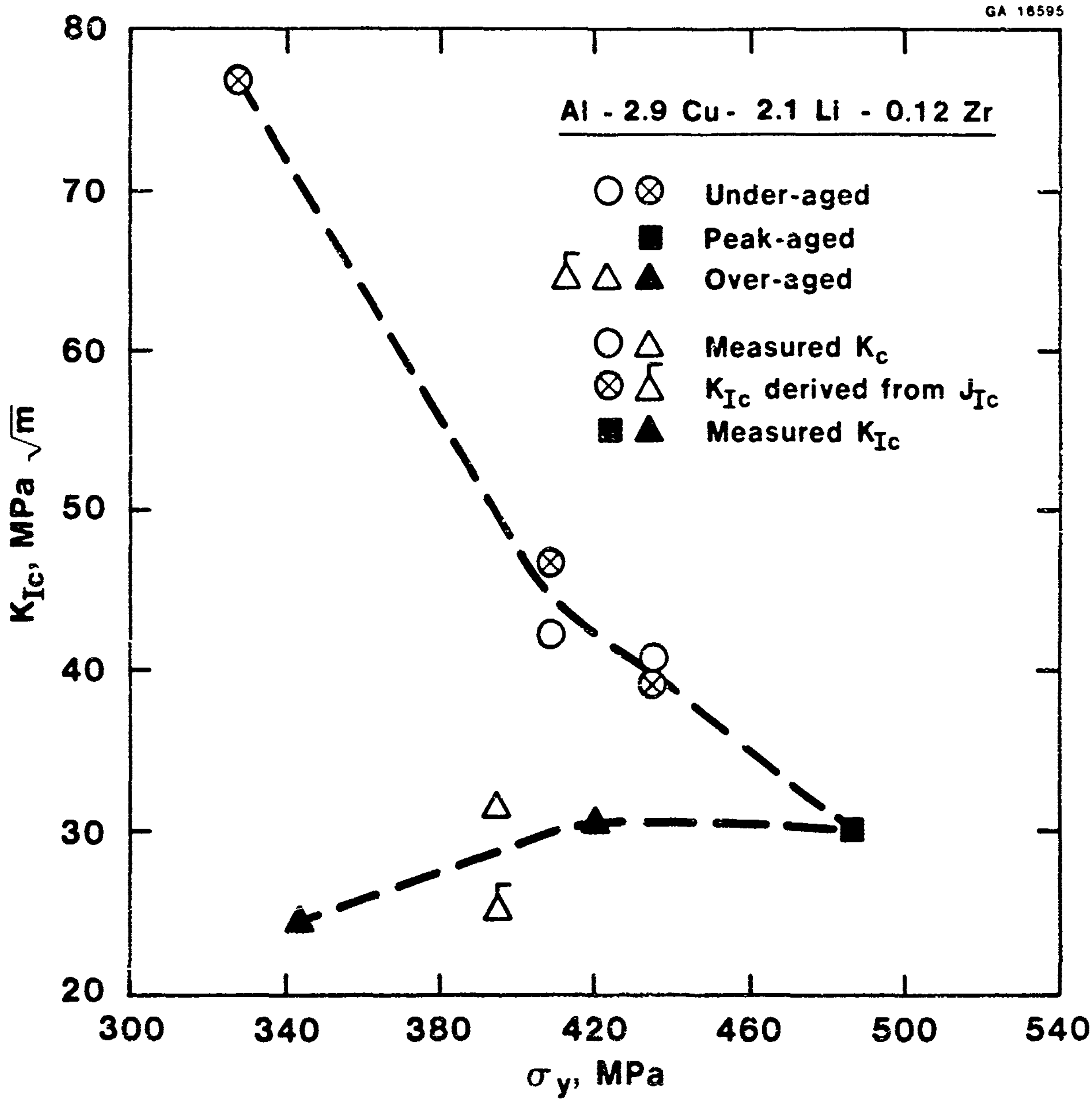

Variation of Nominal Mode I Fracture Toughness, K_{Ic}, with Tensile Yield Strength, σ_y, for the Microstructures Investigated.

Figure 57

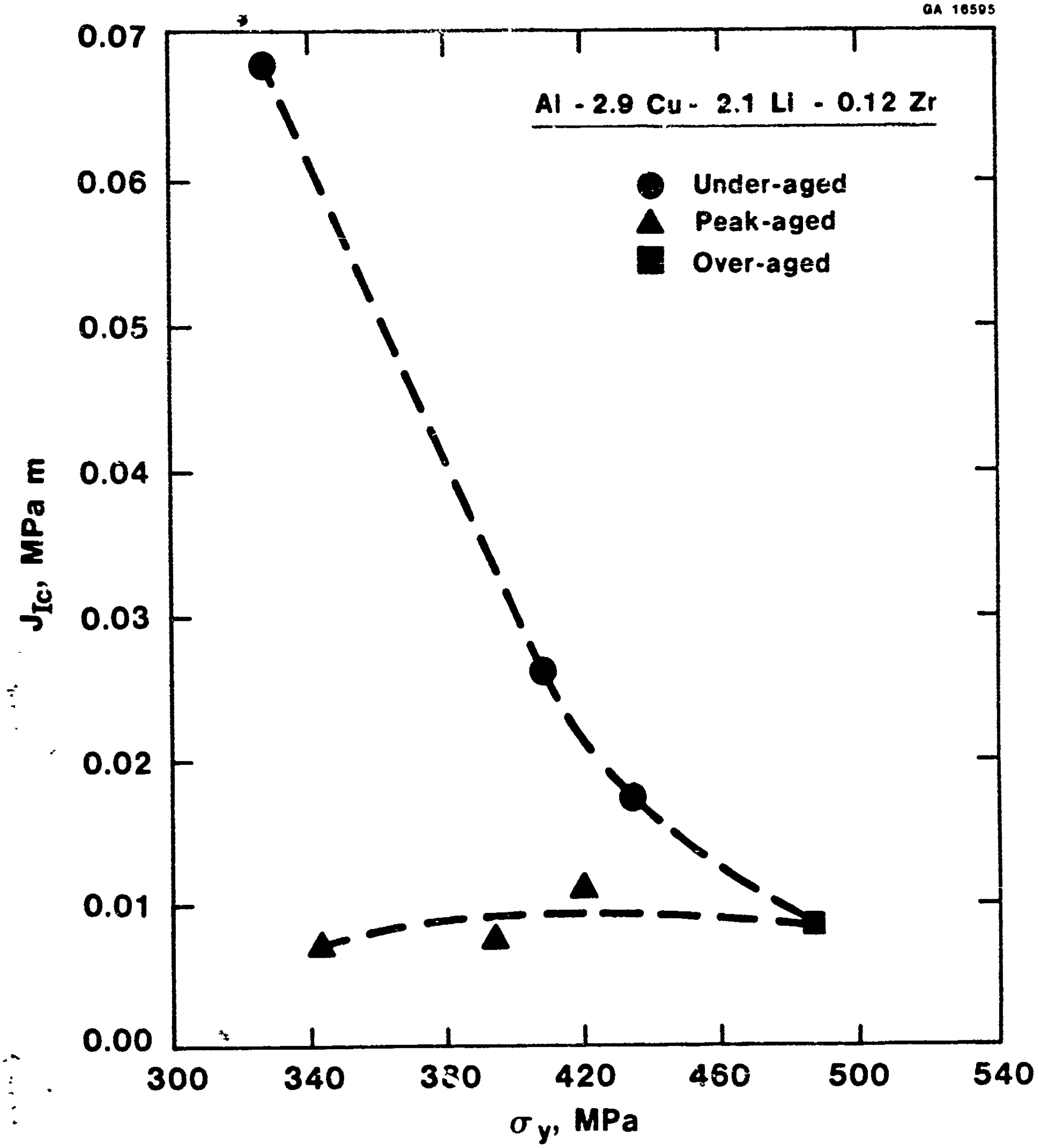

Variation of Nominal Elastic-Plastic Fracture Toughness, J_{Ic}, with Tensile Yield Strength, σ_y, for the Microstructures Investigated.

Figure 58

GA 16595

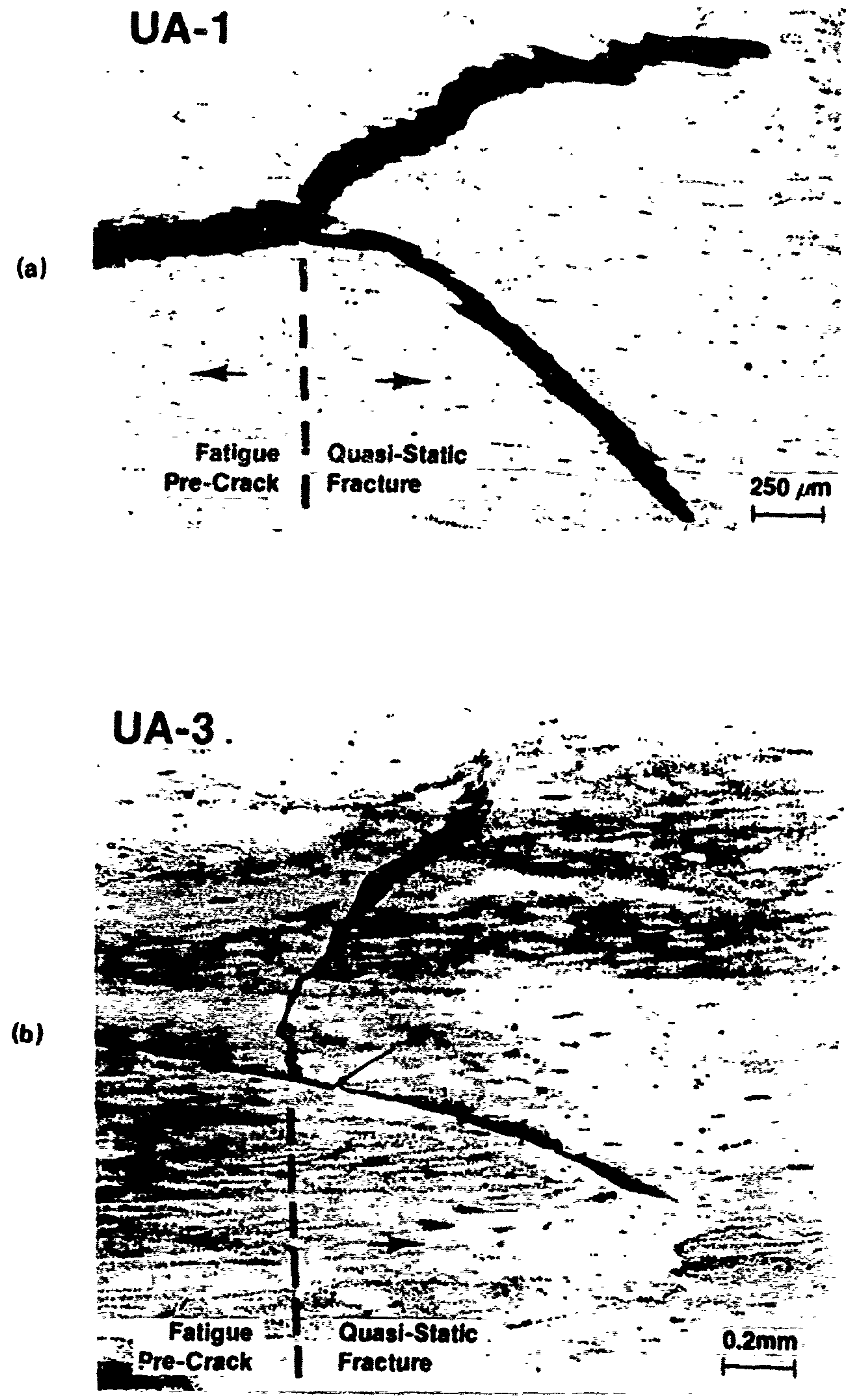

Crack profiles observed on the surfaces of 12.74 mm thick fracture test specimens from Al -2.9Cu -2.1Li alloy in the UA-1 (a) and UA-3 (b) temper conditions.

Figure 59

GA 16595

(a)

(b)

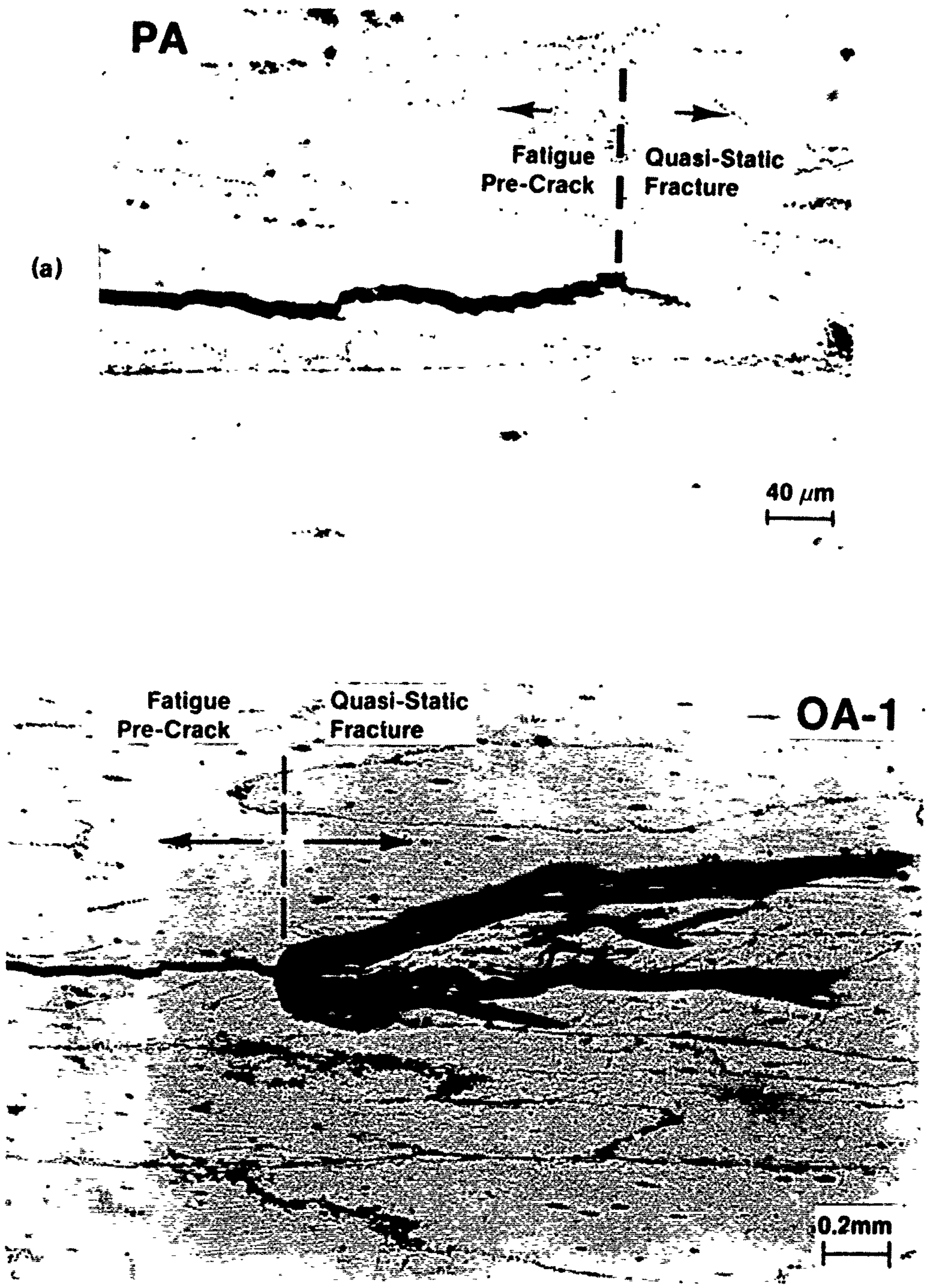

Crack profiles observed on the surfaces of 12.74 mm thick fracture test specimens from Al -2.9Cu -2.1Li alloy in the PA (a) and OA-1 (b) temper conditions. Note the shape of the plastic zone in (b).

Figure 60

GA 16595

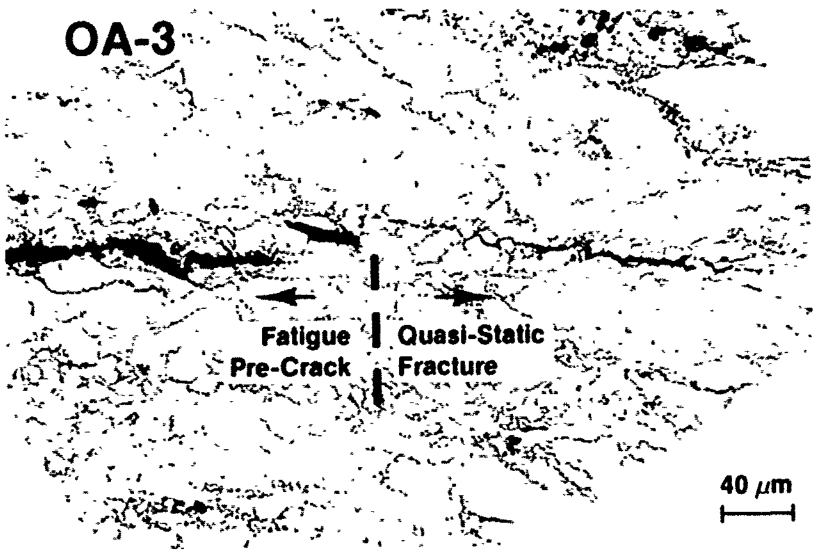

Crack profile observed on a surface of a 12.74 mm thick fracture test specimen from Al -2.9Cu -2.1Li alloy in the OA-3 temper condition.

Figure 61

(a)

(b)

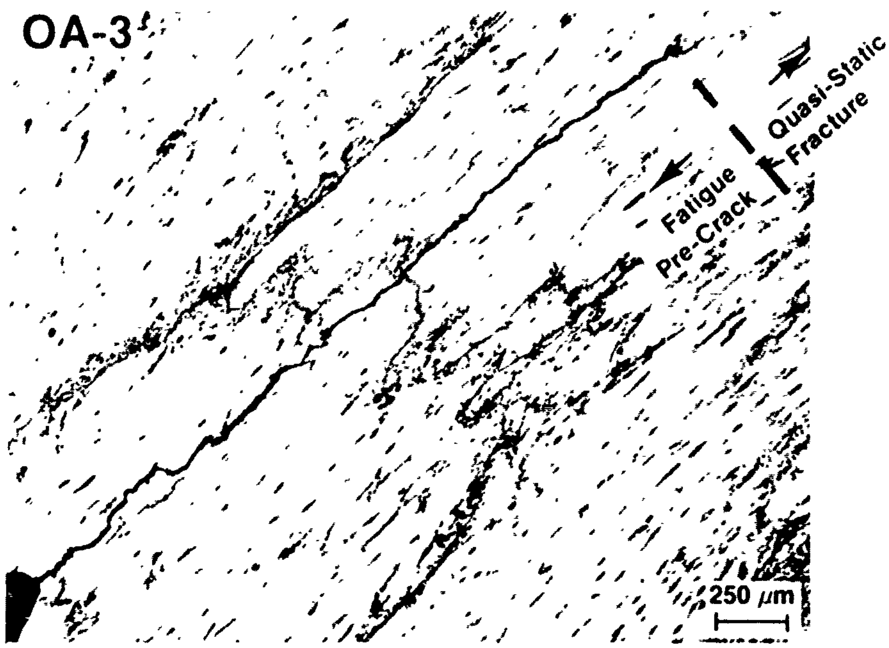

Crack profiles observed at center-thickness sections (6.37 mm from the surface) of 12.74 mm thick fracture test specimens from Al -2.9Cu -2.1Li alloy in the UA-1 (a) and OA-3 (b) temper conditions.

Figure 62

GA 16595

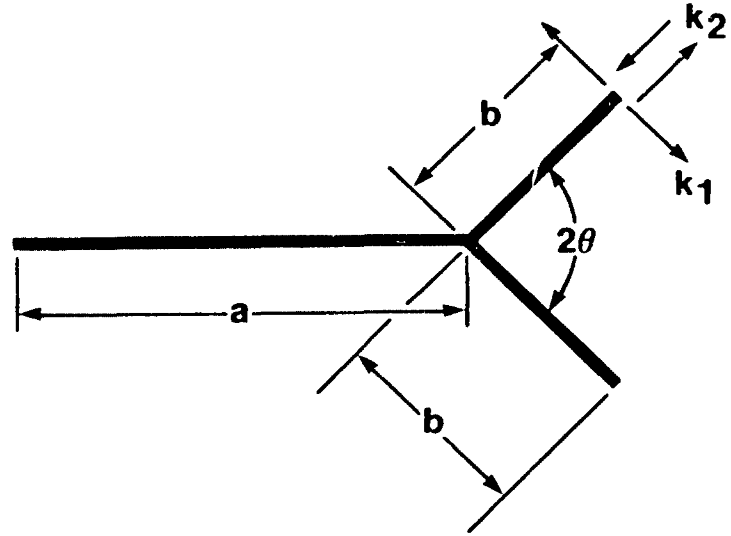

Schematic of a Forked Two Dimensional Crack with the Associated Nomenclature

Figure 63

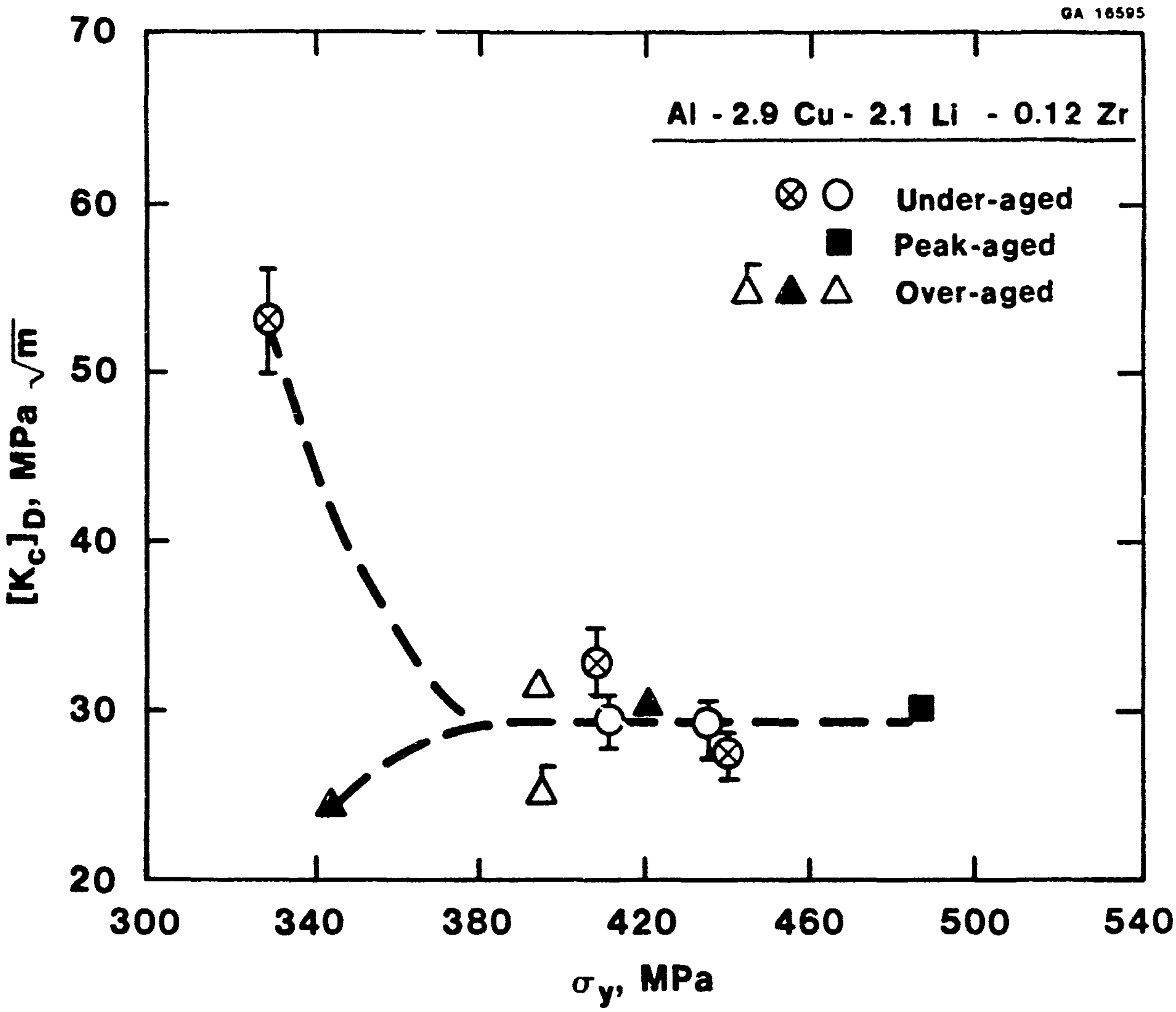

Variation of Deflection-Modified Fracture Toughness, $[K_c]_D$, with Tensile Yield Strength, σ_y, for the Microstructures Investigated

Figure 64

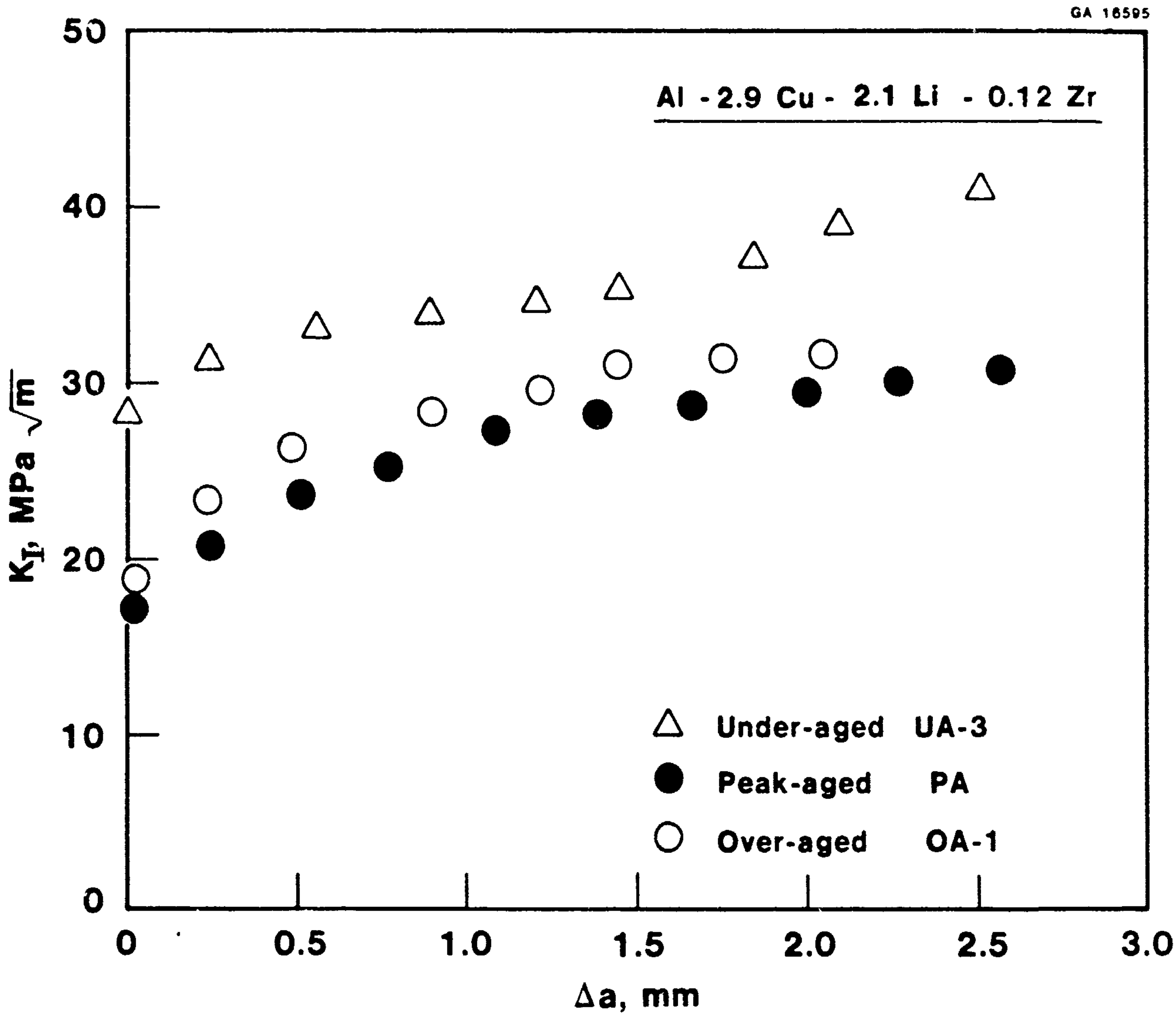

Variation of Nominal Mode I Stress-Intensity Factor, K_I, with Change in Crack Length, Δa, (R-Curve) for UA-3, PA and OA-1 Tempers.

Figure 65

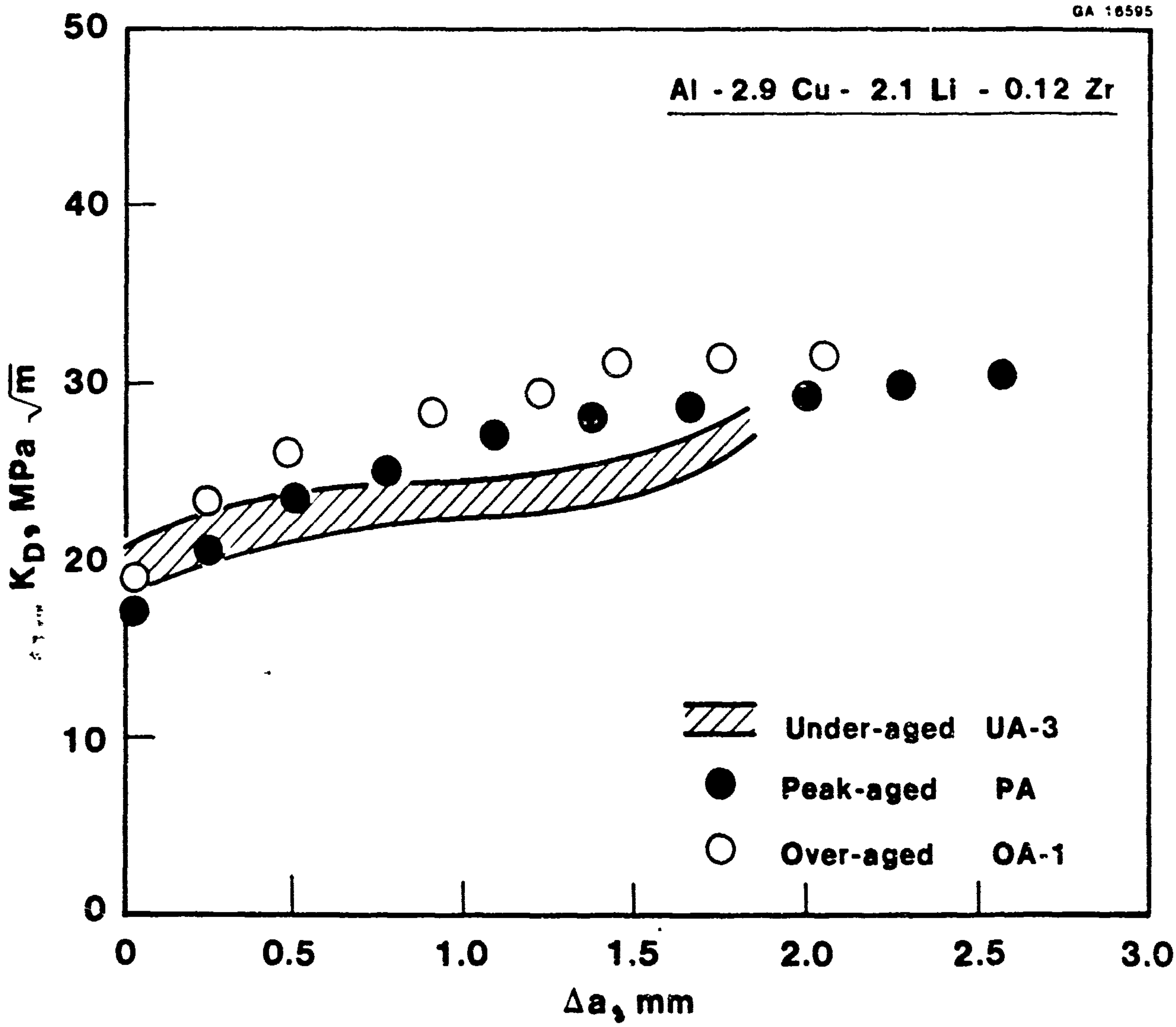

Variation of Deflection-Modified Effective Stress-Intensity Factor, K_D, with Change in Crack Length, Δa, (modified R-Curve) for UA-3, PA and OA-1 Tempers

Figure 66

GA 16595

(a)

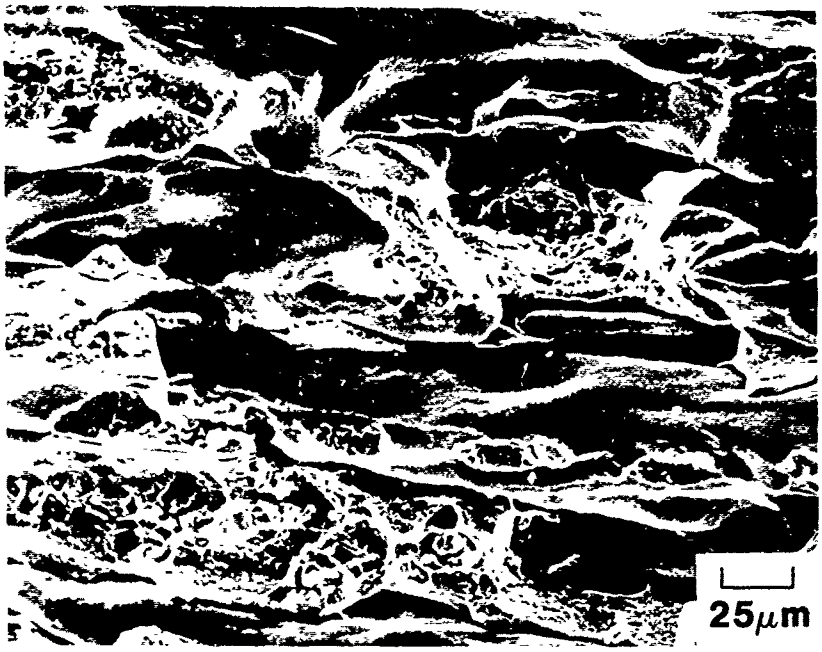

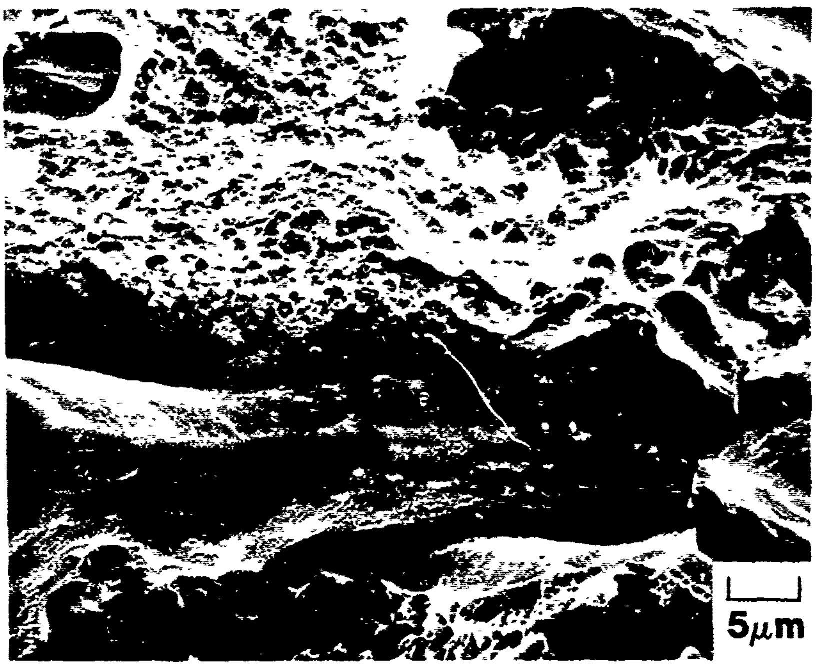

SEM fractographs of a static fracture surface of a fracture toughness specimen from 2020 plate sample 523713-B (peak aged)

Figure 67

GA 16595

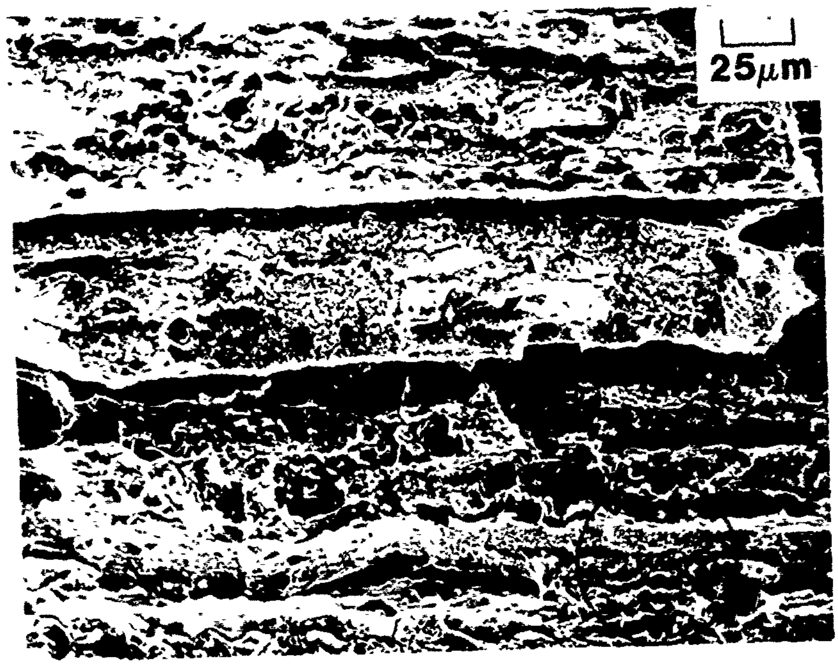

(a) SEM fractograph of a static fracture surface of a fracture toughness specimen from TMP 2020 plate sample 523713-X (peak aged)

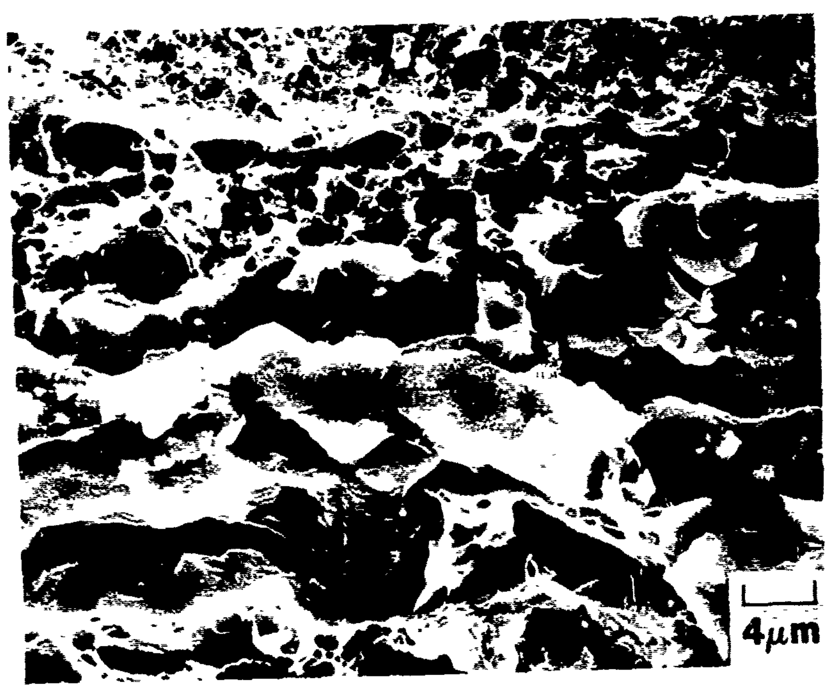

(b) SEM fractograph of fracture surface within circled area shown in (a)

Figure 68

GA 16595

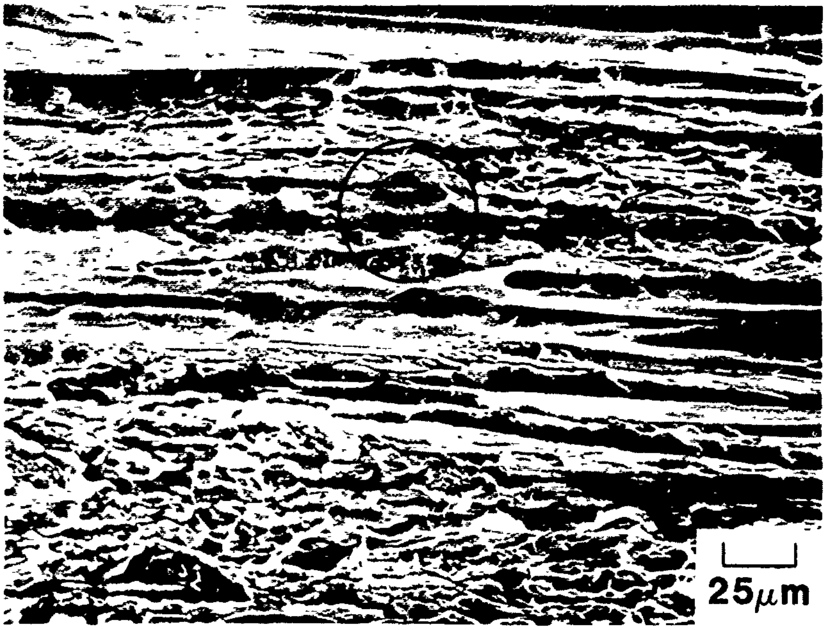

(a) SEM fractograph of a static fracture surface of a fracture toughness specimen from Al - 4.6 Cu - 1.1 Li alloy plate sample 548465 (peak aged)

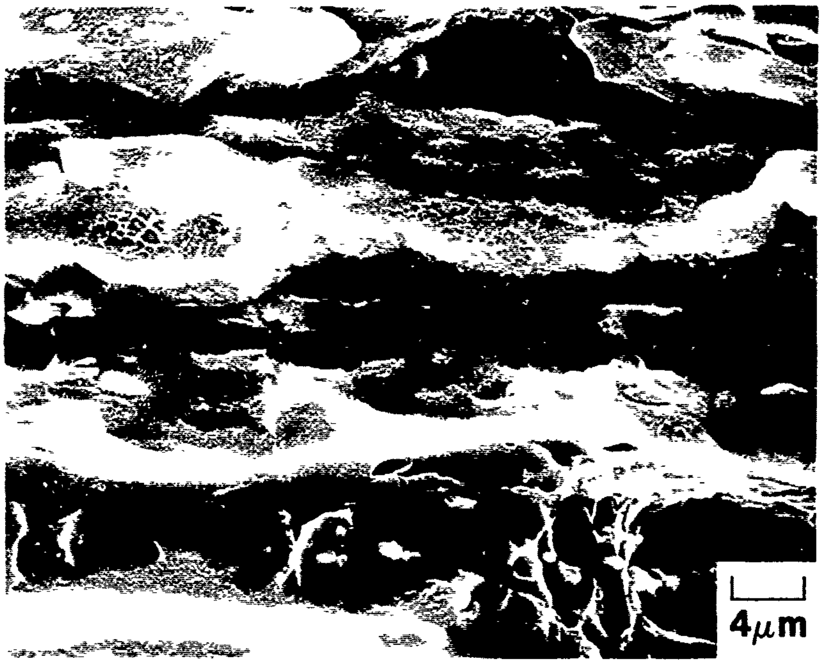

(b) SEM fractograph of fracture surface within circled area shown in (a)

Figure 69

GA 16595

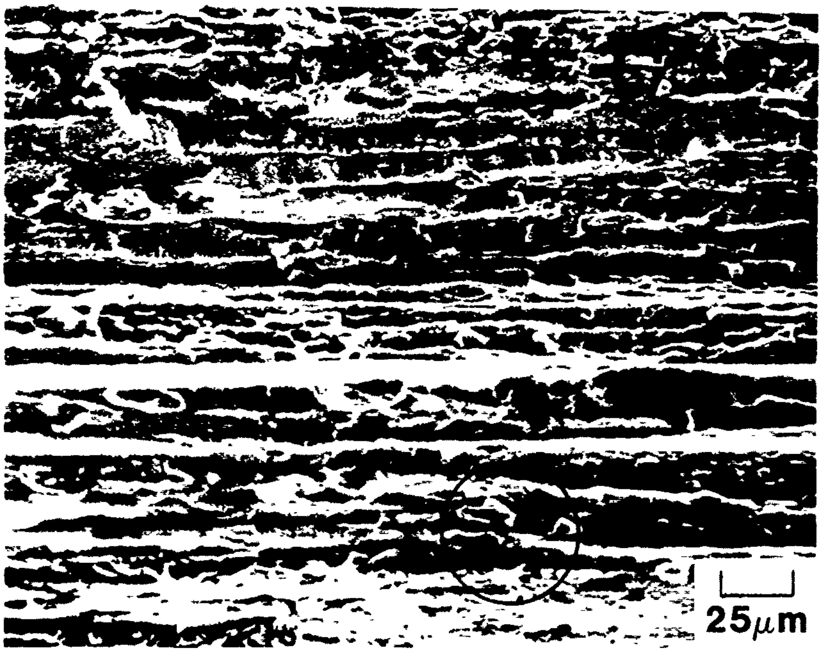

(a) SEM fractograph of a static fracture surface of a fracture toughness specimen from Al -1.1Cu -2.9Li alloy plate sample 548468 (peak aged 50 h/191°C)

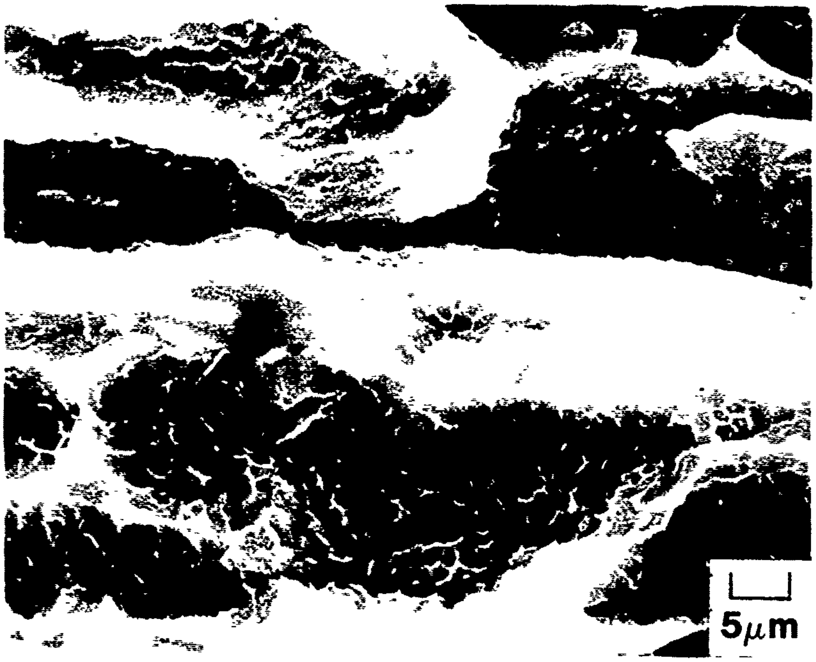

(b) SEM fractograph of fracture surface within circled area shown in (a)

Figure 70

GA 16595

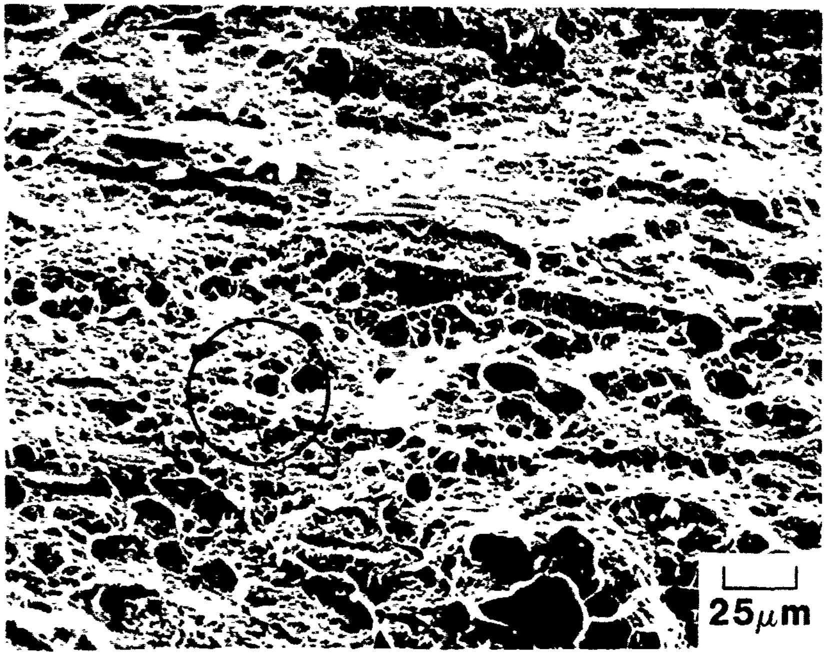

(a) SEM fractograph of a static fracture surface of a fracture toughness specimen from Al -2.9Cu -2.1Li alloy plate sample 548466 (aged 1.25 h/191°C)

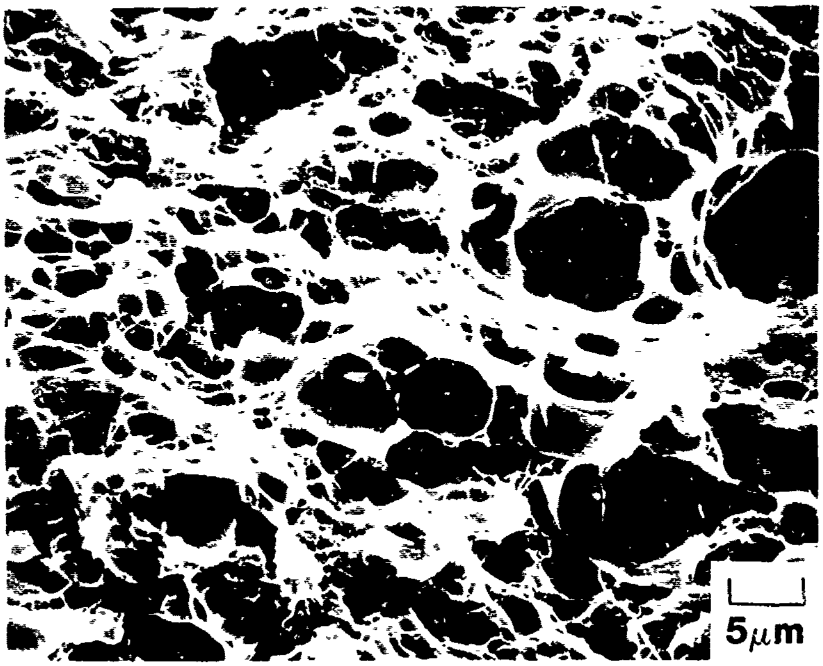

(b) SEM fractograph of fracture surface within circled area shown in (a)

Figure 71

GA 16595

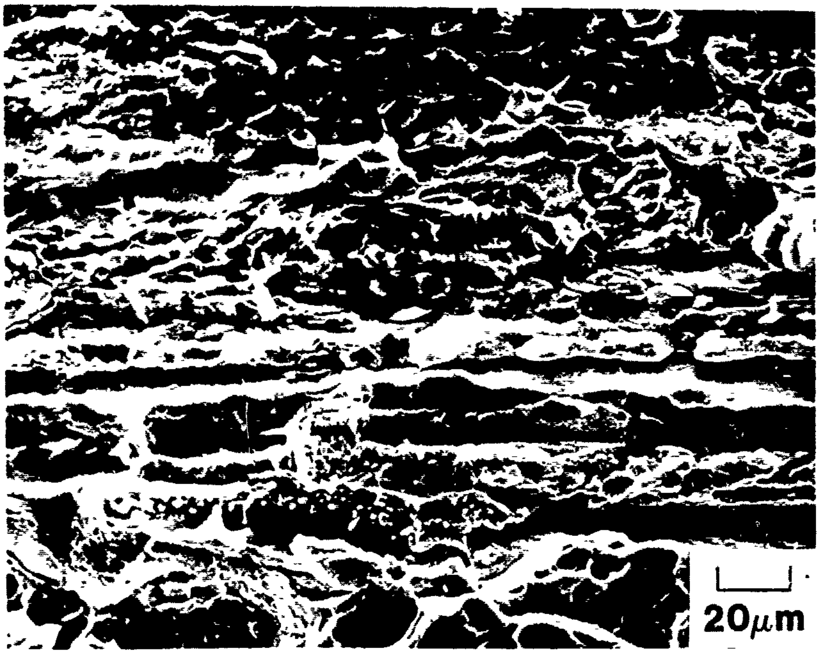

(a) SEM fractograph of a static fracture surface of a fracture toughness specimen from Al -2.9Cu -2.1Li alloy plate sample 548466 (aged 2.25 h/191°C)

(b) SEM fractograph of fracture surface within circled area shown in (a)

Figure 72

GA 16595

(a)
Peak aged
16 h/191°C

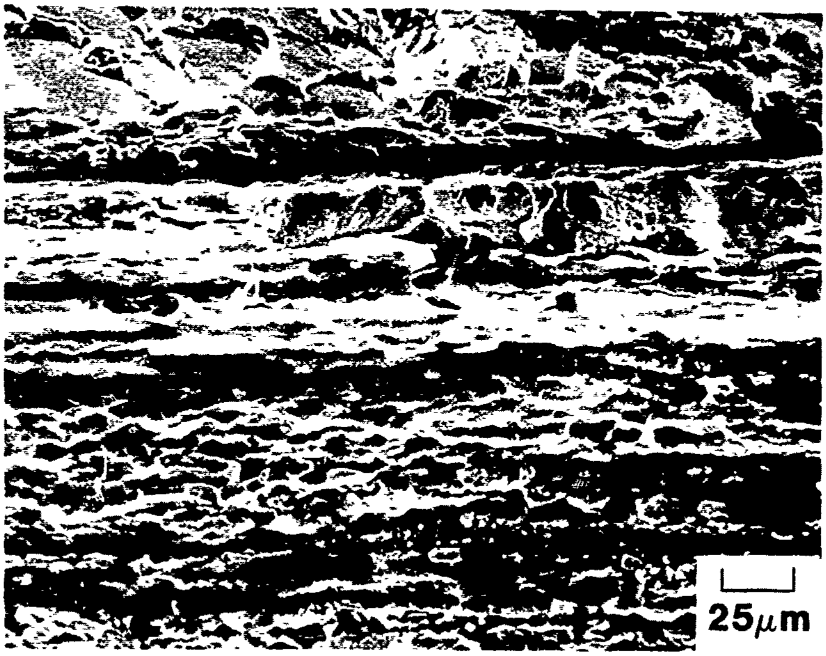

(b)
Overaged
70 h/191°C

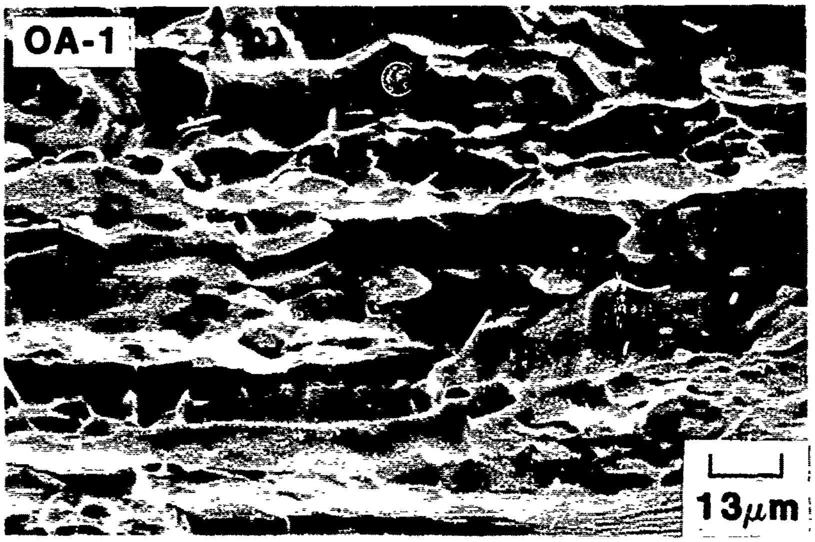

SEM fractographs of static fracture surfaces of fracture toughness specimens from peak aged (a) and overaged (b) sample 548466 (Al -2.9Cu -2.1Li alloy plate)

Figure 73

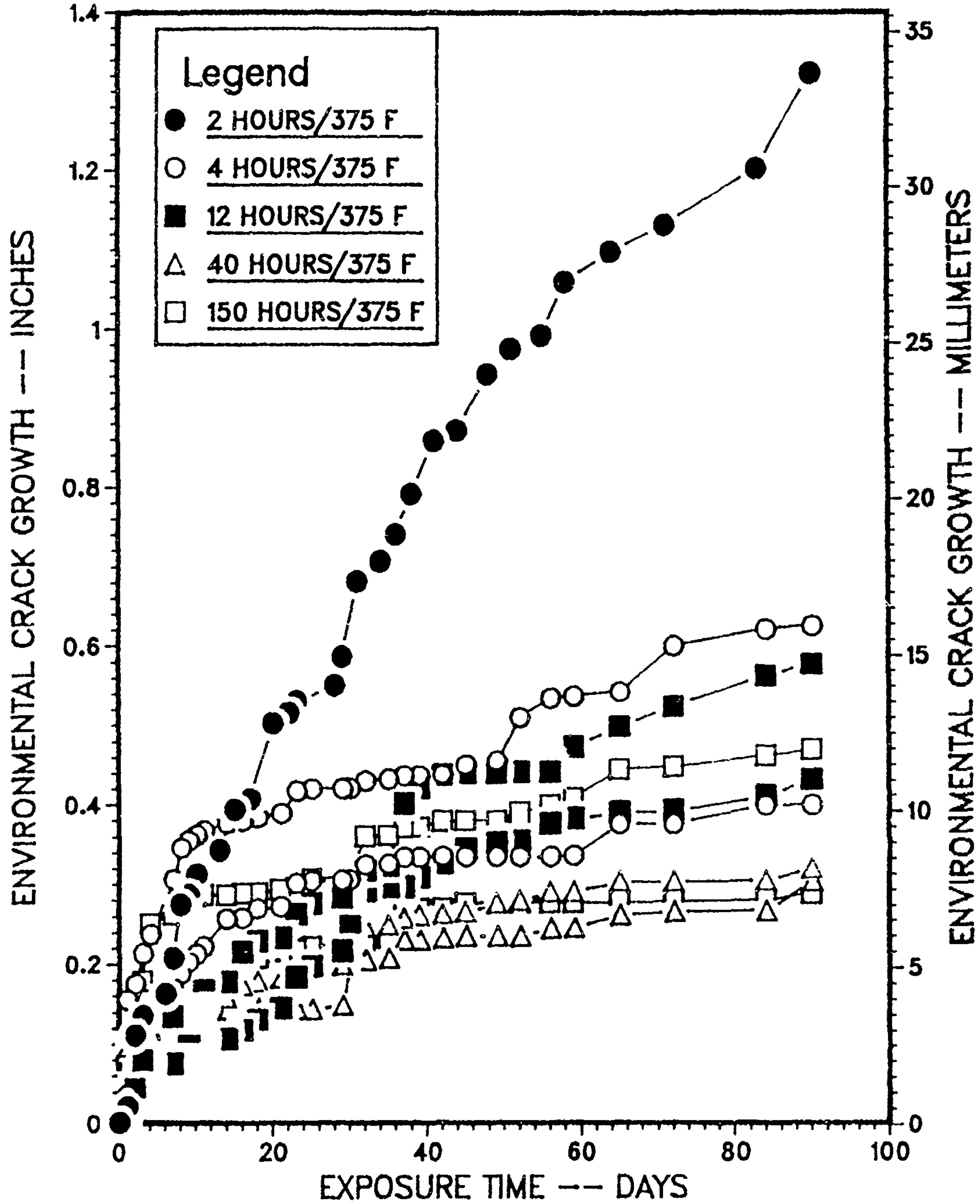

Crack growth vs. exposure time data for various aging treatments of sample 548466 (Al-2.9Cu-2.1Li-0.12Zr alloy)

Figure 74

GA 16595

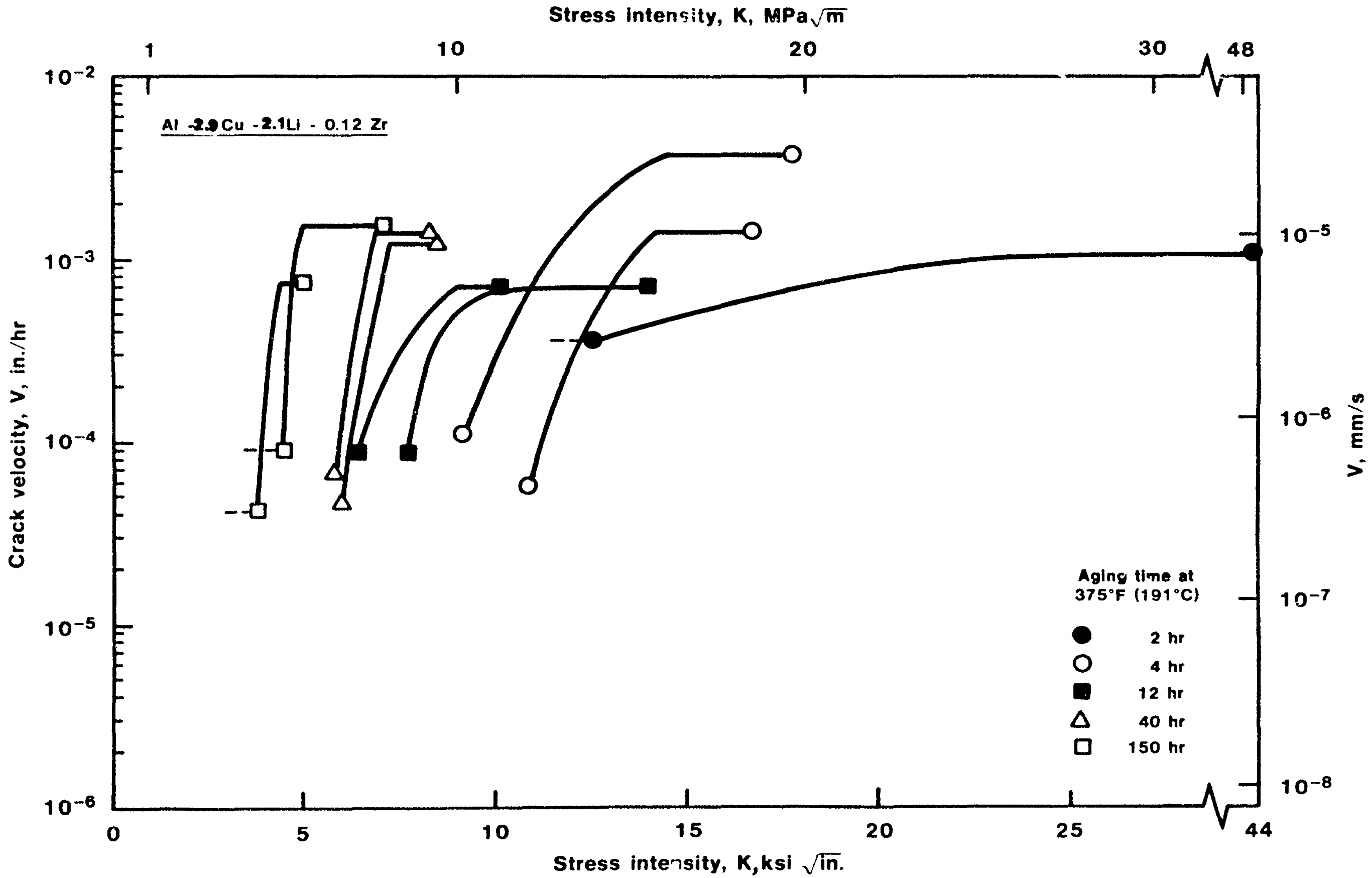

SCC Velocity vs. Stress Intensity Data for Sample 548466 at Various Aging Conditions

Figure 75

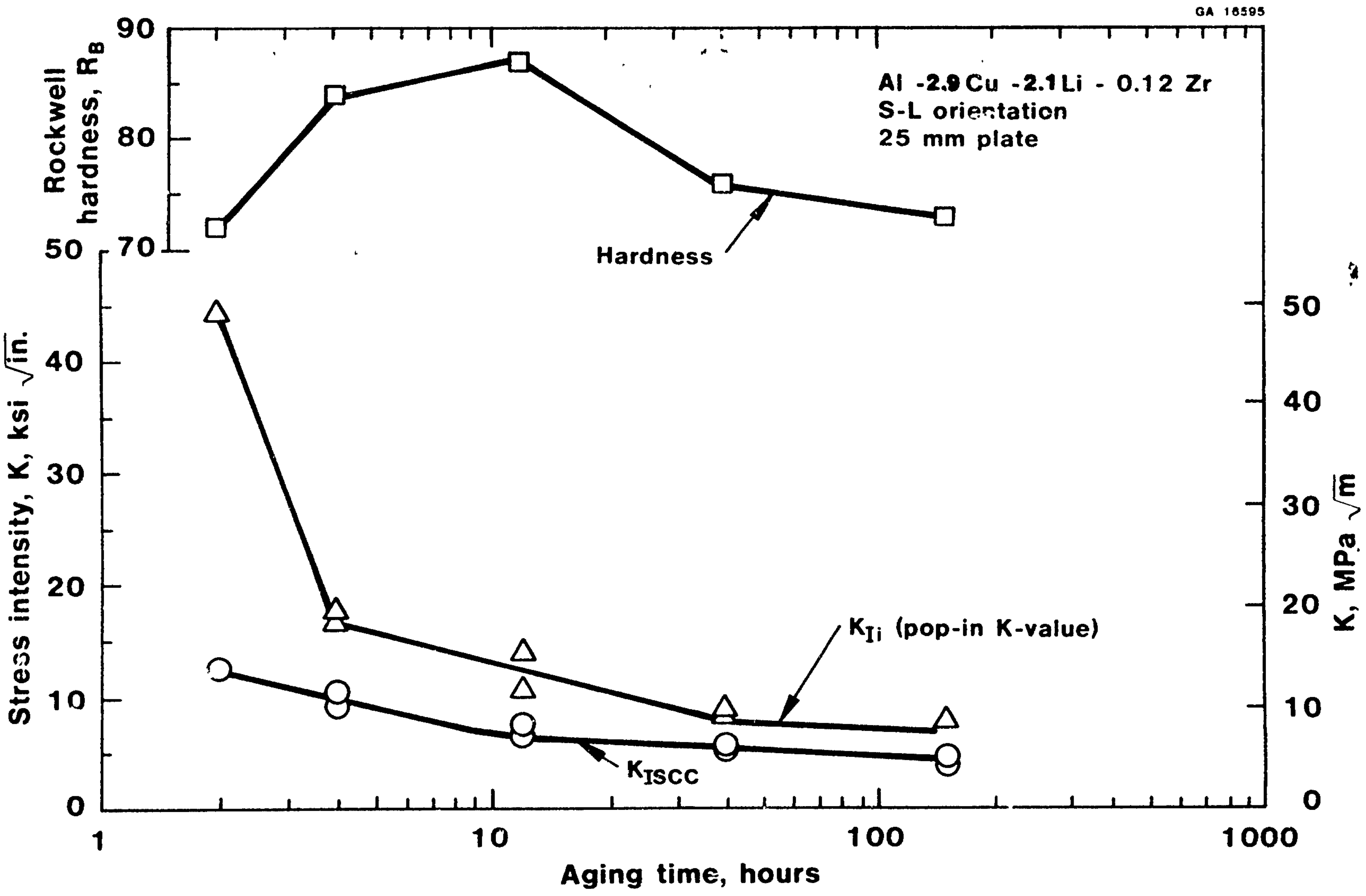

Variation of Hardness, K_{ISCC} and K_{Ii} with Aging Time at 375°F (191°C)

Figure 76

GA 16595

Average environmental crack growth for various S-L DCB specimens removed from various thickness plates and exposed to 3.5% NaCl solution dropwise for 30 days

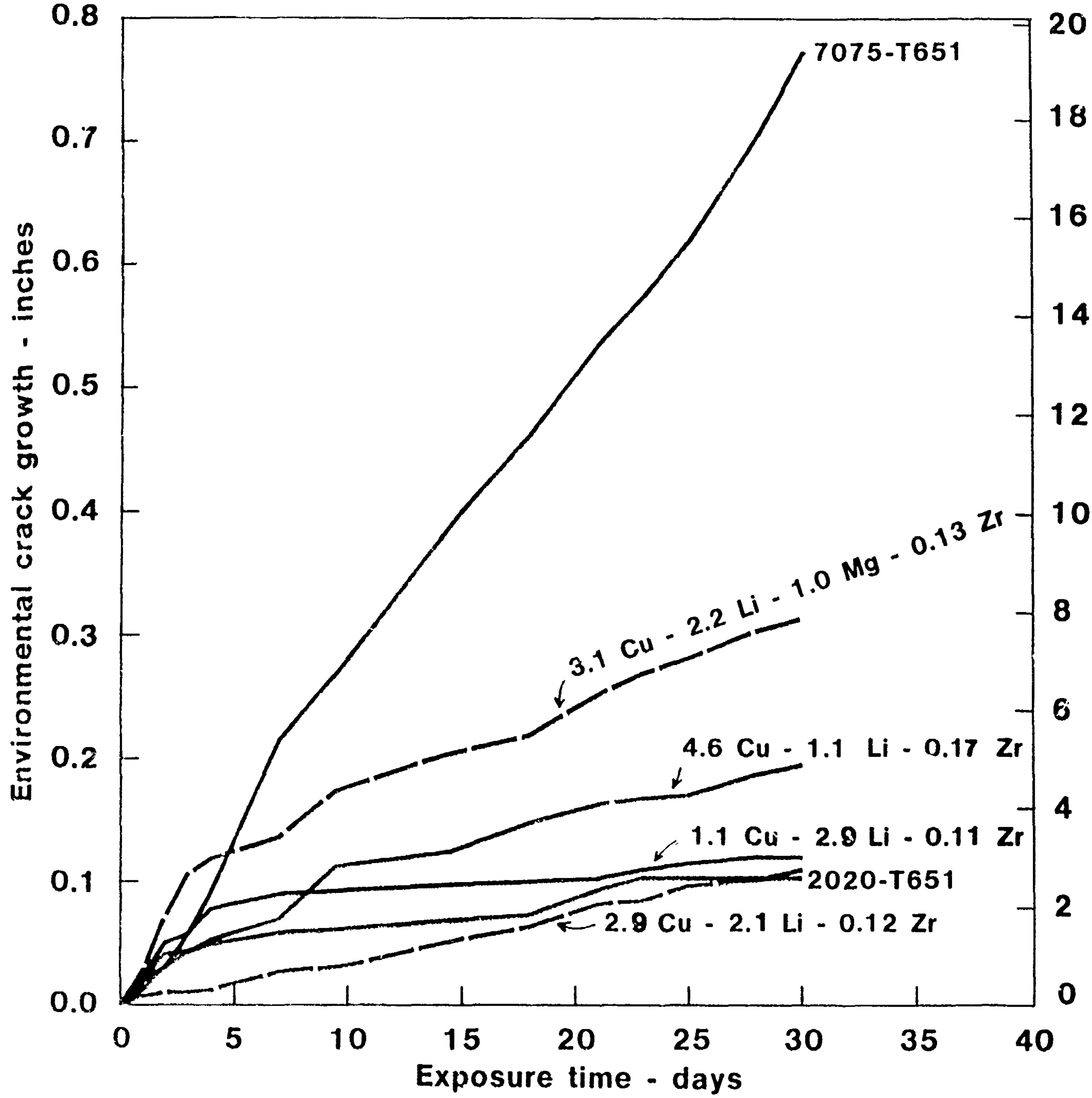

Crack Growth vs. Exposure Time Data for Various Compositions of Al-Cu-Li-Zr Alloys

Figure 77

GA 16595

Estimated K-rate curves for various alloy specimens removed from various thickness plates and exposed to 3.5% NaCl solution dropwise for 30 days

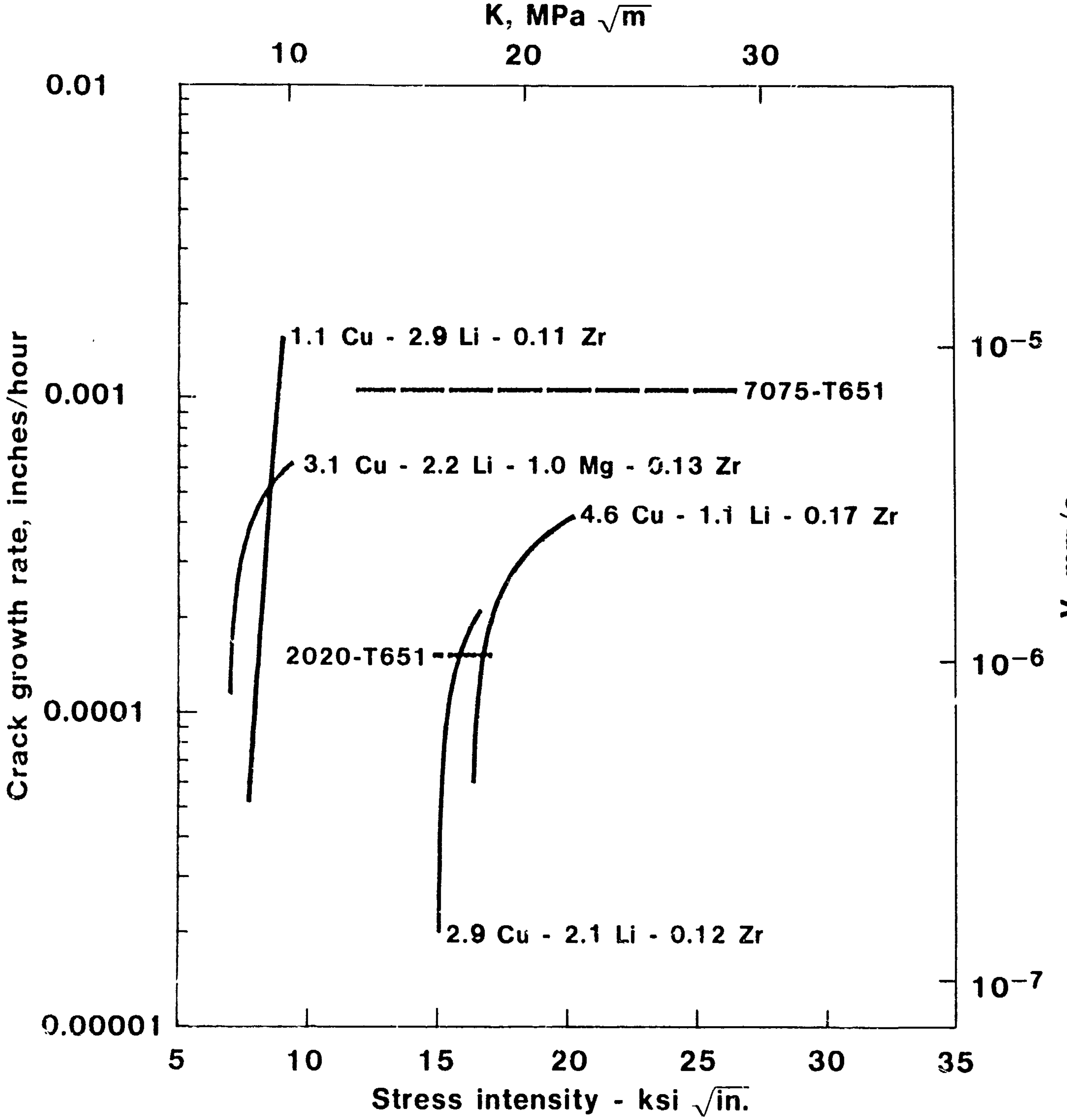

SCC Velocity vs. Stress Intensity Data for Various Compositions of Al-Cu-Li-Zr Alloys

Figure 78

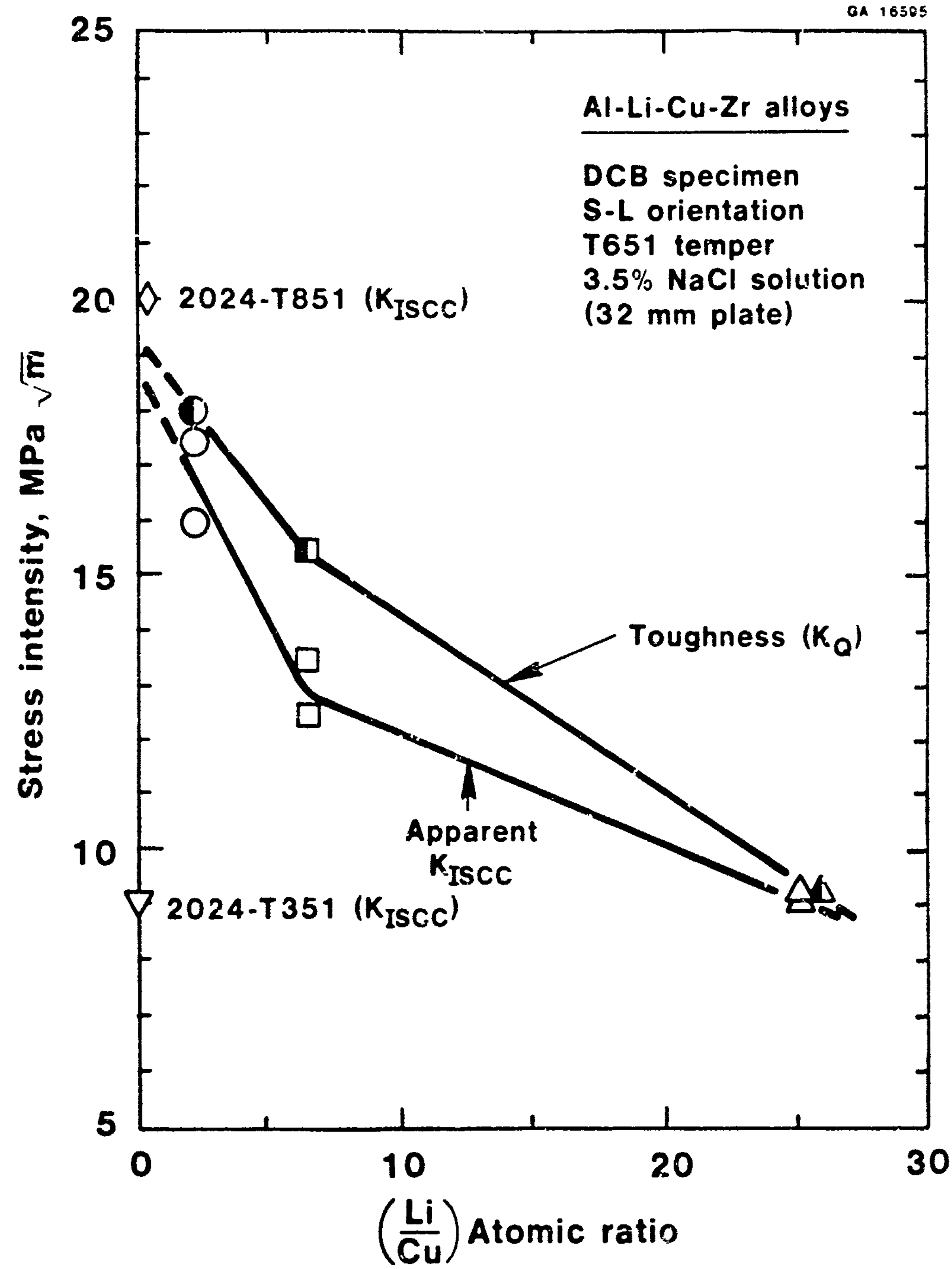

K_{ISCC} and K_Q Toughness Variations with Li/Cu Ratio in T651 Temper

Figure 79

GA 16595

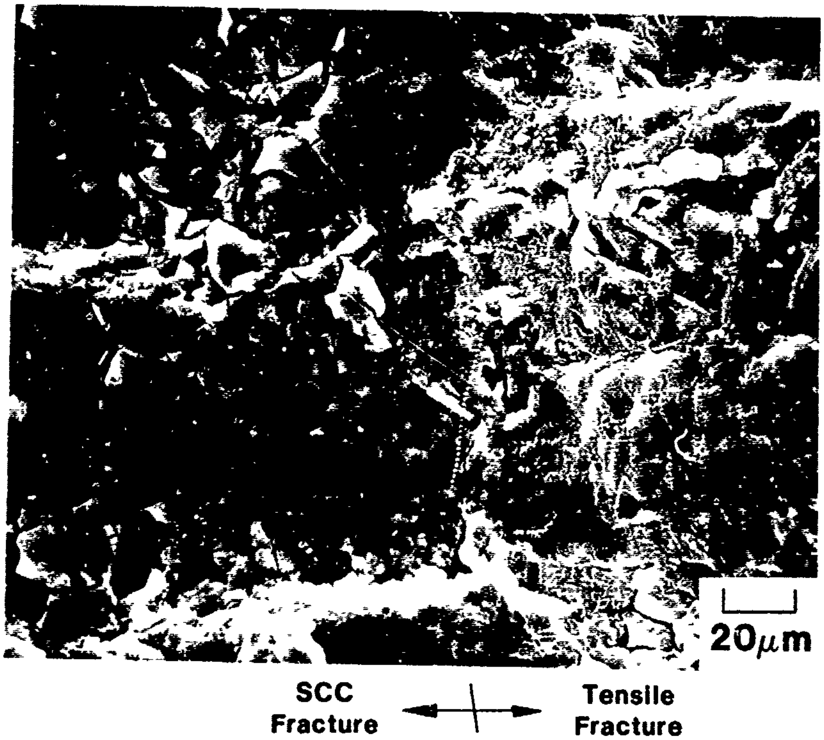

(a) SEM fractograph of a fracture surface of a DCB SCC specimen from sample 548465 (Al - 4.6 Cu - 1.1 Li alloy T651 plate)

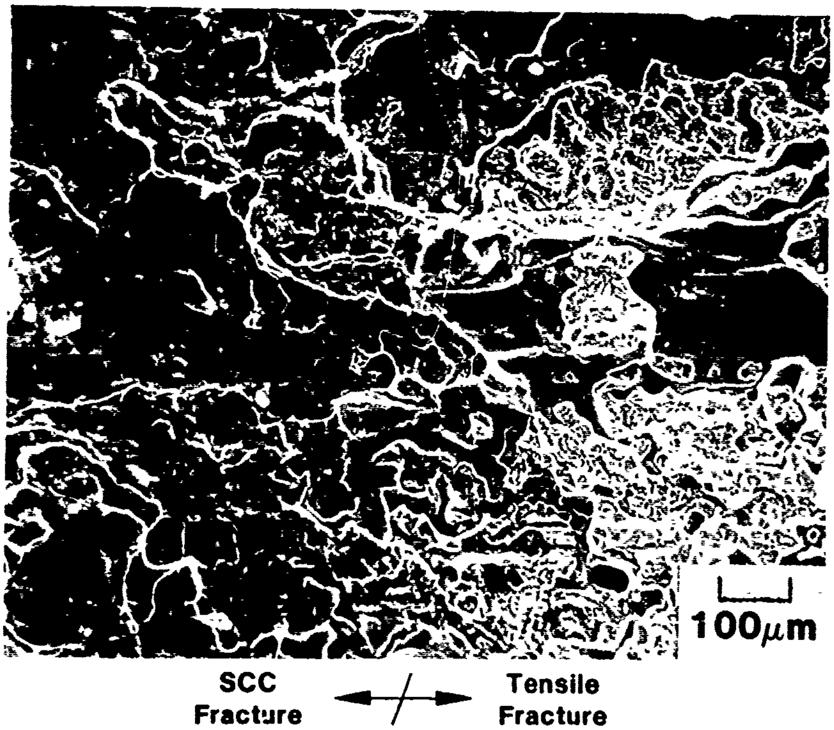

(b) SEM fractograph of a fracture surface of a DCB SCC specimen from alloy 2020-T651 plate

Figure 80

GA 16595

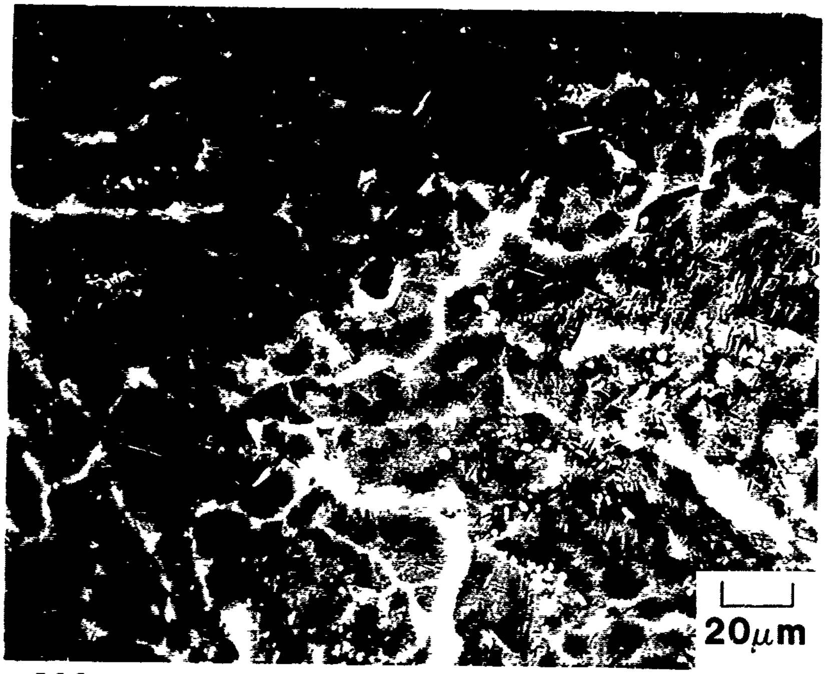

(a) SEM fractograph of a fracture surface of a DCB SCC specimen from sample 548466 (Al -2.9Cu-2.1Li alloy T651 plate)

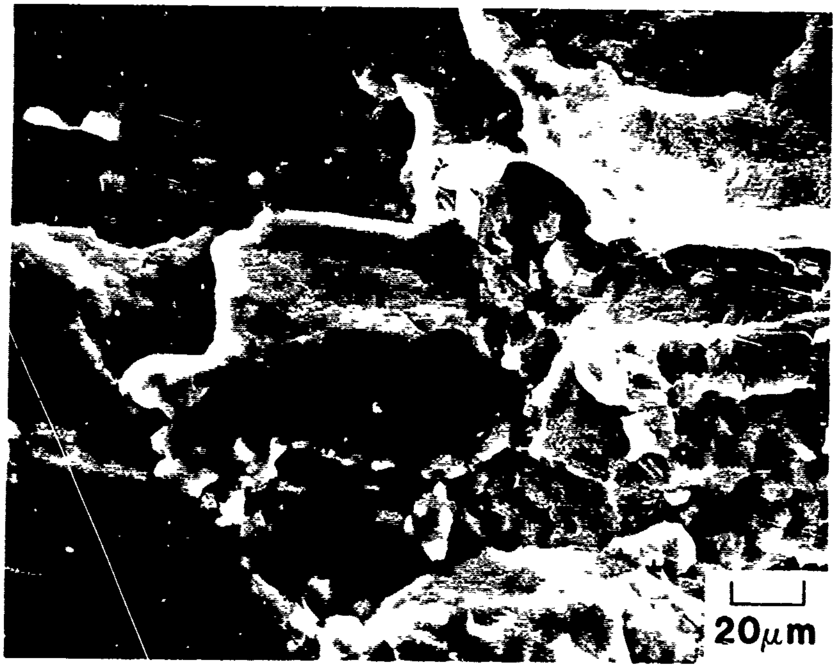

(b) SEM fractograph of a fracture surface of a DCB SCC specimen from sample 504440 (Al -3.1Cu-2.2Li - 1 Mg alloy T651 plate)

Figure 81

GA 16595

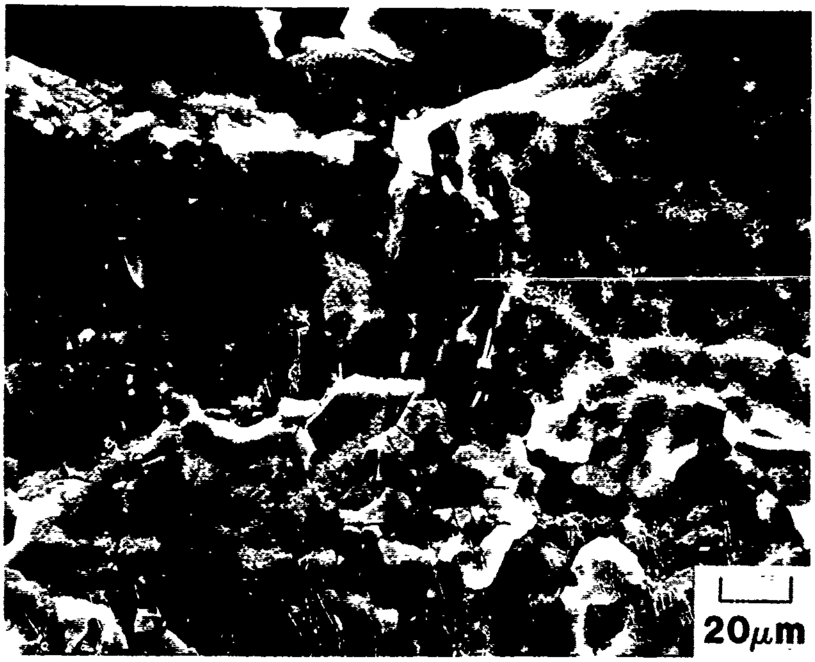

SCC Fracture ⟷ Tensile Fracture

(a) SEM fractograph of a fracture surface of a DCB SCC specimen from sample 548468 (Al -1.1Cu-2.9Li alloy T651 plate)

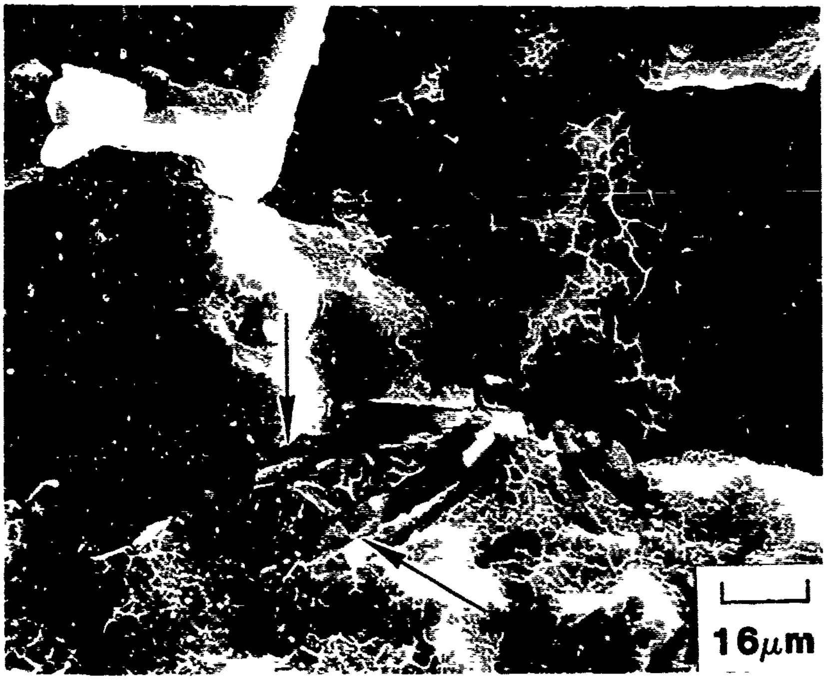

arrows: Al_7Cu_2Fe

(b) SEM fractograph of tensile fracture surface of specimen referenced in (a)

Figure 82

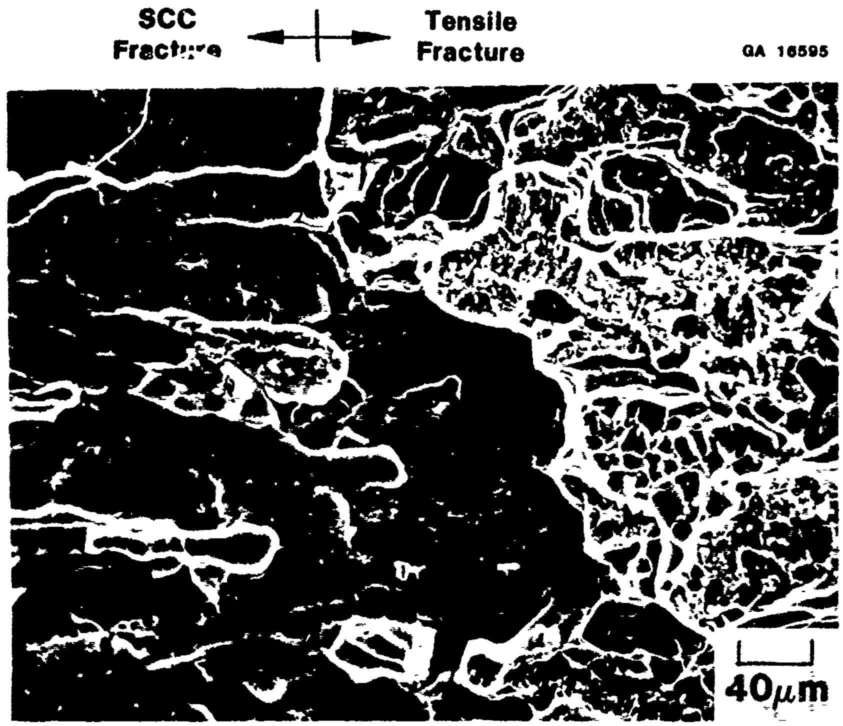

SEM fractograph of a fracture surface of a DCB SCC specimen from alloy 7075-T651 plate

Figure 83

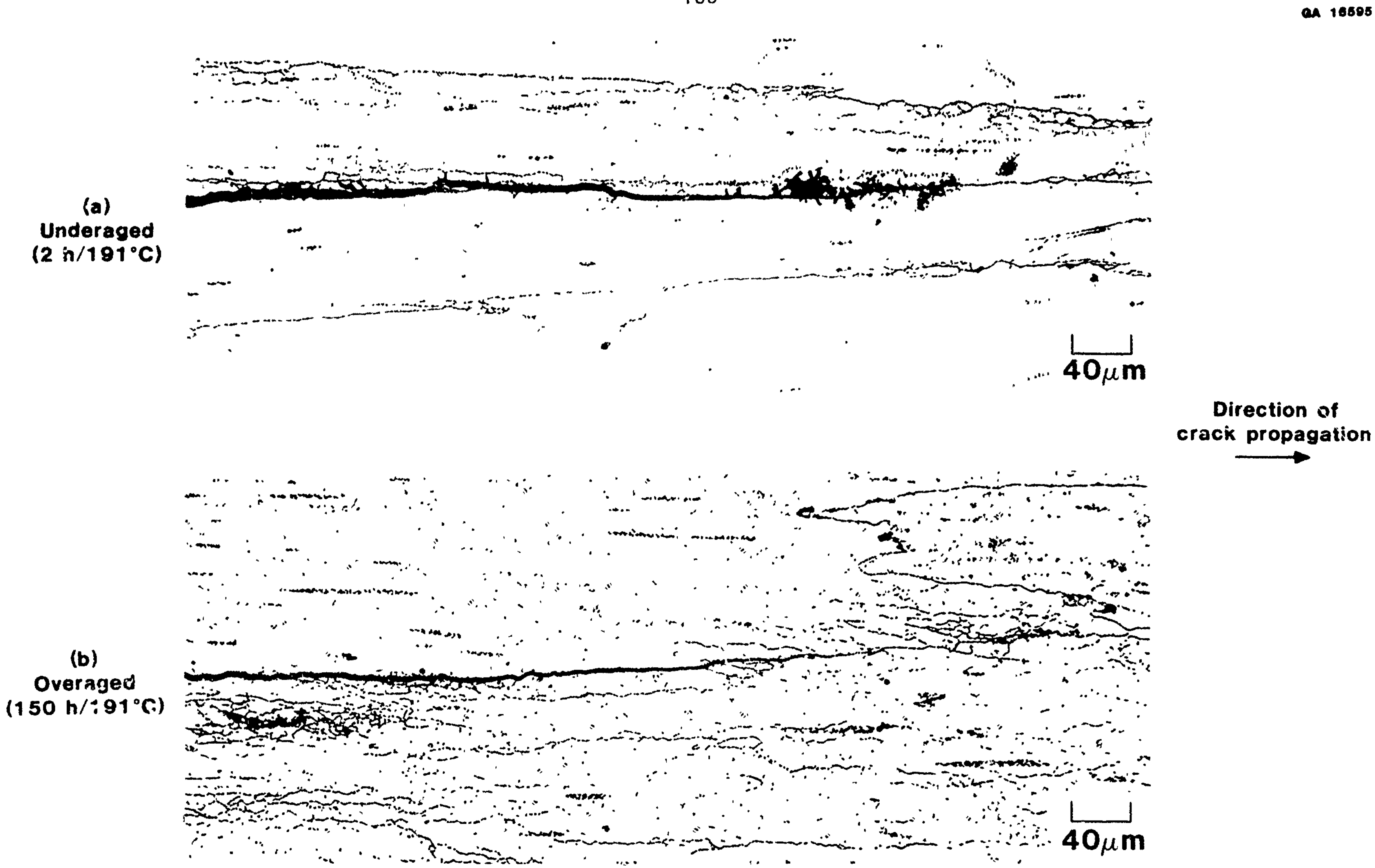

Photomicrographs of tip of the crack in DCB SCC specimens from underaged (a) and overaged (b) sample 548466 (Al -2.9Cu -2.1Li alloy T651 plate)

Figure 84

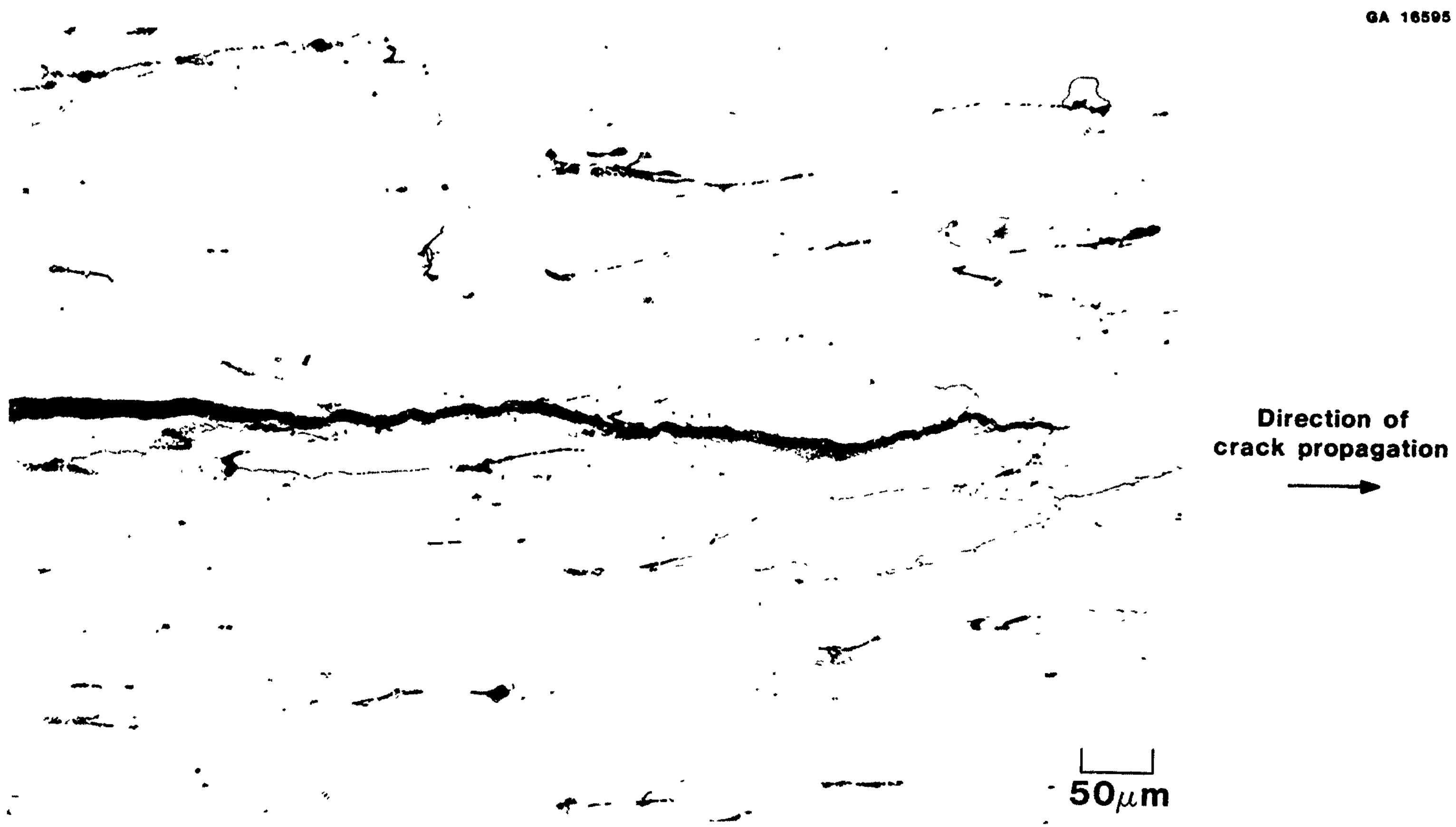

Photomicrograph of tip of the crack in DCB SCC specimen from sample 504412 (7075-T651 plate)

Figure 85

GA 16595

(a)
S. No. 548465

(b)
S. No. 523713-B

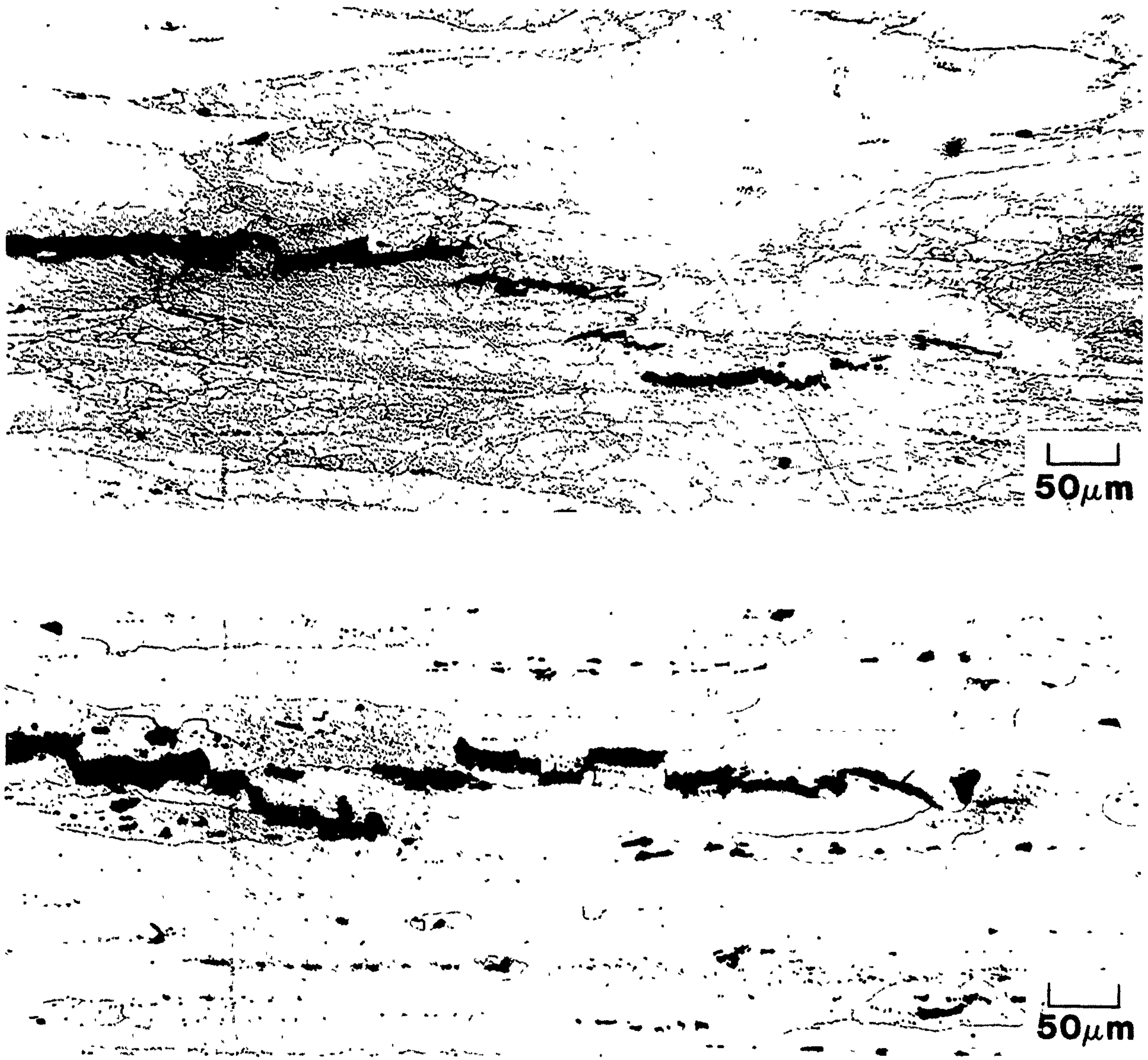

Direction of
crack propagation

Photomicrographs of tip of the crack in DCB SCC specimens from samples 548465 (a) and 523713-B (b) (Al - 4.6 Cu - 1.1 Li and 2020 alloys, respectively, T651 plate)

Figure 86

GA 16595

(a)
S. No. 548466

(b)
S. No. 504440

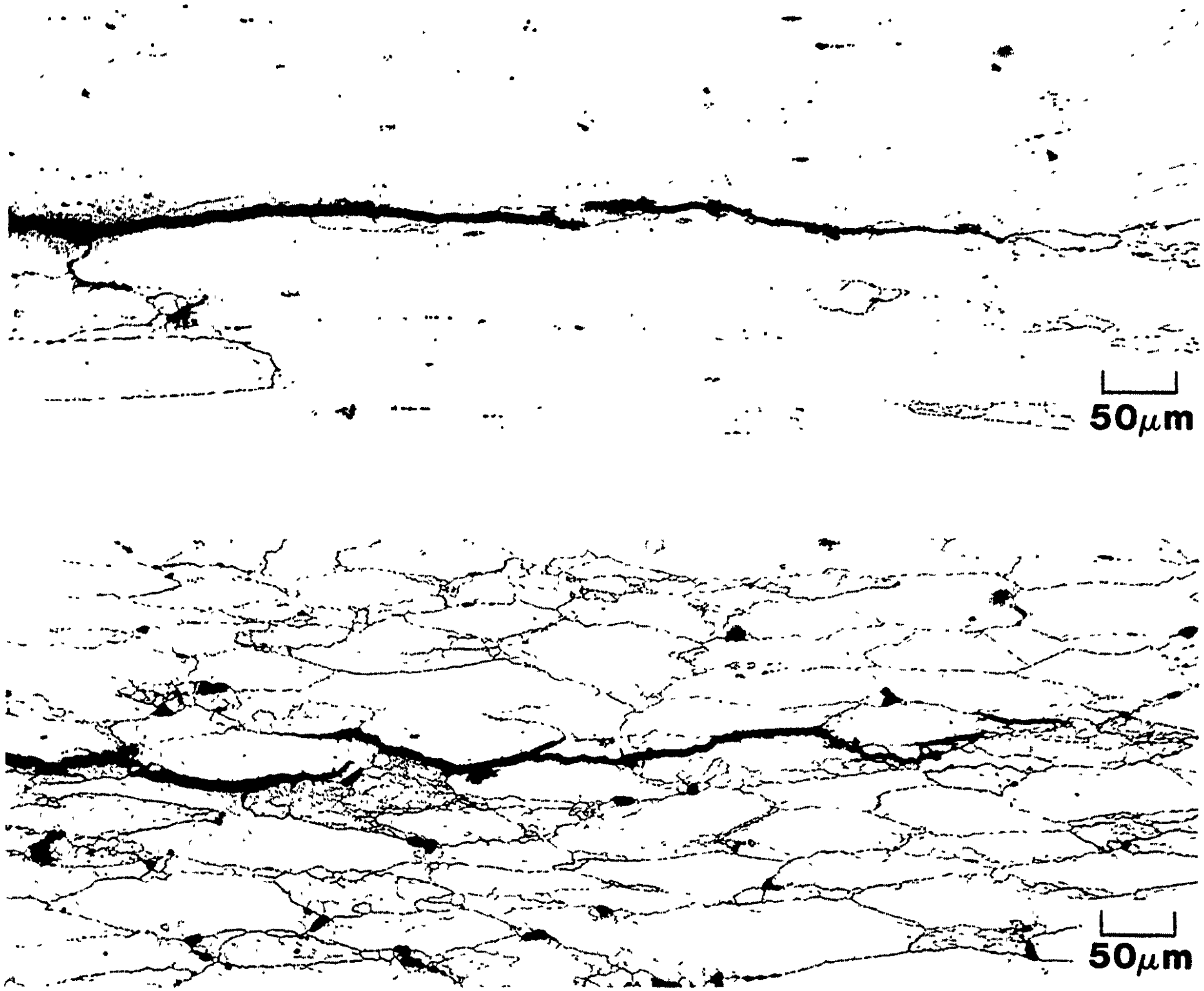

Direction of
crack propagation

Photomicrographs of tip of the crack in DCB SCC specimens from samples 548466 (a) and 504440 (b) (Al -2.9Cu -2.1Li and Al -3.1Cu -2.2Li - 1 Mg alloys, respectively, T651 plate)

Figure 87

GA 16595

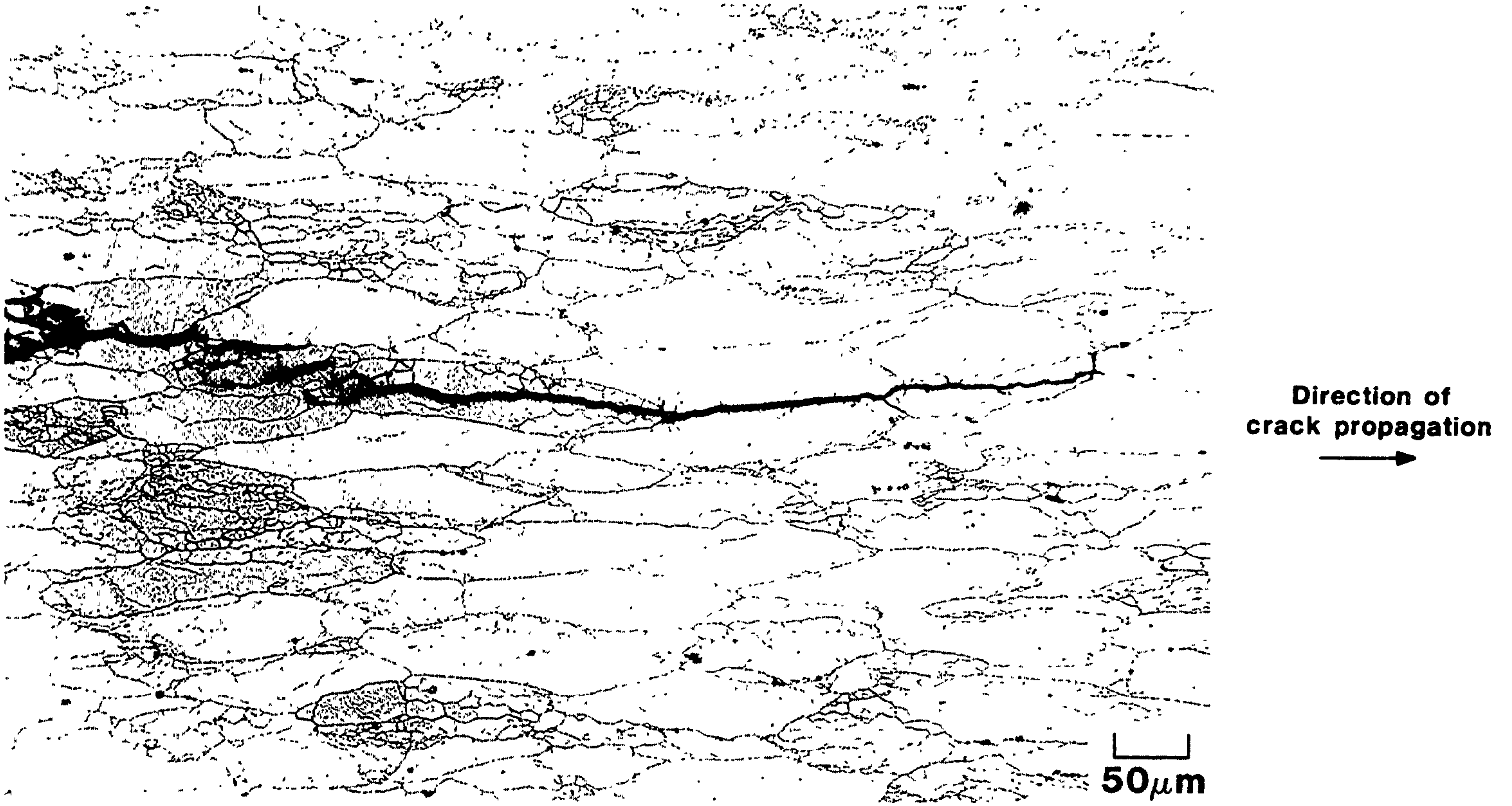

Photomicrograph of tip of the crack in DCB SCC specimen from sample 548468
(Al -1.1Cu -2.9Li alloy T651 plate)

Figure 88

APPENDIX I

CRYSTALLOGRAPHIC TEXTURE OF AL-CU-LI-ZR ALLOYS

35 mm Plate

Since alloys Al-4.6Cu-1.1Li and Al-2.9Cu-2.1Li, respectively had coarse grain sizes, the (111) pole figures used to determine preferred orientation tended to be spotty. In order to smooth out the fluctuations due to sampling problems, the four quadrants of the pole figures were averaged together before plotting. The (111) pole figures for the four alloys studied are shown in Figures I (a) through I (d).

Rolling textures in aluminum tend to have a continuous series of texture components varying from $(\bar{1}01)[1\bar{2}1]$ to near $(\bar{1}12)[1\bar{1}1]$. This range of orientations is indicated in the inverse pole figure of Figure I (e) as a series of points 1 through 6. Although discrete points are plotted, this is only for convenience in discussion, since the distribution is continuous. Grains with all orientations between 1 and 6 were found.

The planes which lie parallel to the sheet surface (ND in Figure I (e)) vary from $(\bar{1}01)$ to near, but not at, $(\bar{1}12)$. The crystallographic directions in those planes which parallel the rolling direction (RD) meanwhile vary from

[$1\bar{2}1$] to near [$1\bar{1}1$]. Usually the number of grains of each orientation is approximately equal, with perhaps a slight preference for orientations towards point 1 in the series.

Some of the orientations have received special names. Orientation 1 has been called the "brass component" and orientation 6 the "copper component" because of their prevalence in those two alloys. The orientation (123)[$63\bar{4}$] is sometimes called the "S-component." It lies near point 4 in Figure I (e).

The orientations 1 through 6 in Figure I (e) produce locations in the (111) pole figure which have a shape indicating that the texture is a characteristic rolling texture as shown in Figure I (f). There is a lip-shaped region across the center of the pole figure which, because the points are roughly equally populated, form a continuous band. Points 4 through 6 overlap just inside the 60° circle so this region tends to be intense. There are other poles in clusters at the top and bottom of the pole figures.

The Al-Li-Cu alloys of this investigation are somewhat unusual in regards to rolling texture. The features are seen most clearly in the pole figure of Figure I (c) for alloy Al-1.1Cu-2.9Li. Experimental data for orientations 5 and 6 are certainly present at the vertical line near the 60° circle. (Only the transmission region was obtained, so no data were collected within the 60° circle). Data for orientations 5 and 6 are also present along the vertical line at the top and bottom of the pole figure. However, the poles for orientations which should appear at the left and right sides of the 30° circle are weak. This probably indicates some sideways wobble to the grains around the rolling direction which would distribute those poles over an area.

What is notable about the experimental pole figures, however, is the almost complete absence of orientations near 1 and 2, the "brass" components. These components would put data at the ends of the horizontal line in the pole figure and in clusters at the top and bottom of the figure about 20° away from the vertical line.

The alloy which is most different from the others (except for grain size effects) is Al-2.9Cu-2.1Li, Figure I (b). There is a suggestion of the presence of the off-axis data clusters at the top and bottom which is probably orientation 4. The location of poles for the S-orientation which is similar to 4 is given in Figure I (f).

It is not certain whether the preferred component of texture is that marked 6 in Figure I (f) which can be described as near $(\bar{1}12)[1\bar{1}1]$ or if it is the exact orientation with those indices. Why the copper-like texture is preferred is unclear, although the implication is that stacking fault energy is higher than in normal aluminum alloys.

<u>12.7 mm Plate</u>

Texture measurements in thinner 12.7 mm thick plate showed similar textures to the 35 mm plate but, because the effective crystallite sizes were smaller, the textures were easier to see without averaging over the quadrants.

One aspect of the texture which was now easier to see was the presence of (110)[001] component, the so-called Goss component. The exact component puts poles on the circumference of the pole figure 55° away from the horizontal axis (Figure I (h)). The practical effect in an actual pole figure is to blend with the poles of the 1, 2 type and make a ring of poles around the outside of the pole figure. In other words, there is a series of (111) planes (the planes used to make the pole figure, and which happen to be the slip planes) which lie perpendicular to the surface of the plate (and make the band around the outside of the pole figure) but which are at almost any angle to the rolling direction except for a tendency to cluster in particular directions.

Again, the copper components of the rolling texture tended to predominate over the brass components. In the thinner gage with the clearer pole figures, it was seen that the exact brass component (locations 1 in Figure I (f)) was actually present and that it was components 2 or 3 which tended to be missing. The experimental alloys had textures similar to 2020 alloy, except that the recrystallized 2020 was so coarsely grained that even after quadrant averaging its texture was not obvious.

It is interesting to compare the compositional effects in texture. The high solute (2.9 Cu - 2.1 Li) alloy tended to have the strongest texture in both thicknesses (Table I-1). Adding 1.0% Mg to this composition, however, produced the weakest texture. To a certain extent the texture would be expected to produce an anisotropy of properties. The difference in properties between the alloys with and without the magnesium addition is too large, and in the wrong direction, to be due to the texture effect. The pole figures for all the 0.5" plate alloys are given in Figure I (j) and I (r).

Table I-1

INTENSITY OF CRYSTALLOGRAPHIC TEXTURES

Specimen Number						Strength of Texture (Point with Max. intensity)	
37 mm Plate	12.7 mm Plate	Cu	Li	Mg	Zr	37 mm Plate	12.7 mm Plate
548465	548465	4.6	1.1	0	.12	13.8	10.0R
548466	504795	2.9	2.1	0	.12	17.5	12.2
504440	504440	3.1	2.2	1.0	.12	13.2	8.1
548468	548468	1.1	2.9	0	.12	12.1	12.3
523713-A	--	2020 coarse grain (1.25") Plate				6.3	--
--	523713-X	2020 Unrecrystallized				--	12.8

LIST OF FIGURES

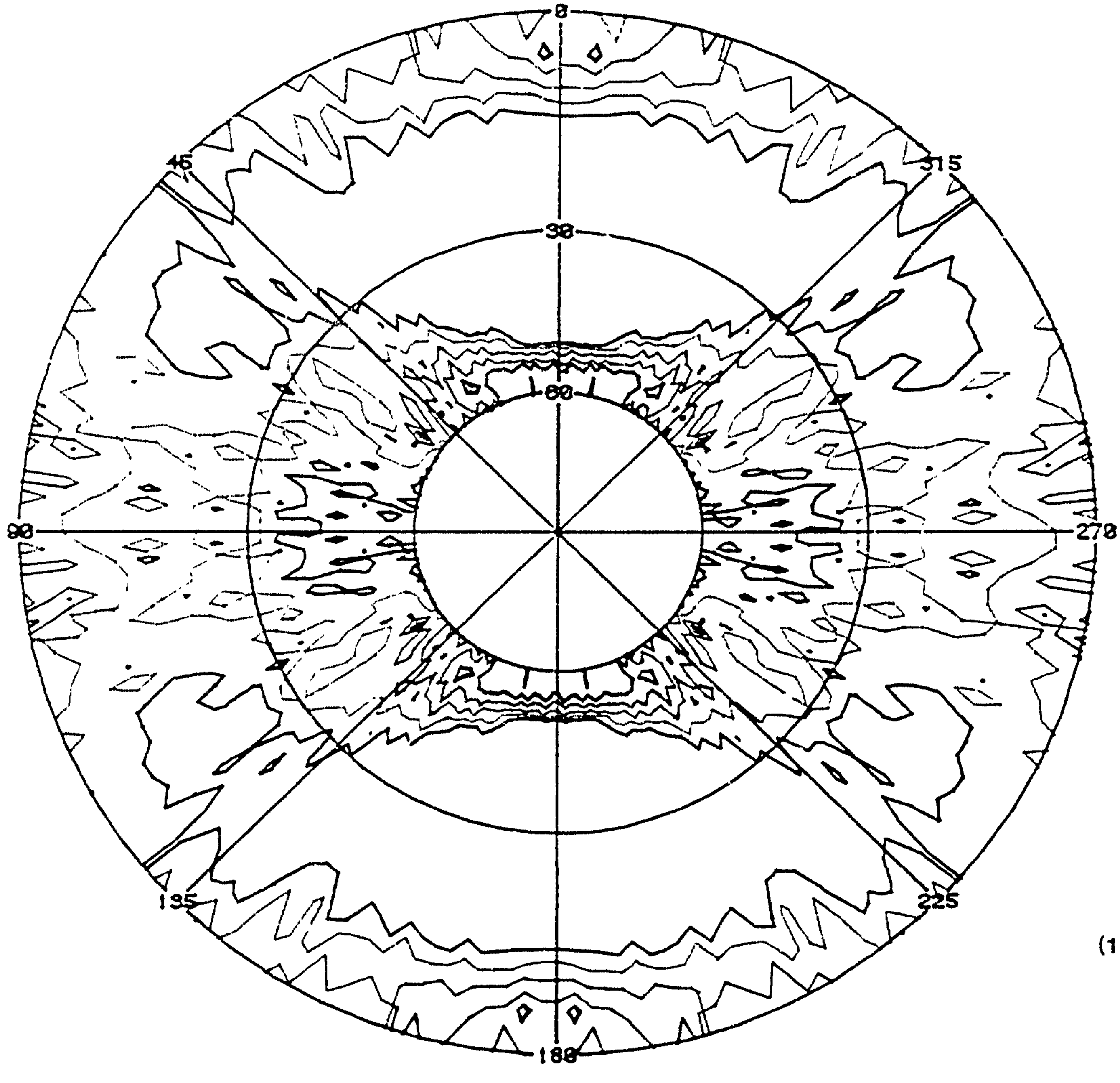

File: DL0:Z10411.PFG

Sample: 548465-A2 AL-LI

1.5" -T6

19-MAY-83 13:04:07

H= 1 K= 1 L= 1

Plot Levels:

5.4%	0.75 R
9.1%	1.25 R
14.5%	2.00 R
21.8%	3.00 R
29.0%	4.00 R

(111) Pole figure of sample 548465

Figure I(a)

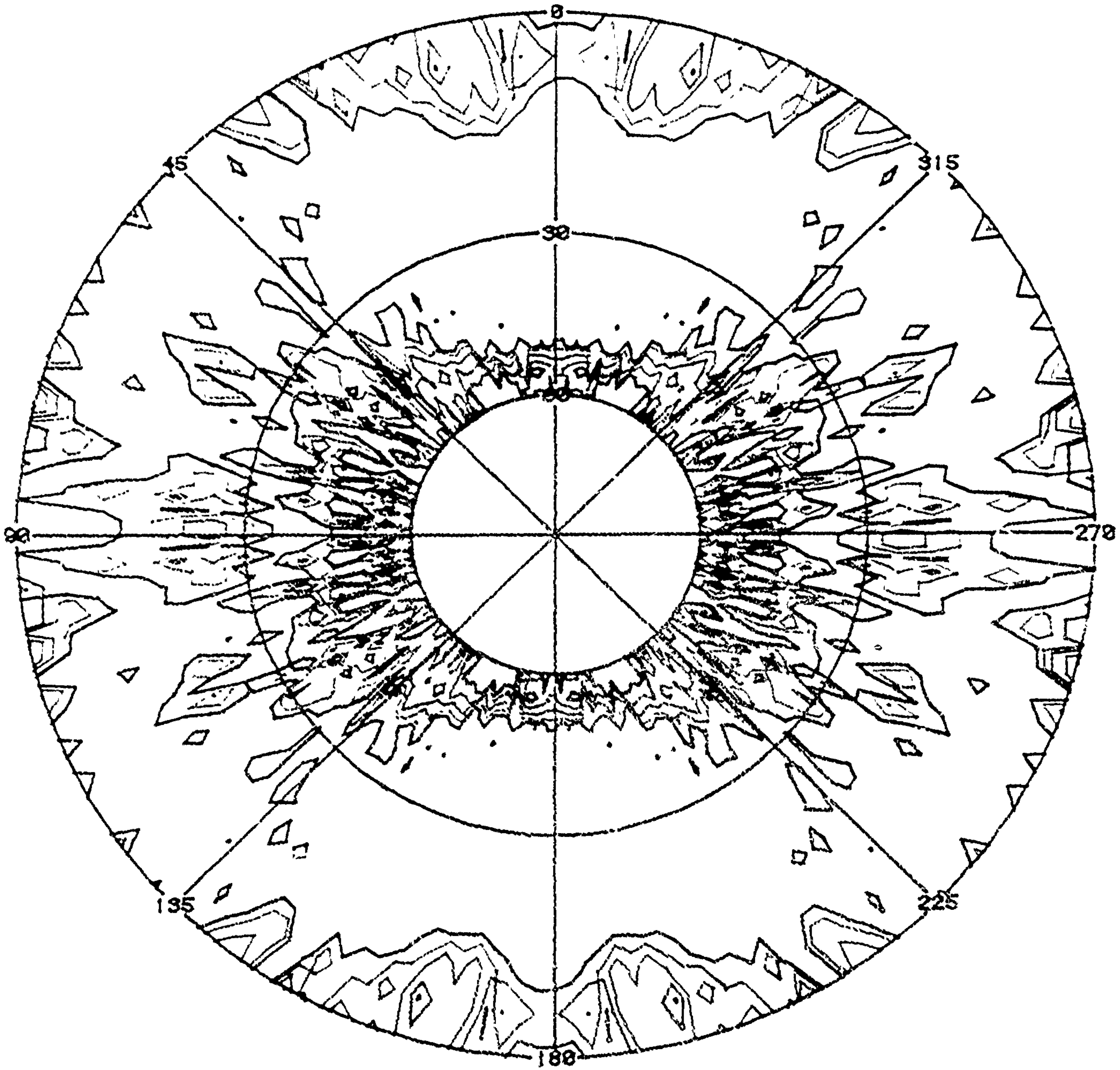

File: DL0:Z10412.PFG

Sample: 548468-A1 AL-LI

1.5" -T8

19-MAY-83 13:39:24

H= 1 K= 1 L= 1

Plot Levels:

—	4.3%	0.75 R
—	7.2%	1.25 R
—	11.4%	2.00 R
—	17.2%	3.00 R
—	22.9%	4.00 R

(111) Pole figure of sample 548466

Figure I(b)

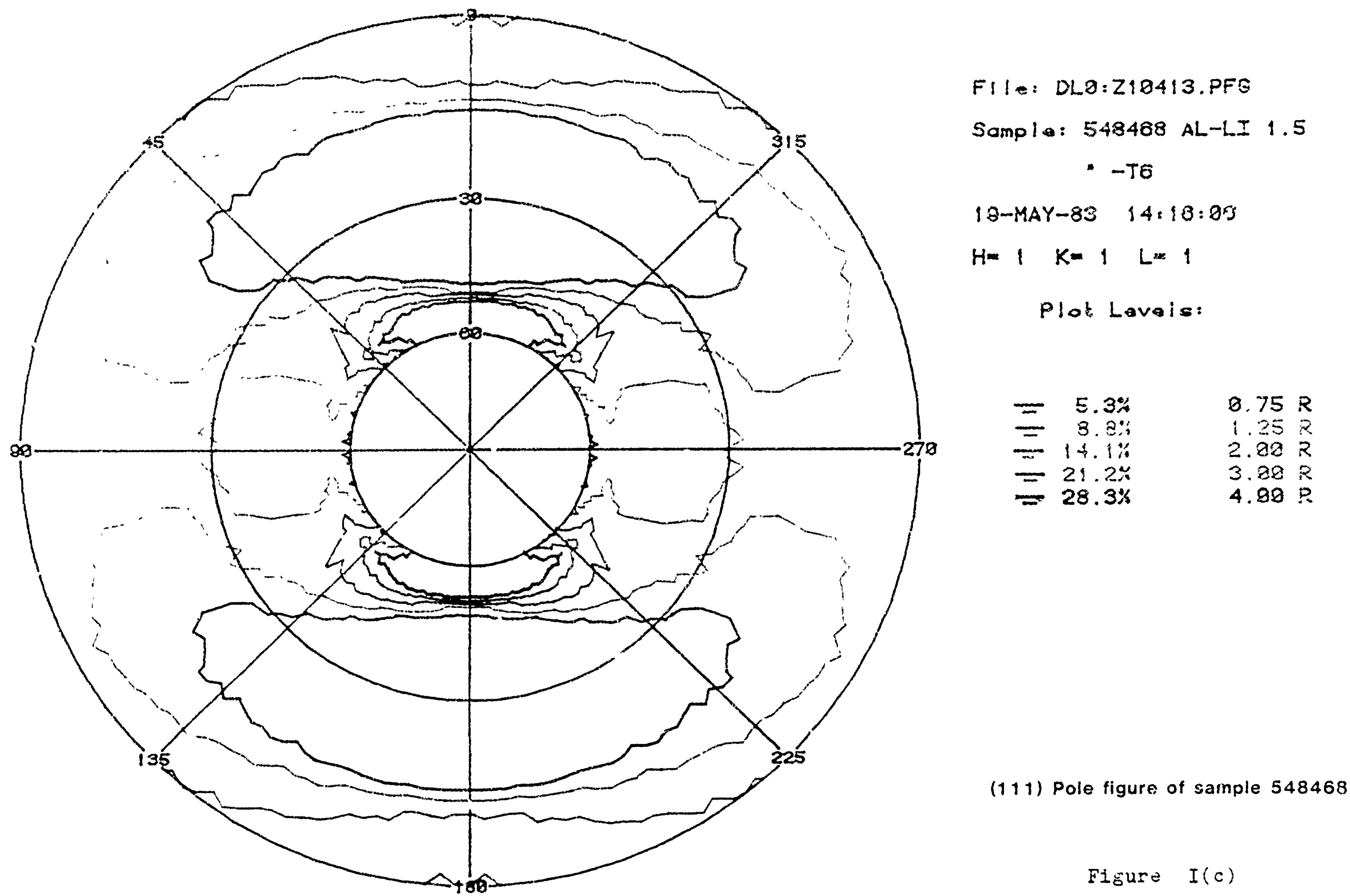

(111) Pole figure of sample 548468

Figure I(c)

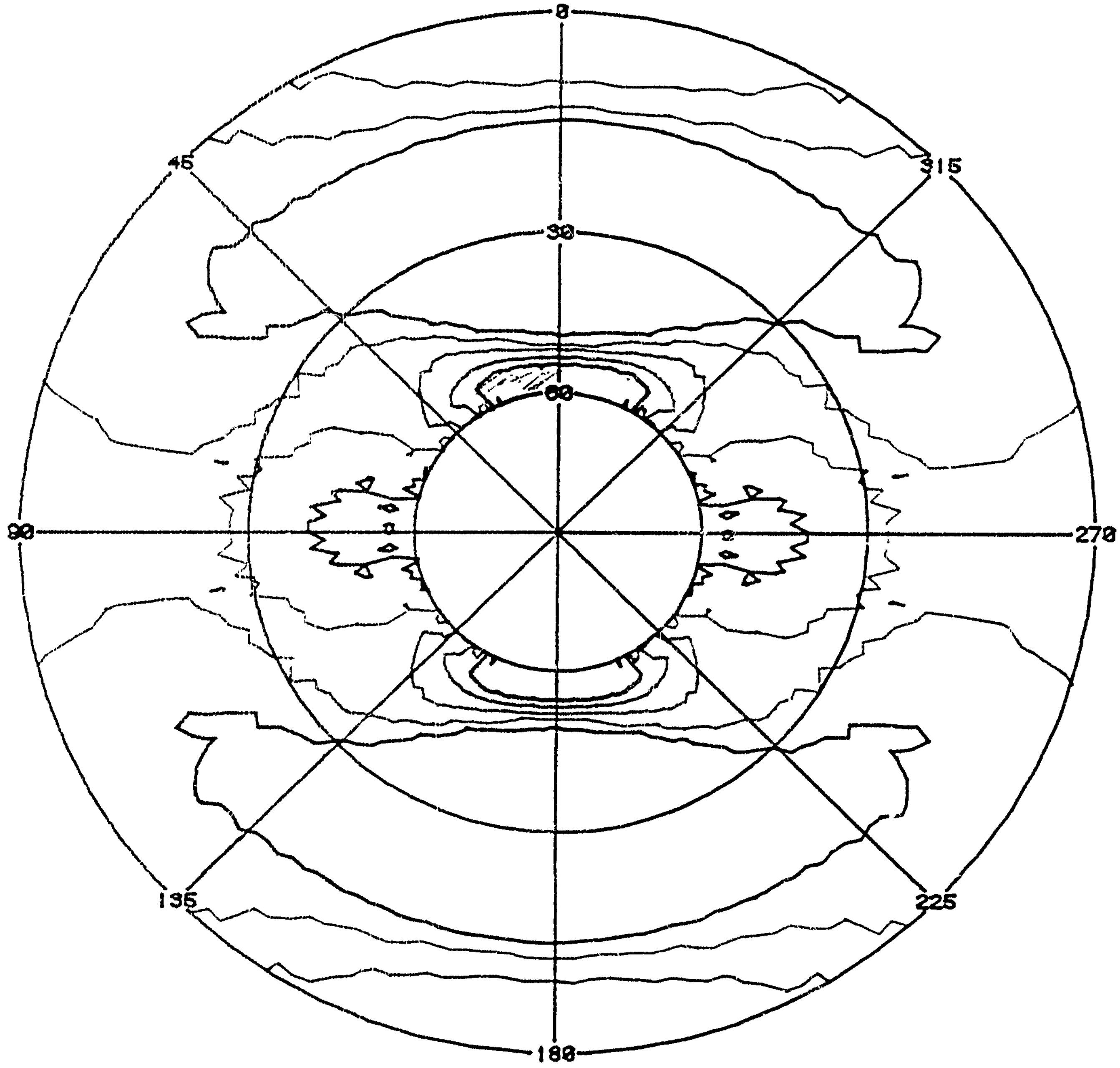

File: DL0:Z10414.PFG

Sample: 504440-A2 AL-LI

1.5" -T8

19-MAY-83 14:50:35

H= 1 K= 1 L= 1

Plot Levels:

6.1%	0.75 R
10.2%	1.25 R
16.3%	2.00 R
24.5%	3.00 R
32.6%	4.00 R

(111) Pole figure of sample 504440

Figure I(d)

GA 16595

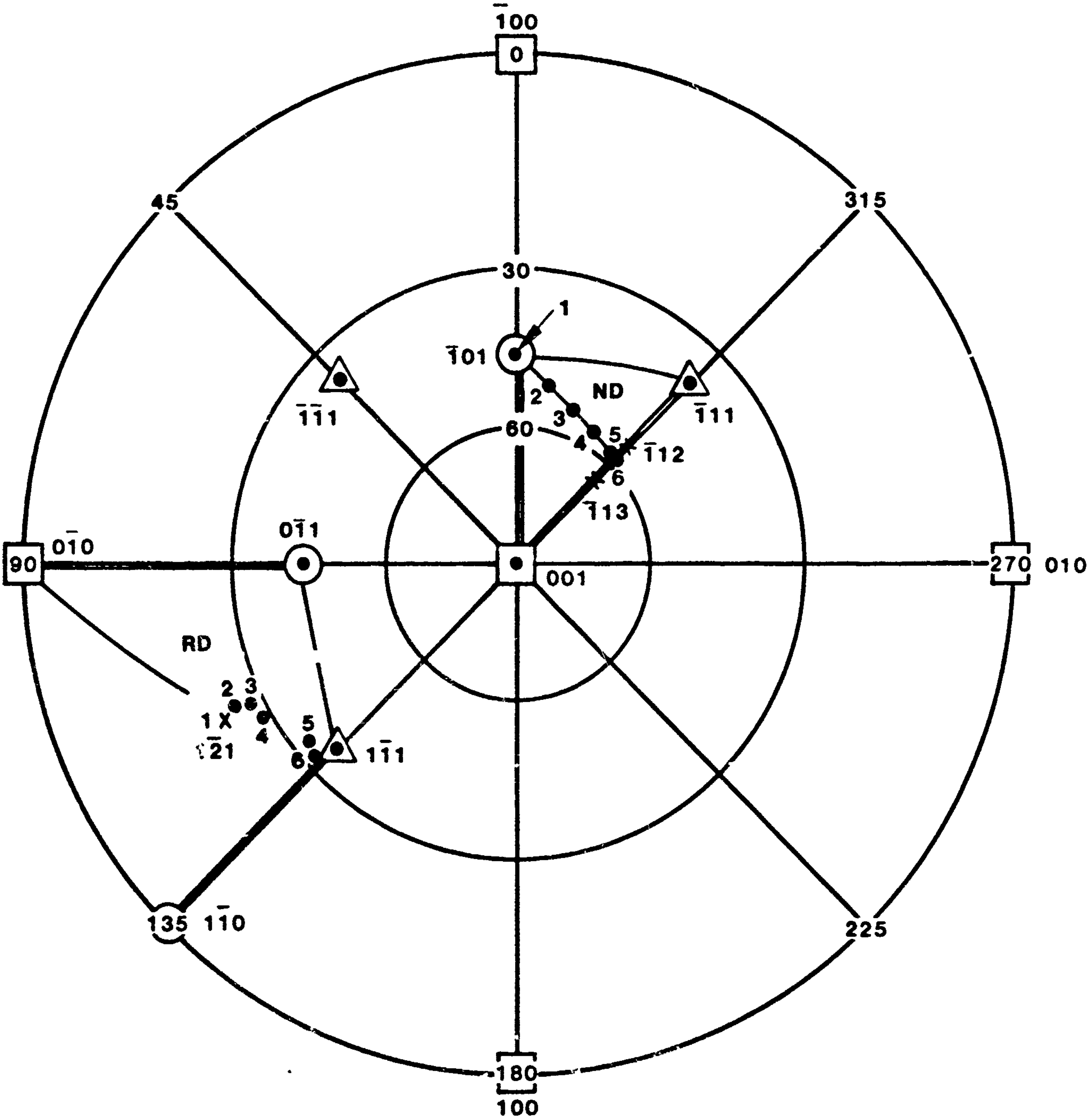

Standard projection showing how the rolling direction and the normal direction (the planes parallel to the plate surface) lie in relation to the crystallographic directions for orientations 1 to 6.

Figure I(e)

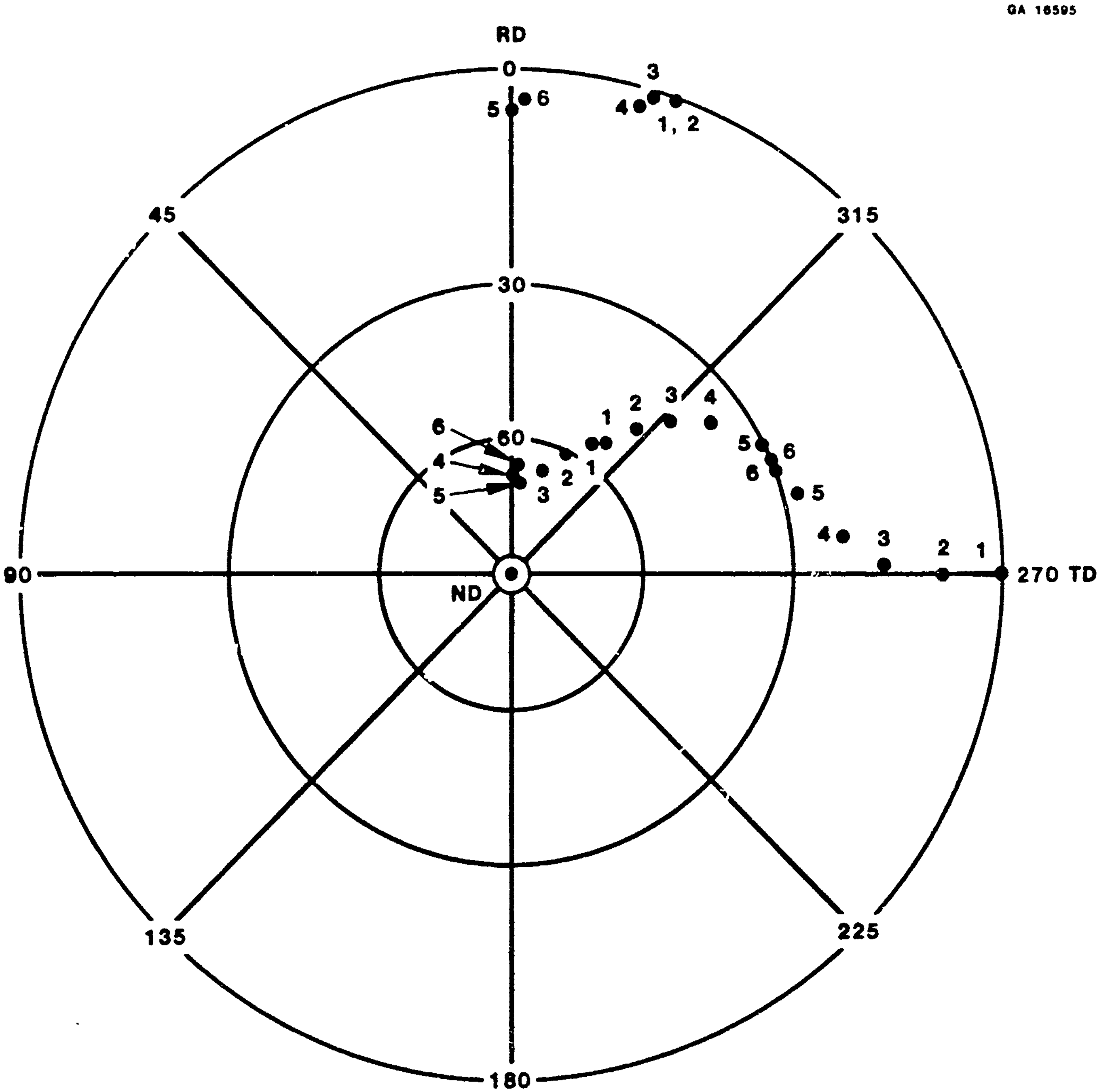

The location of the (111) poles of Figure I(e) replotted into one quadrant. When the relative number of grains having orientations 1 to 6 is factored into this drawing, it becomes the (111) pole figure for the major texture of the hot rolled specimen.

Figure I(f)

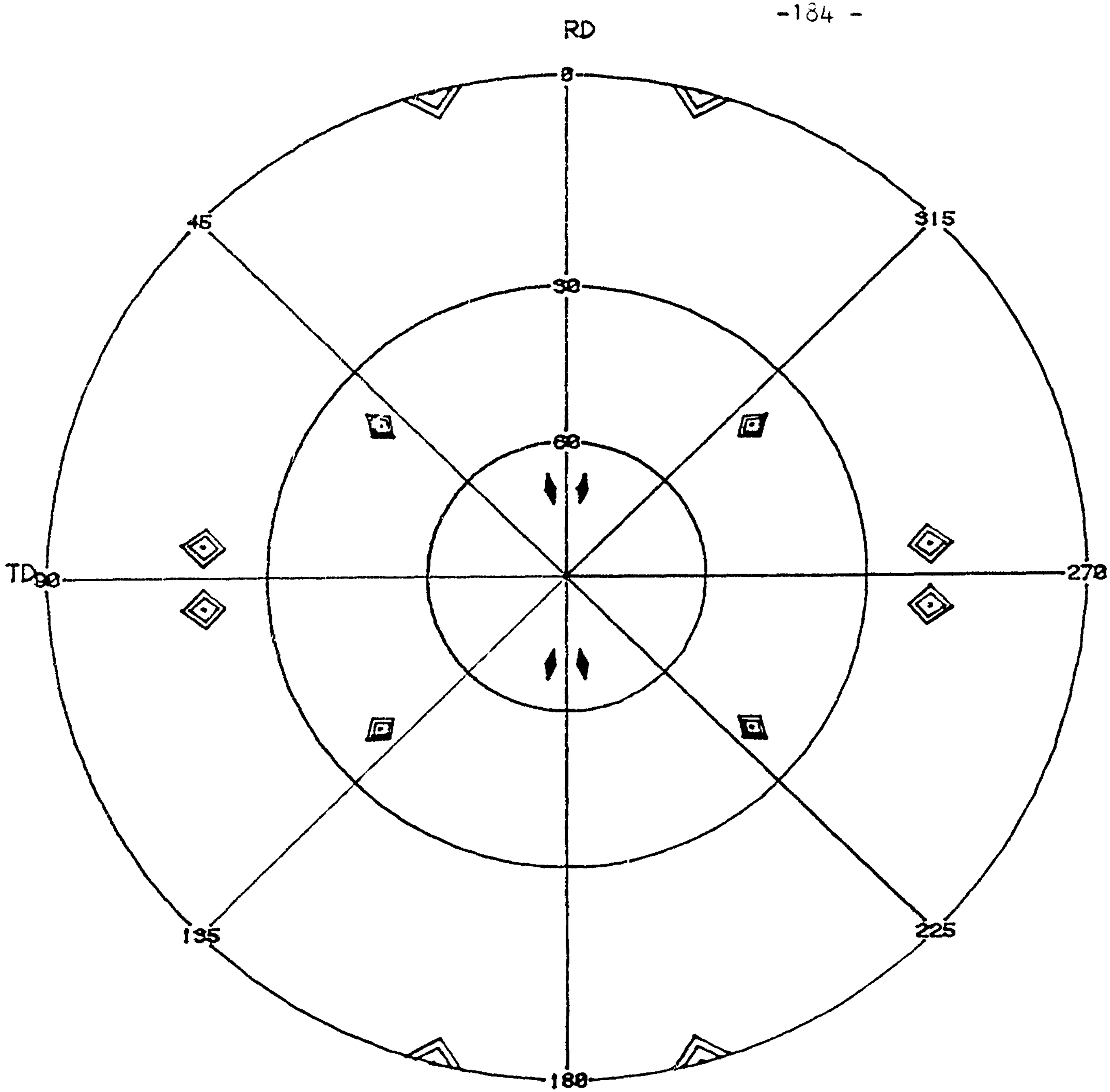

File: DL0:STEXT.PFG

Sample: 1 2 3

6 3 -4

H= 1 K= 1 L= 1

Plot Levels:

	37.5%	0.75 R
	62.5%	1.25 R
	100.0%	2.00 R
	150.0%	3.00 R
	200.0%	4.00 R

S TEXTURE

Standard S-texture pole figure

Figure I(g)

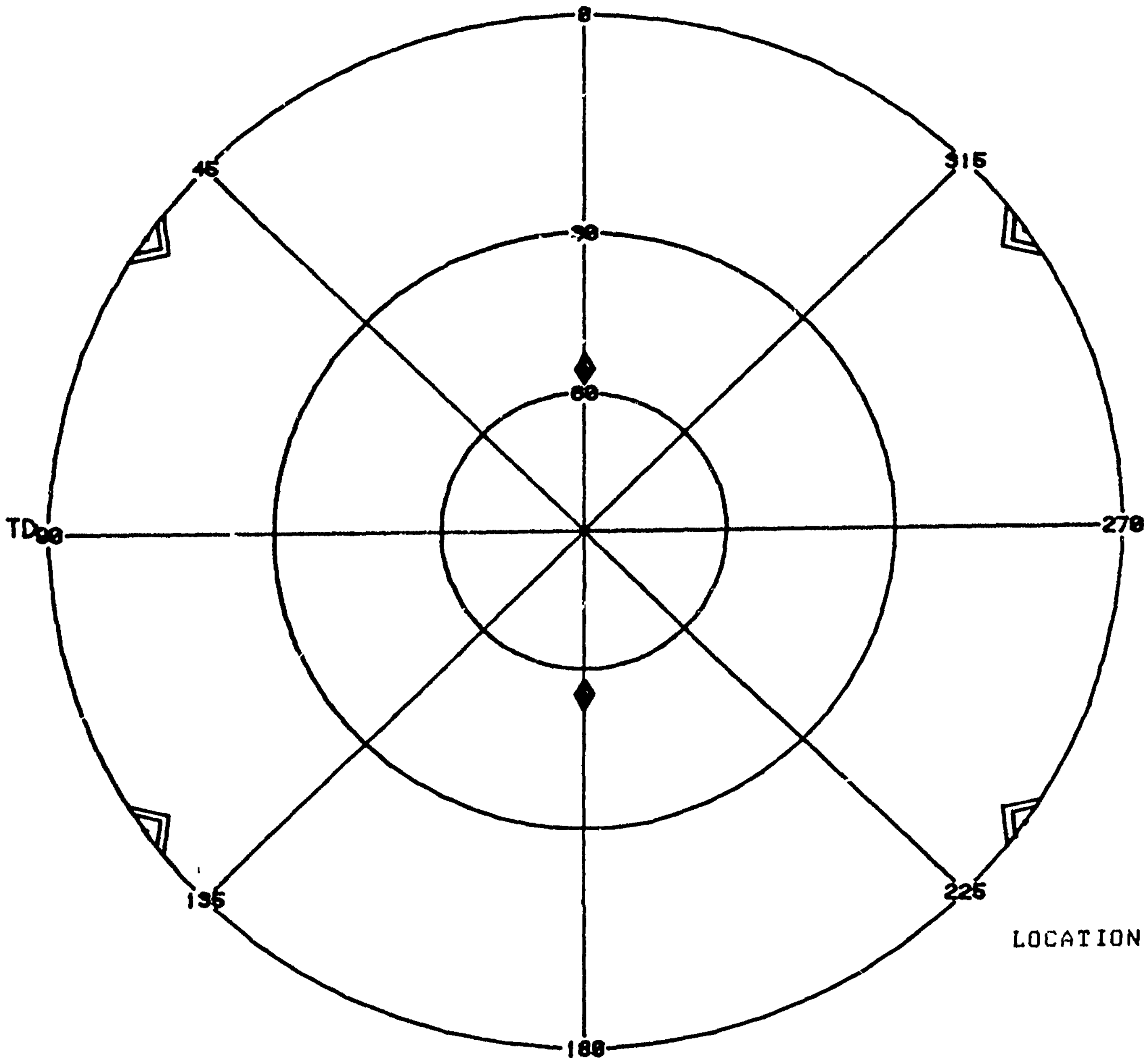

File: DL0:GOSS.PFG

Sample: 1 1 0

0 0 1

H= 1 K= 1 L= 1

Plot Levels:

37.5%	0.75 R
62.5%	1.25 R
100.0%	2.00 R
150.0%	3.00 R
200.0%	4.00 R

Standard Goss-texture pole figure

Figure I(h)

LOCATION OF POLES:

	LATITUDE	LONGITUDE
1	54.7	0.0
2	0.0	54.7
3	54.7	180.0
4	0.0	54.7

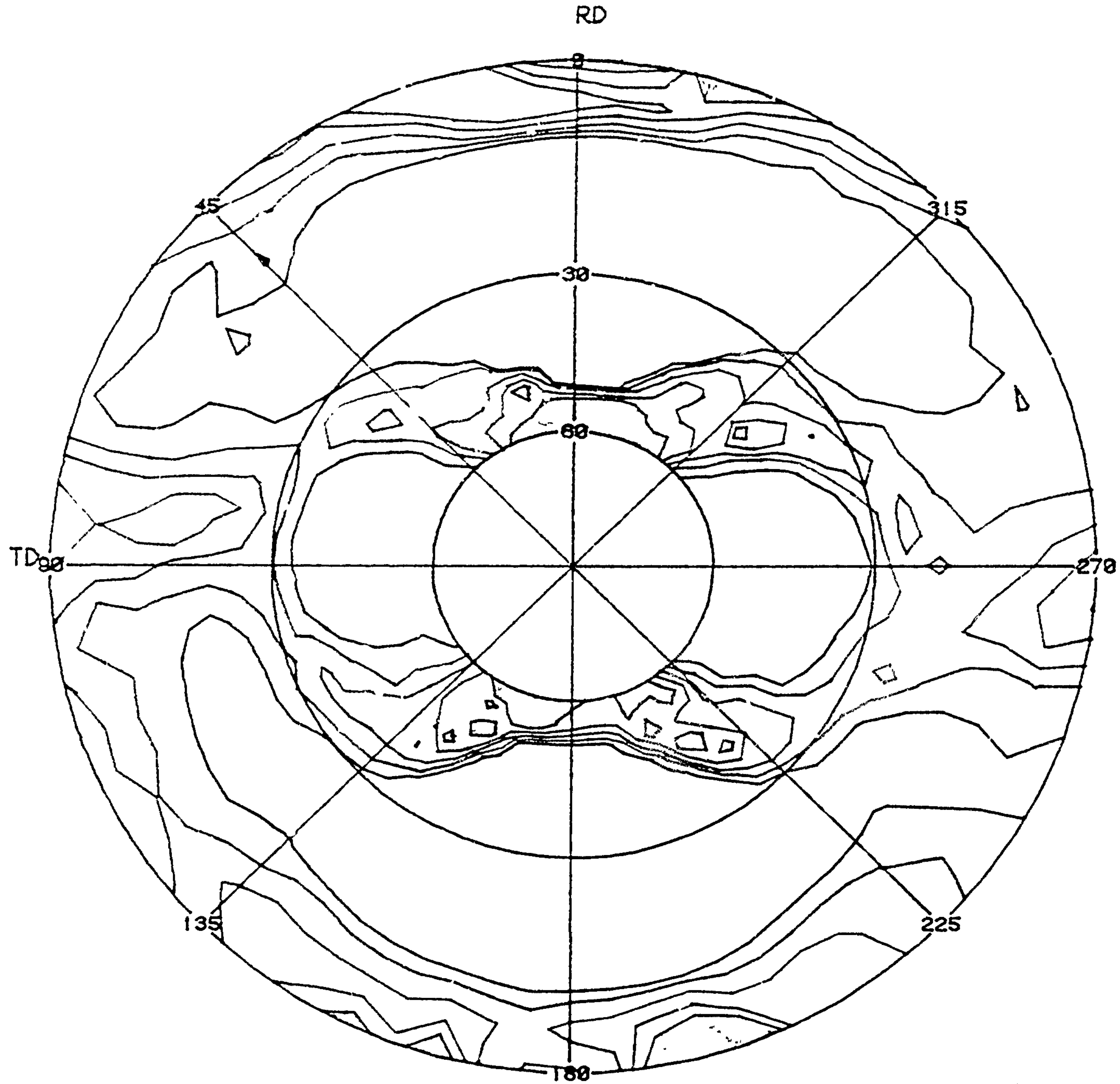

File: DL1:Z01124.PFG

Sample: 548465-6 .5" 1.1

LI-4.5CU-ZR

28-NOV-84 12:57:01

H= 1 K= 1 L= 1

Plot Levels:

▭	7.5%	0.75 R
▭	12.5%	1.25 R
▭	20.0%	2.00 R
▭	30.0%	3.00 R
▭	40.0%	4.00 R

(111). Pole figure of alloy Al-4.6Cu-1.1Li (S.548465), 12.7mm plate

Figure I(j)

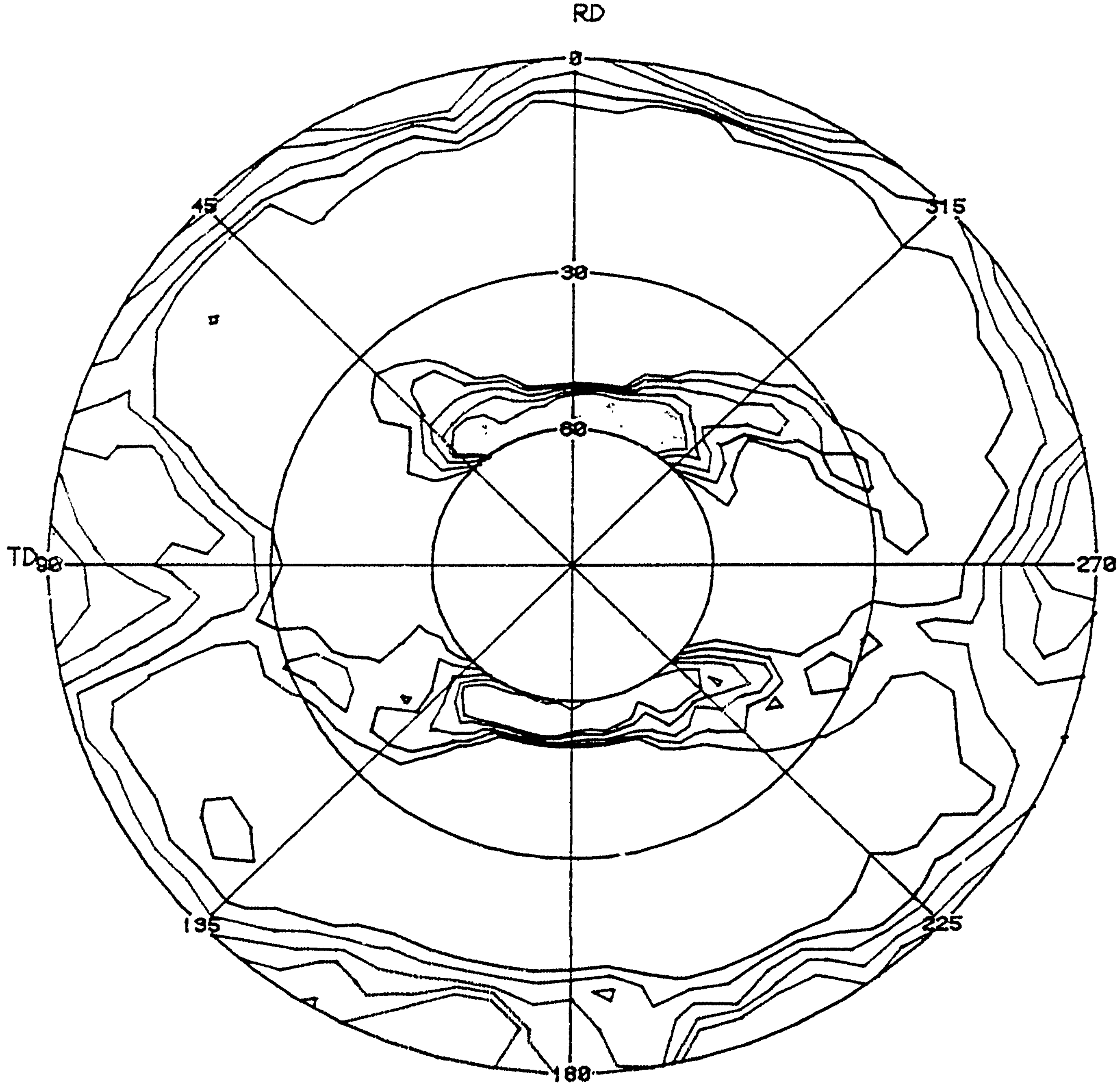

(111) Pole figure of alloy Al-2.9Cu-2.1Li(S.548466), 12.7mm plate

Figure I(k)

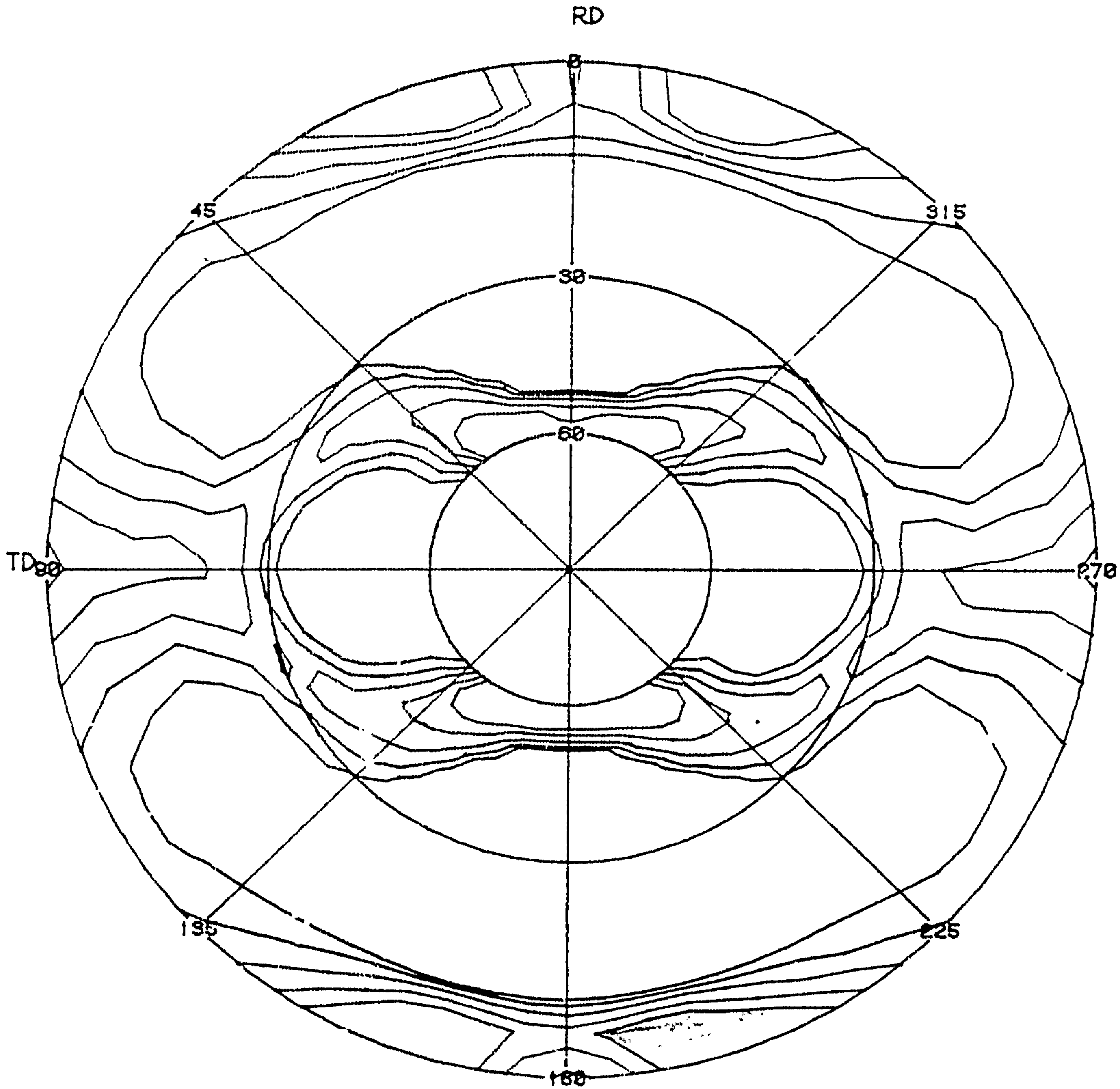

File: DL1:Z01120.PFG

Sample: 504440-4 .5" 2LI

-3CU-1MG-ZR

28-NOV-84 09:43:22

H= 1 K= 1 L= 1

Plot Levels:

▭	9.3%	0.75 R
▭	15.5%	1.25 R
▭	24.8%	2.00 R
▭	37.1%	3.00 R
▭	49.5%	4.00 R

(111) Pole figure of alloy Al-3.1Cu-2.2Li-1.0Mg(S.504440), 12.7mm plate

Figure I(m)

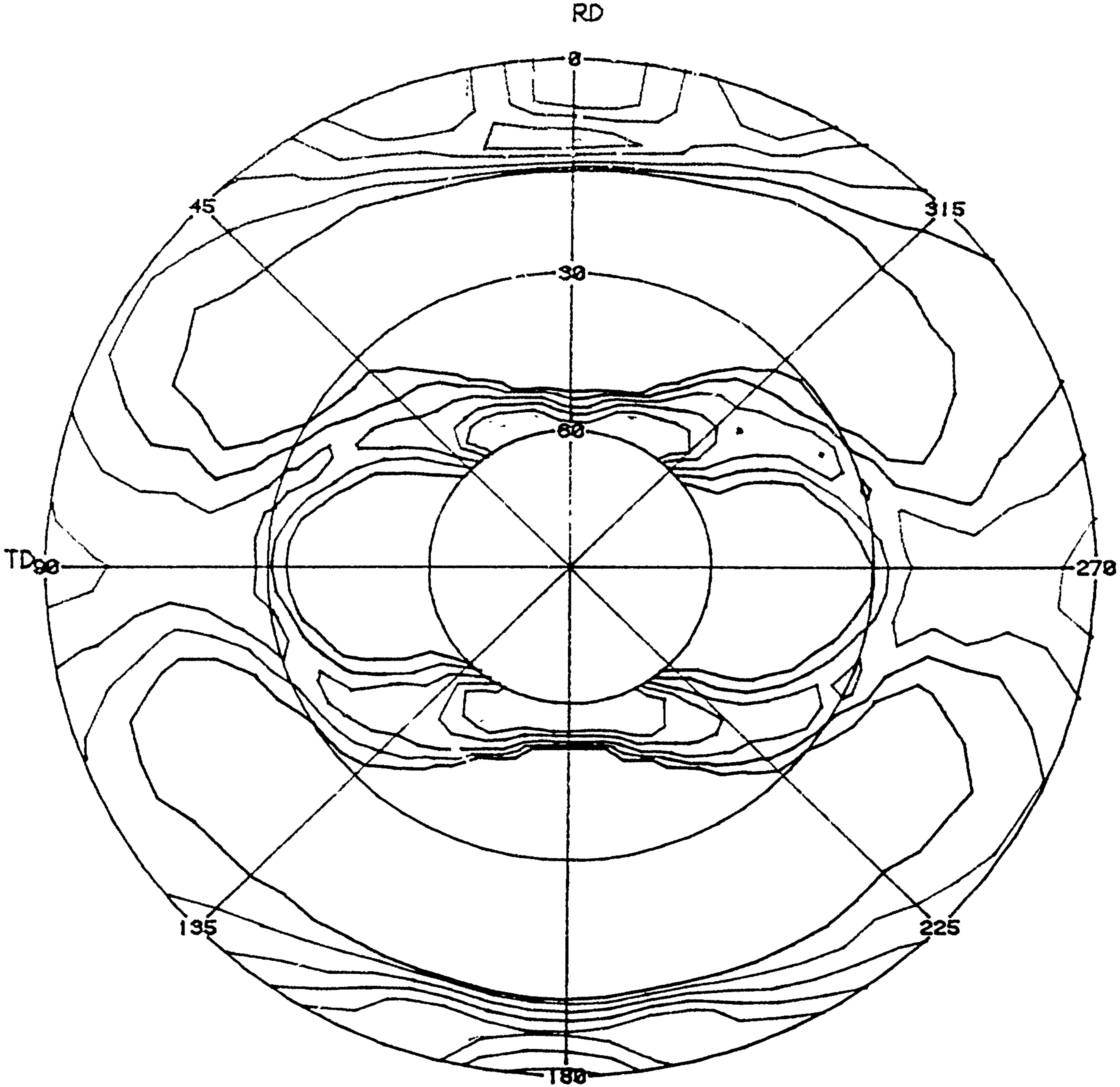

File: DL1:Z01118.PFG

Sample: 548468 .5" 3LI

-1CU-ZR

28-NOV-84 08:01:11

H= 1 K= 1 L= 1

Plot Levels:

▭	6.1%	0.75 R
▭	10.2%	1.25 R
▭	16.3%	2.00 R
▭	24.5%	3.00 R
▭	32.6%	4.00 R

(111) Pole figure of alloy Al-1.1Cu-2.9Li (S.548468), 12.7mm plate

Figure I(n)

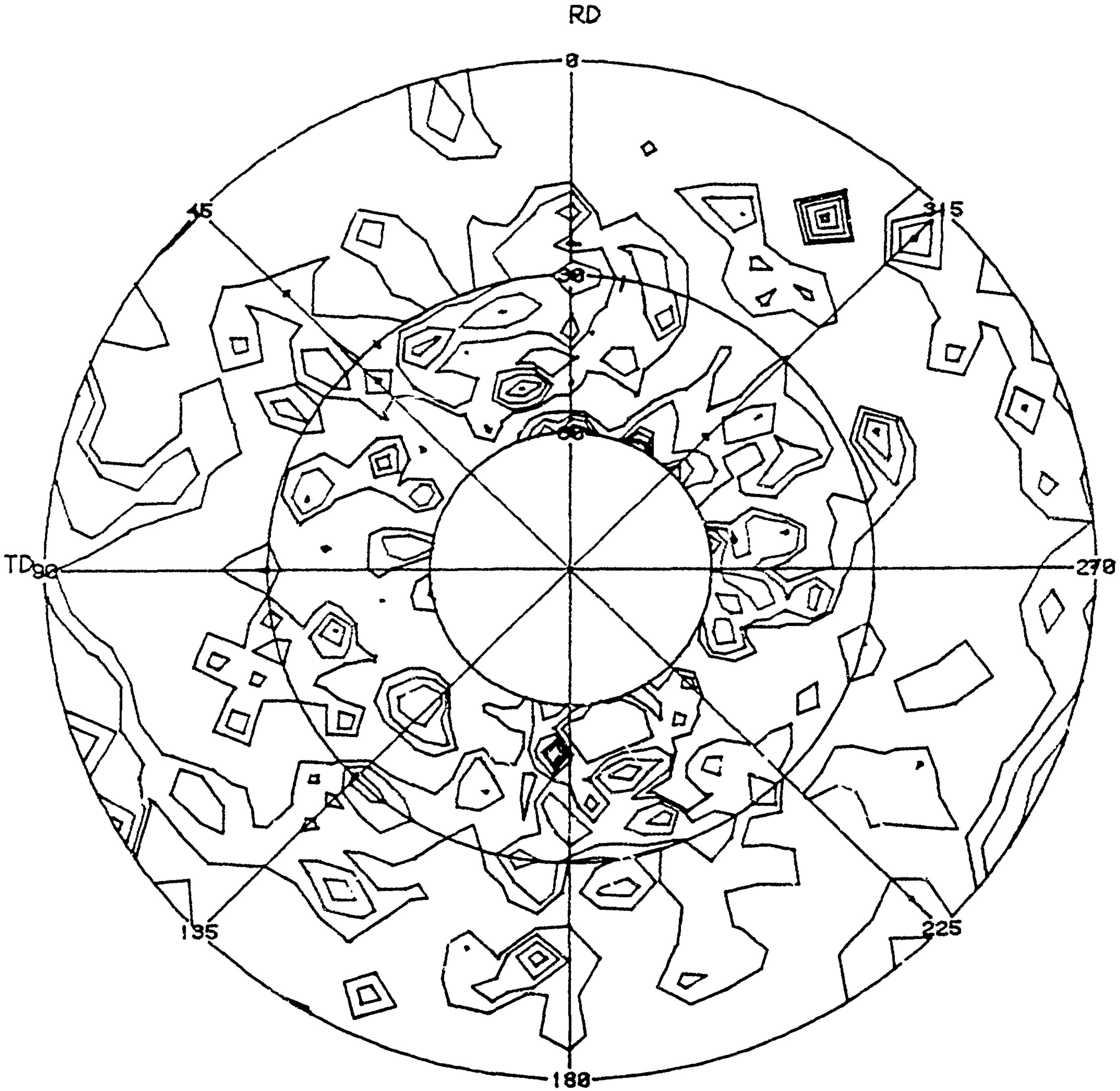

File: DL1:Z01121.PFG

Sample: 523713-A-4 .5" 2

020 COARSE GR.

28-NOV-84 10:31:42

H= 1 K= 1 L= 1

Plot Levels:

▭	12.0%	0.75 R
▭	20.0%	1.25 R
▭	32.0%	2.00 R
▭	47.9%	3.00 R
▭	63.9%	4.00 R

(111) Pole figure of the alloy 2020-recrystallized(S.523713-A), 32mm plate

Figure I(p)

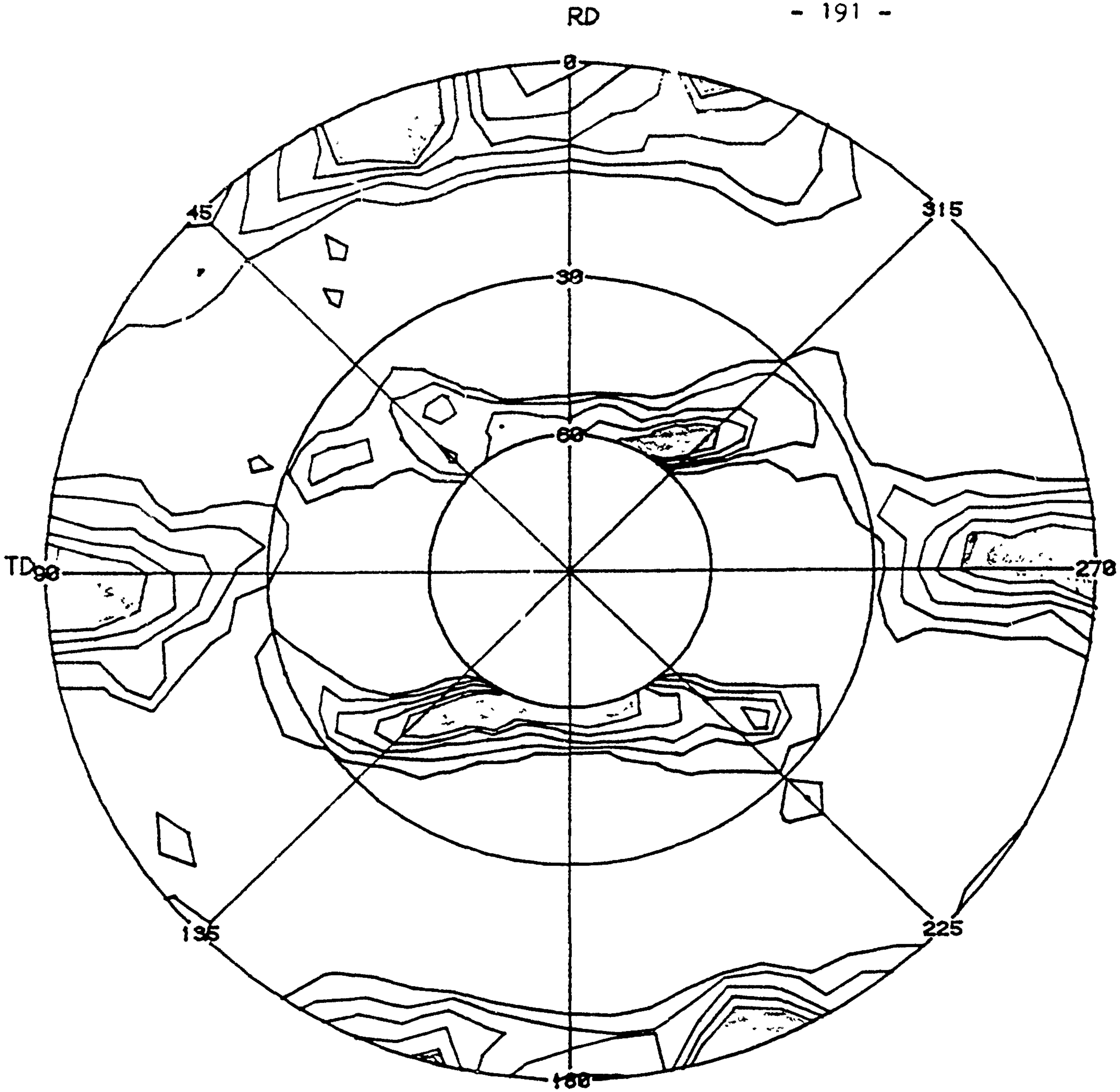

File: DL1:Z01123.PFG

Sample: 523713-1-X .5" 2

020 UNRXTALL

28-NOV-84 12:06:55

H= 1 K= 1 L= 1

Plot Levels:

▭	5.8%	0.75 R
▭	9.7%	1.25 R
▭	15.6%	2.00 R
▭	23.4%	3.00 R
▭	31.2%	4.00 R

(111) pole figure of the alloy 2020-unrecrystallized(S.523713-X), 12.7mm plate

Figure I(r)

APPENDIX II

TEM CHARACTERIZATION OF AL-LI-CU-ZR ALLOYS

The precipitation sequence in a pure binary Al-Li alloy can be represented by (1-4,6):

$$\alpha_{ss} \dashrightarrow \alpha + \delta' \dashrightarrow \alpha + \delta$$

The precipitation sequence in ternary alloys (Al-Li-Cu), however, depends on the composition of the alloy. In general, it can be approximately represented as:

$$\alpha_{ss} \dashrightarrow \alpha + \delta' + \text{T-phase} \dashrightarrow \alpha + \delta + \text{T-phase}$$

T-phase has a composition $Al_xLi_yCu_z$. The composition and structure of such a T-phase depends on the Li and Cu content in the alloy. There has been observations of precursory phases prior to the formation of T-phases (5,7-14). In addition, GP-zone formation have been claimed during the short-time aging treatments (3,8,13). In order to clarify the structure of these phases, detailed TEM characterization are necessary (3,15).

Suzuki, Kanno and Hayashi (7) have suggested that the T_B' and T_1' phases form in high purity Al-4Cu-1Li alloys. These suggestions were made on the basis of superlattice spots in diffraction patterns that could not be explained in terms of the θ' and T_1 phases. No structural analyses of T_B' and T_1' were given. However, it was suggested that T_B' and T_1' were precursors to the T_B and T_1 phases.

Schneider and Heimendahl (11) working on an Al-4.17Cu-1.01Li-0.55Mn-0.23Cd alloy concluded that the predominant metastable phase was θ′ in the temperature range from room temperature to 350°C. These authors argue that incorporation of Li into the θ′ structure gives rise to the T_B phase with the CaF_2 structure (a - 5.83 Å, T_B = $Al_{7.5}Cu_4Li$). Prior to the formation of the θ′ phase, the θ″ phase was resolved. Extra reflections in diffraction patterns [near 1/3 (020) positions in reciprocal space] were attributed to forbidden reflections of θ′ probably due to the incorporation of Cd in the θ′ structure. Schneider and Heimendahl speculated that at aging times shorter than those studied, a competing process between the metastable predecessors to T_B and T_1 is involved. However, no structural discussion was presented.

Hardy and Silcock (12) argued that Al-Li-Cu alloys along the pseudo-binary line Al-T_B could precipitate a structure preceding the T_B phase which could be indistinguishable from θ′. This structure could be formed if Li atoms replace Al atoms. At higher Li contents, the θ′ spots developed tails into the direction of the T_B spots. They interpreted this as a continuous transition from θ′ to T_B, and denoted this phase as θ_B'. They did not observe transition phases to the T_1 or T_2 phases. Noble, McLaughlin and Thompson (13), using electrical resistivity measurements, concluded that in Al-4.5Cu alloys with 0.4 and 1.5 percent Li contents, there are two kinds of clustering phenomena prior to the formation of θ′ precipitates. It was suggested that in the temperature range between 0-50°C, GP zones (similar to Al-Cu alloys) consisting of Cu atoms formed. Furthermore, between 80°C-130°C GP zones consisting of Cu and Li atoms were believed to be responsible for irregular changes in resistivity.

Avalos-Borja, Pizzo and Larson (10) studying an Al-2.6Li-1.4Cu suggested that a precursor to the T_1 phase and δ′ were the phases formed during aging having heterogeneous and homogeneous distributions, respectively.

Experimental Proceaure

Transmission electron microscopy (TEM) was performed in a Phillips 301 (and 420) electron microscope operating at 100kV. Thin foils were prepared by the double-jet polishing method in an electrolyte containing 0.75 Methanol + 0.25 Nitric acid at -25°C. Selected Area Electron Diffraction Patterns (SAEDP) were taken in three orientations, viz, (100), (110) and (112), respectively. Standard imaging techniques were employed, i.e., bright fields (BF) and superlattice dark fields (DF). All the TEM work was performed on a material stretched 2% prior to the artificial aging treatments.

RESULTS

Effect of Composition in T651 Temper Alloys Al-4.6Cu-1.1Li and 2020

The (100), (110) and (112) SAEDP's of the alloy Al-4.6Cu-1.1Li are shown in Figure II-1. Note faint $L1_2$ reflections in the (100) SAEDP. These $L1_2$ reflections correspond to the metastable Zr-rich dispersoids (Al_3Zr). A DF of these dispersoids is shown in Figure II-2, note also T_B' precipitates. Reflections corresponding to the T_1' and T_B' phases are also resolved. Dark field images of plate-like T_B' along the {100} planes and T_1' along the {111} planes are shown in Figure II-1 ((a) and (b) respectively).

Alloy 2020 (sample 523713-B) did not show $L1_2$ reflections (as in Figure II-1), since it does not contain Zr. However, due to the presence of Mn large elongated dispersoids $Al_{20}Cu_2Mn_3$ were resolved as shown in Figure II-3. Other metastable phases, T_1' and T_B', observed in Figure II-2 were also present in the alloy 2020. In both alloys, δ' reflections could not be observed.

Alloy Al-2.9Cu-2.1Li

The (100), (110) and (112) SAEDP's from the alloy Al-2.9Cu-2.1Li are shown in Figure II-4. Notice δ' and T_1' superlattice spots. Also note some T_2' superlattice spots and that the reflections at 2/3 (002) are absent, which corresponds to the (002) θ' planes. DF images of δ', T_2', and T_1' precipitates are shown in Figure II-5. Both T_1' and T_2' precipitates have a plate-like morphology. However, the T_1' phase has (111) habit planes, while T_2' phase has (100) habit planes.

Alloy Al-3.1Cu-2.2Li-1Mg

The (100), (110) and (112) SAEDP's of the alloy Al-3.1Cu-2.2Li-1Mg are shown in Figure II-6. The presence of δ', S' and T_1' reflections can be observed. DF images near (011) revealed a mixture of the three metastable phases as shown in Figure II-7 (a). Notice a high density of S′ precipitates along the {100} planes and a few T_1' plates along the trace of (111) planes. Typical distribution of δ′ precipitates are shown in Figure II-7 (b). The low density of T_1' precipitates observed in DF images is in agreement with the low intensity of T_1' reflections observed in SAEDP's.

Alloy Al-1.1Cu-2.9Li

The (100), (110) and (112) SAEDP's from the alloy Al-1.1Cu-2.9Li are shown in Figure II-8. Superlattice reflections indicate the presence of T_1' and δ′ phases. Also, diffuse streakings along the [100] direction can be observed. Faint superlattice reflections due to the T_2' precipitates are also resolved. Real space images resolved from different precipitates are shown in Figure II-9. The presence of plate-like and spherical precipitates can be observed in the BF images of Figure II-9.

DF images can resolve the morphologies of different phases present. Spherical δ′ and δ′ phase impinging on plate-like T_2' precipitates along the (100) planes are shown in Figure II-9 (b). The T_1' precipitates along the (111) planes and the T_2' precipitates on the (100) planes are shown in Figure II-9 (c) and (d), respectively. Precipitate free zones (PFZ) along the high angle grain boundaries were a common observation in these alloys. Sizes of PFZ ranged from 1000A to 3000A. Typical appearances of PFZ is shown in Figure II-9 (e and f). Grain boundary precipitates (probably δ) were observed these figures, were not identified by electron diffraction.

In the peak-aged condition, the Al-Li-Cu alloys showed increase in amount of δ′ with increase in (Li/Cu) ratio. The amount of T-phase decreased with (Li/Cu) ratio. The vol. %, morphology, and structure of T-phase depended on the amount of Li and Cu in the alloy.

Effect of Aging in Al-2.9Cu-2.1Li Alloy

The alloy Al-2.9Cu-2.1Li was aged at 191°C for different time intervals. TEM observations were made over the entire aging curve. The following is a selected few microstructural characterizations made on the underaged to overaged conditions. The microstructural changes the alloy undergoes due to aging from the very underaged (1.25 hrs.) to severely overaged (520 hrs.) treatments are shown in Figure II-10[(a) through (d)].

δ′ centered dark field image of underaged (1.25 hrs.) alloy, Figure II-10 (a) showed small spherical δ′ and δ′ coated on θ′-like platelets. At peak-age (18 hrs.), the dark field condition, Figure II-10(b), the structure indicated δ′ and θ′-like precipitates. δ′ seems to encase all three variants of the θ′-like precipitates. Overaging the alloy to 70 hrs., resulted in an increase in the number of T_1 type phases, as shown in Figure II-10(c). T_1-type phases were observed in the matrix and on the low angle grain boundaries. With further overaging the alloy to 520 hrs., the structure exhibited predominantly T_1-type precipitates, as shown in Figure II-10(d). In general, δ′ and T_1′-type precipitates coarsened with increase in the aging time. In particular, δ was observed on the high angle grain boundaries and T_1-like precipitates on the low angle boundaries. Occasionally, δ was found on the low angle grain boundaries.

In the previous section, it was pointed out by Rioja (3) that there could be precursory phases such as T_1' and T_2' prior to the formation of the T_1 and T_2 phases. While such transition phases could exist in the underaged to peak aged conditions, the overaged alloys seem to exhibit the T_1-type phase. In addition, there seems to be some controversy (15) on the platelet-like phase identification which needs to be resolved with further TEM analysis.

REFERENCES

1. D. B. Williams and J. W. Edington, Metal Science 9, p. 529, 1975.

2. T. H. Sanders and E. A. Starke, Jr., "Aluminum Lithium Alloys II", AIME, vol. 1, 1983.

3. R. J. Rioja, Unpublished Work, Alcoa, 1984.

4. D. B. Williams and J. W. Edington, Acta Met., vol. 24, p. 323, 1976.

5. B. Noble and G. E. Thompson, Met. Sci. J., vol. 5, p. 114, 1971.

6. S. F. Baumann and D. B. Williams, Scripta Met., vol. 18, p. 611, 1984.

7. H. Suzuki, M. Kanno and N. Hayashi, Jour. Jap. Inst. Light Met., vol. 32, p. 88, 1982.

8. B. Noble and G. E. Thompson, Met. Sci. J., vol. 6, p. 167, 1972.

9. G. H. Narayanan, B. L. Wilson and W. E. Quist, Ibid, p. 517, 1983.

10. M. Avalos-Borja, P. P. Pizzo and L. A. Larson, NASA Technical Memorandum 84385, 1983.

11. K. Schneider and M. Von Heimendahl, Z. Metallkda, vol. 64, p. 342, 1973.

12. H. K. Hardy and J. M. Silcock, J. Inst. Met., vol. 84, p. 423, 1955-1956.

13. B. Noble, I. R. McLaughlin and G. Thompson, Acta Met., vol. 18, p. 339, 1970.

14. R. Nosato and G. Nakai, Trans. Jpa. Inst. Met., vol. 18, p. 679, 1977.

15. M. Tosten, P. R. Howell, Unpublished Work, Penn. State Univ., 1984.

LIST OF FIGURES

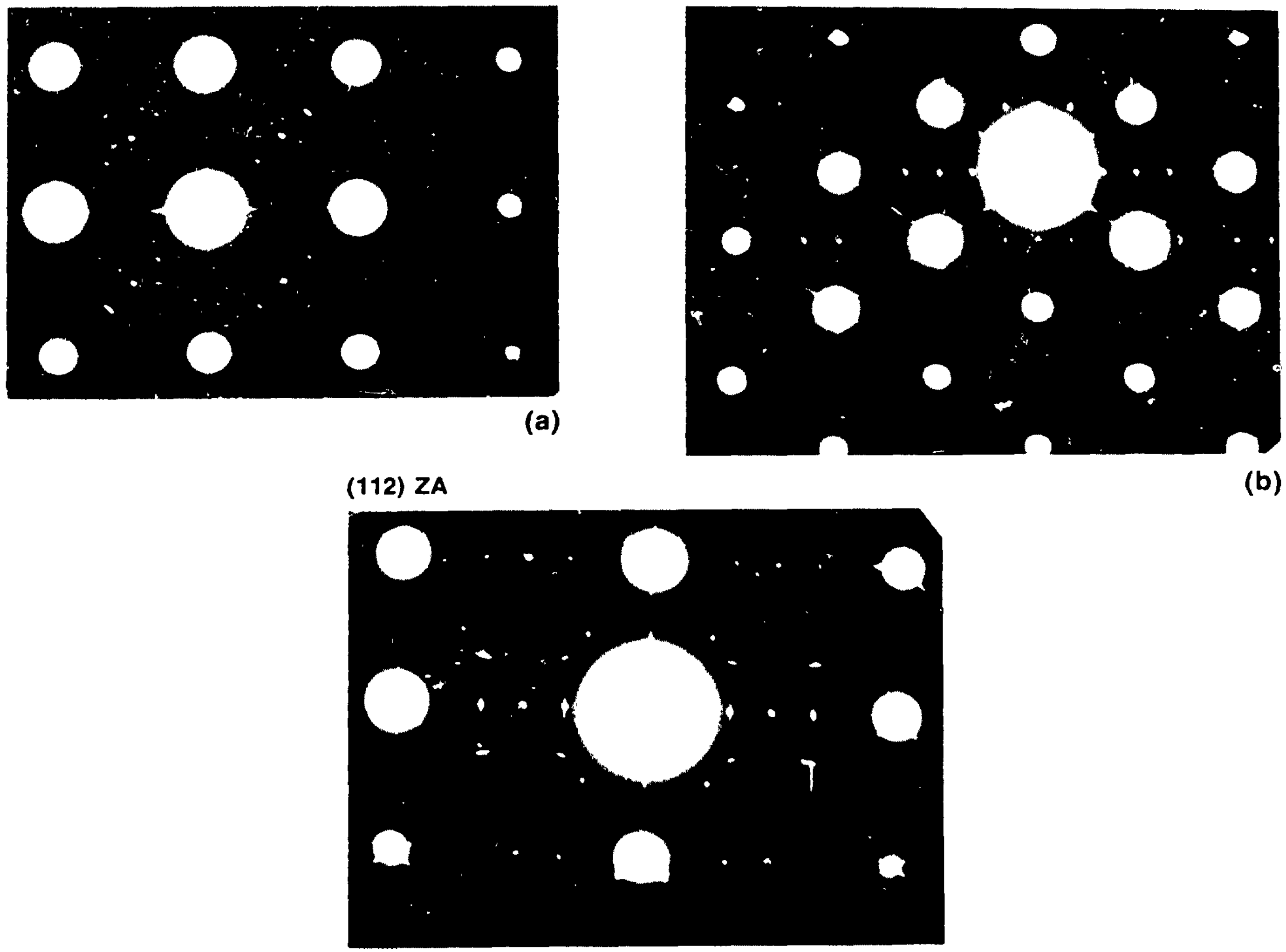

Al-4.6Cu-1.1Li-0.17 Zr
64 Hours at 160°C
Diffraction Patterns from Sample 548465. Note T_1' and T_B' Phases Along with $L1_2$ Spots from Al_3Zr Phase.
Figure II - 1

GA 16609 13

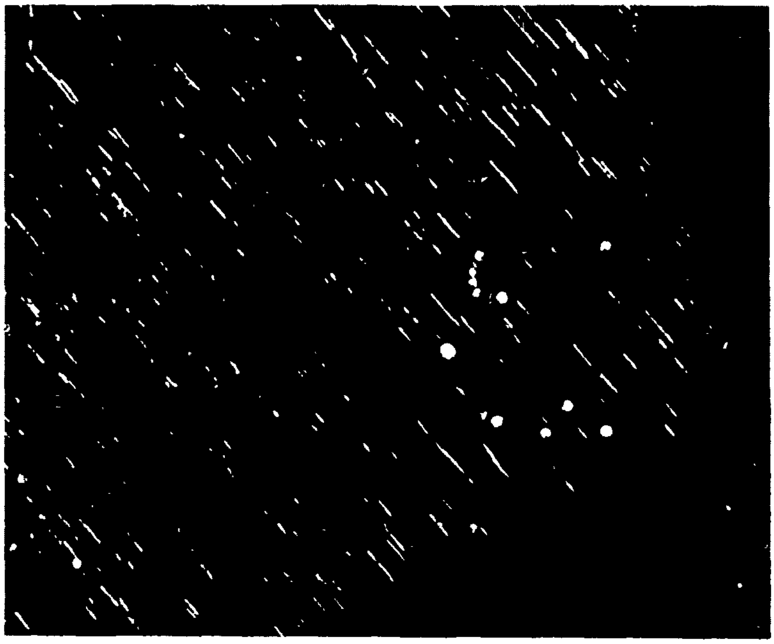

001

DF
(100) ZA
~1/2 (002) $\vec{g}$

$T'_B + Al_3Zr$

178 nm

$1\bar{1}1$

DF
(100) ZA
2/3 (022) $\vec{g}$

T'_1

384 nm

(b) Dark field image showing T'_1 along $(1\bar{1}1)$.

Al-4.6 Cu-1.1 Li-0.17 Zr
64 Hours at 160°C

Figure II - 2

(100) ZA

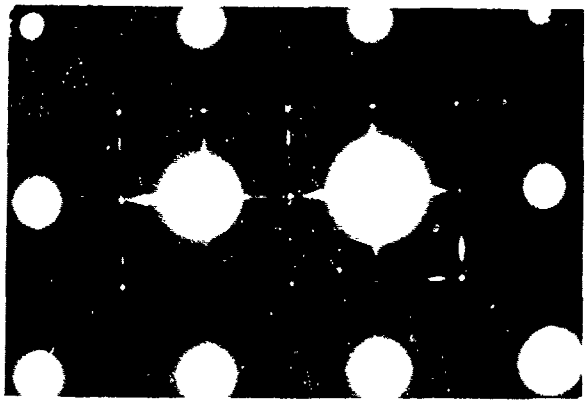

(a) Diffraction pattern showing T'_1 and T'_B phases.
Note that the intersections of streaks at (001) and (011) positions gives the appearance of $L1_2$ reflections.

DF
(100) ZA
~1/2 (002) $\vec{g}$

T'_B + Mn
Rich Dispersoids

139 nm

(b) Dark field showning T'_B and $Al_{20}Cu_2Mn_3$ dispersoids.

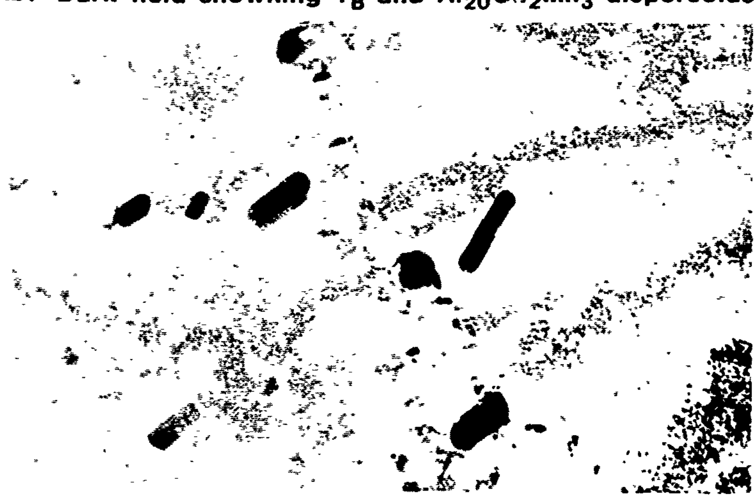

BF
(100) ZA
Multi-Beam

384 nm

(c) Bright field image showing $Al_{20}Cu_2Mn_3$ dispersoids.

Al-4.5 Cu-1.1Li-0.5 Mn
24 Hours at 160°C
Sample 523713-B (2020 alloy)

Figure II - 3

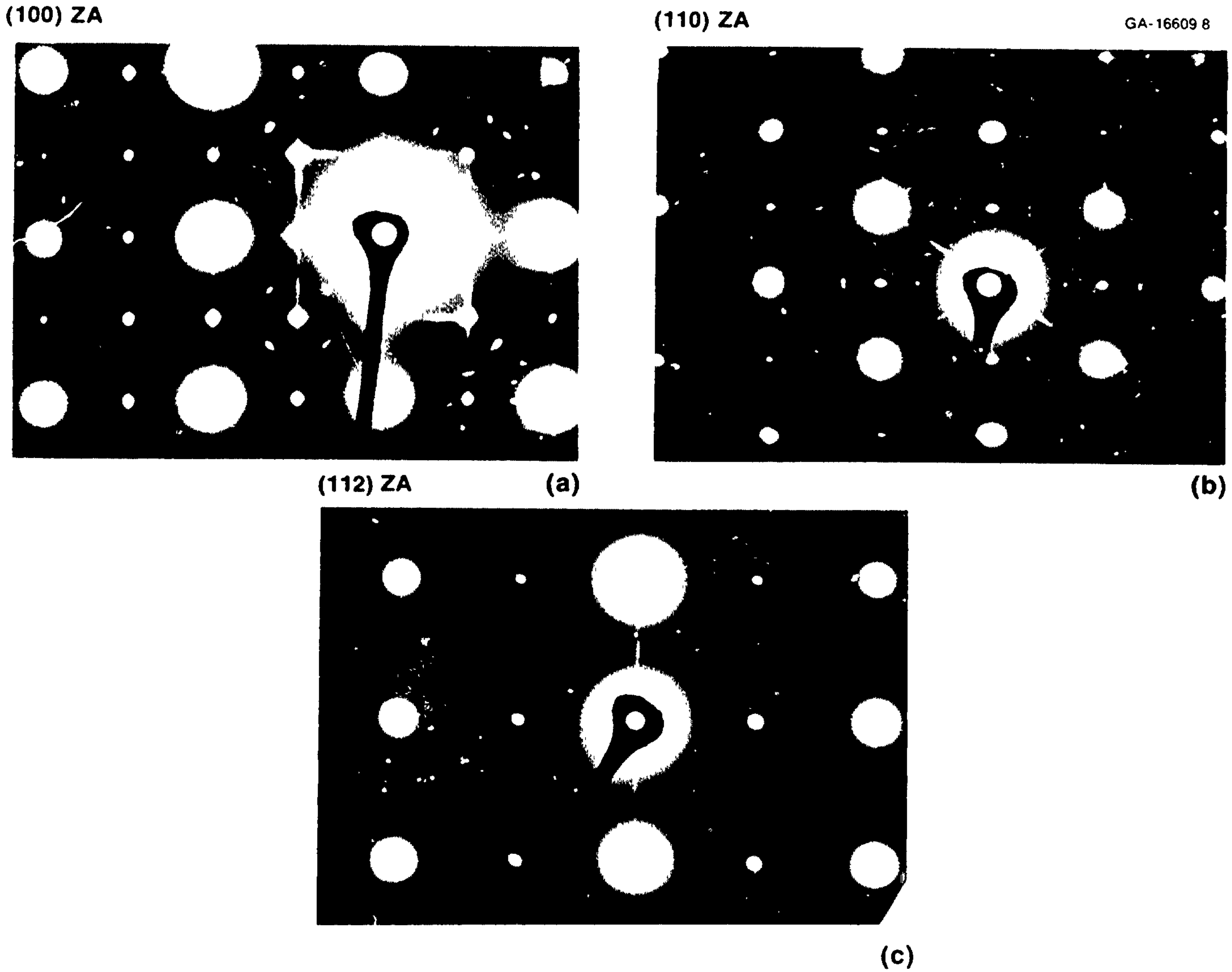

Al-2.9Cu-2.1Li-0.12Zr
18 Hours at 191°C

Diffraction Patterns from Sample 548466. Phases Present at T'_1, T'_2, δ'.

Figure II - 4

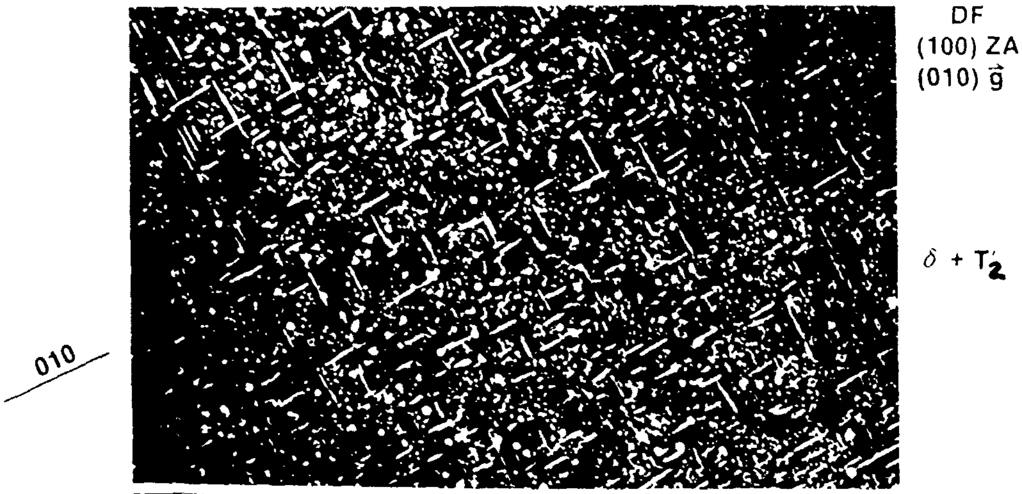

(a) Dark field showing δ' and T_2'

(b) Dark field showing only T_2'

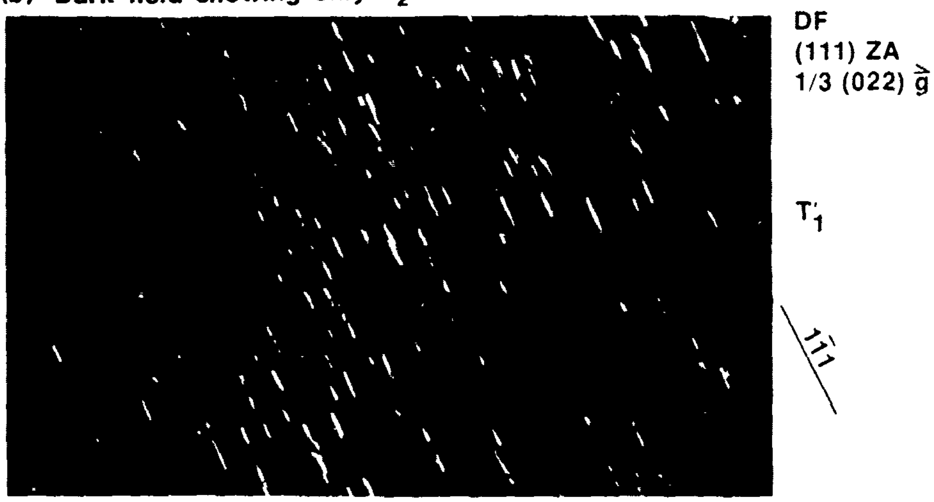

(c) Dark field showing T_1'

Al-2.9Cu-2.1Li-0.12Zr
18 Hours at 191°C

Figure II - 5

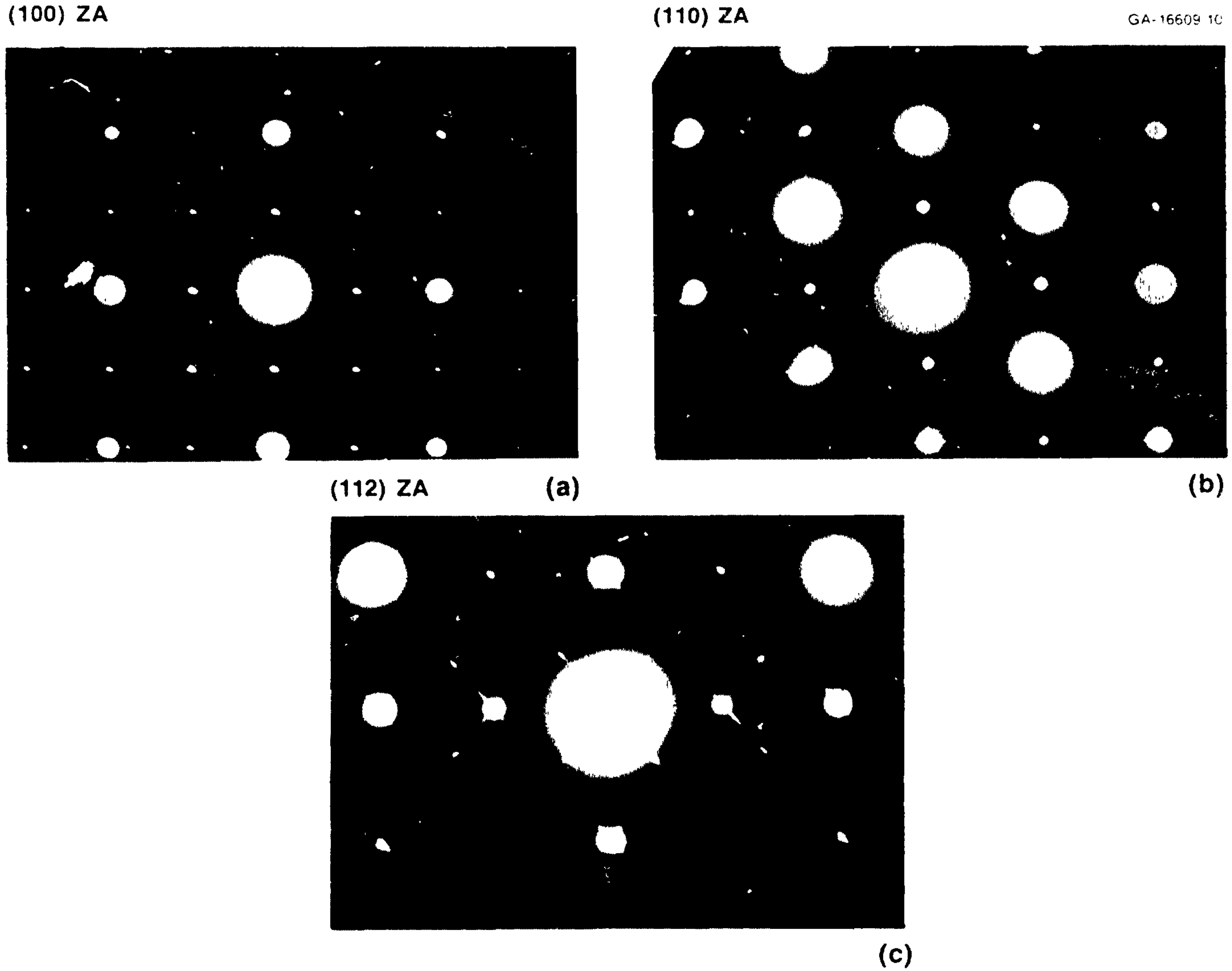

Al-3.1Cu-2.2Li-1.0Mg-0.13Zr
18 Hours at 191°C

Diffraction Patterns from Sample 504440. Note δ', S' and T_1' Phases.

Figure II - 6

GA 16595

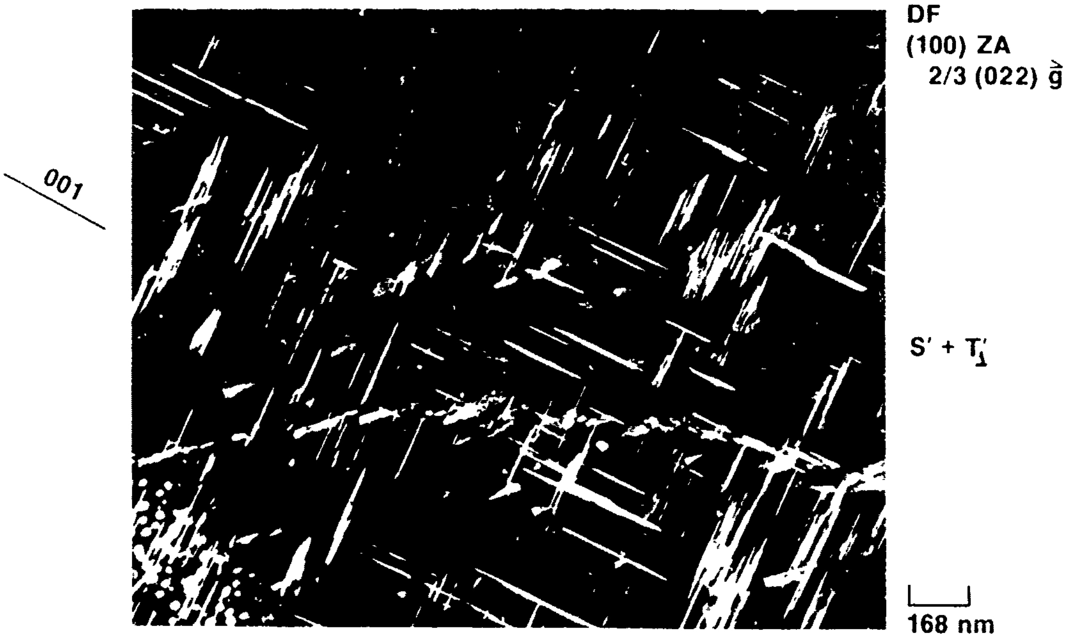

(a) Dark field showing δ' along (100), T_1' along (111) traces, and S′

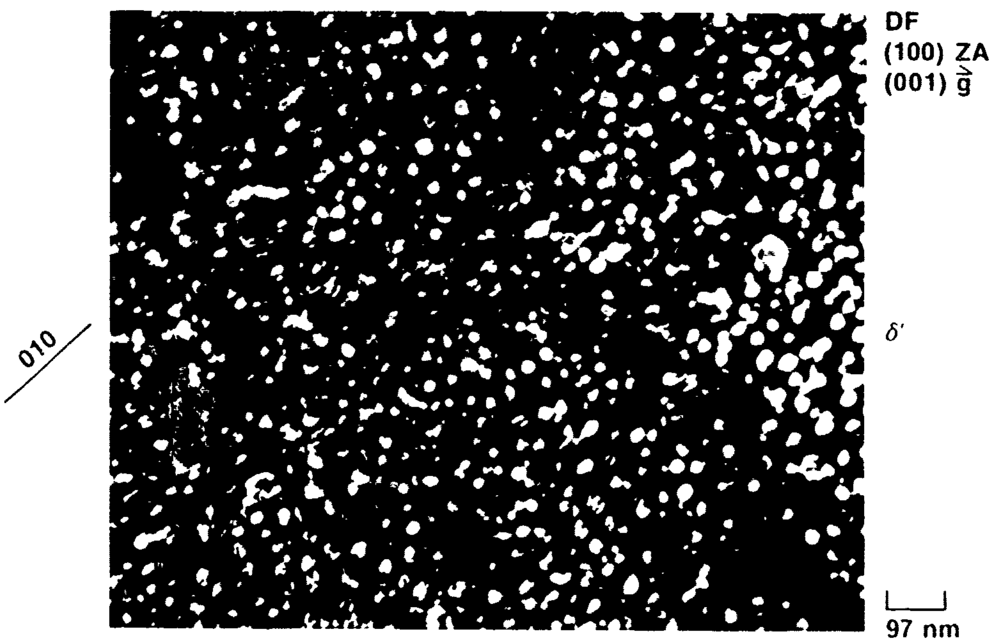

(b) Dark field showing δ' precipitates

Al-3.1Cu-2.2Li-1.0Mg-0.13Zr
18 Hours at 191°C

Figure II - 7

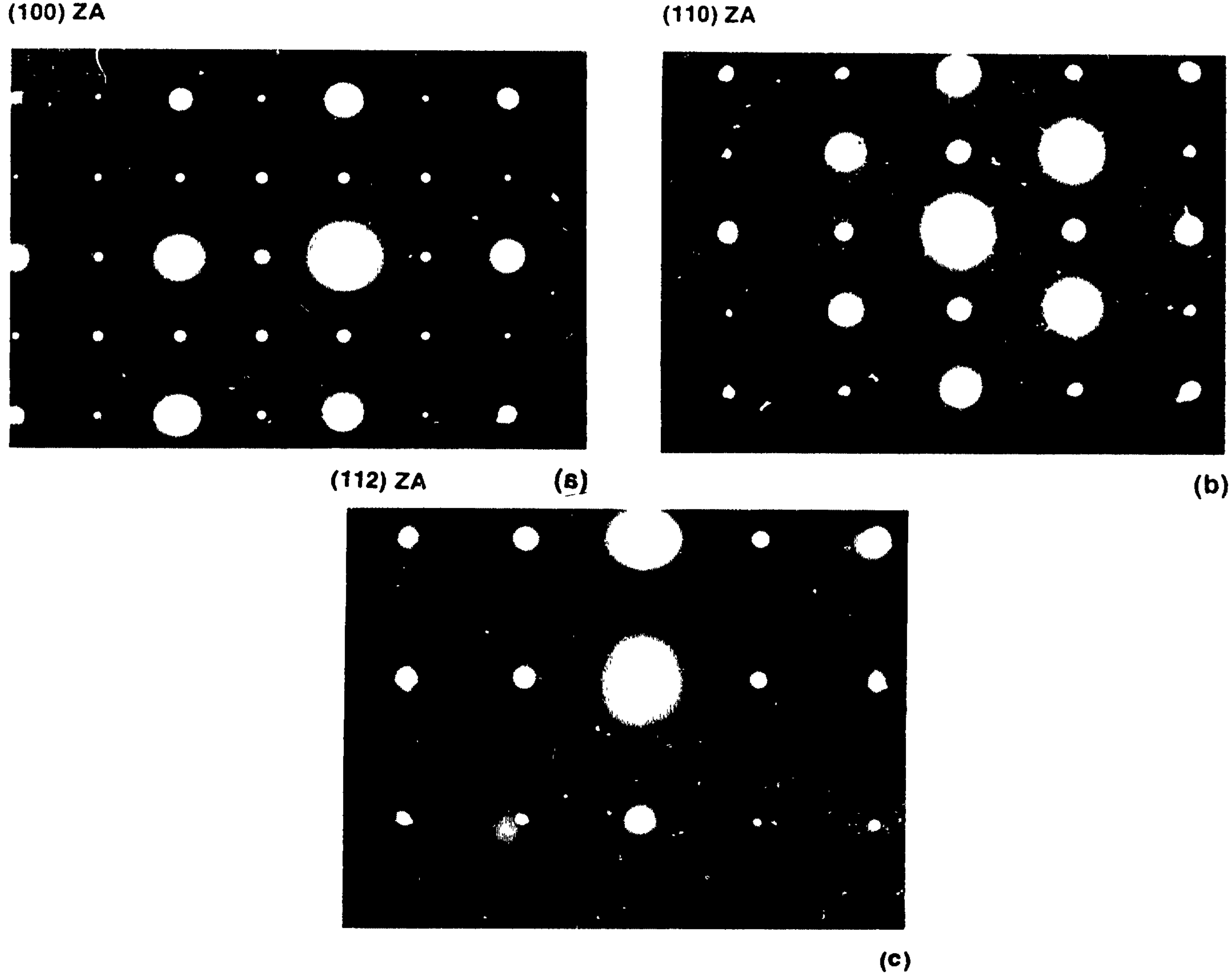

Al-1.1Cu-2.9Li-0.11 Zr
32 Hours at 191°C

Diffraction Patterns from Sample 548468.
Phases Present are δ', T'_1 and T'_2.
Figure II - 8

GA 166096

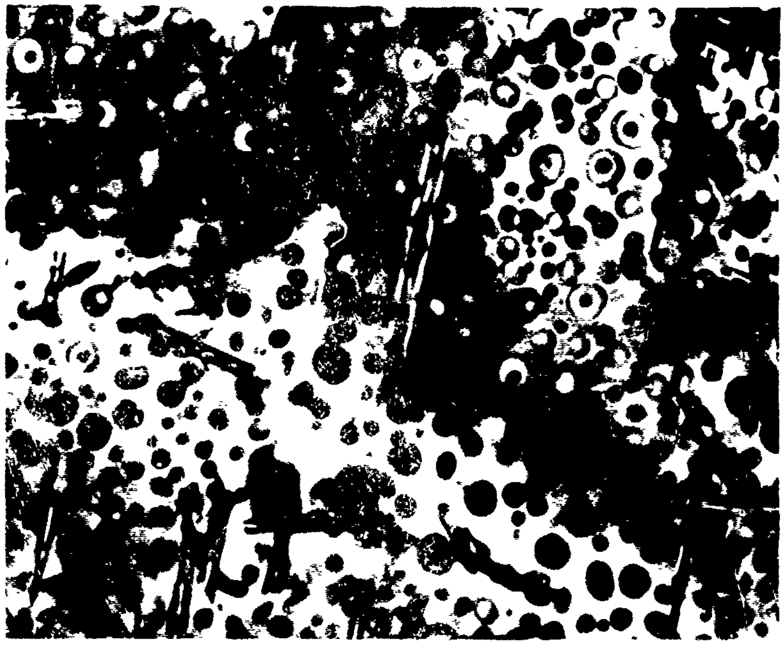

BF
Multi-Beam
(100) ZA

97 nm

(a) Bright field image from sample 548468

010

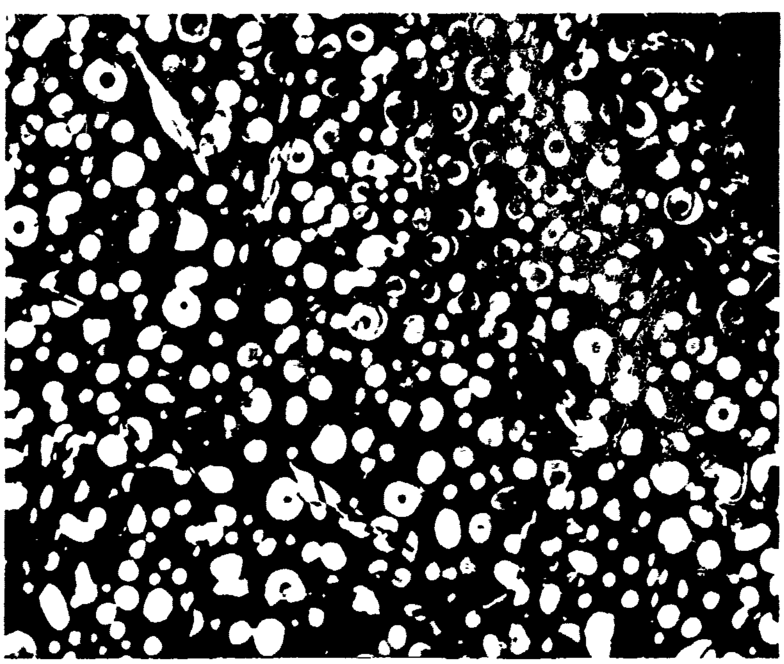

DF
g = 1/2 (022)
(100) ZA
δ'

(b) Dark field image of (a)

Al-1.1Cu-2.9Li-0.11Zr
32 Hours at 191°C

Figure II - 9

GA-16609 7

(c) Dark field of T_1'

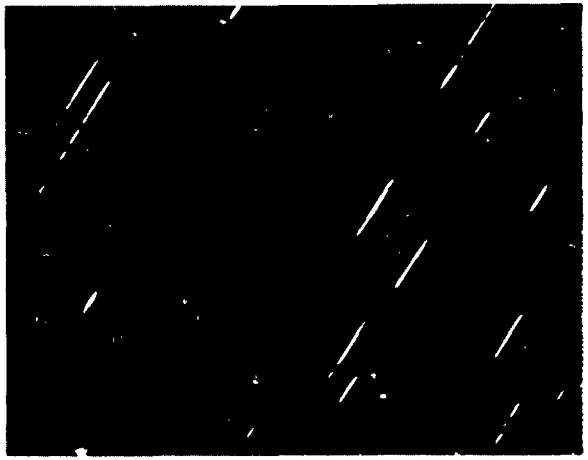

(d) Dark field of T_2'

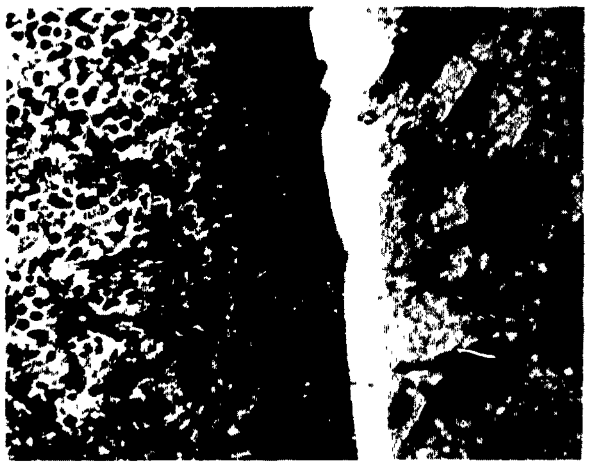

(e) Shows precipitate free zone at grain boundaries

(f) Shows precipitate free zone at grain boundaries

Figure II - 9 contd.

Sample 548466

GA 16595

Aged
191°C/2.25 h

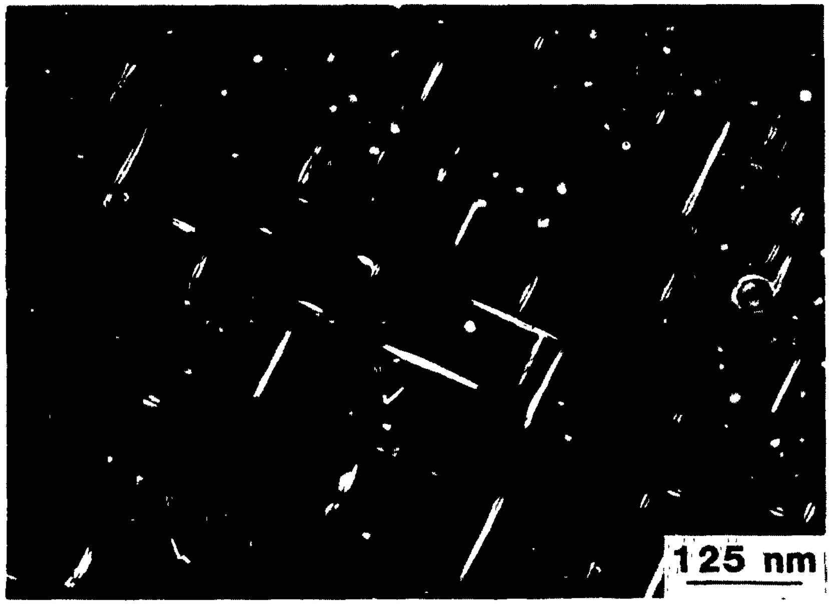

(a) Dark field showing δ' and θ'-like precipatates

Aged
191°C/18 h

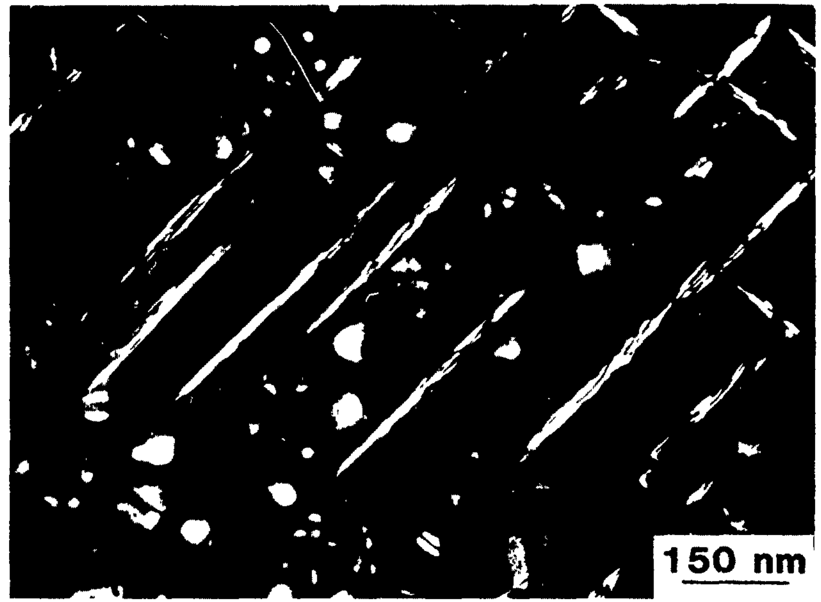

(b) Dark field showing coarse δ' and θ'-like precipitates

Figure II - 10

Sample 548466

GA 16595

Aged
191°C/70 h

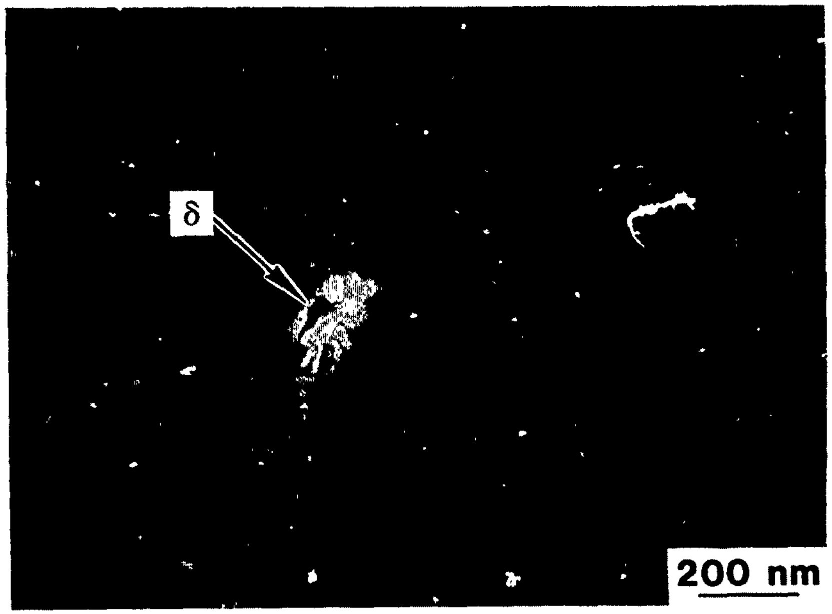

(c) Bright field image showing T_1 and δ on the grain boundary

Aged
191°C/520 h

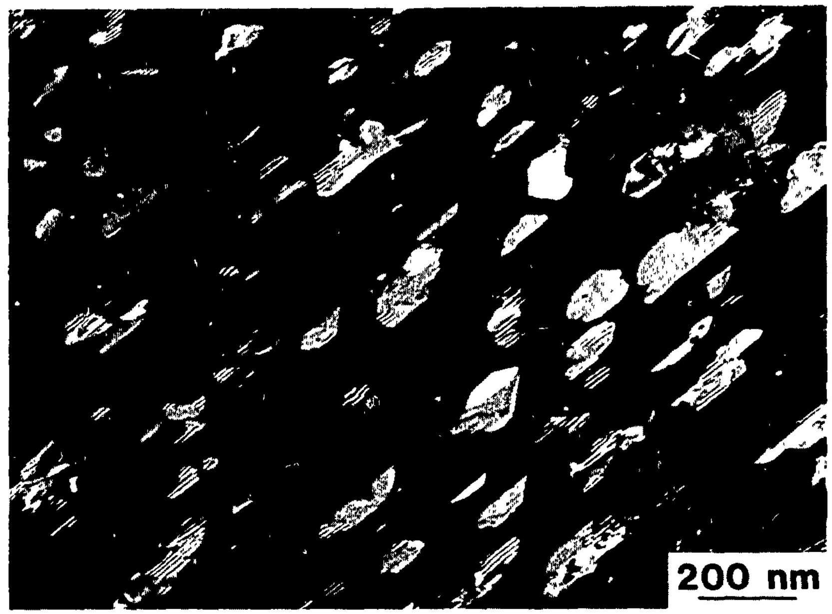

(d) Dark field image showing T_1

Figure II - 10 contd.

APPENDIX III

EXCO RATING OF AL-CU-LI-ZR ALLOYS

EXCO resistance of 12.7 mm (0.5 in.) thick plate of the four Al-Cu-Li-Zr alloys in the T651 temper were evaluated. Specimens were machined from the plates at the T/10 and T/2 plane locations. They were all tested in one group by totally immersing in the EXCO solution (4.0 M NaCl, 0.5 M KNO_3, and 0.1 M HNO_3) at 25°C (77°F) following ASTM Standard G34-79. The specimens were visually rated for exfoliation after one and two days of test duration. The test results are listed in Table III-1. Also, shown in Table III-1, for comparison, are the exfoliation ratings for plate of alloys 7075-T6, 7150-T6, and 2020-T651. Photographs (1X magnification) of the exfoliated specimens are shown in Figures III (a through d), respectively.

All the plate samples of Al-Cu-Li-Zr alloys (including the one with a 1.0% Mg content) showed the same resistance to exfoliation in the EXCO solution after two days, all rated EC (severe). However, the exfoliation developed at a faster rate on the alloy containing 1.0% Mg, as it showed an EC rating after just one day; whereas the other three Al-Cu-Li alloys generally exhibited EA ratings after one day. Generally, there are no differences in the EXCO ratings due to specimen location (T/10 and T/2) after one or two days exposure. Since these are qualitative results, attempts to extrapolate these results to other environments is not warranted.

TABLE III-1

RESULTS OF EXCO TESTS ON PLATE (T651) OF Al-Cu-Li ALLOYS

S. Number	Composition, % Cu	Li	Mg	Zr	Plate Thickness, mm	Machined Specimen Location	Exfoliation Rating (1) 1 Day	2 Days
548465-B1	4.6	1.1	0.0	0.17	13	T/10	EA, EA	EC, EC
						T/2	EA, EA	EC, EC
548466-B2	2.9	2.1	0.0	0.12	13	T/10	N, EA	EC, EC
						T/2	EA, EA	EC, EC
548468-B1	1.1	2.9	0.0	0.11	13	T/10	EA, EA	EC, EC
						T/2	EA, EA	EC, EC
504440-B1	3.1	2.2	1.0	0.13	13	T/10	EC, EC	EC, EC
						T/2	EB, EC	EC, EC
504412-B1-1, -2	7075-T6				38	T/10	EB, EB	EC, EB
547747-14A, -14B	7150-T6				13	T/10	EA, EA	EB, EC
523713-2	2020-T651				36	T/10	EB	EC
523713-1						T/2	EB	EC

Note: (1) Exfoliation rating according to ASTM Standard G34-79: N - no appreciable attack; EA - superficial exfoliation; EB - moderate exfoliation, and EC - severe exfoliation. Specimens totally immersed, machined surface top horizontal, in a solution of 4.0 M NaCl, 0.5 M KNO_3 and 0.1 M HNO_3 at 25±3°C (77±5°F).

LIST OF FIGURES

EXCO - 48 Hours

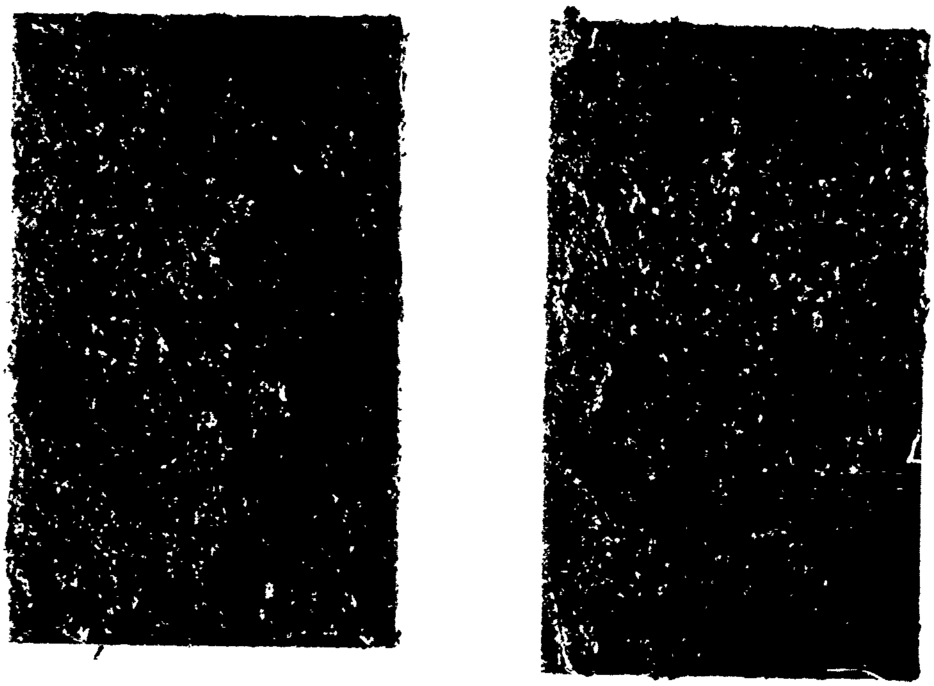

T/10 **T/2**

12.7 mm Plate

Al - 4.6Cu-1.1Li-0.17Zr

Appearance of Al-4.6 Cu-1.1 Li-0.17 Zr alloy specimens (EC exfoliation) at conclusion of the EXCO test. Specimens had not been cleaned after exposure but surface had been wet with deionized water prior to photographing to highlight the exfoliation. (1X mag.)

Figure III (a)

EXCO - 48 Hours

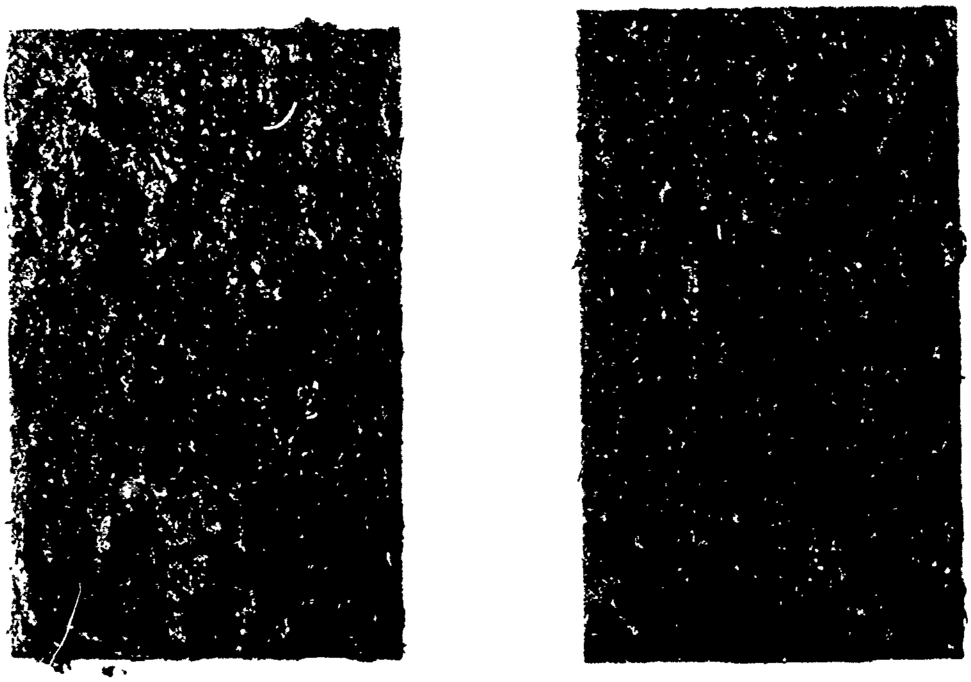

T/10 **T/2**

12.7 mm Plate

Al - 2.9Cu-2.1Li-0.12Zr

Appearance of Al-2.9 Cu-2.1 Li-0.12 Zr alloy specimens (EC exfoliation) at conclusion of the EXCO test. Specimens had not been cleaned after exposure but surface had been wet with deionized water prior to photographing to highlight the exfoliation. (1X mag.)

Figure III (b)

EXCO - 48 Hours

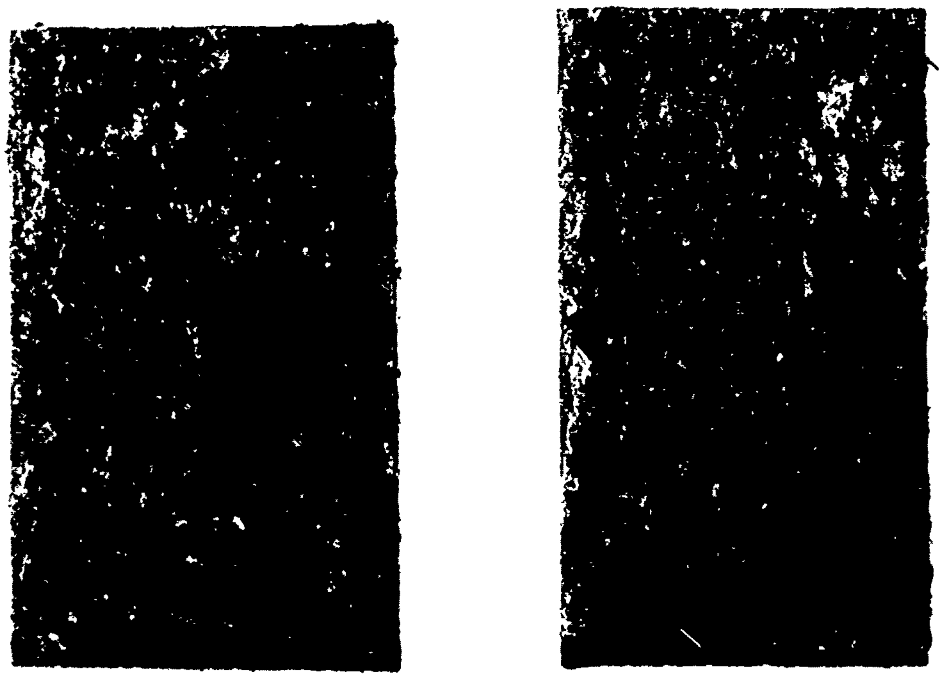

T/10 **T/2**

12.7 mm Plate

Al - 1.1Cu-2.9Li-0.11Zr

Appearance of Al-1.1 Cu-2.9 Li-0.11 Zr alloy specimens (EC exfoliation) at conclusion of the EXCO test. Specimens had not been cleaned after exposure but surface had been wet with deionized water prior to photographing to highlight the exfoliation. (1X mag.)

Figure III (c)

EXCO - 48 Hours

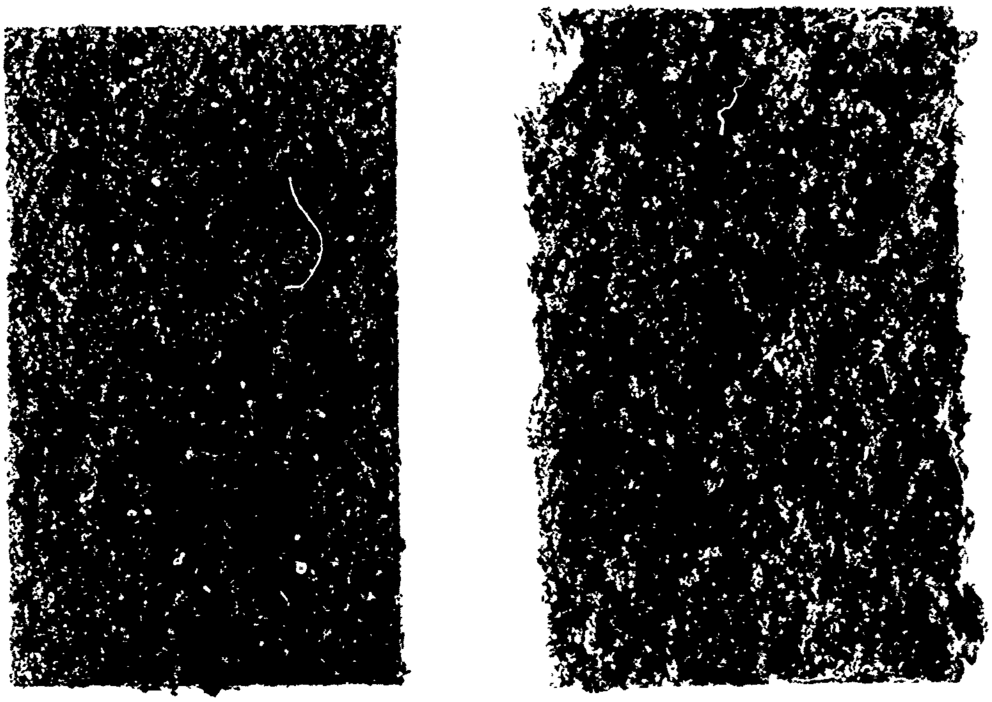

T/10 T/2

12.7 mm Plate

Al - 3.1Cu-2.2Li-1.0Mg-0.13Zr

Appearance of Al-3.1 Cu-2.2 Li-1.0 Mg-0.13 Zr alloy specimens (EX exfoliation) at conclusion of the EXCO test. Specimens had not been cleaned after exposure but surface had been wet with deionized water prior to photographing to highlight the exfoliation. (1X mag.)

Figure III (d)

APPENDIX IV

FATIGUE CRACK GROWTH RESISTANCE OF ALLOY AL-3.1CU-2.2LI-1.0MG-0.13ZR PLATE (T651 TEMPER)

The 1.0% Mg content in alloy Al-3.1Cu-2.2Li-1.0Mg-0.13Zr (S. No. 504440) resulted in about 2.0% by volume S-phase constituents. Median size of these particles was ~5 μm. The grain structure was nearly unrecrystallized (see Appendix I). Constant-amplitude (CA) and single-periodic-overload (OL) fatigue crack growth tests were conducted on plate (12.7 mm thick) of this alloy in the T651 temper, and the results compared to those for T651 plate (12.7 mm thick) of alloy Al-2.9Cu-2.1Li-0.12Zr (S. No. 548466) containing no Mg.

The CA FCG test results of Sample 504440 are compared with those of Sample 548466 in Figure IV-1. At stress intensity (ΔK) levels ≤ 4 MPa$\sqrt{m}$, the growth rates (da/dN) were similar in both samples. However, at higher ΔK levels (>4 MPa$\sqrt{m}$) the Mg-containing alloy showed higher growth rates than those for the alloy without Mg. This appears to be partly related to the lower toughness (K_Q=18 MPa$\sqrt{m}$) of Sample 504440, where high vol. % of constituents are observed, compared to that of Sample 548466 (K_Q=35 MPa$\sqrt{m}$), even though the tensile-yield strength in the longitudinal direction of both samples were nearly the same. SEM fractography of Sample 504440, shown in Figure IV-2, indicates some crystallographic fracture features at low ΔK=2.8 MPa$\sqrt{m}$ compared to high ΔK=8 MPa$\sqrt{m}$ where secondary cracks were commonly observed along with some constituents.

Under the same OL FCG test conditions, the Mg-containing alloy showed similar crack growth (crack length, a, vs. load cycles, N) behavior to the non-Mg-containing alloy for crack lengths $\leq$45 mm and significantly faster crack growth for crack lengths > 45 mm as shown in Figure IV-3. In terms of (da/dN) vs. ΔK, shown in Figure IV-4, the OL FCG behavior of Sample 504440 is comparable to that of Sample 548466 at $\Delta K \leq 6$ MPa$\sqrt{m}$. Above ΔK=6 MPa$\sqrt{m}$ the da/dN rates of Sample 504440 increased dramatically with respect to Sample 548466. At ΔK=6 MPa$\sqrt{m}$, the calculated K_{max}=16.1 MPa$\sqrt{m}$ becomes comparable to the K_Q=18 MPa$\sqrt{m}$ of Sample 504440; hence fast fracture processes can occur. SEM fracture surface features of Sample 504440, shown in Figure IV-5 (a through d), indicate that beyond ΔK=5 MPa$\sqrt{m}$ the crack retardation line spacing increases dramatically with increased ΔK (or crack length). In between crack retardation lines, fast fracture is evident in the form of intergranular fracture. Intrinsic FCG behavior under these OL conditions could be a complex interaction of ΔK (with loading and crack length) and the response of microstructure to FCG.

In order to describe the FCG behavior of alloy Al-3.1Cu-2.2Li-1.0Mg in detail, experiments relating to crack branching, oxide thickness measurement and grain boundary-matrix microstructural analysis is needed.

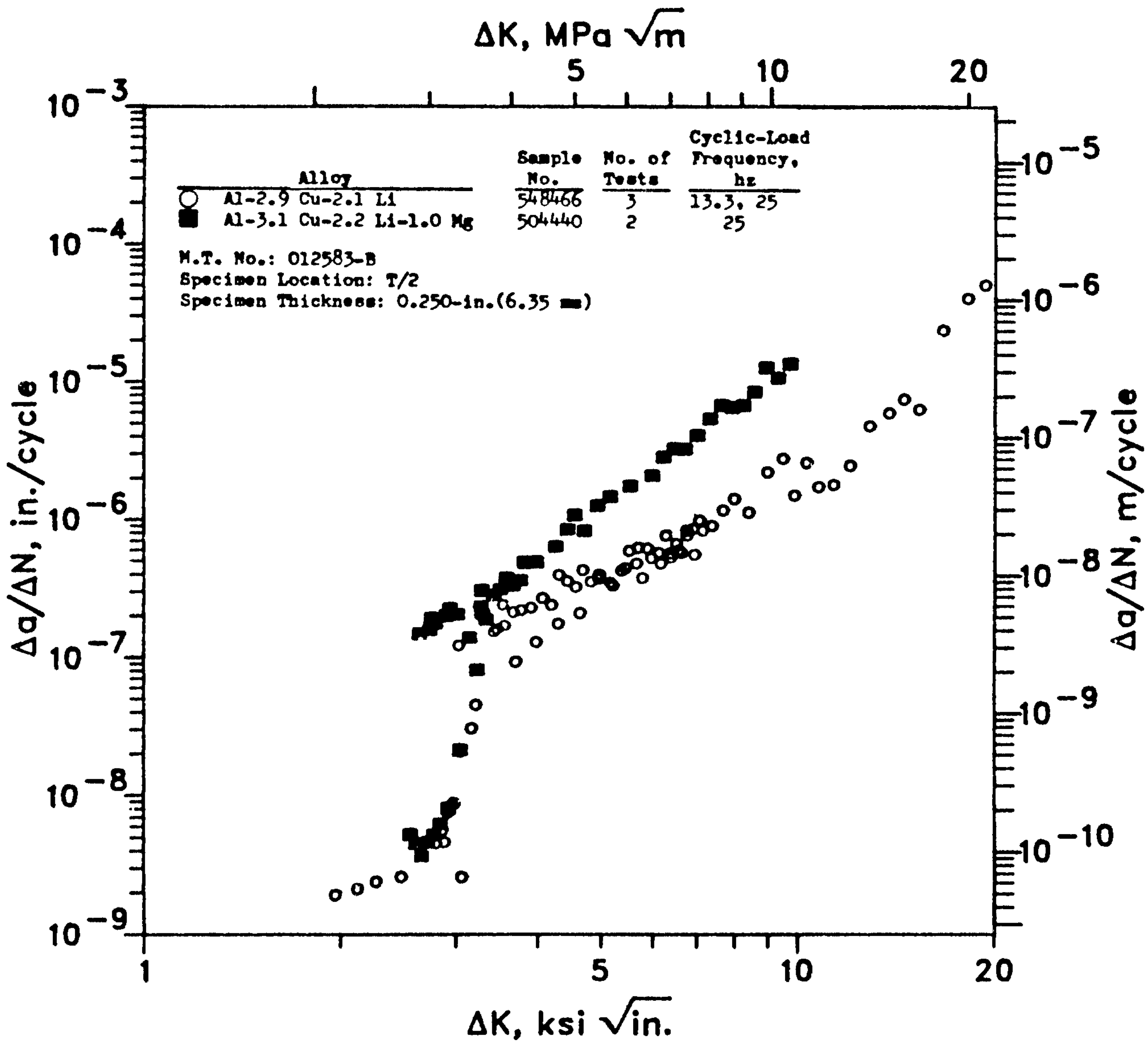

Comparison of Constant–Load–Amplitude Fatigue Crack Growth Data for Laboratory Fabricated Aluminum Alloys (2.9 Cu – 2.1 Li) – T651 and (3.1 Cu – 2.2 Li – 1.0 Mg) – T651 Plate, 0.5–in. (12.7 mm) thick L–T orientation, R–Ratio = +0.33, High Humidity (R.H.>90%) Air

Figure IV-1

GA 17387

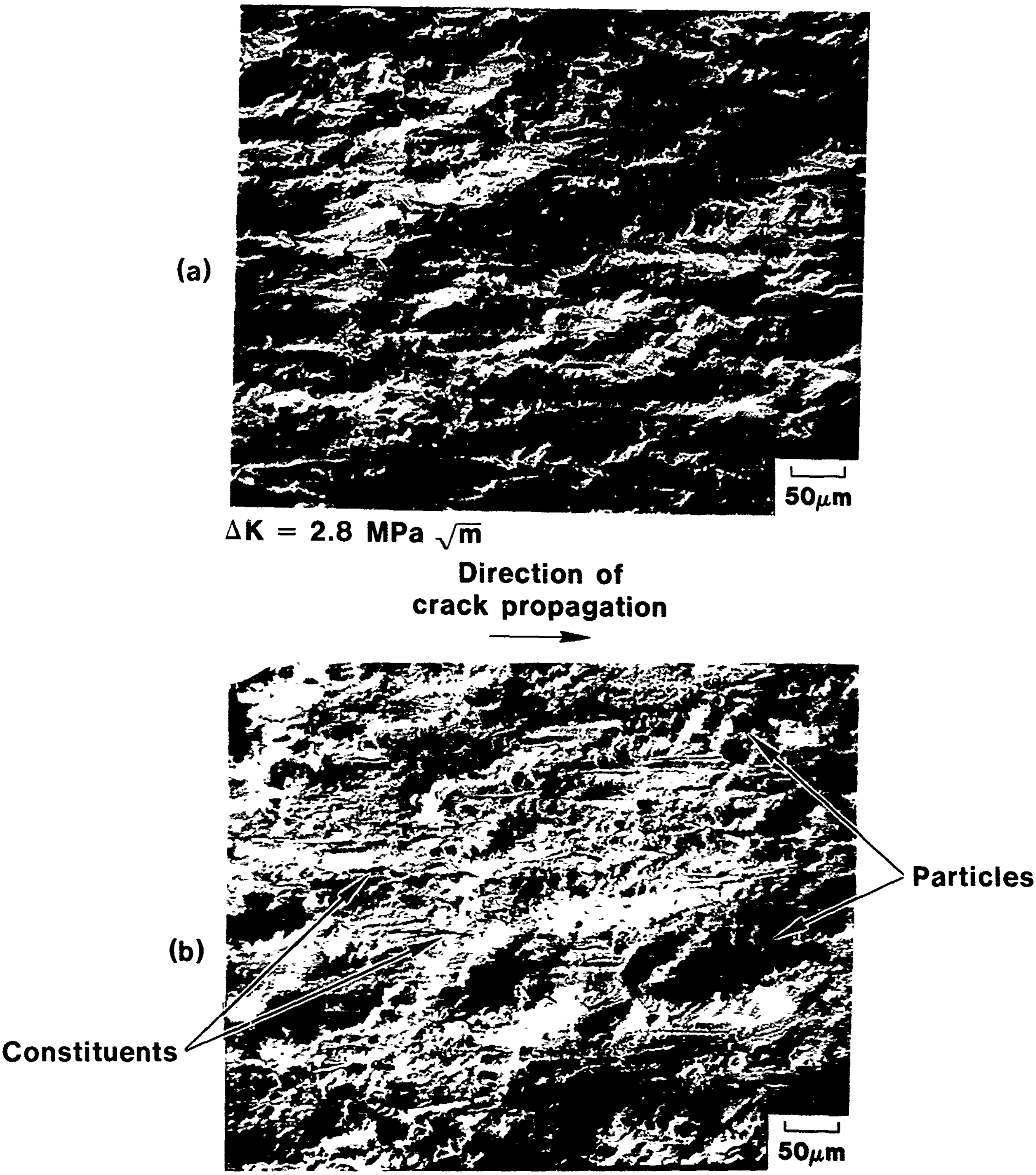

SEM Fractographs of CA Fracture Surface of CT FCG Specimen 504440-L-T-1 (Al-3.1 Cu-2.2 Li-1.0 Mg Alloy T651 Plate) at ΔK = 2.8 and 8 MPa $\sqrt{m}$

Figure IV-2

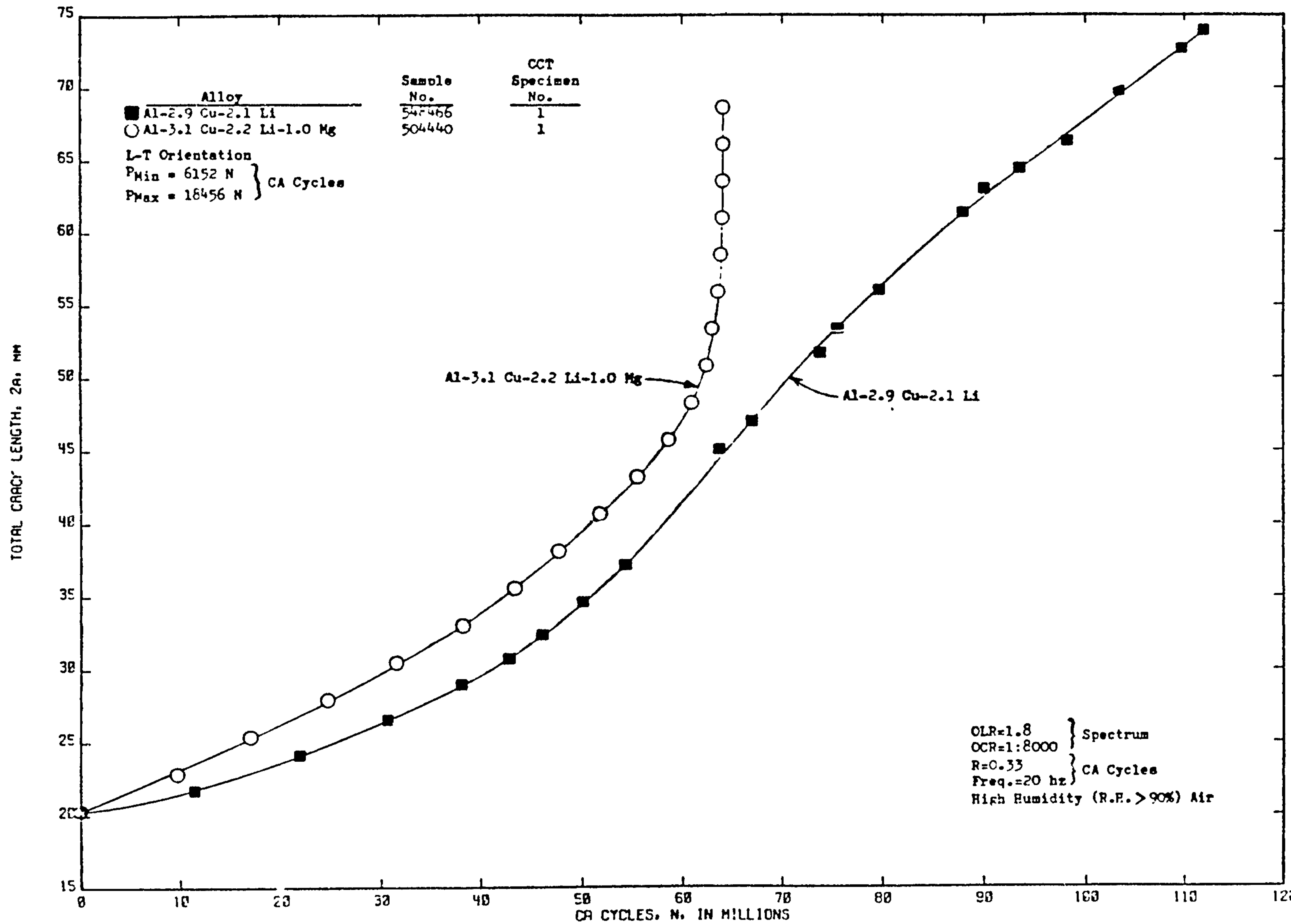

COMPARISON OF TOTAL CRACK LENGTH VERSUS NUMBER OF CA CYCLES DATA FROM SINGLE PERIODIC OVERLOAD FCG TESTS OF LABORATORY FABRICATED T651 PLATES (12.7 MM THICK) OF ALUMINUM ALLOYS (2.9Cu-2.1Li) AND (3.1Cu-2.2Li-1.0Mg)

Figure IV-3

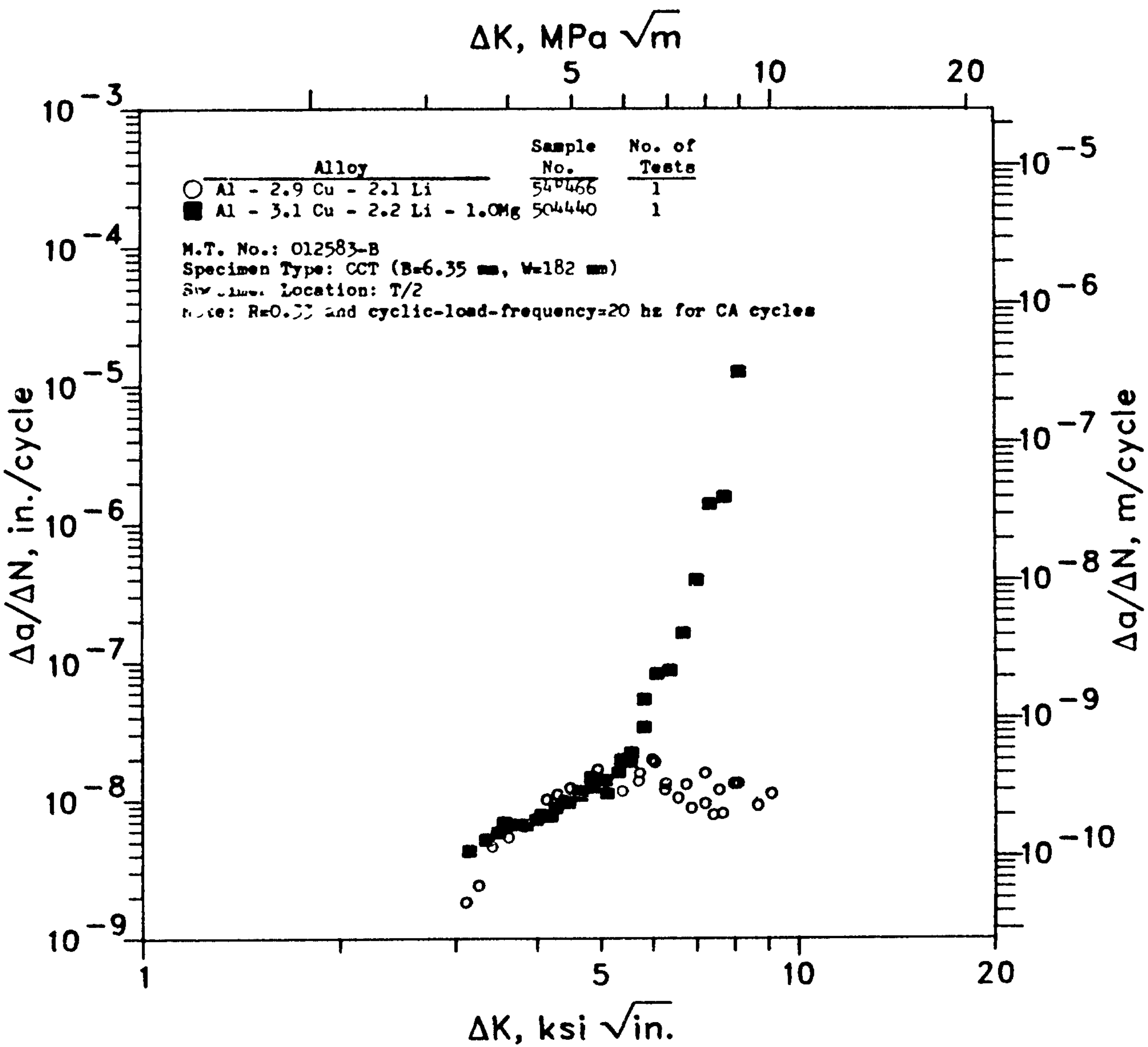

Comparison of Overload Spectrum (OLR=1.3, OCR=1:8000) Fatigue Crack Growth Data for Laboratory Fabricated Plates, 0.5–in. (12.7 mm) thick, of Two Al–Li Alloys (T651 Temper) L–T Orientation, High Humidity (R.H.>90%) Air

GA 17322

(a)

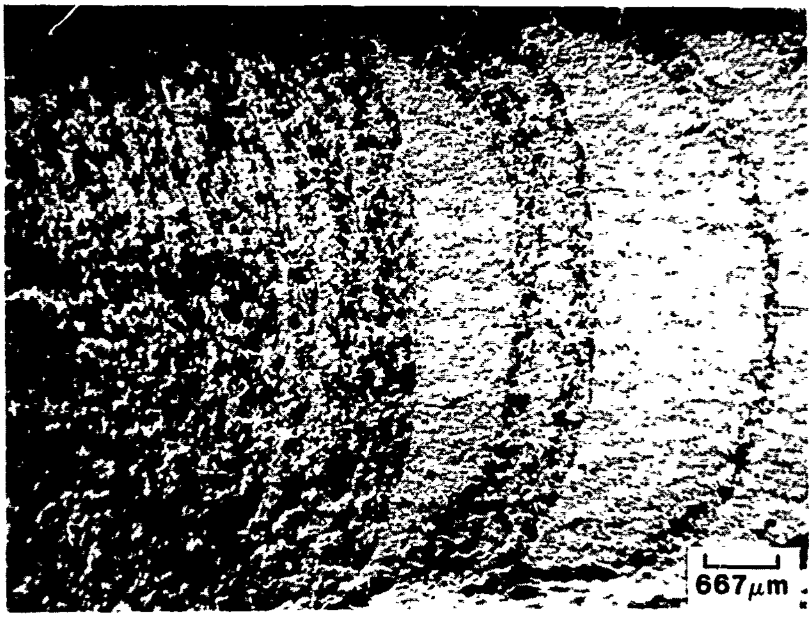

ΔK = 6 MPa $\sqrt{m}$

Direction of
crack propagation

(b)

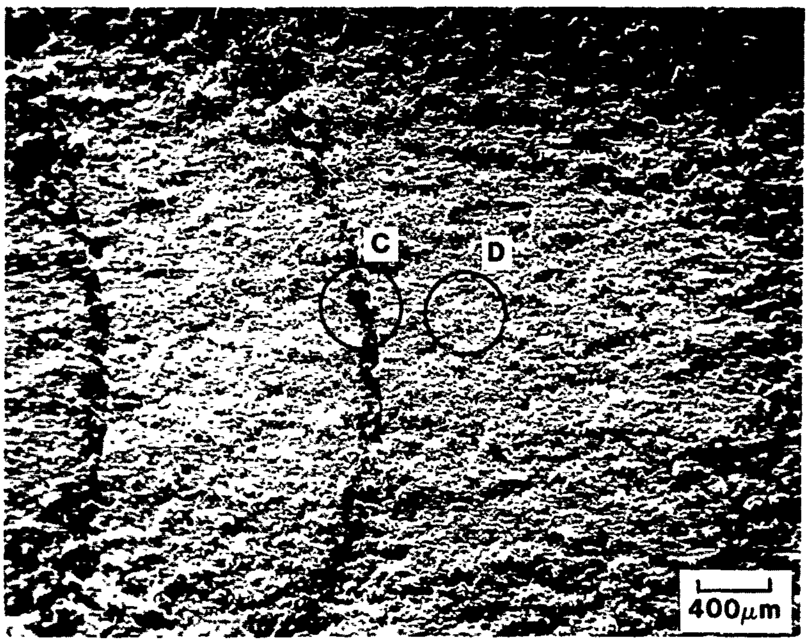

ΔK = 8 MPa $\sqrt{m}$

SEM fractographs of OL fracture surface of CCT FCG specimen 504440-L-T-1 (Al-3.1 Cu-2.2 Li-1.0 Mg alloy T651 plate) at ΔK = 6 and 8 MPa $\sqrt{m}$

Figure IV-5 (a,b)

Direction of
crack propagation

GA 17322

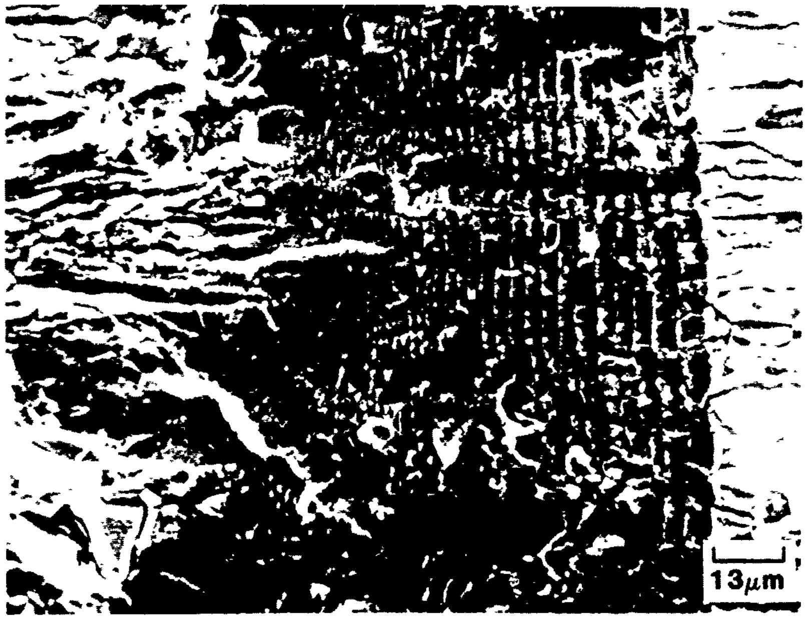

$\Delta K = 8$ MPa $\sqrt{m}$

(c) SEM fractograph of fracture surface within circled area "c" shown in (b)

$\Delta K = 8$ MPa $\sqrt{m}$

(d) SEM fractograph of fracture surface within circled area "d" shown in (b)

Figure IV-5 (c,d)